CRANFIELD UNIVERSITY

R EVANS

FOCUSED ION BEAM MACHINING OF HARD MATERIALS FOR MICRO ENGINEERING APPLICATIONS

SCHOOL OF APPLIED SCIENCES

PhD THESIS

Academic year: 2008-09

Supervisor – D. Allen

May 2009

CRANFIELD UNIVERSITY

SCHOOL OF APPLIED SCIENCES

PhD THESIS

Academic Year 2008-2009

R EVANS

Focused ion beam machining of hard materials for micro engineering applications

Supervisor: D Allen

May 2009

Abstract

The Focused Ion Beam (FIB) milling of single crystal diamond was investigated and the beam drift and mill yield were quantified. The effect of water assistance on the milling of diamond was found to double the yield. The surface morphology that spontaneously forms during milling was measured and the mechanisms behind its formation investigated. The effect of gallium implantation on the diamond crystal structure was measured by x-ray diffraction.

Chemical vapour deposited polycrystalline diamond (PCD) has been machined into micro scale turning tools using a combination of laser processing and FIB machining. Laser processing was used to machine PCD into rounded tool blanks and then the FIB was used to produce sharp cutting edges. This combines the volume removal ability of the laser with the small volume but high precision ability of the FIB.

Turning tools with cutting edges of 39µm and 13µm were produced and tested by machining micro channels into oxygen free high conductivity copper (OFHCC). The best surface quality achieved was 28nm Sq. This is compared to a Sq of 69nm for a commercial PCD tool tested under the same circumstances. The 28nm roughness compares well to other published work that has reported a Ra of 20nm when machining OFHCC with single crystal diamond tools produced by FIB machining.

The time taken to FIB machine a turning tool from a lasered blank was approximately 6.5 hours. Improvements to the machining process and set up have been suggested that should reduce this to ~1 hour, making this a more cost effective process.

PCD tools with sinusoidal cutting prongs were produced using FIB. The dimensions of the prongs were less than 10µm. The tools were tested in OFHCC and the prongs survived intact. Changes to the machining conditions are suggested for improved replication of the prongs into metal.

Sapphire was FIB machined to produce nano and micro patterns on a curved surface. The sapphire is part of a micro injection mould for replication of polymer parts. The comparative economics of hot embossing and injection moulding have been studied. Injection moulding was found to be the more cost effective process for making polymer parts at commercial production levels.

Acknowledgements

I wish to thank the following people:

My supervisor Prof David Allen for his support and guidance during my time at Cranfield.

Dr Silvia Marson for her help during my work.

Mr Andrew Cox of Contour Fine Tooling for supplying the diamonds for my work.

Dr Isidro Durazo – Cardenas and Mr Alan Heaume for the machining trials of the tools.

Mr Andy Dyer for assistance with the FIB.

Dr Paul Jones for his time and AFM skills.

Dr Tan Jin for help with the CAD designs.

Prof Moreton Moore at Royal Holloway University for his advice about x-raying of diamond.

The Nanotechnology group 10.30am coffee crowd for their collective wit and wisdom.

My office mates for their thoughts on a whole range of subjects most of them totally unrelated to engineering.

Leigh Kirkwood, Stuart Martin, Kate Panikowska and Jo Zawadzka for the good times.

The 06/07 Apocalyptic cows Ultimate Frisbee team for being and continuing to be a great group of friends.

Contents

List of figures

List of tables

List of notation

AFM – atomic force microscope
CAD – computer aided design
CVD – chemical vapour deposition
FIB – focused ion beam
HPHT –high pressure high temperature
HSS – high speed steel
LMIS – liquid metal ion source
OFHCC – oxygen free high conductivity copper
PCD – polycrystalline diamond
SCD – single crystal diamond
SEM – scanning electron microscope
T_g – Glass temperature
UFA – unwanted face angle
WC – tungsten carbide
XeF_2 – xenon difluoride

Chapter 1

1.0 - Thesis structure

The thesis is structured as follows:

Abstract and acknowledgements

Chapter 1: introduction.

Chapter 2 describes the 3D-Mintegration project, the need for diamond tooling that has arisen from it and a comparative cost study of polymer processing methods.

Chapter 3 is the literature review covering FIB technology, diamond tooling, FIB processing in general, FIB processing of diamond in particular, FIB created diamond tooling and some of the models created to describe aspects of diamond behaviour during FIB processing.

Chapter 4 describes the equipment, materials and methods used during the experimental work.

Chapter 5: the results obtained and the discussion of them.

Chapter 6: conclusions and suggestions for further work.

References: a list of the published outputs resulting from my work and the formal presentations I have given. In the appendix is the material relating to an x-ray synchrotron study of FIB machined single crystal diamond.

1.1 – Introduction

The drive to reduce the size of modern engineering products and devices is creating a need for smaller machining tools to produce metal parts with micro features. These parts need to be of the same quality, or better, than the macro parts made by larger conventional tools.

The production of micro medical devices is one of the aforementioned drivers. Methods need to be found to produce cheap disposable devices for medical testing in an efficient cost effective manner and one such method is injection moulding. The extension of this polymer mass production technique to the micro scale requires micro moulds to be fabricated. This raises challenges for the machining of the mould as the feature sizes shrink. The features need to be produced with surface finishes of less than 1µm Ra. This degree of quality is currently provided by single crystal diamond or tungsten carbide tooling. Diamond tooling delivers a better surface finish but the tools are more expensive than tungsten carbide and the shrinking of diamond tooling to the micro scale is non trivial. The conventional grinding techniques used to produce diamond tools have limitations at the scale of tens of microns, the size of fluid channels that are needed for micro/nanofluidic devices.

Fluidic devices also known as lab on a chip devices, are designed to carry small amounts of liquid (micro/nano litres) for testing purposes (Marson 2008). Medical diagnostics is one of the uses of this technology. The attraction of microfluidics for testing blood is the low fluid volume required. This is beneficial for patients as they do not have to provide large volumes of blood, of which they may not be capable, for example the elderly or babies. The small volume of blood means small flow channels are needed with widths in the order of 100µm with tolerances of ~5µm. These narrow channels are the driver for the small diamond tools.

A technique that has previously been shown capable of producing tools at this scale is FIB machining (Vasile 1996). FIB machining uses a beam of accelerated ions to remove material from a sample by transfer of kinetic energy from the ions to the atoms in the sample. As this is a non contact process it causes little stress in the sample and has sub micron beam control resolution. Any solid material can be machined as it is not a chemical process. This ability to remove precise amounts of material with minimal damage makes FIB machining a powerful technique at the nano and micro scale. However if FIB is to be used as part of a manufacturing process chain it must be economical to produce diamond tools by this method. Showing that the cost of tools produced by this method is not prohibitive is important.

The micro medical device work is part of a larger EPSRC project called 3D-Mintegration. This is looking at the production of integrated 3D micro devices from the modelling and design stage, through manufacturing, to the final assembly and packaging. The micro fluidic device is one of the project demonstrators designed to show the capabilities and potential of integrating the production chain. The Cranfield part of the microfluidic process chain is shown in figure 1.1.

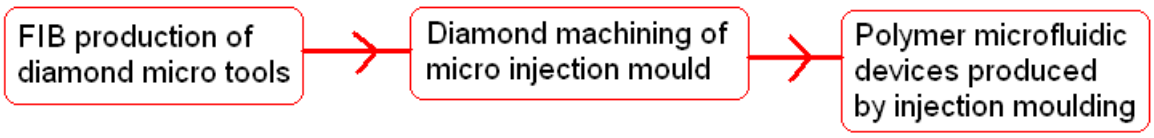

Figure 1.1 – Part of the microfluidic device production chain

1.2 - Aims of work

- To understand the FIB milling behaviour of diamond.
- To produce micro scale diamond tools by FIB machining.
- To show that the metal surfaces generated by the tools are good enough to meet the standards required for micro injection moulding of microfluidic devices.

- To show that the cost of FIB produced tools can be economic in the production chain.
- To use the precision machining capabilities of the FIB to provide micro machining options for the other 3D-Mintegration demonstrators.

Chapter 2

2.0 - The 3D-Mintegration project

This chapter sets out the background to the 3D-Mintegration project, the microfluidics demonstrator, how FIB relates to micro moulding and the economics of micro moulding.

2.1 – Project background

This PhD is part of the 3D-Mintegration Grand Challenge funded by the Engineering and Physical Sciences Research Council through their research grant, EP/C534212/1, “3D-Mintegration – The Design and Manufacture of 3D Integrated Miniaturised Products” (3D-Mintegration). This is a nine million pound, four year project, which started in October 2005, involving Brunel University, University of Cambridge, Cranfield University, Heriot-Watt University, University of Greenwich, Loughborough University, University of Nottingham and the National Physical Laboratory. The main industrial partners are Unilever, Unipath, Epigem, Tecan, Battenfeld and MBDA. Cranfield’s role is to provide 3D processing capabilities for producing parts of the demonstrators.

The aim of the 3D-M project is “To provide a radically new way of thinking for the end-to-end design, processing, assembly, packaging, integration and testing of complete 3D miniaturised/integrated ‘3D Mintegrated’ products” (3D-Mintegration); essentially moving beyond the existing 2D and 2.5D micro manufacturing techniques that industry uses today. These are often derived from the silicon processing industry, and are not suitable for producing truly 3D devices. The project deliverables are demonstrators which will show the techniques and knowledge developed during the four years. The demonstrators were a microfluidic device for a medical application, a health and usage monitoring multifunctional sensor, a rotary encoder and a micro probe measuring system. Wherever possible, commercially available equipment is to be used to ease the transfer of any new techniques and knowledge from the project to industry.

2.2 – Microfluidic demonstrator

The PhD research has been primarily towards providing FIB technologies for the manufacture of the microfluidic demonstrator. This is a red blood cell separator for detecting and separating foetal cells in the blood of pregnant women. The foetal cells can then be tested for abnormalities. This will be a less invasive test than those currently used (Marson 2008). It is a disposable one time use product that requires only a small blood sample of micro litres. It is to be made out of polymer by the micro injection moulding process which allows large numbers of devices to be made for a low unit cost. Cranfield purchased a Battenfeld Microsystem 50 micro injection moulding machine in 2006 and is investigating the techniques and mould design needed for successful replication of complex polymer parts, (Kersaudy-Kerhoas 2007), (Marson 2009a), (Marson 2009b). How blood moves through narrow channels, the efficiency of the separation and the possible damage to red blood cells has also been studied, (Benade 2007), (Kersaudy-Kerhoas 2008), (Marson 2008).

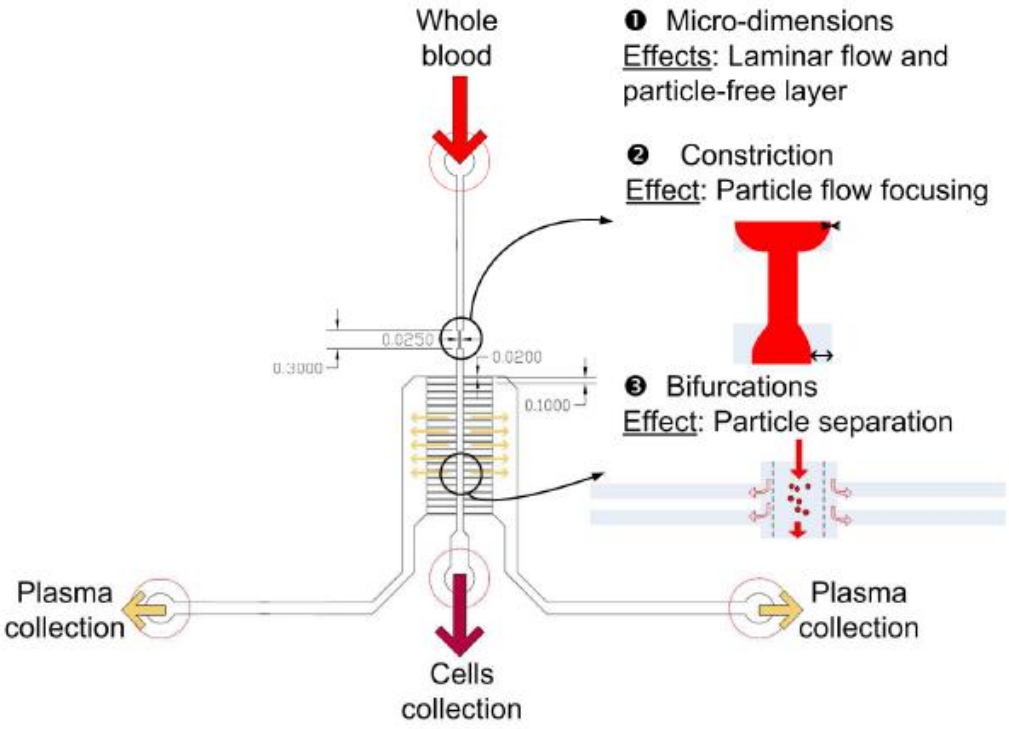

Figure 2.1 – 2.5D Blood cell separator (after Kersaudy-Kerhoas 2008)

The early design of the 2.5D separator is shown in figure 2.1. The blood is injected into the top and travels towards a 25µm wide, 300µm long constriction. The flow is laminar before passing through the constriction. The narrowing of the channel causes the blood cells, ~8-20µm in size, to travel down the middle of the channel. The smaller sized blood component, the plasma, which is mostly water, flows along the walls at the channel edges. This flow change is called the Fahraeus-Lindqvist effect (Marson 2009b). The plasma acts as a lubricating agent for the cells. The flow is still laminar after the constriction but the red cells are concentrated in the middle of the channel, with a thicker plasma layer on either side.

The series of bifurcation channels after the constriction cause the plasma to preferentially flow out of the main channel. Each side channel is 20µm in width compared to the 100µm wide main channel. This loss of plasma to the side channels is caused by another process, the Zweifach-Fung effect. This causes the blood cells to preferentially travel in the main channel as it has a higher flow rate than the side channels (Yang 2006) (Marson 2009b). The cells follow the streamlines of the unperturbed flow down the centre of the main channel whereas the plasma flow at the main channel edges is affected by the turbulence caused by the side channel entrances. Part of the plasma is lost at each bifurcation until the two blood components are collected at the device exit.

The 2.5D design has been improved on by the full 3D design. This is made up of circular injection moulded polymer discs that are assembled into a cylinder (Marson 2009b). The moulded discs are shown in figure 2.2.

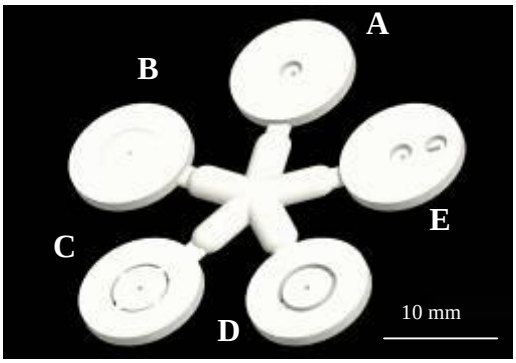

Figure 2.2 – Design of the injection moulded component discs
(after Marson 2009b)

The assembled discs' dimensions are shown in figure 2.3. The narrowest dimension of the blood channels is 50µm for the bifurcation channels. A model of an assembled device with multiple bifurcation discs is shown in figure 2.4.

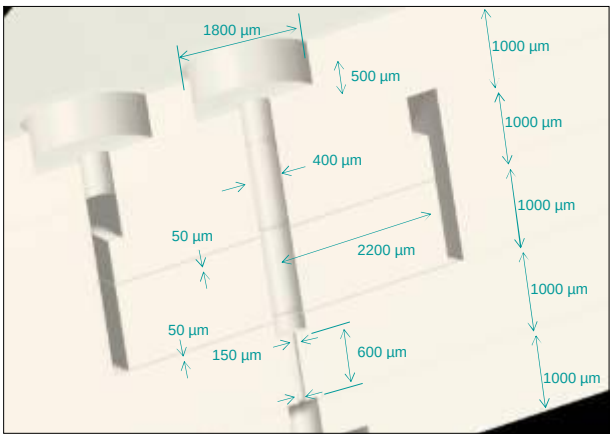

Figure 2.3 - Critical dimensions in the 3D microfluidic device (after Marson 2009b)

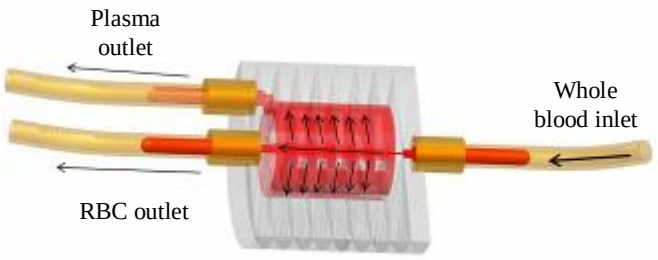

Figure 2.4 – CAD model of the assembled device including inlet and outlet tubing
(after Marson 2009b)

The cells are sorted with a high degree of efficiency, an injection moulded prototype with three pairs of bifurcation channels sorted 79% of the red blood cells into the correct collection point (Marson 2009b).

2.3 – FIB for micro mould fabrication

The production of micro polymer parts requires micro scale features to be produced in the polymer mould. The surface finish on the mould surfaces has to be of high enough quality to ensure that the blood flows in the required way in the device. (Prentner 2009) found a significant difference in the flow behaviour of horse blood in channels with roughnesses (Rz) of 1.8µm and 60nm. In the 1.8µm channel the plasma layer flowing at the edges of the channel was thicker than in the smoother channel. This effect will be greater in human blood than in horse blood due to the larger human red blood cells. Thus the surface roughness will have a greater effect on the flow of human blood (Prentner 2009). The available conventional micro tools either do not provide a good enough surface finish (steel or tungsten carbide) or have limitations on the shape that can be produced (ground single crystal diamond). Hence the aim of showing that micro tools can be made from diamond to the required shapes for a reasonable cost.

The prototype in (Marson 2009b) was made using an aluminium (Alumold 1-500) mould machined with tungsten carbide milling tools. The surface finish was ~1.7µm Rz.

The blood channels machined for the tests carried out in (Marson 2008) are described in (Zdebski 2008). These tests were to study the damage caused to red blood cells as they pass through flow constrictions. Channels of 100, 50 and 20µm width, 100µm depth and 300µm in length were planed into aluminium 6061-T6 with single crystal diamond tools of the same widths. This is the same length as the constriction in the separator design. After optimizing the cutting strategy, the surface finishes on the floor of the channels were 19, 15 and 8nm Ra for the 100,

50 and 20µm tools respectively. This is an improvement over the tungsten carbide tools. The surface roughness produced by FIB tools needs to be of this order.

2.4 - Comparative economics of polymer micro device production

The comparative economics of the microinjection moulding process were investigated early on during the PhD in conjunction with Dr Silvia Marson, resulting in a conference keynote paper (Marson 2007) at the 20th International Conference on Computer-Aided Production Engineering CAPE 2007, Glasgow, 6th-8th June 2007. This was based on cost figures obtained for an earlier MSc project at Cranfield (Carson 2004). This work was carried out to confirm that the injection moulding process was the correct process to use for the blood separators at commercial production levels. The rest of this section is extracted from (Marson 2007).

The polymer moulds needed for injection moulding are one of the main issues and costs of the process. Moulds need to be long lasting as they are expensive to produce, requiring machining with the cost rising with the complexity of the part. Moulds wear out due to the effect of repeated injection/ejection cycles which subject the mould to high temperatures and pressures, and also the chemical effects of the polymer. This limits the materials that the mould can be made of to hardened steel and hard electroformed metals like nickel. Moulds of these materials can produce millions of parts before needing replacing. The cycle time for each part is normally only a few seconds. The high cost of the mould means that large numbers of parts need to be produced before injection moulding becomes competitive compared to hot embossing.

Hot embossing uses a preheated stamp pressed into a thermoplastic polymer sheet. For small scale production the stamp is usually made of silicon or electroformed nickel instead of steel. They are made from a master stamp as

pressing stamps wear out after ~250,000 hits and need replacing. Any number of pressing stamps can be made from one master stamp.

The pressing stamp is hotter than the glass temperature (Tg) of the polymer causing the stamp features to be replicated in the polymer. The stamp is then cooled below Tg and retracted from the polymer. The cycle time is dependant on the size of the features being created and the polymer being used. It can range from a couple of minutes to half an hour. The slowness of this method, compared to injection moulding, is balanced by the lower cost of the stamp compared to a mould, and the fact that hot embossing machines are cheaper than injection moulders.

The economics of the two processes were compared to see what production levels are needed for injection moulding to become competitive. Due to the limited nature of the study, it was assumed that equal amounts of labour were required for each processing route. The influences of labour and cycle time were discussed in a qualitative way. As both processes are mostly automated, there is little need for labour during production and most of the labour is for the process set-up and for quality inspection. When considering the set-up work, hot embossing is typically quicker than injection moulding because it is easier to insert a holder and stamp into a hot embossing machine than it is to install and connect up a more complex injection mould.

In the estimation of costs for injection moulding the cost of the mould or moulds needed was considered fixed for a particular job. For hot embossing, the master and the first stamp is a fixed cost, whereas any more stamps required represents a variable cost dependent on the number of parts being produced. The cost per part made can be reduced by increasing the number of parts per stamp/mould. This extends the cross-over point at which injection moulding becomes cheaper. However, as the number of part cavities increases, the dimensional control over

the produced part starts to be lost. This is particularly relevant when producing micro components. Once moulded, the parts need to be diced up which is an additional processing cost.

The costs detailed in table 2.1 do not include the initial investment for purchasing equipment. However, this was taken into account by amortising into the variable cost per hit. The indicated cost for the hot embossing stamp refers to a stamp produced by an electroformed master and the hot embossing hit variable cost is the same regardless of the number of parts per stamp. The cost figures had been previously provided by Unipath Ltd., Bedford; Epigem Ltd., Redcar and Accuromm UK Ltd., Milton Keynes for a Cranfield MSc group project (Carson 2004). However their analysis of the data, and the resulting conclusions regarding comparative costs, contained errors. These were corrected in our analysis.

Hot Embossing	**Injection Moulding**
Fixed costs	
Holder £5000	Mould £16000
Stamp £2500	
Master £1000	
Variable costs	
Material per part £0.0065	
Variable cost per hit £0.6	Variable cost per injection (including material) £0.3

Table 2.1 - Typical fixed and variable costs for HE and IM

The total cost of making a given number of parts is

Total cost = fixed costs + (N/n) x variable costs

where N is the number of parts to be produced and n is the number of parts per mould/stamp.

The cost for an injection moulded part is:

$$CostIM = 16000 + 0.3 \cdot (N / n) \qquad \text{Equation 1}$$

The cost for a hot embossed part is:

$$CostHE = 6000 + 2500 \cdot S + 0.6 \cdot (N / n) + 0.0065 \cdot N \qquad \text{Equation 2}$$

where $S = N/(n \cdot 250000)$ to account for the replacement of the stamp every 250,000 parts.

Equations 1 and 2 were plotted for production numbers up to 5 million. Figure 2.5 shows the trend in the costs for a large-scale production. Figure 2.6 shows the trend for a small to medium scale production.

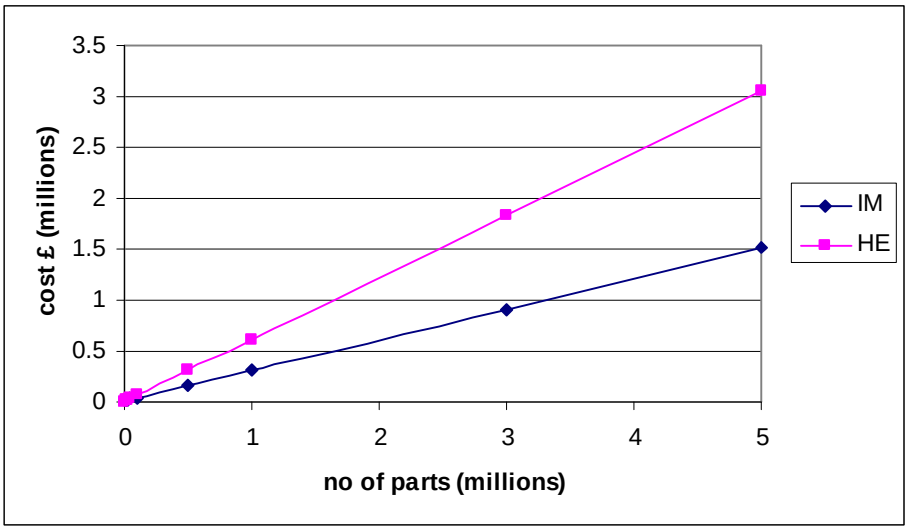

Figure 2.5 - Comparative costs of IM and HE for large-scale production for 1 part per mould/stamp

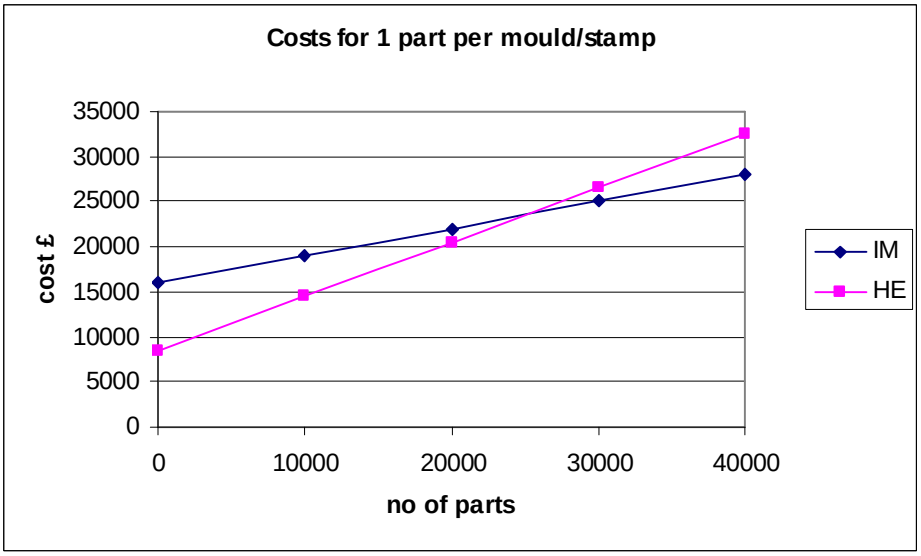

Figure 2.6 - Comparative costs of IM and HE for small to medium scale production.

Figures 2.5 and 2.6 show that for large scale production injection moulding is the better choice based on economics, whereas for small scale production the lower fixed costs involved make hot embossing the most economically viable choice. The number of parts which determines the switch over point between the two methods was calculated from equations 1 and 2, table 2.2.

Switch over point (no of parts)	Parts per mould/stamp
24470	1
170455	8
297030	16
394737	24

Table 2.2 – Switch over point for varying number of parts per mould/stamp

In equation 2, it was assumed that the job is a one-off, i.e. all stamps not used up to their maximum lifespan are scrap. If all stamps with life remaining could be used for a known future job then equation 2 would become:

$$CostHE = 6000 + 0.61 \cdot (N/n) + 0.0065 \cdot N \qquad \text{Equation 3}$$

In which case, the production level at which injection moulding is economically competitive becomes as in table 2.3.

Switch over point (no of parts)	Parts per mould/stamp
31596	1
220995	8
386473	16
515022	24

Table 2.3 - Switch over point for varying number of parts per mould/stamp when stamps are reusable

When considering commercial production, a few hundred thousand parts is a low production volume. This means that hot embossing is typically only suitable for prototyping or low to medium production volumes. However, in a commercial environment where millions of parts need to be manufactured, injection moulding represents the most economically viable solution unless the characteristics of hot embossing become essential for the product functionality/properties. The production levels of a functional blood testing device would be in the millions so injection moulding is the right technique for developing the device at Cranfield.

Chapter 3

3.0 - Literature review

This review gives an overview of FIB equipment, the FIB milling mechanism and an introduction to diamond tooling. The various measures of surface roughness used in engineering are then described. The literature on general FIB processing, FIB diamond processing, FIB induced surface morphology and tooling produced by FIB are described. Finally some of the models suggested for surface features formed on diamond during milling are described.

3.1.0 - Focused ion beam equipment

Originally invented for use in the semiconductor industry, FIB machining spread to universities as a materials analysis technique during the 1980s. Since the mid 1990s the use of FIB as a micro/nano machining technique has soared, contributing to the sharp increase in the published literature on the subject, figure 3.1.

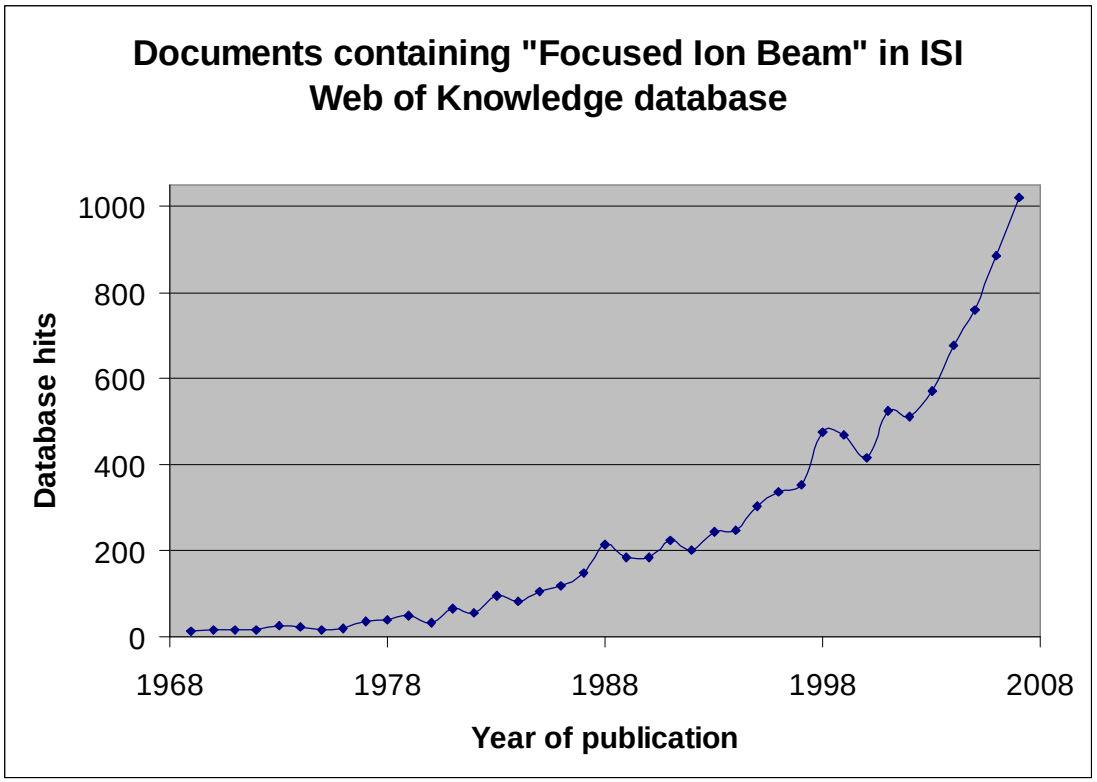

Figure 3.1 – Increase in focused ion beam use over time

FIB machining uses a beam of accelerated ions to remove material from a sample by transfer of kinetic energy from the ions to the atoms in the sample. As this is a non contact process it causes little residual stress in the sample and has sub micron beam control resolution. Any solid material can be machined as it is not a chemical process. This ability to remove precise amounts of material with minimal damage makes FIB machining a powerful technique at the nano and micro scale.

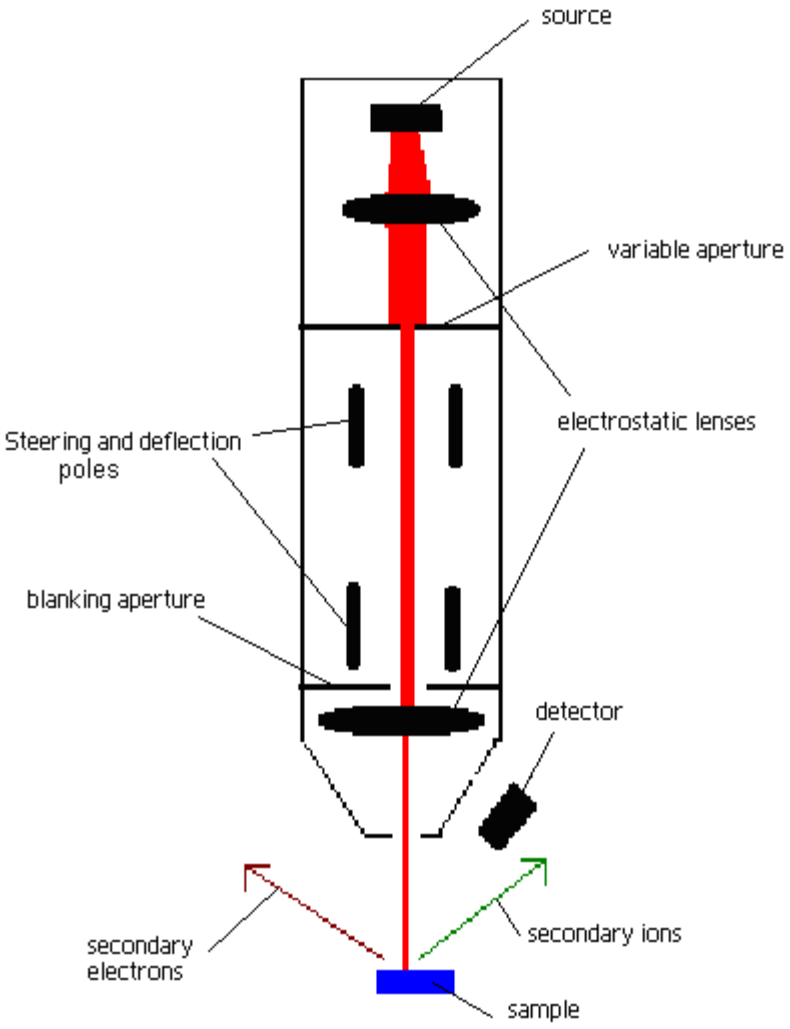

Figure 3.2 – Schematic of a FIB column (not to scale)

The key components of a FIB column are shown in figure 3.2. The major components of the FIB column are described below, starting from the top of the column.

3.1.1 – Liquid Metal Ion Source

The liquid metal ion source (LMIS) works by heating a reservoir of gallium metal which then flows to wet the tip of a tungsten needle, figure 3.3. The needle has a tip radius of ~2-5μm. Gallium is used for several reasons. It has a low melting point of 29.8^{o}C, meaning that the metal only needs to be given a small amount of heat to make it liquid and reduces any reaction with the tungsten needle. Liquid gallium has a low volatility which helps extend the source lifetime. It is viscous in liquid form and so sticks to the needle. Gallium has a low vapour pressure and so does not evaporate, again extending the source lifetime. Each source contains a few milligrams of gallium which gives a lifetime of ~400μA-hours/mg (Giannuzzi 2005).

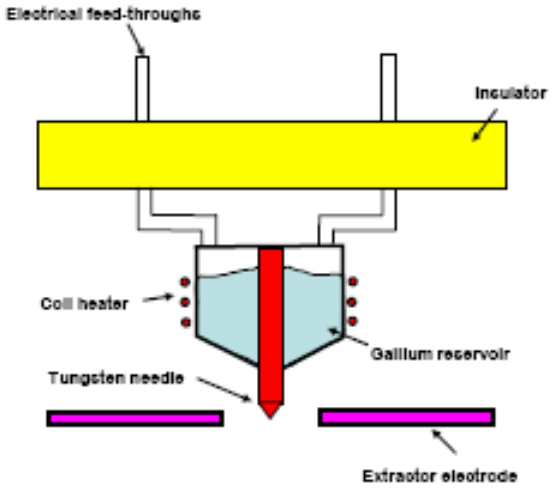

Figure 3.3 – Liquid Metal Ion Source (after Allen 2009)

Once the gallium has wetted the tip it can remain molten for several weeks because it has super cooling properties. If the FIB is used irregularly then the gallium solidifies between milling sessions and the source needs to be reheated each time it is used. This remelts the reservoir and wets the tip again. With regular use the source only needs reheating every few weeks, as using the source keeps the gallium in the reservoir mobile, delaying solidification. Each reheat reduces the volume of the reservoir until the source needs replacing. At Cranfield a source lasts

approximately one year, however heavy university users can use three sources a year (O'Neil 2009).

The 7kV extraction voltage across the extractor electrodes generates a field of ~10^8 V/cm at the needle tip. This causes the gallium at the tip to form a Taylor cone. This is a conical shape formed when the surface tension and electrostatic forces are in equilibrium. The tip of the cone is ~4nm in diameter and acts as an ion point source. The extraction voltage pulls gallium out of the cone and ionizes it. The current density of the extracted ions is ~10^6 A/cm^2. The source emission current is 2.2μA; it being this low because a small emission current reduces the energy spread of the beam. The energy spread is dependent upon the emission current because each ion extracted from the source experiences a slightly different electric field due to the varying number of neighbouring ions. The effect of this is to give each ion a small random velocity in addition to the downward velocity induced by the extraction voltage. Those ions whose random velocity is normal in relation to the FIB system's direction of ion acceleration, increase the effective size of the source compared to the actual size of the Taylor cone. The ions whose random velocity is in the same axis as the downward ion acceleration will have a slight increase or decrease in overall velocity. This spread of downward ion velocities results in an energy spread amongst the ions that hit the sample. A lower emission current results in fewer ions being extracted, giving a lower number of interactions between neighbouring ions and thus a smaller random velocity applied to each ion (MeIngailis 1987).

3.1.2 – FIB column

After the ions are pulled out of the cone they are accelerated down the length of the column by the ion acceleration voltage. For the FEI FIB 200 this is 30kV but other machines can have voltages up 50kV. On their way down the column the ions are collimated by the first electrostatic lens and then pass through a variable aperture which defines the beam current by selecting the number of ions that pass

down the column. Because the LMIS has a very high current density at its surface the beam has an energy spread of ~5eV. This causes chromatic aberration which is the limiting factor for the quality and size of the beam spot. There is also spherical aberration but the effect of this is smaller than the chromatic. The column lenses are designed to reduce the chromatic aberration to a minimum by using asymmetric three element lenses. The limit of the lenses' focusing abilities means that spot diameter increases with the variable diameter/beam current. The increased repulsion between charges in the ion beam cannot be overcome by the lenses.

The now narrower beam passes through two sets of poles which steer, align and remove aberrations such as stigmation from the beam. The beam then passes through a blanking aperture. This deflects the beam away from the sample when moving between the sample areas that are to be milled. This prevents unwanted milling of the sample between the target areas.

The beam is then focused to a point by the second electrostatic lens and travels down to the sample. The working distance between sample and second lens is 16.5mm for the FEI 200 and is typically of the order of 20mm. The beam spot is at a minimum at 16.5mm, however the divergence is slight and the beam would still be usable at a distance of 75mm (FEI manual 2000). The spot is primarily a Gaussian shape due to the range of ion energies in the beam. It also has exponentially decaying side tails that start at one order of magnitude lower than the peak current density (Frey, 2003), (Langford, 2002a), (Melngalis, 1987). This combination of a Gaussian and exponential tails is called a Holtzmark distribution (Shabalin, 1992). An example of these is shown below in figure 3.11. The side tails cause 'halo effects' around the edges of milled features where the tails have removed material from areas that remained untouched by the main beam spot.

The ion column is kept at a high vacuum of ~10^{-7} mbar to ensure the ion beam has a very long mean free path. When the beam leaves the second lens it enters a vacuum chamber containing the sample, stage and detector. The maximum operating chamber pressure allowed is $5x10^{-5}$ mbar.
The beam voltage affects the beam diameter. As the voltage decreases the ions take longer to travel down the column giving them more time to interact with each other and spread out. Thus the optimal column performance is at its highest possible voltage.

The magnification of the FEI FIB 200 column ranges from 234x to 50,000x, though beyond 20,000x the usefulness of the resulting milling/images is dependent on the material being processed. Insulating materials exhibit huge amounts of beam drift when depositing charge into a small area; for example a 16µm sided square for 20,000x.

The preset ion currents selectable, using the variable aperture and their corresponding spot diameters, are shown in table 3.1.

Beam current (pA)	Typical current use	Spot diameter (nm)
1	imaging	8
4	imaging	12
11	imaging	15
70	imaging	25
150	milling	35
350	milling	55
1000	milling	80
2700	milling	120
6600	milling	270
11500	milling	500

Table 3.1 – Spot diameters for different ion beam currents

The 1, 4, 11 and 70pA currents are used for imaging purposes. The remaining currents are for milling, though the 11.5nA current is too imprecise in its effect to be used for anything other than bulk material removal. This is due to the charging up

of the surface caused by the large number of incoming positive gallium ions. This has only been used for taking the end off rounded tools when creating straight edges during the tool work. The 6.6nA current is more accurate but still causes unwanted material removal, again due to beam drift. Below 6.6nA the drift is much reduced to the point where it can often be ignored. This makes 2.7nA the favoured current much of the time. Beam drift is discussed in greater detail in Chapter five. Drift can be counteracted by using the charge neutraliser in the FIB chamber. This is an electron gun that fires a stream of negative charge at the work piece to counteract the gallium build up. The electron current can be varied to match the ion beam current being used. The amount of charging caused by a given ion beam current will vary from material to material. The primary reasons for this are varying amounts of ion channelling, the amount of free charge already in the material, the amount of redeposition and the incidence angle of the beam. These factors affect the distribution of the new net positive charge being implanted into the sample. The 150 and 350pA currents are useful for fine detail high magnification work as the low mill yield gives more controllable material removal and reduces the impact of mistakes.

3.1.3 – FIB resolution

The resolution of the beam steering system is magnification dependent. The surface area visible is split into a 4096x4096 pixel grid i.e. 12 bit. The pixel size for common milling magnifications is given in table 3.2.

Magnification	Pixel size (nm)
1500	42
2000	31
2500	25
3500	18
5000	12.5
6500	10
8000	8

Table 3.2 – Magnification dependent FEI FIB 200 resolutions

The combination of spot size, magnification and beam drift means that the process of defining the resolution of the FIB machining process is not a simple one. The closest thing to a definite resolution is when the spot size is less than the pixel size, for example milling nano sized dots at 70pA and 2000x magnification. However this could be affected by the material being machined. Is the beam spot being placed exactly where the pattern is placed or is it drifting? The only sensible definition of resolution is the smallest machined feature that can be reliably produced on the particular material being used.

3.1.4 - Imaging

The detector is an electron multiplier that can be biased to detect either secondary electrons or ions. The collected charge is then amplified into a signal voltage which is digitized and displayed as a real time image. Because the imaging process is removing material from the surface, low currents are used to minimize the damage caused by rastering the beam over the surface. Only one of the detector modes can be used at a time, the electron mode gives a better depth of field and is the default mode. However for materials that are insulating there are not enough electrons ejected from the surface to form a good image so the ion detector is used instead.

3.1.5 – Gas injection systems

The FIB has two gas injection modules installed for gas assisted milling and deposition. These are mounted onto the back of the chamber and each is connected to a motorized metal pipe which travels into the chamber and stops 100μm above the sample surface. The external black modules and the pipes inside the chamber are shown in figure 3.4.

Figure 3.4 – FEI FIB 200 chamber gas injection system

The modules contain hydrated magnesium sulphate and trimethyl platinum. When heated by electrical current these give off water and a platinum containing gas respectively which is deposited onto the surface of the sample. The water layer boosts the milling yield of materials with high carbon content. The oxygen in the water binds to carbon ejected from the sample, forming carbon monoxide preventing carbon from being redeposited back onto the sample. The platinum gas deposits platinum onto the surface when the ion beam passes over a gas covered area.

There are other possible gases that can be injected during milling including methanol (CH_3OH), xenon difluoride (XeF_2), oxygen (O_2), iodine (I_2) and hydrogen (H_2). These all reduce the amount of redeposited material. XeF_2 is a common boost gas as it works for a wide range of materials. The boost to the milling yield given by any of these depends on the surface chemistry reaction of the gas and the sample. Injection gases can also reduce the mill yield, for example water assisted milling

reduces the yield when processing silicon and aluminium and has no effect on the yield for gold (Stark 1995). As well as platinum, tungsten can also be deposited.

3.1.6 – FIB milling mechanism

When a gallium ion hits the surface of a sample it displaces atoms from the surface region by transfer of kinetic energy from the ion to the sample atoms. The ion will hit multiple atoms until it comes to rest inside the sample. The displaced atoms hit other atoms causing a cascade of collisions inside the sample. Some of the displaced atoms loose some electrons in the collisions and become secondary ions. For collisions near the surface there is a chance of the displaced material being ejected from the sample. Most of the ejected material is redeposited back onto the surface again, but some has enough energy to escape from the surface and is sucked away by the chamber vacuum. Some of the ejected material is attracted towards the detector inside the chamber by the bias current. The displaced atoms that are not ejected or are redeposited form an amorphous layer on top of the region that was not affected by the collision cascade. The process is shown in figure 3.5; the gallium beam initially strikes the yellow atoms in the left hand image. These are knocked from their lattice position and start the collision cascade. As the beam starts to raster across the surface new cascades are started. The result of this is displaced ions (blue), secondary electrons (purple) and displaced atoms (yellow) moving around in the top layers of the sample, shown in the right hand image. Some escape the surface (arrowed particles) and these are the yield.

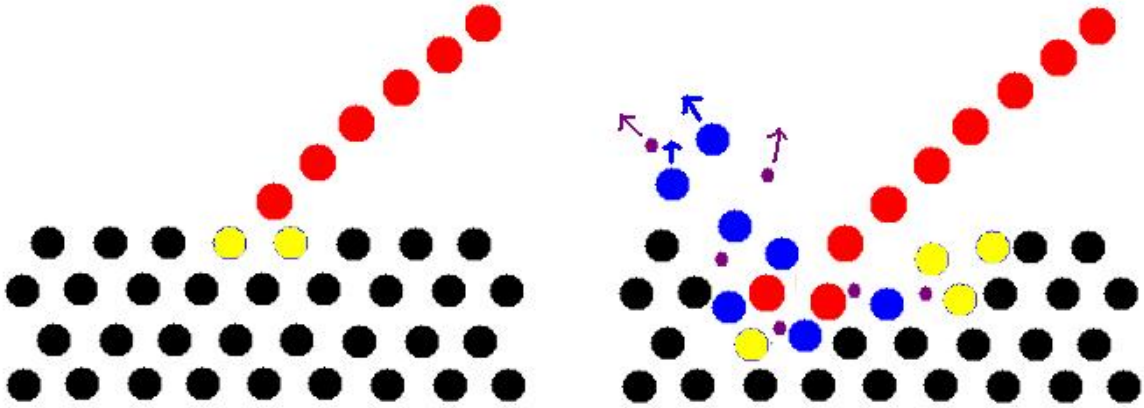

Figure 3.5 – Gallium ion/target atoms collision cascades

The strength of the inter atomic bonds in the sample determines the ease of material ejection. This is why single crystal materials tend to have lower yields than polycrystalline ones. A strong crystal structure means that more of the gallium ion's energy is used in breaking the bonds and less is available to provide atom movement within the crystal. Polycrystalline materials are normally easy to mill because their structure contains weak points for the gallium to attack. The gaps between crystallites can act as channels for the gallium to travel down and attack the sample from beneath the surface as well as on top. The grain boundary bonds are thus preferentially broken rather than the intra crystal bonds (Reyntjens 2001).

This difference in crystalline/polycrystalline milling means that crystalline surface milling results in smoother surfaces due to the more uniform gallium/surface interaction. Polycrystalline milling gives a more varied surface with areas of differing height due to varying grain size and orientation. Examples of this are shown in figure 3.6 in which the aluminium has a rough uneven surface compared to the smooth holes in the silicon. Around the edges of the silicon holes are partially milled areas caused by the beam side tails described in section 3.1.2. The halo effect on these holes is asymmetric, with the left hand side of the circles having a wider affected area. This is caused by a slight astigmatism in the beam giving a non-circular spot shape. Astigmatism can be corrected by altering the

column lens settings on the FIB's control panel. On the aluminium, shown in figure 3.6, the right and bottom edges of the square hole have been partially milled by side tails and astigmatism. The astigmatism was in a different direction and larger when the aluminium was milled.

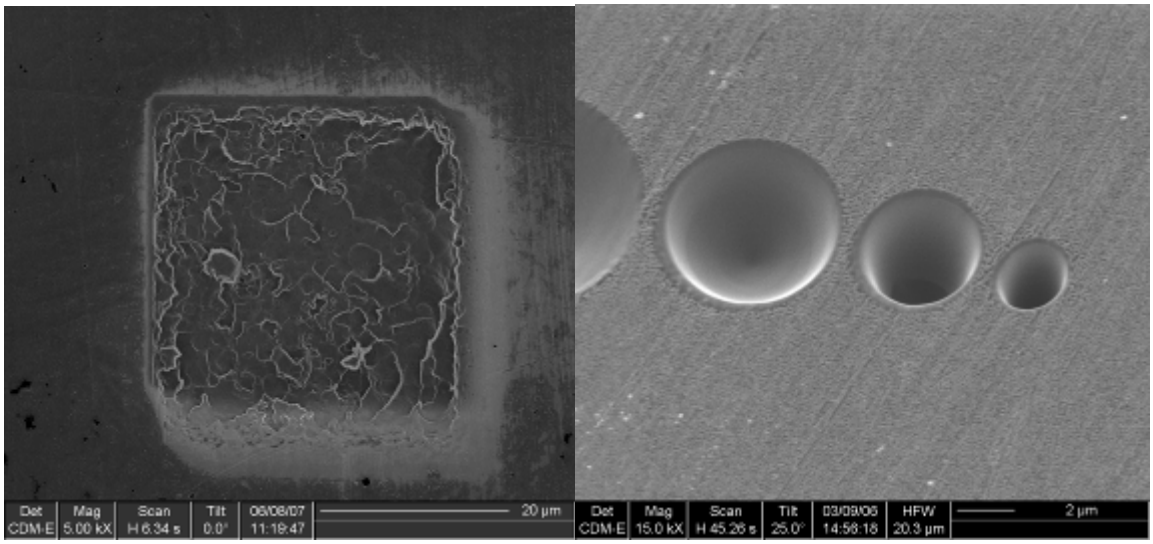

Figure 3.6 – Ion milled aluminium (left) and silicon (right)

When an ion approaches the surface at the normal then most of the incoming energy is transmitted down into the sample. Most of the cascade collisions will tend to keep displaced material in the sample. As the angle of incidence of the beam increases then the energy is more likely to be transmitted closer to the surface of the sample. This makes it more likely that the collision cascade will result in ejected material. This increase in milling yield with angle continues until the incidence angle is ~80^{o}. At this point the gallium ions start to glance off the sample surface instead of impacting into it. This causes the yield to drop dramatically to zero at ~86^{o}. A typical yield curve is shown in figure 3.7 which shows the curve for iron. The peak angle of the curve varies with the choice of sample material depending on the atomic strength and structure.

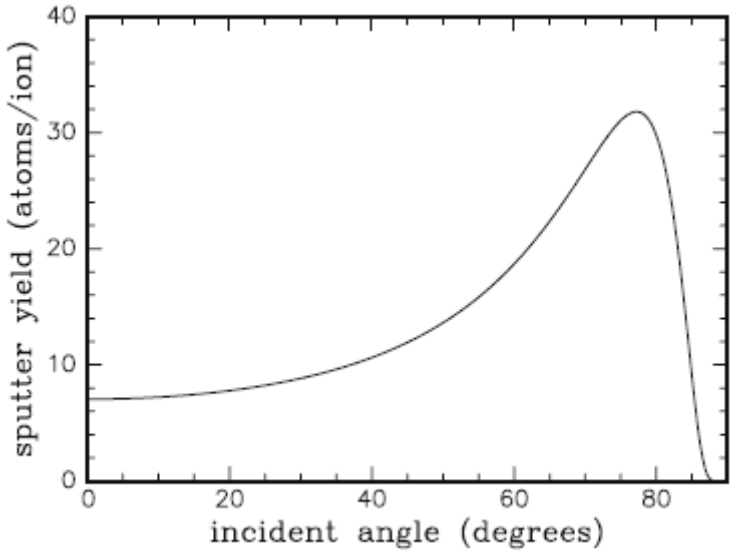

Figure 3.7 – Typical FIB yield curve (after Vasile 1999)

3.1.7 - Stage movement

The sample stage in the vacuum chamber can move in x, y and z, rotate in the x-y plane and tilt in the x-z plane, figure 3.8.

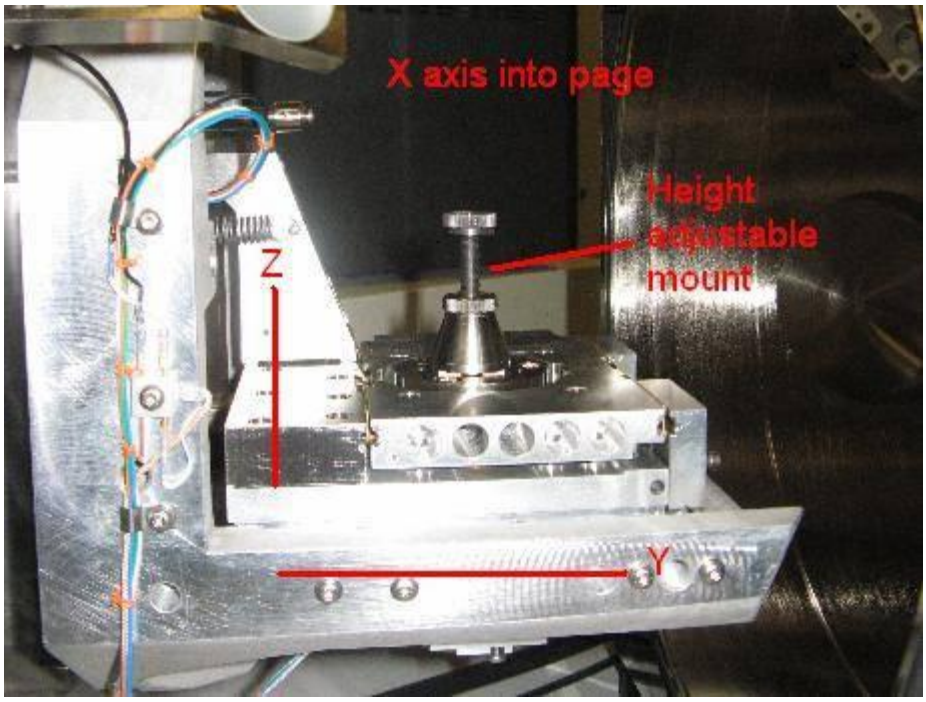

Figure 3.8 – FIB chamber sample stage and mount

The tilt range is from -10^{o} to +60^{o} and the maximum travel in the x, y and z is 50, 50 and 12.5mm. The sample is held on a mount giving a height adjustment of 25mm, allowing a range of 40mm in the z dimension of the sample. This allows a variety of sample size and shapes to be milled. The largest a sample can be is 100mm in x or y, though rotation and tilt of a large sample may need to be restricted to avoid hitting the detector inside the chamber. When a sample is inserted into the chamber the stage height needs to be set at the eucentric height. This is the height at which the sample area under the beam output point doesn't change when the sample is tilted.

3.2 - Diamond tooling

Diamond tooling has long been used for obtaining high quality surface finishes on non-ferrous metals. The strength and homogeneity of the diamond structure means that it has a lower wear rate and is less likely to break up into chips than any other tool material. Rival materials such as steel and tungsten carbide being multi-grained are intrinsically weaker, leading to higher wear rates. The granular multi-element nature of these materials also provides natural weak points for machining stresses to act on, making chipping of the tool edges more likely. However they have the benefit of being easier to machine into complex shapes by processes such as electro discharge machining. Also tungsten carbide can be used to machine steel and other ferrous materials, which diamond cannot. This is because diamond reacts chemically with steel, leading to very high wear rates on the tool.
Traditionally diamond tools have been single crystal natural stones that have been ground to a sharp edge by grinding with diamond grit. The tool stones are selected by eye from stones that do not meet the clarity standards for being gemstones. The stones are then ground to rounded or flat tips with clearance and rake angles as specified by the end user. The tools can be reground when the edge becomes worn or chipped.

Single crystal synthetic diamonds were first successfully grown in 1955 and have, since then, replaced natural stones in many industrial applications (Pierson 1993). They are primarily created by the high pressure high temperature (HPHT) method of packing graphite inside an anvil cell with pressures of ~60kbar and a temperature of ~2000 Kelvin. The resulting stones have the same physical properties as natural stones but are normally coloured due to impurities. A yellow colour due to small amounts of nitrogen impurities ~ 0.1% is common. These have been used as a cheaper alternative to natural stones. Later work has produced clear synthetic diamonds such as Monodite MCC 110 (Element six) without the nitrogen impurities which can act as weak points and concentrate the machining stress. Single crystal synthetic is ground in the same way as natural stones for making tools.

Polycrystalline diamonds were first created by binding together small pieces of natural diamond. The binder is normally cobalt or a metal alloy with a high cobalt content. The diamond and binder are pressed together under high pressure as for HPHT. The resulting diamond has good wear characteristics but cannot be finished to as good a finish as a single crystal. Polycrystalline diamond has a higher fracture toughness than single crystal because the isotropic grain structure stops force from propagating in straight lines, whereas single crystal will preferentially cleave along the (111) plane (Thoe 1996).

An alternative method of making polycrystalline diamond is to grow it by chemical vapour deposition, CVD. This method involves passing a low pressure carbon-containing gas over a substrate and causing the gas to break down by exciting it with microwaves, an electric discharge arc or a hot filament. The carbon atoms drop out of the gas and form diamond and sometimes graphite. By varying the process parameters it is possible to create polycrystalline diamond with varying grain sizes. The quality of surface finish achievable with polycrystalline depends on the grain size for CVD. The size of the natural pieces and the effectiveness of the

binder define the quality of high pressure diamonds. CVD diamonds are harder, have better wear properties and are chemically and thermally more stable than conventional polycrystalline (Belmonte 2003). Polycrystalline/CVD diamond can be turned into tools by grinding, electro discharge machining and also laser machining.

The use of FIB to produce tool edges has been investigated previously as described in section 3.7 below. The inability of grinding to produce a shape other than a rounded nose or a flat edge limits the bespoke potential for diamond tooling. Electro discharge machining can create unconventional shapes but because it works by sparking pieces out of the work piece it can never give the finish needed for a precision tool (Olsen 2004a, 2004b). However, for shaping tungsten carbide tools this technique is good. Laser machining is limited by its inability to give a sharp edge to a tool. The extension of FIB to machining polycrystalline diamond aims to combine PCD's positive qualities of lower cost, superior wear and toughness relative to single crystal diamond, whilst giving it an edge quality that makes its competitive with single crystal for machining surfaces down to a few tens of nanometres Ra.

The angles relevant to the tool production process are shown in figure 3.9. The ion beam angle and the front face clearance angle are shown.

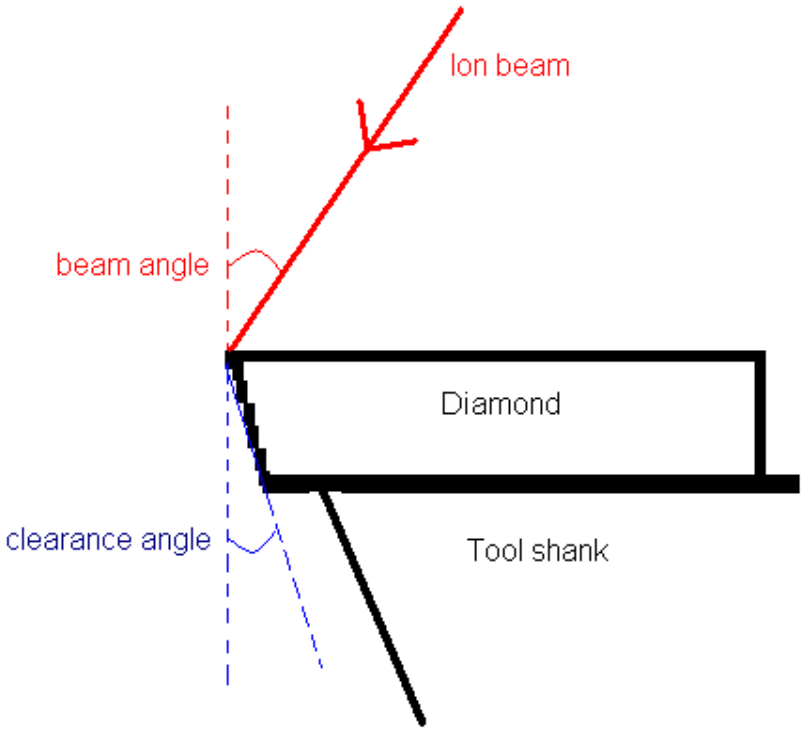

Figure 3.9 – Tooling and ion beam angle definitions

3.3 - Measures of surface roughness

When quoting figures for the roughness of surfaces, care is required to ensure that the correct measure is used. Modern measuring equipment can provide a large number of measures of roughness for profile lines and area scans. The results of area scans are often reported as R numbers even though it is a 3D roughness measurement and should be an S number. R numbers describe 2D measurement profiles across a surface whilst S numbers describe the roughness over a whole 3D scan area. The common measures of roughness are shown in table 3.3.

Roughness measure	Meaning
Ra, Sa	Mean average of absolute values
Rq, Sq (also known as R_{RMS}, S_{RMS})	Root mean square average of values
Rv, Sv	Maximum valley depth
Rp, Sp	Maximum peak height
Rt, St	Rv,Sv + Rp,Sp over the measurement length or area
Rz, Sz	Rv,Sv + Rp,Sp averaged over the number of sampling lengths in the measurement
R_{max}, S_{max}	The largest Rv,Sv + Rp,Sp in any one of the sampling lengths in the measurement
R_{sk}, S_{sk}	Skewness of the measurement.

Table 3.3 – Surface roughness measures

Rq and Sq are often referred to as RMS numbers instead. R values are often the result of a filter being applied to profile data, whilst any measures referring to the unfiltered data are P values.

RMS is typically about 20% bigger than Ra, this is important because some of the measurement software used does not give Ra values only RMS values; and comparisons have to be made between this data and Ra figures from the literature. If Rt is much larger than Rz then there is a feature that is much higher or deeper than the typical features (Lowe 2007). The skewness of the measurement refers to the distribution of the profile above and below the mean line. A negative value means deep valleys and shallow peaks; a positive value means high peaks and shallow valleys.

3.4 - FIB processing

The chapter by Miyamoto in 'Energy beam processing of materials: Advanced manufacturing using various energy sources' (Tanigughi, 1989) is a summary of the sputtering mechanism, ion beam equipment and the practicalities of ion machining supported by examples from the literature. Miyamoto was one of the main publishers on using FIB as a machining tool during the 1980s and he uses some of his work as examples. As the book was published 20 years ago it has now been superseded by 'Introduction to focused ion beams' (Giannuzzi, 2005), particularly as Miyamoto's work was done with a broad ion shower low energy beam. This equipment has been replaced by the FIB as a research tool. (Giannuzzi 2005) is the most recent book on FIB and covers all the aspects of FIB equipment and the main applications of the technology. This is the first point of call for general enquiries about FIB and its uses.

(MeIngalis 1987) is an early review of FIB technology and its applications. Parts of it are no longer correct given the advances in FIB technology, particularly in the column optics and the control and patterning software. The Gaussian profile of the ion spot with its exponential side tails is described. (Reyntjens 2001) is a good review of the modern FIB and its uses. Deposition, cross sectioning, TEM sample preparation and micromachining are discussed. (Gerlach 2001) gives a brief overview of FIB technology and its applications. 2001 saw the start of a large increase in the use of FIB as a research tool with three more useful reviews published by 2005.

(Langford 2002a) looked briefly at the micro/nano engineering capabilities of FIB and the devices being produced with it at that time. The Gaussian profile of the ion spot with its exponential side tails is described. (Tseng 2004) gives a good description of the FIB, the ion sputtering process and the beam raster movements needed for achieving uniform ion flux over each pixel. The differing effects of using single and multiple beam passes when machining were examined using the

example of micro channels. The need to adjust the milling sequence for 3D shapes, to avoid redeposition problems, was explained. Examples of 3D milled structures like probe tips, diamond tools (Adams 2000, Picard 2003) and curved substrate milling were given. (Tseng 2005) looked at FIB for nano scale work. The FIB basics section is similar to his 2004 review. The problem of sample swelling caused by amorphisation of the surface was discussed as this was only a problem when machining features below the micro level. The use of FIB implantation was described, along with nano scale deposition techniques and examples. Gas assisted milling and its accuracy was discussed, concluding that the accuracy ~10nm was not considered to be high enough for achieving consistent nanostructures.

(Volkert 2007), (Langford 2007) and (Moberlychan 2007) are from an issue of the Materials Research Bulletin published by the Materials Research Society. This special issue contained five articles introducing the main aspects of FIB; micro and nano machining, TEM sample production and the effect of FIB on the surface and subsurface of the sample. They are a good introduction to FIB and its main aspects.

(Frey 2003) discussed the effects of the Gaussian beam shape and its side tails on nano size features where the varying ion density has an effect on the material removal rate, implantation of gallium into the sample and the angle of nominally straight side walls. At low ion doses gallium implantation caused the sample to swell as the material removal rate was lower than the increase in mass of the sample. Above a critical ion dose net material removal began. The effect of redeposition was noted to be important at the nano scale, mainly for high aspect ratio structures. The side tails of the Gaussian beam spot (figure 3.10) affected the angle of the side walls.

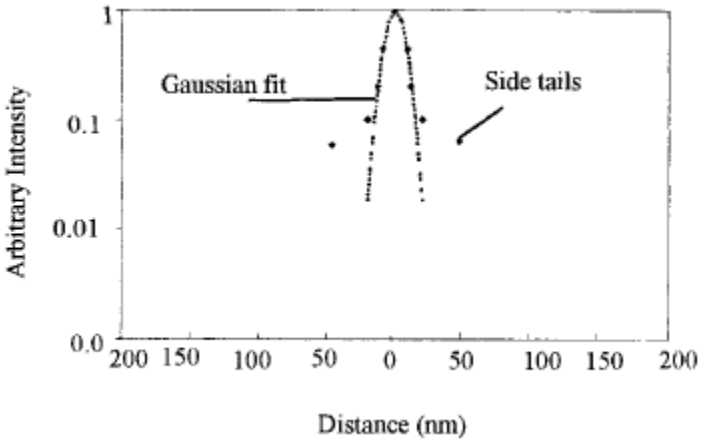

Figure 3.10 - Profile of a 300pA 30keV ion spot (after Langford 2002a)

At the centre of the spot, the ion incidence was normal to the floor of a trench, whereas the ions in the tails hit the side walls at various angles all greater than normal, with many reflecting off. These ions then hit the bottom of the trench causing a greater amount of material removal there. This gave the trench a v shaped bottom instead of a flat one. This was in addition to the halo effects of the side tails around milled features.

(Winter 2007) found that, when milling nano features in silicon with beam currents of greater than 6pA and doses of 10^8 ions or more, gallium droplets formed on the surface.

(Gierak 2006) developed a nano FIB system for high resolution machining at spot sizes of less than 10nm. The low current (5-10pA) used meant long machining times so they developed an unconventional ion source that was more stable than a LMIS over long periods. This source had a tungsten needle with a tip radius of 20-50μm instead of 2-5μm as in a typical LMIS, see section 3.1.1. This gave a more stable ion flow at low currents because small radius tips become electrohydrodynamicly unstable at low currents. The sharper the tip the greater the current that can be extracted. The drawback is that the tip gallium coverage

becomes uneven at low currents. This puts a lower limit on the operation of conventional high current LMIS's, ~0.75μA (Melngailis, 1987). The low current source was not designed to give a high current so a blunter tip could be used giving the stable low current performance. The column optics were designed for the narrow beam to minimize aberrations. The nano FIB was then used to demonstrate the possibilities of nano feature generation, such as arrays of 45nm diameter holes with aspect ratios of 2:1 in silicon carbide.

(Yongqi 2000) looked at the effect of overlapping the Gaussian tails across the surface to give smoother sidewalls, the importance of the milling order for reducing redeposition in complex shapes and the improvement in shape quality that came from reducing the pixel dwell time and increasing the number of passes compared to long dwell times and fewer passes. Short dwell times were found to be a solution to various problems in FIB machining.

(Langford 2002b) demonstrated a method of reconstructing the actual shape of non symmetrical milled 3D holes. The milled shape varied from the design shape due the effect of varying mill yield during the mill and redeposition of material. The mill yield varied due to the ion beam incidence angle, relative to the surface, varying as the surface changed shape. This was compensated for by altering the dwell time for some of the pixels when milling surfaces of known curvature, for example hemispheres. The resulting shape could also be examined by cross sectioning the sample. For non symmetrical shapes a single cross section wouldn't provide all the needed information, however the use of an AFM may do. For non symmetrical high aspect ratio shapes the use of an AFM is impossible due to the tip geometry. Langford's method takes multiple cross sections across the structure taking images of each one. The coordinates of the profile are measurable from alignment marks that have been milled on the sample surface in the x axis around the hole. The y and z direction is measured using the FIB's imaging software. Fifteen sections were imaged for a 1μm square hole. The coordinates are used to

construct x-z and y-z plots of the hole showing the actual hole shape. While this is an interesting method for understanding the subtle complexities of milling features, the limitation of the method is the large number of sections needed to create an accurate profile and the long time needed to mill and image them.

(Adams 2006a) reported the accurate production of micro curved features including hemispheres, parabolas and sinusoidal wave forms. The dose per pixel was varied allowing for the material specific angle dependent sputter yield, the beam current and the Gaussian ion spot distribution. The angular sputter yield for silicon, silicon carbide, sapphire, gold, aluminium, tungsten and diamond was found experimentally. The yields for single crystal metals were found to be lower than predicted by a sputtering model due to the effect of ion channelling. The sputtering was reduced due to ions penetrating deeper into the material. Falls in the yield due to channelling down the major miller indices were observed in Au. Changes in yield associated with surface morphology of diamond were observed. Redeposition was found to be greater for the low mass target materials silicon and diamond. This is thought to be because when gallium ions hit heavier target atoms the distribution of ejected material peaks along the normal distribution. Lighter ejected material tends to have forward biased distributions that point to the bottom or sides of the feature being milled giving greater redeposition.

(Edinger 2001) developed a model of gas enhanced milling and tested it with iodine and chlorine enhanced silicon milling. They find a strong yield dependence on the dwell time chosen. They also found that the gas flux sticking coefficient in the model was higher in the area under ion bombardment compared to the rest of the surface. The gas flux sticking coefficient is a measure of how well the injected gas sticks to the surface of the sample. The increase implied that the bombarded area gave a more reactive surface for the gas molecules to stick to. The damaged surface would have more dangling bonds for the gas molecules to attach to.

3.5 - FIB and diamond processing

The first mention of using ion sputtering to machine diamond was by (Spencer 1972). This demonstrated the use of an argon ion shower to produce holes of a few mm in diameter and depth in natural diamond. The ability to polish diamond surfaces was also demonstrated. The ion energies used for this work was 7.5keV, much lower than modern FIB's, however the beam currents of 7.7μA and 100μA used were higher.

(Stark 1995) compared the factor increase in mill yield due to water assisted milling for a range of materials finding a decrease of 4 for aluminium and an increase of 20 for polyimide. The increase for diamond was a factor of 10.

(Russell 1998) compared the mill yields for diamond when water and XeF_2 assisted. The XeF_2 increased the mill yield by a factor of 3.5 when milling in the centre of a diamond and by 4 when milling on the edge of the diamond. The water assisted milling factors were 5.6 and 12.2, the actual yields were 0.51μm^3/nC and 1.1μm^3/nC. (Taniguchi 1998) found a factor increase in yield of 4 when milling (100) plane diamond with XeF_2. The mill yield was lower for the (110) and lowest for the (111). (Datta 1999) found a factor of 4 increase in yield with XeF_2 on (100) diamond. Oxygen was found to double the yield and chlorine to have no effect.

(Stanishevsky 1999) compared the mill yields of different forms of carbon and found that the yield for polycrystalline CVD diamond was 0.1μm^3/nC compared to 0.08μm^3/nC for single crystal diamond. (Stanishevsky 2001) produced 30nm wide trenches in diamond using a 3pA (10nm diameter) beam. Milling of amorphous carbon films produced a yield of 0.11μm^3/nC. This was boosted by milling with the assistance of XeF_2, ammonia and water. Water increased the yield by a factor of 2.5. The yield for amorphous carbon is of interest as the surface of diamond is broken up during milling so the gallium ions are interacting with a mixture of diamond and amorphous carbon as they penetrate the sample.

(Datta 2001) described experiments into the mechanisms behind the formation of ripples on the surface of (100) diamond during milling. The critical milling angle at which the ripples formed on a previously smooth surface was found to be 40^{o}-50^{o}, depending on the energy of the ions. For 10keV the angle was 50^{o} and 40^{o} for 50KeV. The orientation of the ripples was found to be independent of the beam scan direction. The ripple wavelength was found to be lower for the 10keV ions (~60nm) compared to (~200nm) for the 50keV ions. The ripple wavelength was not found to be sensitive to the angle of milling until 75^{o} when the ripple pattern turned into a broken ripple structure. The sudden appearance of the ripples showed that it was not a chemical reaction causing them. The surface of the milled diamond was found to be smoother than the polished diamond for milling below 40^{o} with the roughness inversely related to beam energy. The feature size was found to be independent of the spot size. In the model they suggested for the surface features the primary mechanisms were the slowing down and redistribution of ion enhanced surface mobile species. This did not involve thermal equilibrium with the surroundings like the ion enhanced or inhibited diffusion as used in earlier models.

(Adams 2003) reported the effect of water assisted milling on (100) diamond. They found that the increase in yield was constant for gas injection tube-sample separation distances of 100-250µm, above this the yield dropped rapidly. The peak yield for water assisted milling at 75^{o} was 2.2 times higher than the dry peak at 85^{o}. They speculate that the effect of water was reduced at high angles due to the incoming ions preferentially removing water instead of interacting with the diamond surface. They observed no change in yield with dwell time for dry milling but an inverse relationship for wet milling, due to the increasing depletion of water from the surface the longer the beam stayed in one spot. The surface structures reported in (Datta 2001) were observed, the smooth, rippled, stepped progression with milling angle. The ripple onset angle was found to be 5^{o} lower for water milling compared to dry. The ripples formed with water assisted milling had a lower wavelength than the equivalent dry ripples. They observed that the steps were

formed by shadowing between neighbouring surface features. At high angles the beam couldn't access all of the existing surface ripples and preferential sputtering of the peaks occurred, causing local planarisation. Water milling created lower amplitude steps and a lower surface roughness. The amorphous carbon layer after milling was measured as 35nm deep for dry milling and 25nm for wet milling. The reduction was attributed to the increased material removal with wet milling.
(Murakawa 2004) demonstrated the processing capabilities of FIB by producing in diamond a 10µm diameter gear wheel and a 15µm diameter turbine shape with eight blades.

(Mayer 2005) expanded on the observations in (Adams 2003) of changing diamond morphology. The ripple wavelengths showed a slight increase with increasing ion fluence, which then saturated at ~10^{18} cm^{-2}. This is equal to 0.1 seconds mill time on the lowest beam currents for the FEI FIB 200. They fitted their results to the models suggested by (Bradley 1988) and found a good fit for 40^{o} to 70^{o}. For less than 40^{o} they found that the data supported the suggestion of (Datta 2001) that there was a surface smoothing mechanism other than surface transport. Mayer found evidence for ion induced atomic drift parallel to the surface. (Adams 2006b) looked at the effect of the changing surface morphology on the milling yield of diamond. There was no change in yield from 0^{o} to 40^{o}- 45^{o} i.e. the smooth region. The rippled surface occurred from 45^{o} for dry milling and 40^{o} for water assisted. The yield dropped by ~35% for an increase in fluence from 10^{18} to 10^{19} ions cm^{-2}. The surface became increasingly rough with the dose increase. This yield drop occurred for all angles in the ripple regime. For the step features >70^{o} and >65^{o} for dry and water assisted milling respectively the yield fell with increasing dose as the steps lengthened. This was true for increasing angle for dry milling, however for water assisted milling after 80^{o} the surface became smooth again and the yield remained constant with angle.

(Kawabata 2004) analysed the damage to diamond caused by broad ion beam machining using x-ray photoelectron spectroscopy. XPS measures the binding energy of the bonds at the surface and gives a plot of relative intensity for the energies measured. Diamond has a tall narrow peak due to its homogenous crystal structure. Although the ion energy is only 1keV in this work the results are still of interest. (110) diamond was milled for one minute and one hour. Even after one minute the tall narrow diamond bond peak had shortened and widened due to amorphisation. After one hour the main peak had the same binding energy as the peak for graphite, showing how the diamond surface had been altered by incoming ions.

3.6 - Ripple formation theory

The mechanisms behind the formation of ripples on single crystal materials have been investigated and models suggested. The most highly cited model of ripple formation is the Bradley-Harper model (Bradley 1988). This model combined earlier work on sputtering modelling by (Sigmund 1973), with classical surface diffusion to explain several major features observed in ripple formation. The main idea behind the model is that the milling yield at any point on the surface depended on its curvature. The surface 'valleys' erode faster than the 'hills', causing the rate of surface roughening to increase with initial surface roughness, figure 3.11.

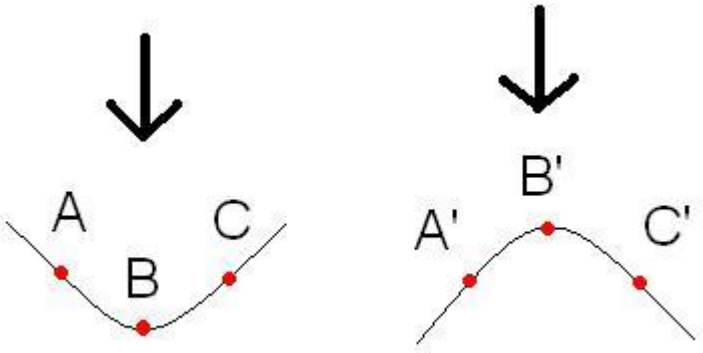

Figure 3.11 – Ion milling of negatively and positively curved slopes (after Bradley 1988)

When an ion hits the surface at point A part of its energy is transmitted downwards into the bulk. The same applies at point C. Thus the bulk below point B receives energy from ions hitting point B directly and also from ions hitting points A and C. There is also the effect of ions reflecting off the sides of the valley and then causing sputtering elsewhere in the valley. When ions hit points A' or C', very little of the transmitted energy will travel upwards in the bulk by back-scattered ions towards point B'. The energy will instead remove material from the base of the hill, making it taller. This means that the valley will deepen relative to the hill for the same number of incident ions. The overall height of the sample is reduced but this occurs heterogeneously over the surface. This surface roughening is counteracted by the surface diffusion of atoms. These are free to move as the crystal structure of the material has been disordered by the incoming ions. This atom movement will have the effect of partially filling in the valleys being created. The result is ripples with a wavelength (average peak to peak separation) that depends on the milling conditions.

Bradley-Harper is only strictly true for amorphous surfaces because the surface diffusion is modelled as encountering no barriers such grain boundaries. Thus it works best for single crystal materials such as diamond, as it has problems with polycrystalline materials which change the way the surface atoms diffuse. The roughening process occurs for any milling angle. However, it is outweighed by the smoothing diffusion process up to a critical angle of beam incidence above which ripples form. The model predicts the wavelength of any ripples formed to be $\lambda = (fT)^{-1/2} \exp(-\Delta E/2k_BT)$ for low flux f and high temperatures T. ΔE is the activation energy for surface diffusion. The high temperature and low flux condition mean that this equation is not directly applicable to most focused ion beaming work with its high flux and lack of sample heating. However later models build on and expand the Bradley-Harper model.

(Chan 2007) produced a review paper that described the current understanding of all the models suggested for ripple formation. At 46 pages it is the best available

summary of the pros and cons of the models and discusses where the models conflict with each other. (Carter 2001) is an earlier shorter review of the field. Some of the models discussed by Chan are (Koponen 1997), (Makeev 1997), (Chason 2006) and (Zhou 2007). Koponen simulates the ripple formation on amorphous carbon. The entirety of the collision cascades are calculated using a Monte Carlo method. The surface diffusion of the atoms was modelled by maximising the number of neighbouring atoms. The ripple orientation was found to be dependent on the angle of ion incidence and the ripple wavelength on the magnitude of the surface diffusion. At a 30^{o} beam angle, the ripples formed perpendicular to the direction of beam travel, and parallel to it for 60^{o}. Koponen's model does not include the effect of ion enhanced 'effective' surface diffusion, which was introduced by Makeev.

Makeev's model suggests that 'effective' surface diffusion is responsible for ripple formation. This is a temperature independent preferential surface erosion effect which is dominant over thermally induced surface diffusion below a material dependent threshold temperature. A threshold temperature of ~330^{o}K is quoted for gallium arsenide and fused silica. Above the threshold, the ripple wavelength increases with temperature. The effective surface diffusion is not an actual diffusing movement of surface atoms. Instead, it is a preferential sputtering of atoms from the valleys compared to the hills, as in the Bradley-Harper model.

Chason (co-author of Chan 2007) produced a kinetic phase diagram for copper describing four zones with different dominant surface mechanisms, figure 3.12. The mechanisms suggested were: kinetic roughening; diffusive; non-roughening; and erosive (Bradley-Harper). The high temperature and flux area is the Bradley-Harper zone. For high temperatures, but lower fluxes, non roughening processes dominate, thermal surface diffusion counteracting any heterogeneous material removal by the ions.

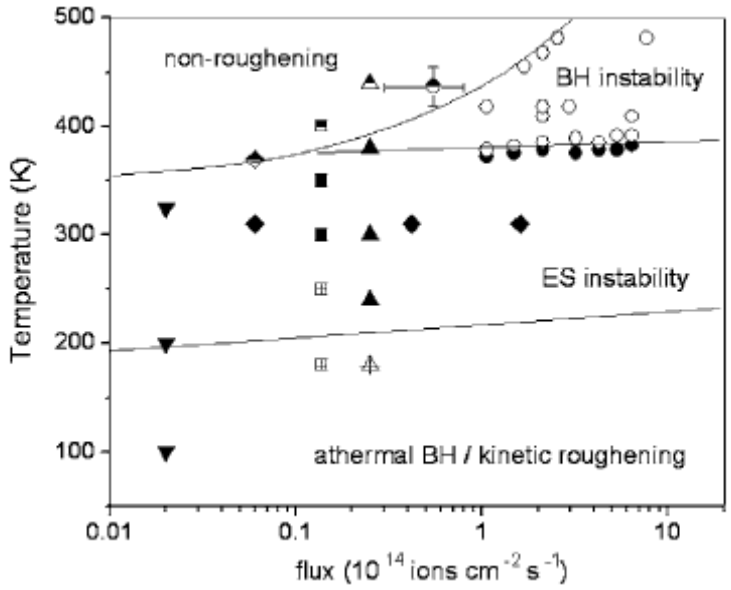

Figure 3.12 – Kinetic phase diagram for ripple formation on copper (after Chan 2007)

Low temperature processing led to ripples formed by effective surface diffusion as suggested by Makeev. Mid range temperatures, the typical working region for most processing, gave Ehrlich-Schwoebel (ES) zone ripples. This is a region where ripples form with their orientation dependent on the surface crystallography (Chan 2007).

The ion fluxes used for this copper work are ~10^5 times lower than the flux of a typical FIB source and the crystal orientation dependent ripples were not seen during the experimental work in this thesis. This suggests that at higher fluxes any crystallographic effects are prevented by the destruction of, or severe damage to, the crystal surface by the much greater flux.

Zhou's work was specifically about the wavelength tunability of ion bombardment induced ripples on sapphire. The wavelength could be varied from 20nm to 2µm by changing the ion energy, beam angle and sample temperature. However the ion fluxes and energies used were 10^6 and 15 times lower respectively than a typical

FIB system delivers. Ion induced smoothing was suggested as the dominant mechanism at low temperatures and relaxation by surface diffusion at higher temperatures. The low energy and flux used mean that the suggested dominant mechanisms in sapphire can not justifiably be assumed to be the same for FIB systems. The greater ion penetration depth and longer collision cascades will affect the balance of competing mechanisms.

All the detailed modelling and experimental work on rippled surface formation has been carried out at low flux. This raises the question as to the usefulness of the modelling work for normal FIB processing. The alternative mechanisms suggested in (Datta 2001) and (Mayer 2005) may provide a more useful avenue for future higher flux work in the area.

3.7 - FIB and tooling

The first papers on use of ion sputtering for sharpening diamond tools were by Miyamoto and co-authors starting in the early 1980s and continuing through to 1990. The first paper (Miyamoto 1982) reported investigations into the disordered surface layer created by the ion impacts, and the topography of the resulting surface finish. They reported that the topography is not dependent on sputtering conditions but on quality and inherent defects of the pre sputtered surface. This was later shown to be untrue by work in the 1990's using higher energy focused ion beams. Miyamoto was working with 1keV argon ion shower equipment. They went onto produce sub micron radius stylii (Miyamoto 1983). In subsequent work by (Miyamoto 1987) the production of indenters, styli and knife edge and single point tools were described. The single point tool had a tool radius of 30nm. Duo plasmatron ion beam equipment was described, this having ion energies of 10-20keV. This is the basis of the modern FIB as the beam is a narrow beam steered by electrostatic lenses, not an ion shower broad beam. (Miyamoto 1990) described ion beamed tools with cutting edge radii of 20-30nm compared to mechanically produced edges of 70nm. The improvement was put down to much

reduced micro chipping. Aluminium was turned using these tools giving a surface roughness R_{max} of 30nm. (Miyamoto 1989) looked at the effect of ion bombardment on diamond crystal structure. Machining with argon ions of 0.4 and 2keV reduced the fracture strength of the diamond by 3 and 5GPa respectively. The pre-milling fracture strength was 39GPa. This was due to the disordered carbon-argon mix of material at the surface. Miyamoto wrote a book chapter (Taniguchi 1989) on ion beam processing, partly drawing on the papers (Miyamoto 1982), (Miyamoto 1983) and (Miyamoto 1987). A common aspect to all of Miyamoto's papers is that the tools and indenters were all mechanically ground to the correct shape before being ion beamed. The ion beaming improved the finish on an already completed piece. The later work from Vasile onwards instead created the cutting edges by ion beaming from tool blanks.

There was then a quiet period in the literature until 1996 when Vasile, Adams and others started to publish. Most of the useful work comes out of the Sandia national laboratory in the US. From this point on all the ion machining was carried out with focused ion beams unless stated otherwise. (Vasile 1996) described the production of M42 cobalt hardened high speed steel tools with 25μm long facets and two cutting edges. The problems associated with milling sharp edges using an ion beam were mentioned here for the first time. A technique that avoided creating rounded edges due to the Gaussian beam profile, by rotating the tool, was described. The tools made were used to cut trenches into Perspex. (Friedrich 1996) described the same work but with greater emphasis on the machining of the Perspex. (Friedrich 1997) described the same 1996 FIB tools but used for machining x-ray lithography masks. (Vasile 1998) described the production of M42 steel tools with one, two, four and six facets. Attempts to partly automate the FIB process for multiple tools were described. Microsurgical tools for mice experiments were also made from stainless steel needles. The tools had hooks and other desired shapes, varying from 5-15μm in size. Two approaches for milling micro scale cavities to exact shapes were examined. Direct programming sets a different

dwell time for each pixel depending on the depth of the feature at that point. This took no account of ion dose from adjacent pixels or the changing mill yield with angle at each pixel as the feature developed. The exact solution approach was computationally more complex as it included varying mill yield, beam overspill into adjacent pixels and pixel size combining these into an equation based on surface contours. (Vasile 1999) described the production of a steel shaping tool with a width of 18μm capable of 30μm depth of cut. The Gaussian effect during facet milling and the angular dependence of the mill yield were discussed, along with the need for reducing spot size during the milling process.

(Taniguchi 2000) produced a 30nm radius field emitter tip from a (111) plane synthetic single crystal diamond. (Adams 2000) described the steps involved in making micro grooving tools from M42 steel and C2 tungsten carbide. The taper angle of 5^{o} -10^{o} formed on nominally flat surfaces due to the peak yield angle was first mentioned here. This is the effect described in section 3.1.6 and figure 3.7. Cutting edge radii of 400nm were produced on tool sizes of 15-20μm. Tools were produced in ~5 hours. Cutting tests with the steel tools gave surface Ra's of 300, 120 and 220nm for Perspex, aluminium 6061 and brass respectively. (Adams 2001) described the production of micro end mills ~25μm in size from steel and tungsten carbide (WC), figure 3.13. Edges with radii of ~100nm were created. Machine tests gave surface roughnesses of 93, 82, 139 and 162nm for Perspex, aluminium 6061, brass and 4340 steel respectively.

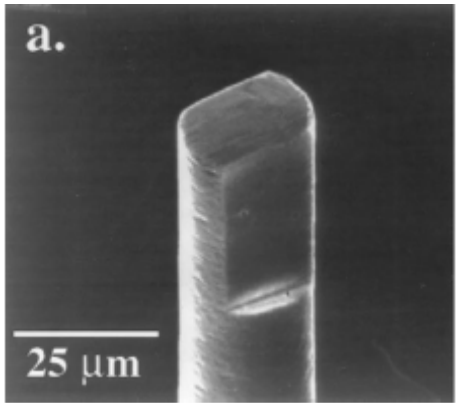

Figure 3.13 – SEM image of a FIB made tungsten carbide end mill
(after Adams 2001)

(Picard 2003) extended the work to single crystal diamond and increased the variety of tool shapes. This was the last journal paper on tooling from the Sandia group, after which their output shifted to the morphology and other effects caused by FIB milling on diamond. They produced WC, high speed steel (HSS) and single crystal diamond (SCD) tools with cutting edges varying from 15-100µm. The cutting edge radius of curvature of the SCD and WC tools was measured as 40nm. The edge roughness Ra was 50nm for WC and HSS, and 40nm for SCD. Single (23µm edge) and double tip (10µm edge) SCD tools were produced. The single tip tool is shown in figure 3.14. The surface morphology caused by FIB is obvious in the close up image of the tool.

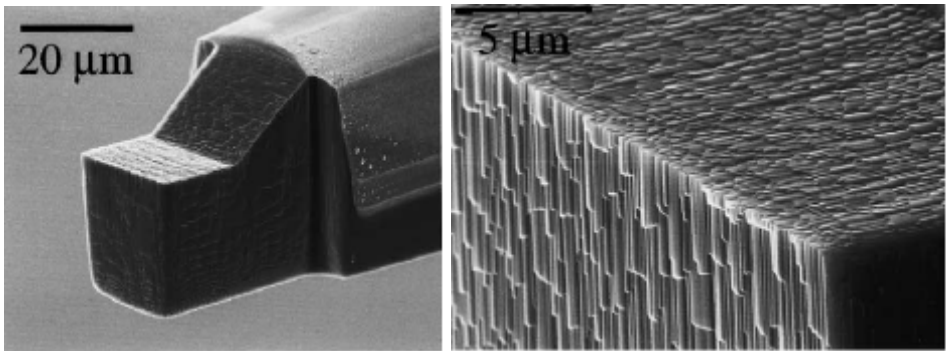

Figure 3.14 – Sandia laboratory single crystal diamond tool (after Picard 2003)

A single edge custom ground HSS tool was finished using the FIB, giving an edge radius of less than 1µm. This was used to machine grooves into polymer rods. A double tip tool with triangular cutting faces was produced, the tips being 24µm long and 20µm wide at the base. These were also used to machine polymer grooves.

(Ding 2008) produced an SCD tool with a single cutting edge of 28µm, figure 3.15. The tool edge radius was 15nm and the Ra of the tool facets was better than 40nm, the rake angle was 0^o and the clearance angles were 7^o. The clearance angles formed naturally due to the sharp drop in mill yield. The tool was used to produce shallow microgrooves of 380nm depth to demonstrate the production of cutting chips of less than 250nm in size. It was then used to machine arrays of micro pillars and thin wall channels in aluminium 6061. The paper also looked at diamond surface morphology change during milling, yield variability with beam angle and redeposition/amorphised material. Most of this had been covered previously by (Adams 2003), (Mayer 2005) and (Adams 2006).

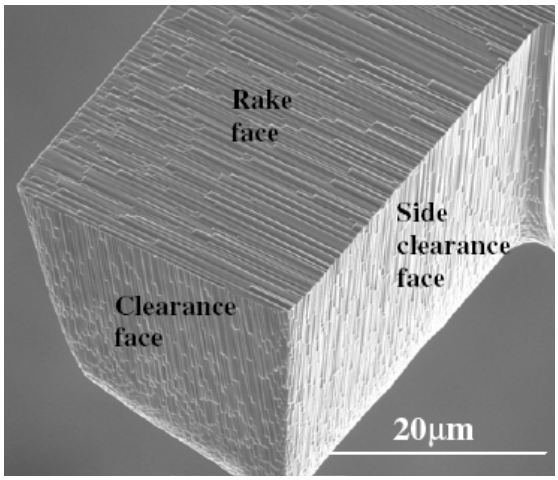

Figure 3.15 – Singapore group single crystal diamond tool (after Ding 2008)

(Ding 2009) wrote about the testing of the tools made in (Ding 2008) by machining aluminium 6061, RSA095 (a small grained aluminium alloy), oxygen free high conductivity copper and nickel phosphorus. The Ra roughness values achieved for

these materials were 28nm, 58nm, 20nm and 27nm. The effect of grain size on cutting performance was measured. The change in cutting force was found to be related to the grain structure the tool encountered along the cut line. This work was carried out using similar equipment and techniques to those used at Cranfield and thus is discussed in greater depth in chapter five.

3.8 - Modelling of the FIB process

Various models of the FIB process have been developed. The better models produce the scan strategy needed to produce a particular shaped feature taking into account the angle dependent milling yield and redeposition (Kim 2007, 2007a). (Edinger 2001) is a less common model because it models gas assisted milling. As part of the 3D-Mintegration project, the School of Computing and Mathematical Sciences at the University of Greenwich was interested in the modelling of the FIB process with a view to a joint publication. A model that predicts the shape and depth of features given the dwell times and beam current, or the dwell times needed for a given feature shape has been developed (Stoyanov 2009, Tang 2009). The model is described in a conference paper (Stoyanov 2009).

3.9 – Summary

The published literature for FIB is not extensive compared to other areas of precision engineering or physics. This is due to the relative youth of the subject and the fact that the spread of FIB systems into universities has occurred mainly over the last fifteen years. It is possible to arrive at a list of ~20 papers on the subject of diamond processing and tooling production that describes all the important and most relevant work. The Sandia lab papers make up about half that list.

FIB processing has been described and reviewed many times over the last twenty years. The machining issues have been discussed and advances in the field recorded. General models of ion induced surface morphology and the causal

processes have been produced. However, the usefulness of the detailed modelling to normal FIB processing is questionable due to the low fluxes and ion energies used. The FIB processing of diamond has been widely studied and the angle dependent morphology of its surfaces investigated with suggestions made for the surface transport processes at high fluxes. The increase in yield from the use of gas assisted milling has been recorded for all the major assist gases. The use of FIB for tooling has mostly been in the US in recent years after the initial Japanese work. The Sandia lab during the period 1996-2003 has produced most of the useful papers on the subject.

Chapter 4

4.0 - Equipment, materials and methods

The equipment used for processing and measuring the tools, samples and work pieces is described below. Then the methods used during the experimental work are described.

4.1 - Focused ion beam system

Cranfield has a FEI FIB 200 system bought in 2003, figure 4.1. This was upgraded in late 2005 for the PhD work. It is a single column system with a gallium Liquid Metal Ion Source (LMIS).

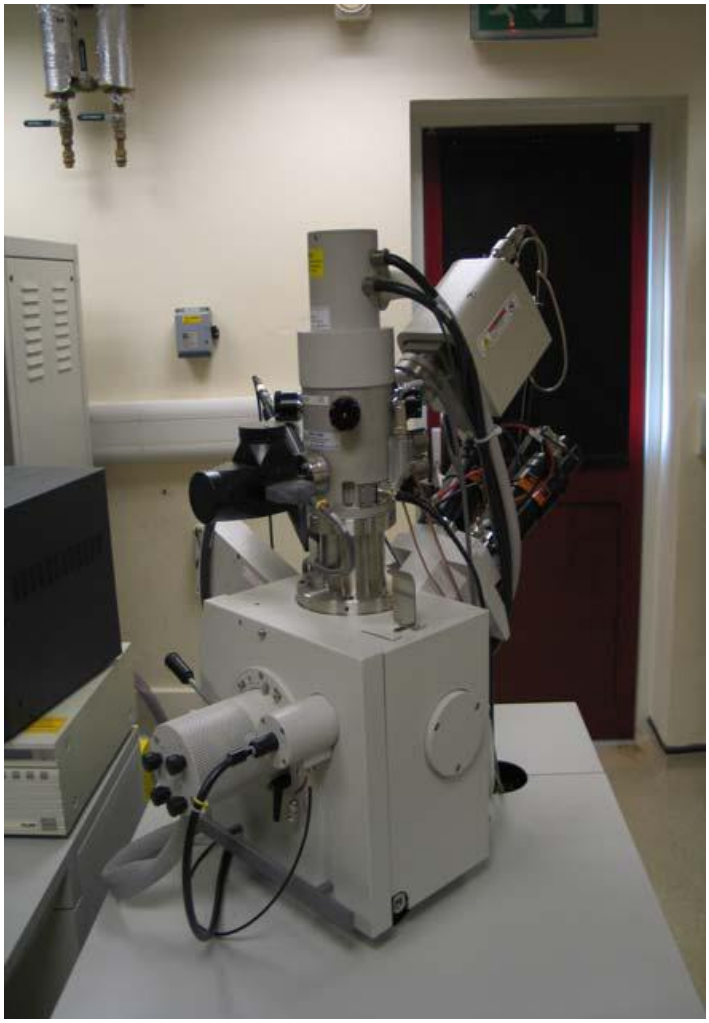

Figure 4.1 – A FEI 200 FIB system

The upgrade consisted of installing a charge neutralizer in the chamber, adding an extra water vapour injection system (described in section 3.1.5) and having a second milling control/pattern design software package by Raith GmbH added to supplement the original FEI software.

4.1.1 - Control software

The standard software that is supplied with the FEI 200 allows the milling of simple shapes (circles, rectangles, lines etc) and more complex, user-defined quadrilaterals. Regular and cleaning cross-sectioning patterns are also available for producing depth profile analysis pits. When milling a pattern the time is calculated by the choice of material file and the pattern depth entered. The material file is a setting that defines some of the beam parameters (spot overlap and pixel dwell time) and the yield for the material chosen. There are files for common materials and modes such as aluminium, silicon, water assisted milling of carbon and platinum deposition. If there is not a suitable material file for the sample to be milled then a mill time can be entered manually. Patterns can be milled sequentially or in parallel. The beam spot moves in a raster motion across the pattern from top left to bottom right. Multiple beam passes over the pattern area are made until the pattern depth entered has been reached. The depth of a completed feature is often lower than the entered pattern depth due to the effects of redeposition during milling. For more complex milling, Raith 3-D Quantum software (Raith 2009) is used. This allows more complex shapes and arrays of identical shapes to be milled. CAD files can be imported allowing a degree of pattern complexity far beyond what the FEI software can provide. The ion dose across the pattern elements can be varied, allowing great variety in milling. Different patterns can be set to run in sequence with the sample being moved to the correct stage coordinates for each pattern. Long runs of patterns can be set up and left until completion. The FEI software is limited to patterning the area that is visible on the screen with the sample having to be repositioned for further patterns.

4.2 - Metrology equipment

The following equipment was used to measure and examine tools and samples.

4.2.1- Scanning Electron Microscope

A FEI XL30 SEM was used for examining tools, milled samples and machined metal pieces.

4.2.2 - Atomic Force Microscope

A Veeco Dimension 3000 AFM was used, this has a Z range of 5μm and a vertical resolution of 0.01nm. This was used for profiling FIB milled surfaces and diamond machined copper. The images were processed using the software that came with the microscope and WSxM version 2.2. This is scanning probe microscopy software developed by Nanotec Electronica S.L, (Horcas 2007, WSxM user manual).

4.2.3 - Taylor Hobson Form Talysurf 120L

This is a contact probe linear measuring system with a 2μm diameter ruby probe ball. It has a maximum vertical range of 1mm with a resolution of 12.8nm. The horizontal range and resolution is 120mm and 250nm. This was used for measuring the profile of sinusoidal tool machined copper.

4.2.4 - Wkyo Topo 3D

This is a single wavelength (633nm) interferometric microscope. The surface height is measured by a Mirau phase shifting interferometer. The vertical resolution is 0.3nm. This was used to measure the roughness of machined copper.

4.2.5 - Taylor Hobson Talysurf CCI – Lite

This is a white light coherence correlation interferometer with a vertical resolution of 0.01nm, and horizontal resolution of 500nm. This was used for measuring the roughness of machined copper trenches.

4.3 – Materials for FIB machining

The following materials were used during the experimental work.

- Monodite MT - Cuboidal samples of synthetic single crystal diamond from element 6. These are grown using the high temperature high pressure method and are yellow in colour due to them containing about 0.2% nitrogen impurities (Element 6 Monodite). The samples were 4x3x1.2mm in size and cut along the (100) plane on all faces.
- Polycrystalline diamond – Compax 5025 TS.
- Polycrystalline chemical vapour deposited diamond – sourced from element 6 via Contour Fine Tooling (Element 6 PCD). This was used for creating the FIB tools, see section 4.4.
- Synthetic sapphire – A disc of sapphire sourced from UQG optics, Cambridge and custom grown curved sapphire pieces from PBTsilicon, Switzerland.

4.4 - FIB production of tools

Polycrystalline blanks were laser processed and mounted on diamond tooling machine compatible kite shaped shanks, figure 4.2. The laser processed blanks were supplied by Contour Fine Tooling Ltd, Stevenage.

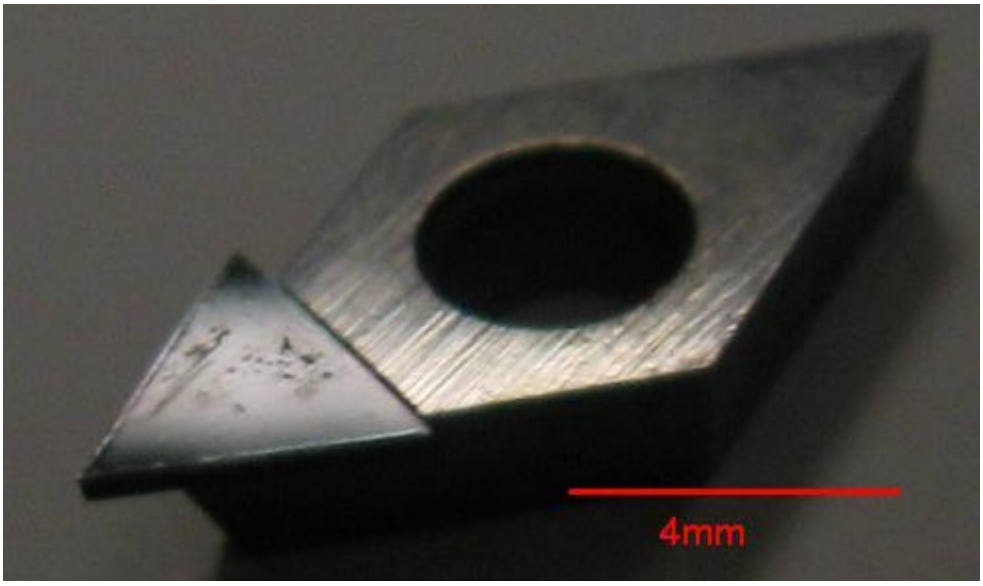

Figure 4.2 - Laser cut CVD tool blank mounted on shank

The kite shanks are held in horizontal and vertical holders provided by Contour, figure 4.3. The stub of each holder fits into the FIB chamber sample holder mount.

Figure 4.3 – CVD tool blanks in the horizontal and vertical holders

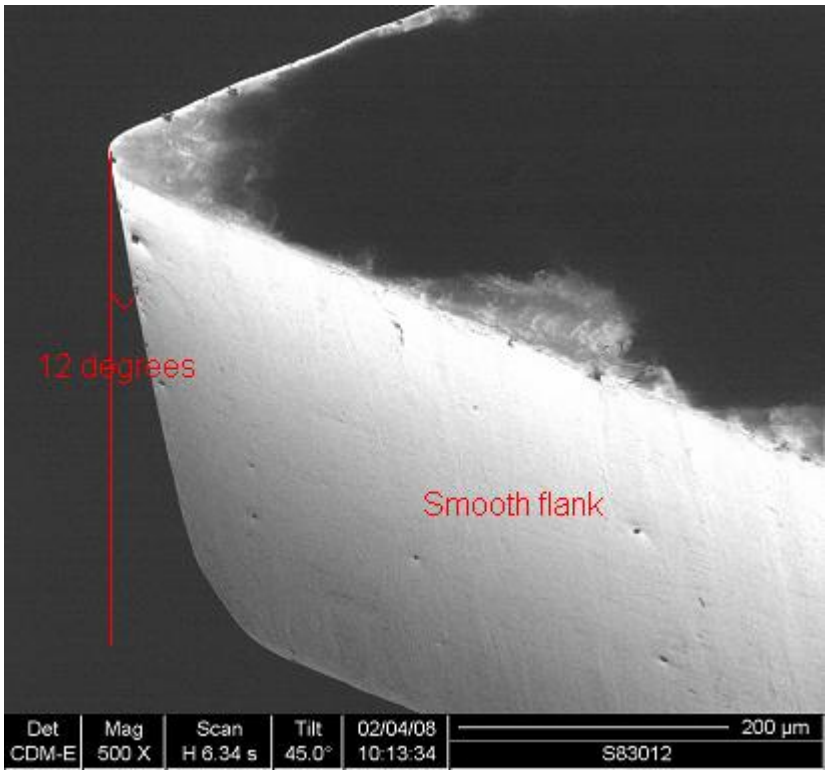

Figure 4.4 - Side view of CVD tool blank showing the front clearance angle

The clearance angle on the front face of the diamond blanks is 12^{o} as shown in figure 4.4. The flanks of the tool are smooth enough to not be a problem when using the tool for turning.

4.5 - Diamond tools testing

A Moore Nanotech 350 Ultra Precision Lathe diamond turning machine made by Moore Precision Tools was used for the tool testing, figure 4.5. This has a positioning resolution on its axes of 34pm and has a programming resolution of 1nm. This resolution allows precise movement of the tool with a minimum step size of 10nm for the tool stage. Diamond turning machines are designed to be very stiff and stable so that the effect of vibration on the work piece and the tool is minimized. The tool stage is moved by hydraulics, electric motors and piezoelectric actuators to avoid direct mechanical linkages and the stage sits on top of an air suspended granite block along with the spindle and vacuum chuck. The spindle is isolated from the electric motor that spins it by an air bearing.

Figure 4.5 – A Moore Nanotech 350 UPL diamond turning machine

4.5.1 - Turning tool testing

The tools were tested by machining trenches into oxygen free high conductivity copper (OFHCC). This is copper that is at least 99.95% pure due to its very low copper oxide content, (West 1979, 1982). Copper was chosen because the chance of the tools surviving the machining process was unknown and to decrease the chances of tool breakage a soft metal was chosen. 2 inch diameter discs, with a thickness of 1cm, were cut. These were then faced off (machined flat) with a round nosed single crystal tool until a mirror finish was achieved. This gave a surface roughness of ~20nm Sa. This was important for two reasons: firstly, a smooth finish was needed when bringing the tool into contact with the work piece as the initial material removal was hard to spot. Secondly, the rough surface of the cut disc would overwhelm the smooth surface of the diamond cut area making AFM measurement of the test areas difficult. The Z range of the AFM would be exceeded when measuring across the trenches.

The first turning tool (S83011) was tested by milling 5, 10 and 20µm deep trenches, with three trenches cut for each depth. The trenches were concentric circles as visible in figure 4.6. The disc shown has its centre without mirror finish due to a non standard tool holder configuration that prevented the whole disc surface being faced off for this test. The difference in surface quality between the mirrored and non mirrored surface is obvious. All the other discs used for the tests were machined with the standard tool holder configuration, allowing the whole surface to be faced off. The non standard tool holder configuration was due to the test being fitted into a schedule gap in a long running job that required a modified vacuum chuck.

Figure 4.6 – A diamond machined OFHCC disc

The copper disc was held by a vacuum chuck and the tool holder on the z axis was brought into contact with the disc, as in figure 4.7, which shows the standard vacuum chuck.

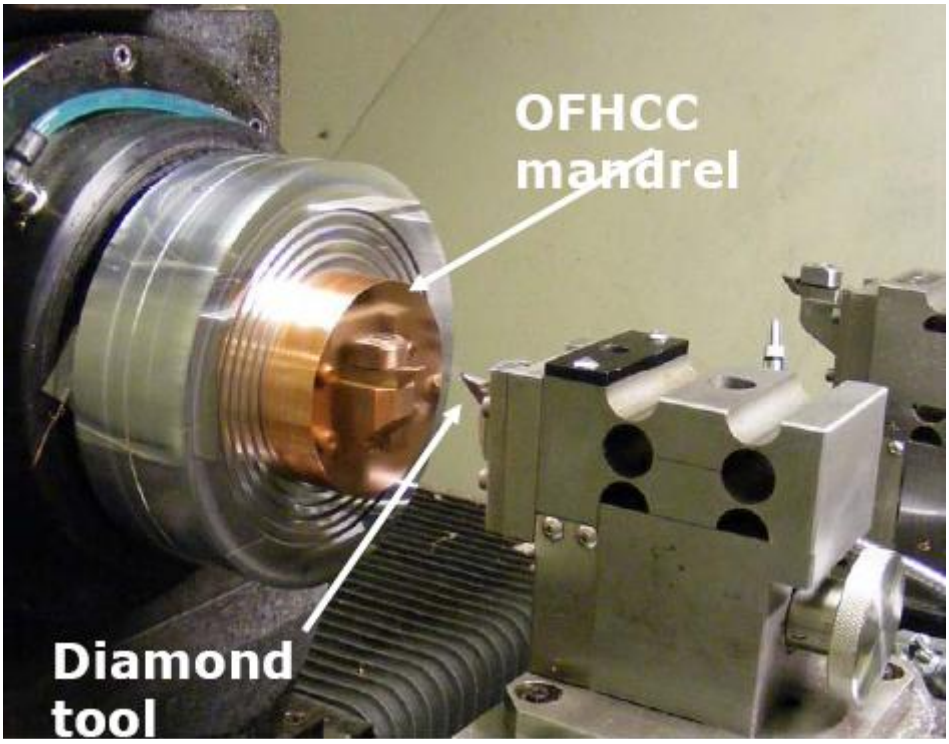

Figure 4.7 – Standard machining setup on the Moore machine

The machining conditions chosen for the tests are given in table 4.1.

Work piece rotation speed	1200 rpm
Depth of cut per rotation	10nm
Coolant	White spirit sprayed across tool and disc

Table 4.1 - Machining conditions

The white spirit was used to remove swarf from the cut zone making analysis of the trenches easier.

A dynamometer was attached to the Moore for the tests of turning tool S83011 and the first sinusoidal tool S87355. However, the machining forces were below the minimum threshold of the device due to the low depth of cut and the slow rotation speed.

The second turning tool, S83012, and the second sinusoidal tool, S87356, were tested under the same conditions as S83011 except that instead of 5, 10 and 20μm deep trenches the depth was kept to 5μm. This meant that all trenches could be measured by AFM.

4.6 – Sapphire FIB machining

Synthetic sapphire was machined to create part of a mould for microinjection moulding of polymer. Patterns were milled onto the inner surface of a curved sapphire gutter. The gutter is shown in figure 4.8 after being coated with a thin layer of metal for improved imaging properties.

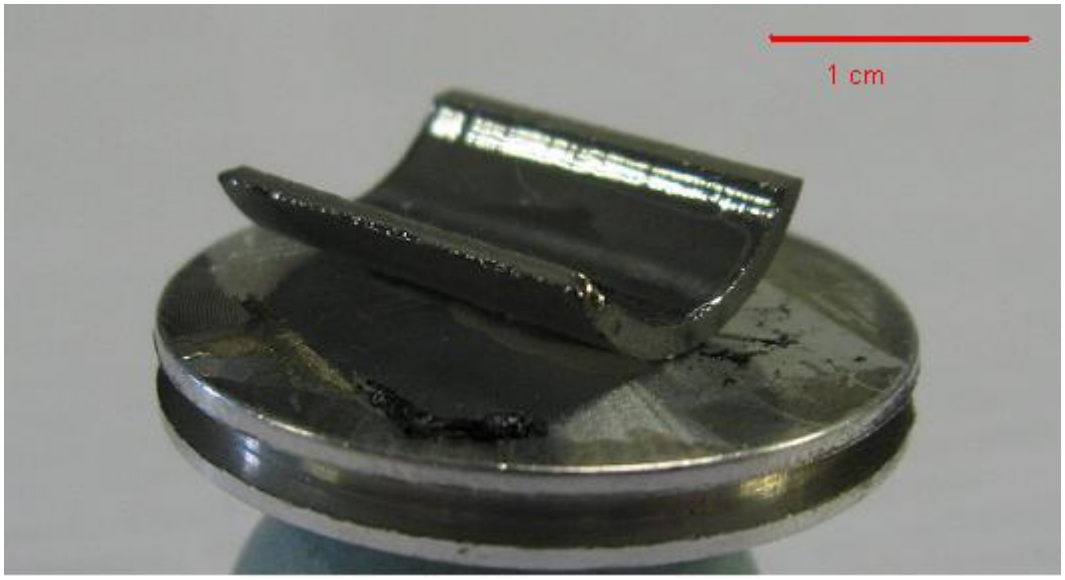

Figure 4.8 – A sapphire gutter that has been sputter coated

Chapter 5

5.0 - Results and discussion

This chapter describes:

- The initial work done on the FIB milling of single crystal diamond, section 5.1
- The surface morphology of milled single crystal materials, section 5.1.6
- The FIB milling of sapphire, section 5.2
- The manufacture of polycrystalline diamond turning tools, section 5.3
- The manufacture of sinusoidal shaped tools, sections 5.4

5.1 - Milling of single crystal diamond

The first part of this work was carried out to understand the behaviour of single crystal diamond (SCD) during FIB milling. The following sections will explain pattern movement issues (5.1.1), the measurement of mill yield (5.1.2), the natural occurrence of non vertical surfaces (5.1.5) and diamond surface morphology (5.1.6).

5.1.1 – Pattern movement tests

The charging up of the diamond during milling is an issue because diamond possesses few free electrons and therefore a net positive charge builds up in the region where the Ga^+ ions impinge on the surface. This is because some of the gallium ions remain embedded just below the sample surface. There is also the effect of positive carbon ions being created during gallium-carbon collisions that are not ejected from the diamond. The net effect is that there is a distortion of the placement of the beam spot. This problem increases with milling time and for higher beam currents above 1nA and is described as beam drift. The insulating nature of SCD affects also the quality of the collected images. For SCD the ion imaging mode has to be used as the electron mode images provide very low contrast (see section 3.1.4).

The cumulative movement this causes for milling patterns was investigated for three of the larger beam currents 1, 2.7 and 6nA. These currents were selected because they are typically used in the milling process. Figures 5.1 - 5.3 show the milled square features. The number at the centre of each feature indicates the milling time in minutes. The 2.7nA beam squares were milled for twice as long as the other two currents because this is the primary milling current. As such, it would be used for longer periods of time in the same area of the sample than other currents. With hindsight the other two currents should have been milled for the longer time as well to give an equal view of the movement over all three currents. Knowing the movement over longer periods is useful when removing bulk material before carrying out finer detail milling. Ensuring that the region of bulk removal will not shift into unwanted areas during a long mill is necessary.

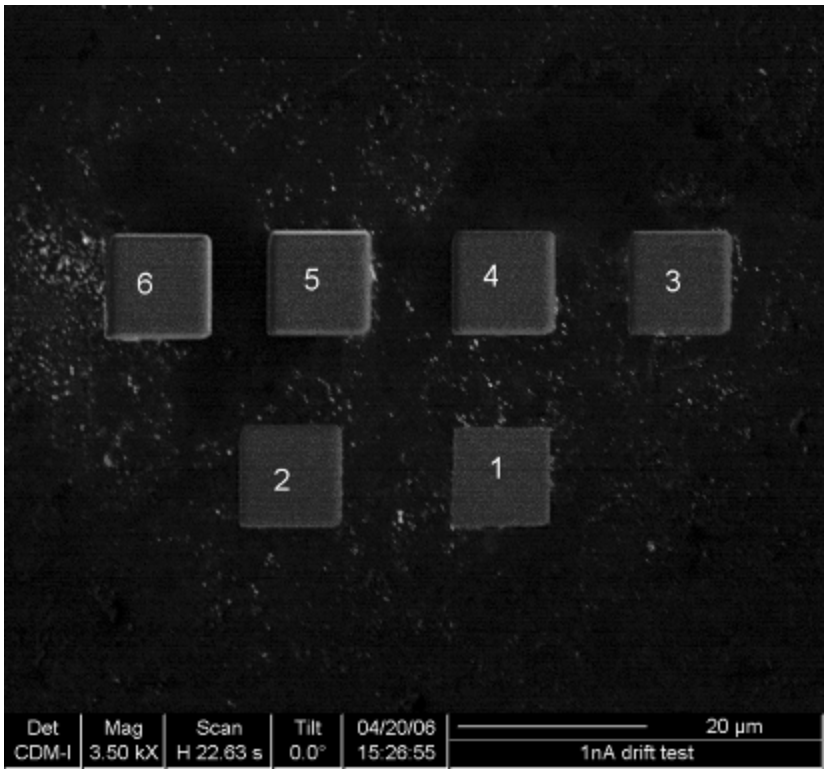

Figure 5.1 – Pattern movement on SCD for 1nA beam current. The mill time in minutes for each hole is superimposed on the hole.

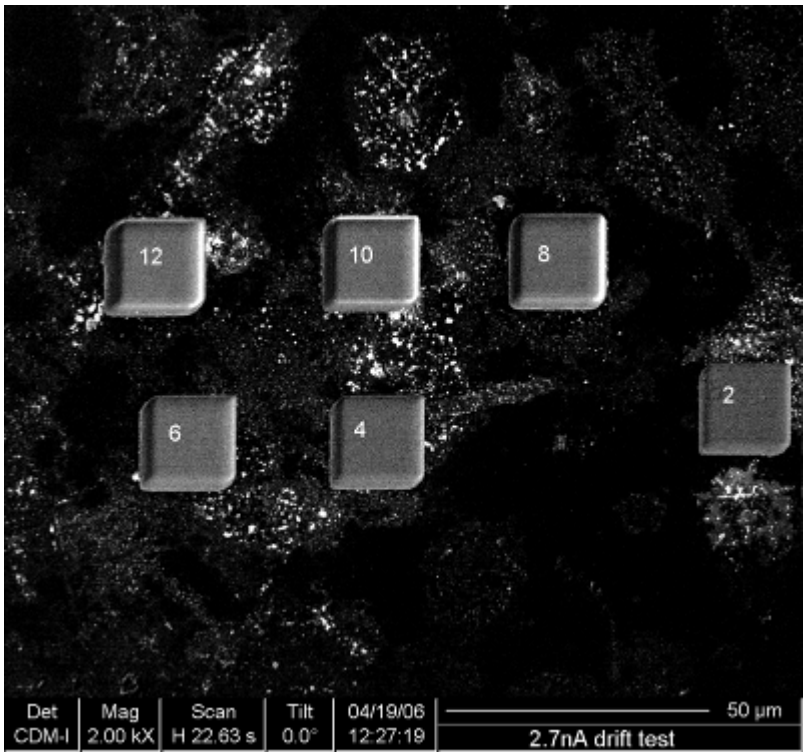

Figure 5.2 – Pattern movement on SCD for 2.7nA beam current. The mill time in minutes for each hole is superimposed on the hole.

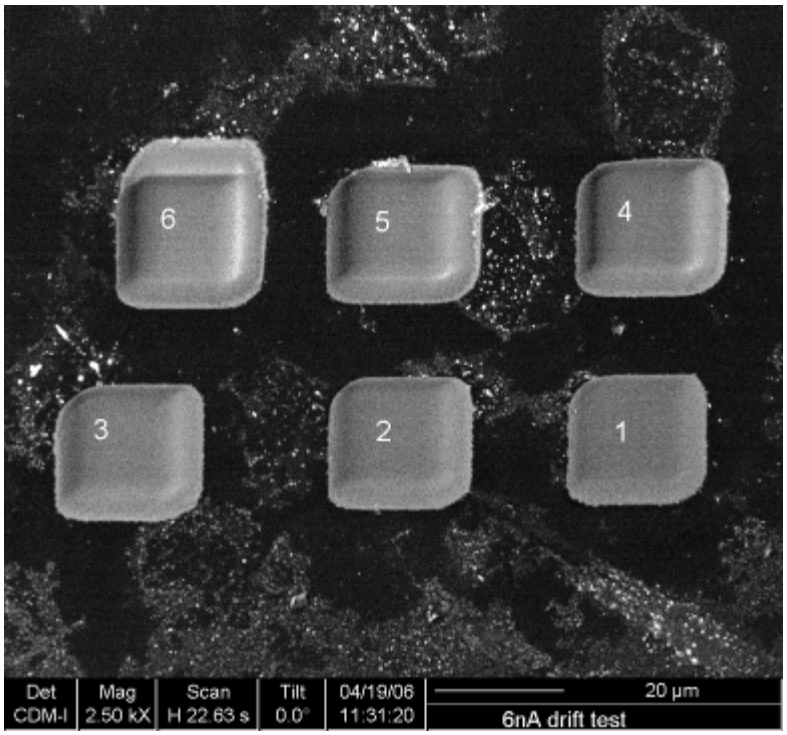

Figure 5.3 – Pattern movement on SCD for 6nA beam current. The mill time in minutes for each hole is superimposed on the hole.

The 6 minute hole in figure 5.3 is an anomalous result since the extra milling on the northern edge of the hole could not be repeated for other mills using the same variables. These holes resembled the 1-5 minute holes, with pattern movement to the east and south only. One of these holes was used when measuring the movement distances.

Movement was measured for all the squares in the north-south and west-east directions. Figure 5.4 shows the movement obtained using the 2.7nA and 6nA currents. The 1nA movements were less then 0.5µm in either direction for each square. The movement obtained using the 2.7nA current is small enough to be taken into account during pattern placement. With time variable movement in one direction only the pattern can be placed with a corrective displacement. The movement for 6nA patterns cannot be so easily compensated for this way.

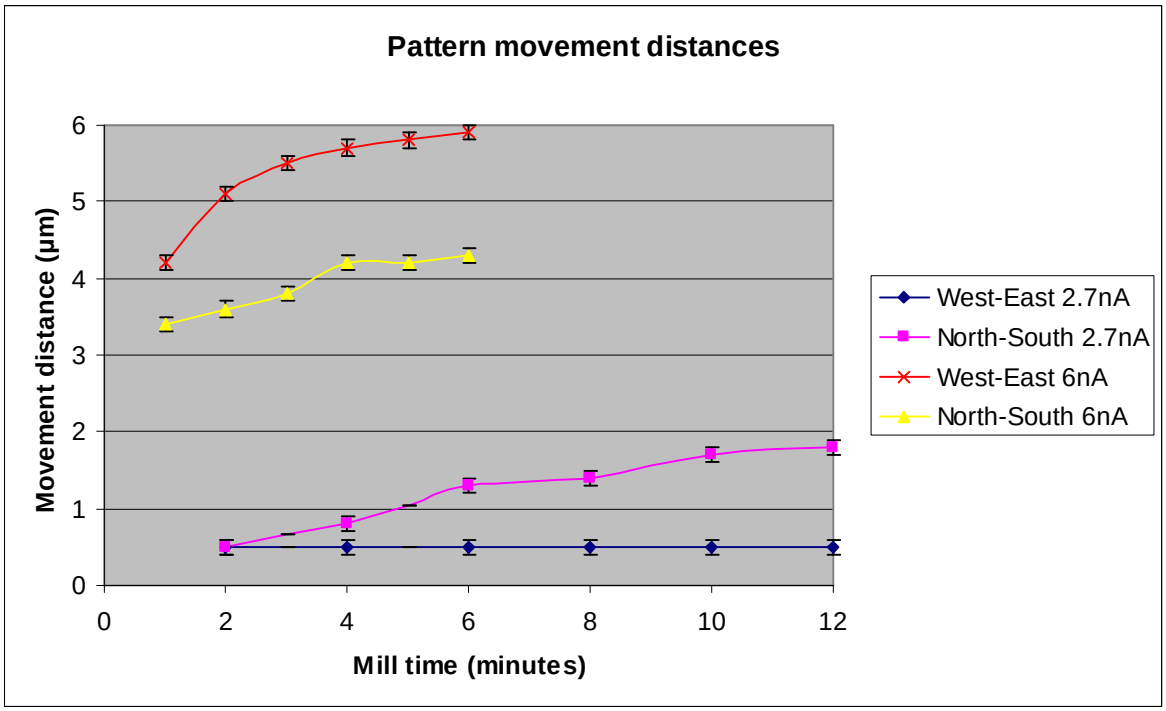

Figure 5.4 – Pattern spread distance on SCD

The pattern movements in both axes were combined into a single figure of merit by square summing the distances. This gives a measure of the overall movement which is plotted in figure 5.5. A reason for the much smaller movement for the 2.7nA holes compared to the 6nA is the smaller addition of positive charge to the diamond.

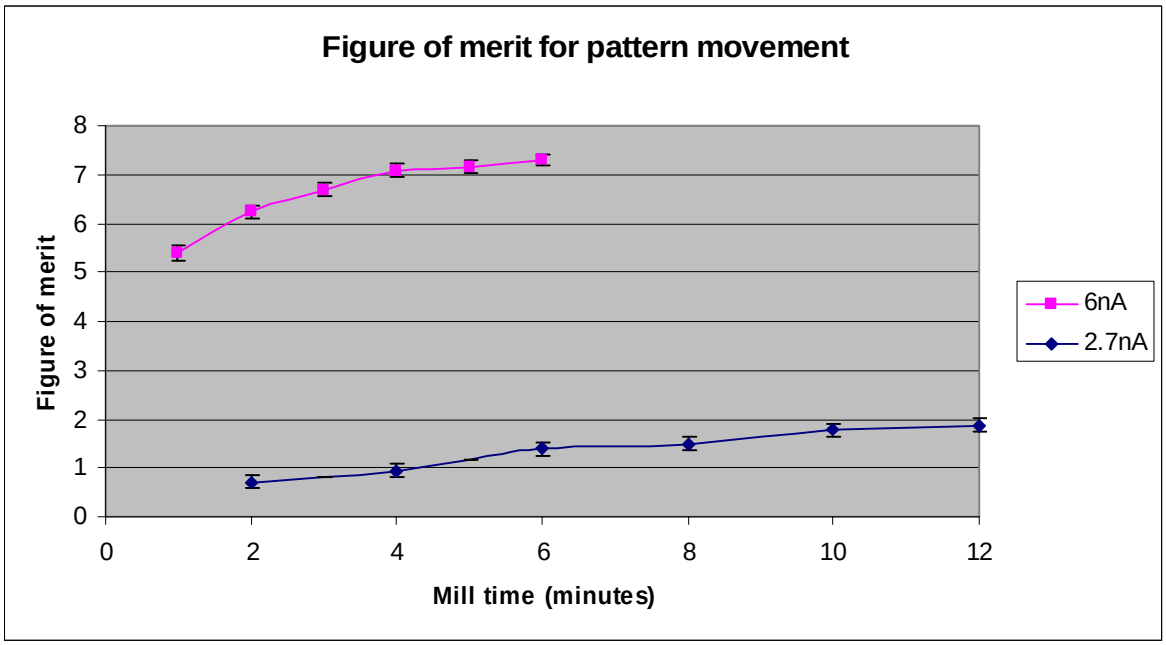

Figure 5.5 – Pattern spread figure of merit

The increase in the pattern movement with time is partially due to the beam drifting as described above. There are also the possible effects of a non-symmetrical beam spot and the layout of the metal components inside the chamber causing charge asymmetries. A non-symmetric beam spot will cause milling outside of the desired pattern area emanating from the distorted spot itself and also its side tails (section 3.4). The effects of the side tail milling will increase with time as the number of ions in the tails is low compared to the main spot. Thus for short mill times the effect of the tails will be low, but over several minutes noticeable pattern enlargement will become visible. This, however, cannot produce enlargements of up to 6μm as for the 6nA current. A possible cause of the large enlargements may be chamber induced charge asymmetries. The chamber, as shown in figure 3.4,

contains two gas injection tubes, the charge neutralizer, the detector and the stage. The asymmetric arrangement of these metal components, all of which have free electrons, causes a local electric field. This local field may distort the beam and cause a directional shift in the pattern placement. This would explain the shift to only the east and south of the pattern. However, the predominant, but unexplained, shift direction is different for the 2.7nA and 6nA beams being southwards for 2.7nA and eastwards for 6nA.

The increase in pattern movement with beam current is therefore caused by the increase in charge at the surface of the diamond, the drift, and the increasingly large side tails of the spot. The direction of the drift may be caused by the charge asymmetry in the chamber.

In order to minimise the pattern movement caused by the charging of the surface, a charge neutraliser (section 3.1.2) was used. The charge neutraliser settings were found by trial and error, altering the beam energy for successive milled holes until the movement was cancelled out. The use of the charge neutraliser reduced the movement to less than 1µm in either axis for all currents except for the 11.5nA beam. For this current the movement was approximately 5µm but varied too much between different holes milled under the same conditions. This lack of predictability meant that the 11.5nA beam could only be used for bulk material removal where accuracy was not important. The cause of this larger movement is probably to be ascribed to a too high charge implantation that the charge neutraliser cannot realistically counteract with any degree of accuracy.

5.1.2 - Yield tests

Figures for the milling yield of single crystal diamond are available from the literature (see section 3.5), but the milling angle dependent yield with the FIB 200 was required. 10x10x4µm squares where milled at 6.7nA beam current at different angles. For milling angles above 45^{o} the diamond was mounted on a 45^{o} angled

stub. This caused problems with setting the eucentric height, as, unless the sample area chosen for milling was directly above the central axis of the stub, there was a translation of the area under the beam spot as well as a change of beam-sample angle. This caused the working distance to change and gave less than optimal milling. The further from the stub axis the chosen area was the worse the problem became. This, combined with the fact that when the sample is at a given angle, picking different sample areas to mill away from the centre by varying the x and y coordinates also varies the z coordinate. This is also true for a flat stub when tilted, but the changes in z are a bigger issue for the 45^{o} stub. A temporary solution to this was to recheck the eucentric height when the sample was tilted and to avoid moving the sample in y unless the movement was very small, ~few 10's of microns and in x only if the movement was parallel to one of the sample edges.

Without knowing that the height was set correctly the water injection tube could not be used as there was only 100µm height clearance between the tube end and the sample. With time and practice the setting of the height for 45^{o}+ became less of an issue with the first attempt being good enough to allow problem free milling. Another solution is to change the stop limit on the stage tilt. This is a bolt that stops the stage being tilted beyond 45^{o} but which can be moved to another position allowing tilts to 60^{o}. This is a practical solution as it is not difficult to do and allows most of the gains in mill yield due to increased angle to be used.

The depths of the 10x10x4µm squares were measured using the measuring tool in the FEI software. The measuring tool works by calculating the distance between two lines placed on the screen by the user. The lines can be placed in the x or y axis and the distance between them given in µm or nm. Due to the pattern movement, however, the squares were not as deep as they should have been and any calculated yields would be too low. As many of the ions as possible needed to fall within the design pattern for a yield calculation to be valid as it is based on the

beam current and the duration of milling. Using the charge neutraliser to minimize drift is necessary.

Another problem with calculating the volume of the removed material was that, as the sample was, tilted the y dimension extends as (1/cosθ), where θ is the tilt angle. This leads to highly stretched out shapes at the higher angles. Figures 5.6 and 5.7 show the stretching of the squares. The 80^{o} patterns were placed too close together and overlapped. From here onwards features milled with water assistance will be referred to as wet, and the normal milling as dry. Adjusting the dimensions of the squares as the sample was tilted was required.

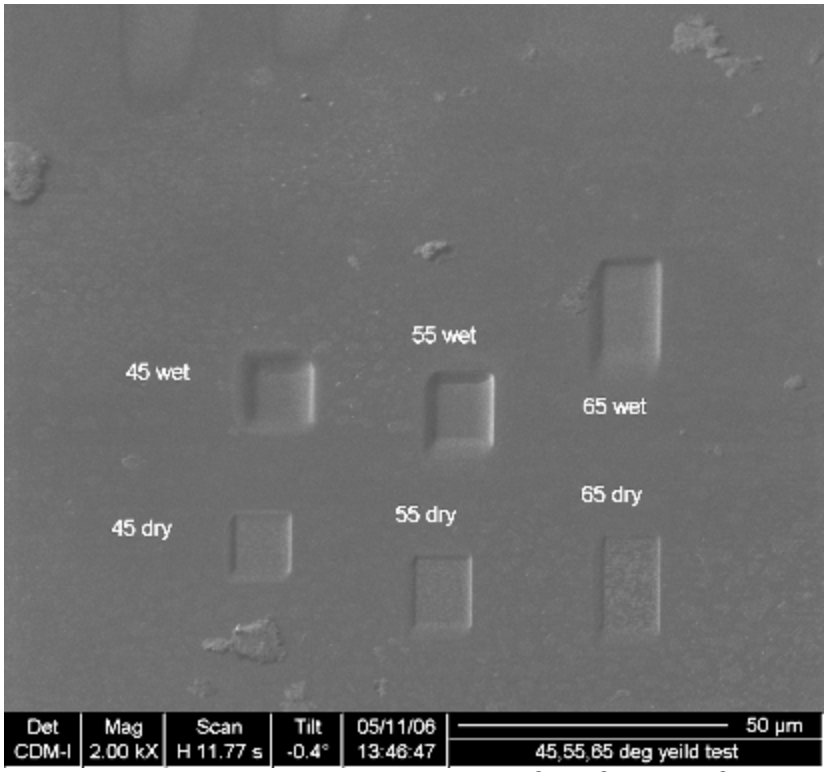

Figure 5.6 – Y dimension extension for 45^{o}, 55^{o} and 65^{o} mill angles

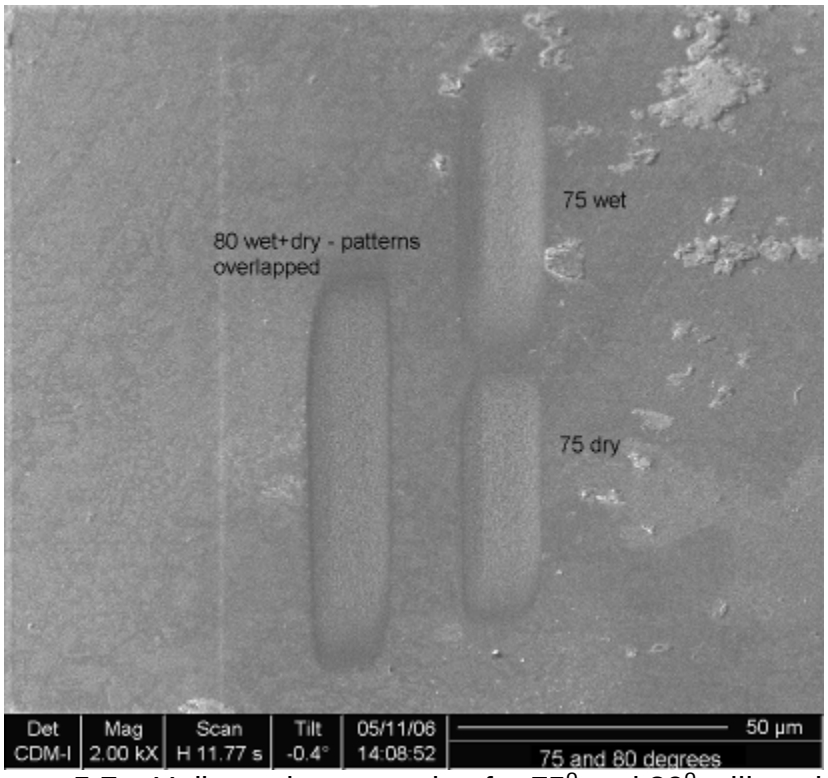

Figure 5.7 – Y dimension extension for 75^{o} and 80^{o} mill angles

5.1.3 - Measurement discrepancies

Multiple sets of holes were milled with different currents with and without water assistance throughout the angle range. However, the yields derived from the hole depths proved to be confusing, figure 5.8.

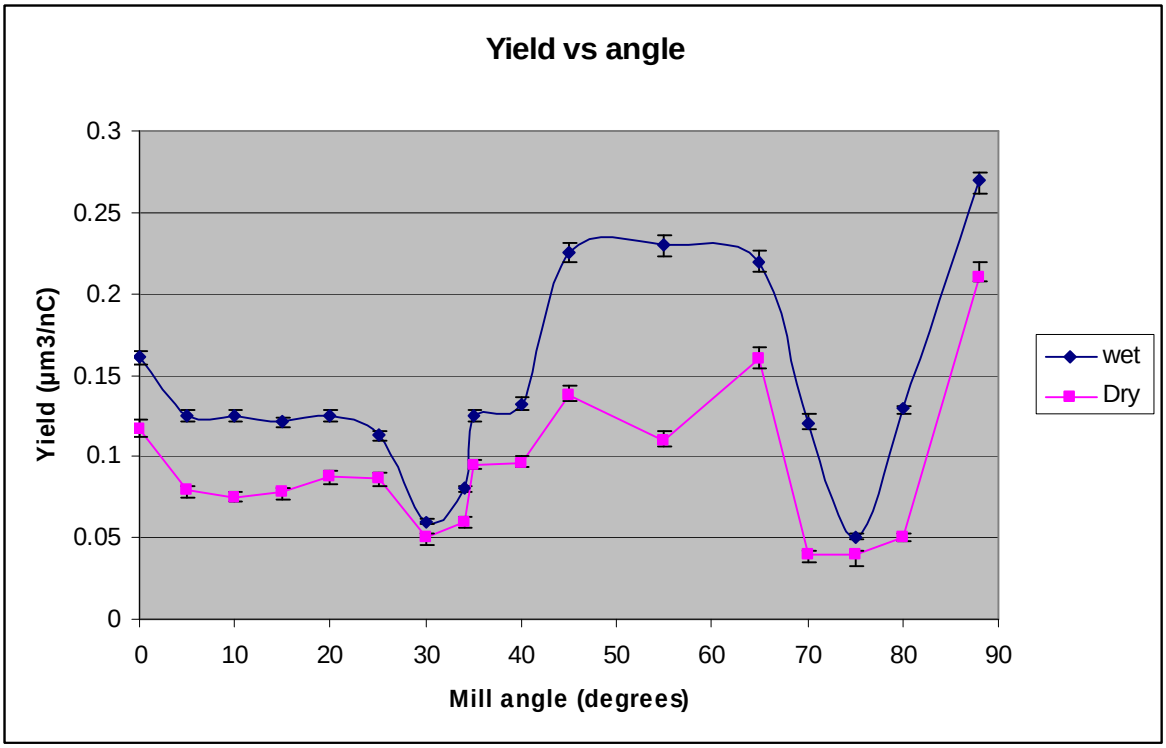

Figure 5.8 - Initial FIB angle dependent yield values for SCD

The yields bore no correlation with those in the literature, figure 5.9.

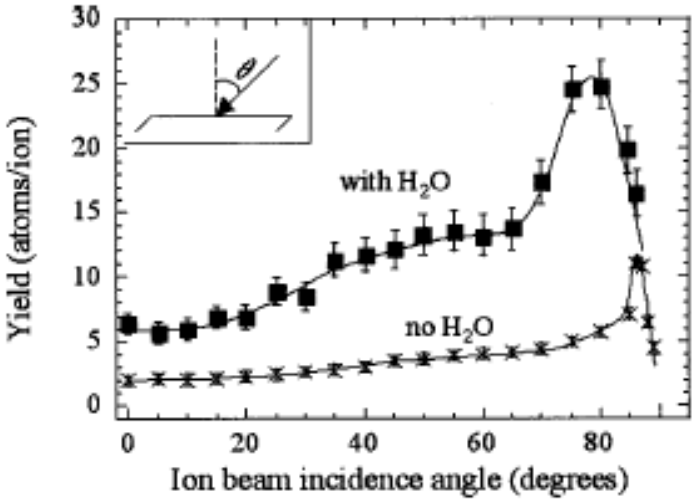

Figure 5.9 – Typical diamond FIB yield curve (after Adams 2003)

The measurement of the hole depths seemed to give false answers. The depth measuring method being used was to tilt the sample to 45^{o} and to use the FEI software measurement tool to measure the height of the back wall of the hole. Two

other measuring methods were also then used to obtain hole depths. Some holes were remeasured with the FEI software at a sample tilt of 0^{o}. The holes were also remeasured with the FEI software with the sample tilted to the angle at which the hole in question had been milled. The depth results from the three methods are shown in figures 5.10 to 5.12. Each graph line is described by the angle of the sample during measuring and whether water assistance was used.

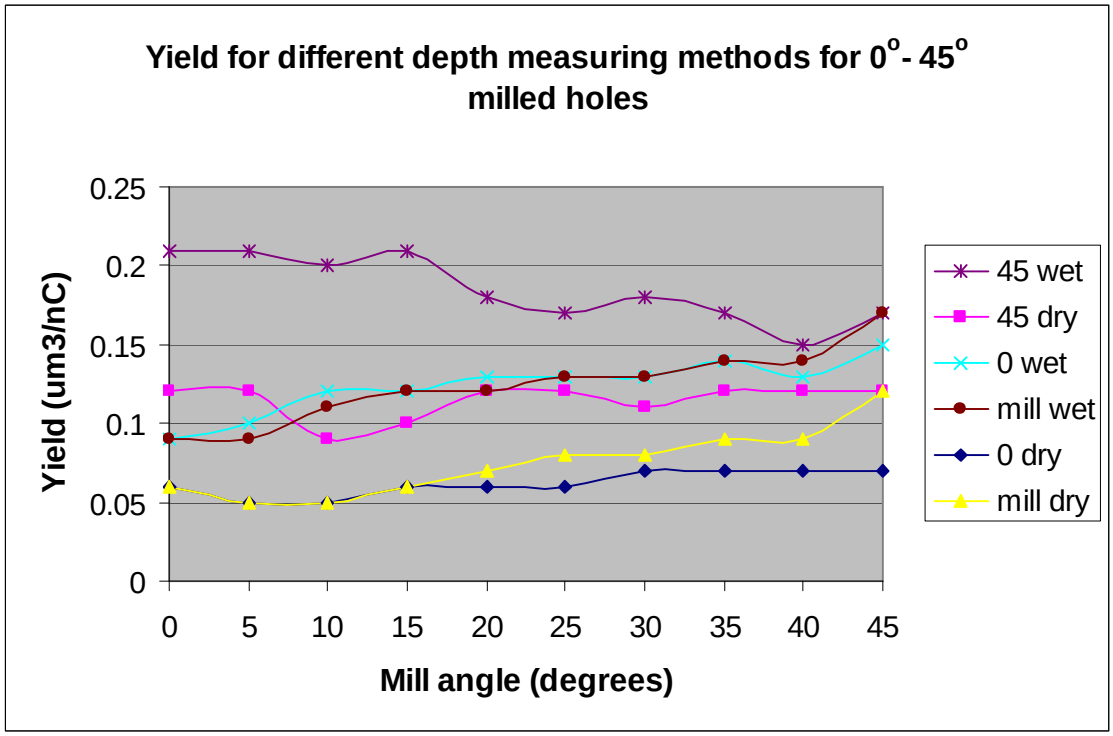

Figure 5.10 – Calculated mill yields for various depth measuring techniques (0^{o} – 45^{o} mill angles)

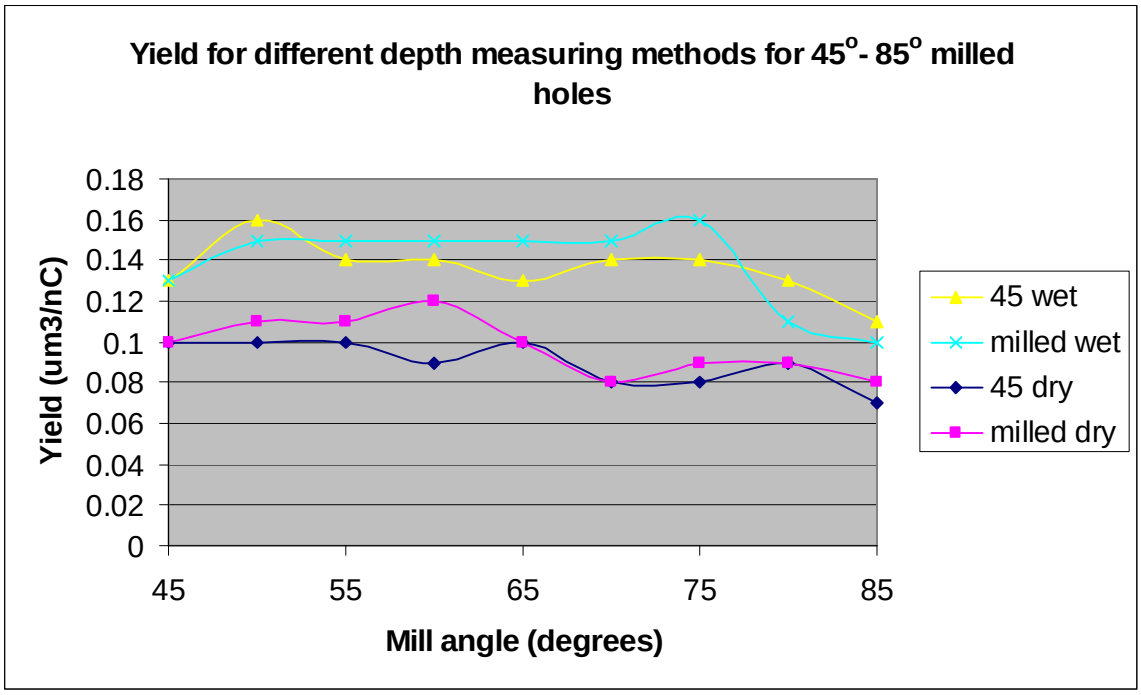

Figure 5.11 - Calculated mill yields for various depth measuring techniques (45° – 85° mill angles)

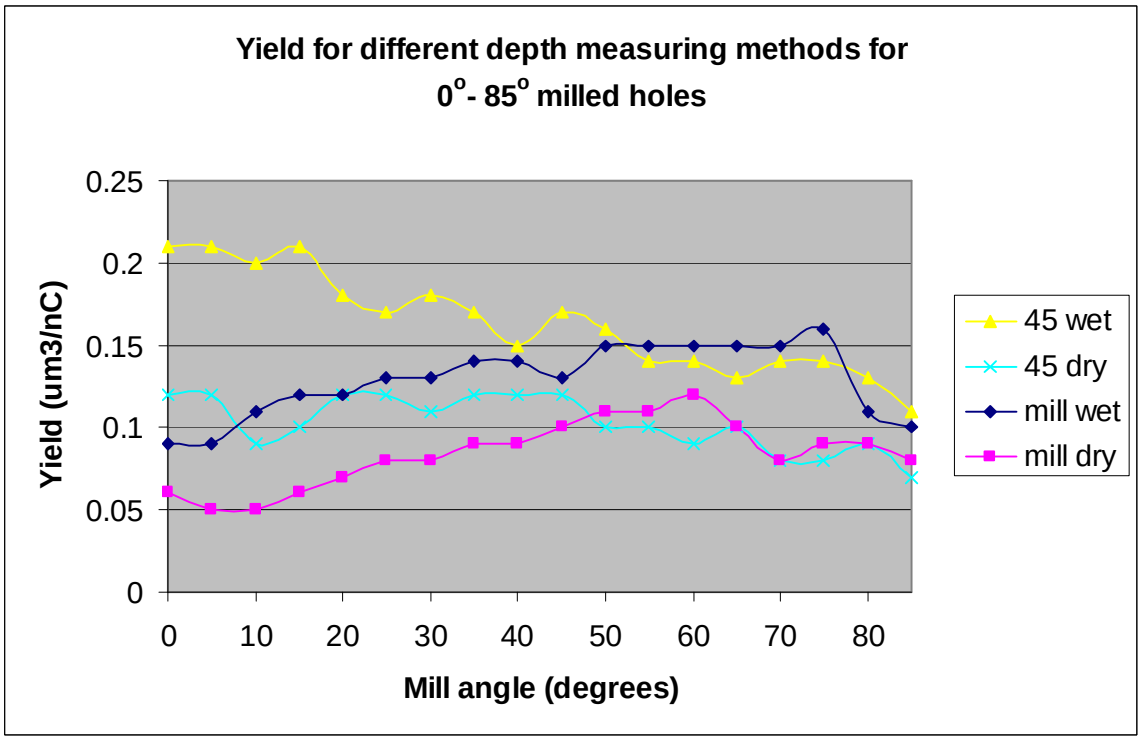

Figure 5.12 - Calculated mill yields for various depth measuring techniques (0° – 85° mill angles)

None of the three methods produced yield curves of a sensible shape, so for accurate hole volumes atomic force microscopy was used. The reason for the erroneous depth measurements is that the measuring tool is designed for measuring the depth of features milled at 0^o and then tilted to 45^o for measurement. This is because the FIB has primarily been a materials analysis technique. The measuring tool is designed for examining the thickness of layers in coatings etc. For holes milled at low angles the depth measured should be close to the actual depth but, as the angle increases, the result becomes increasingly incorrect causing the yield for 45^o+ milling to apparently fall with increasing angle.

5.1.4 - AFM measured yields

An AFM was used to measure the depth and shape of dry and wet milled holes. The shape was important as the milled hole shape was not a straight sided box due to the effect of redeposition and the angle of the beam. The exact shape was needed to get an accurate estimate of removed material. Holes from 0^o to 80^o were milled with 2.7nA, 2000x magnification and 10x10x3.5µm nominal hole dimensions. The AFM tip has an angle of 47^o and a radius of 60nm. When the tip was at the bottom of the deepest measured hole the width of the tip body at the diamond surface was 2.5µm. This was far smaller than the hole width meaning the tip was capable of contacting the sides of the hole properly. Figures 5.13 – 5.20 show the profiles of the wet and dry holes. There was still some extension of the hole y dimension even with the ($1/\cos\theta$) compensation factors being applied. The maximum angle of the dry hole side walls was 41^o for the 75^o hole. The 0^o hole had 6^o walls and the 45^o hole had 9^o walls. The shape of the hole changed little between 0^o and 50^o with the wall angle remaining similar. As the holes stretched out there was a decrease in depth as there were fewer ions per unit area of the pattern. The increase in the efficiency of each impacting ion did not compensate for the reduction in ion density. Above 75^o the natural decrease in ion efficiency and the y axis stretching led to depths less than 1/3 of that at low angles. The maximum dry hole depth of 1.3µm (figure 5.15), compared to the nominal depth of

3.5µm, shows the effect of redeposition when milling in relatively confined conditions. The aspect ratio didn't allow the ejected carbon to escape. This meant that the yields calculated from the AFM scans could be regarded as minimum yields. When milling on the edges of samples and for lower aspect ratios the ejected material was far more likely to escape and result in a higher yield.

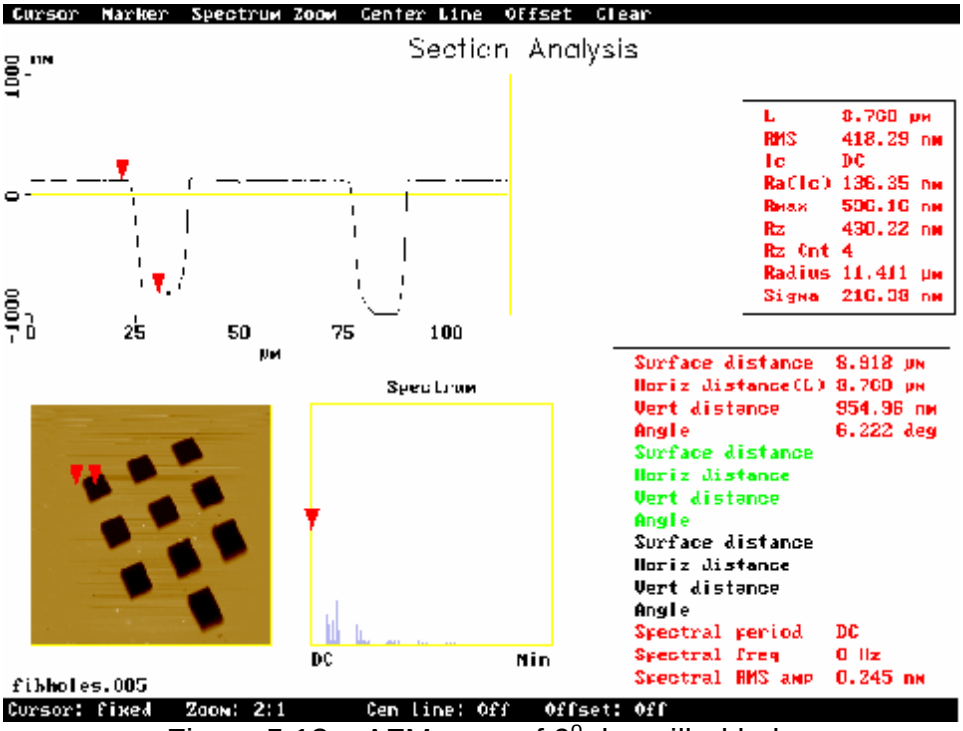

Figure 5.13 – AFM scan of 0^{o} dry milled hole

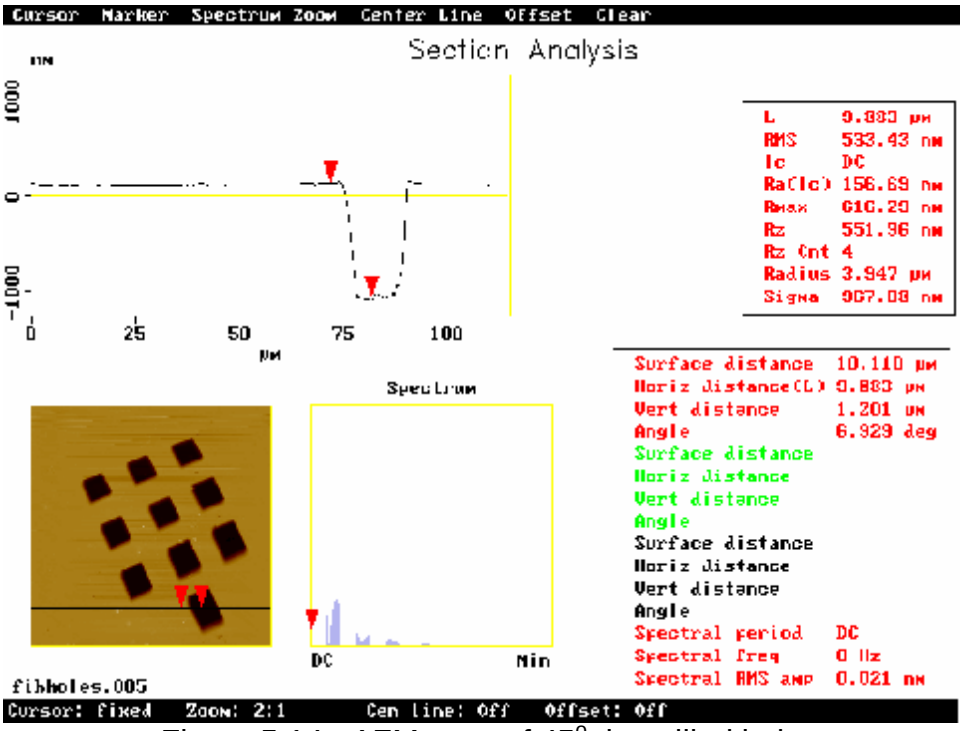

Figure 5.14 - AFM scan of 45^{o} dry milled hole

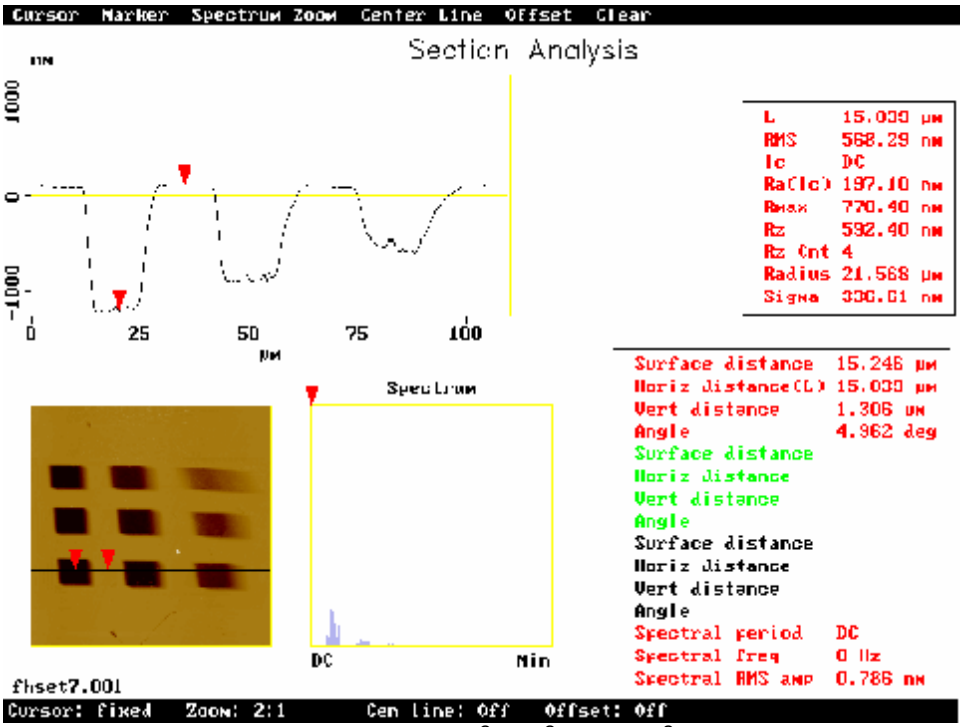

Figure 5.15 – AFM scan of 45^{o}, 60^{o} and 75^{o} dry milled holes

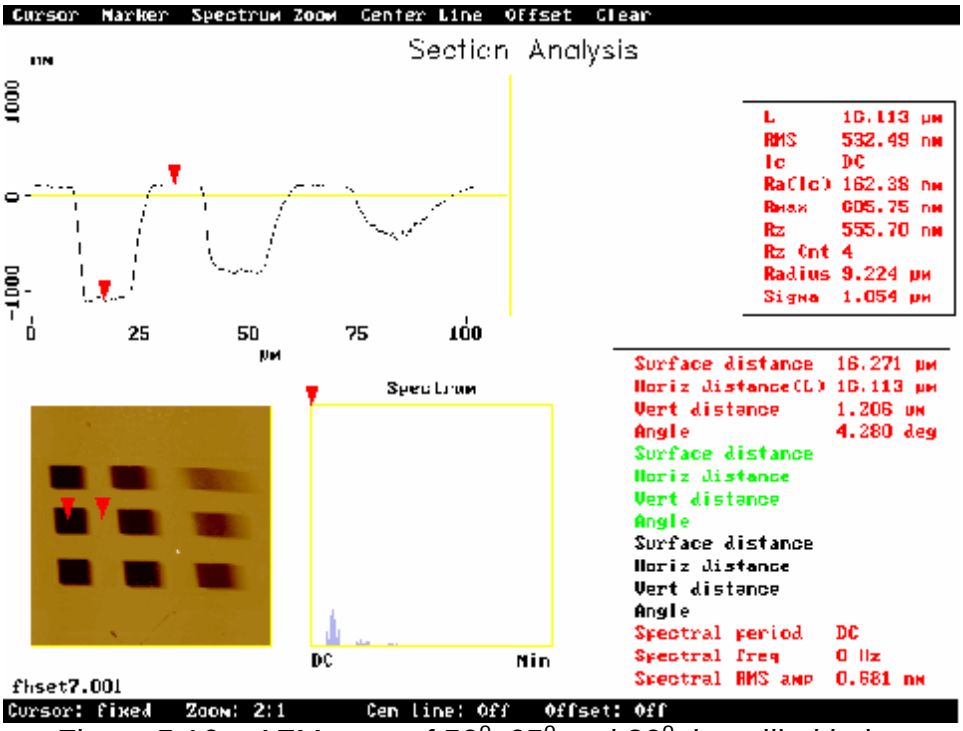

Figure 5.16 – AFM scan of 50°, 65° and 80° dry milled holes

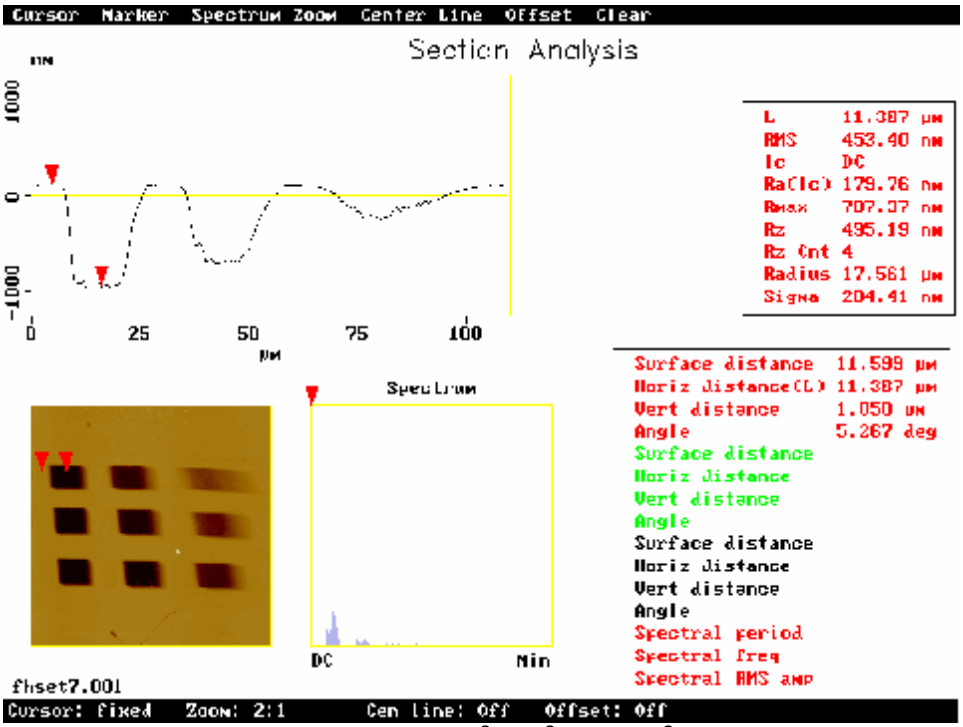

Figure 5.17 – AFM scan of 55°, 70° and 85° dry milled holes

The depths of the wet holes was ~2.5 times more than the dry. The increased material removal led to a different hole shape. As the hole deepened the material removal became more difficult and the distribution of the water on the surface became less uniform. Towards the end of the mill time the bottom of the hole was likely to have dry areas, leading to reduced yield. A lot of material would be redeposited giving the V shape of the hole, with the bottom becoming more rounded with decreasing depth. Again there was stretching of the y axis widening the hole mouth. The increased escape of material via the wider mouth at higher angles may have caused the lower angled hole yields to be under estimates compared with high angle holes.

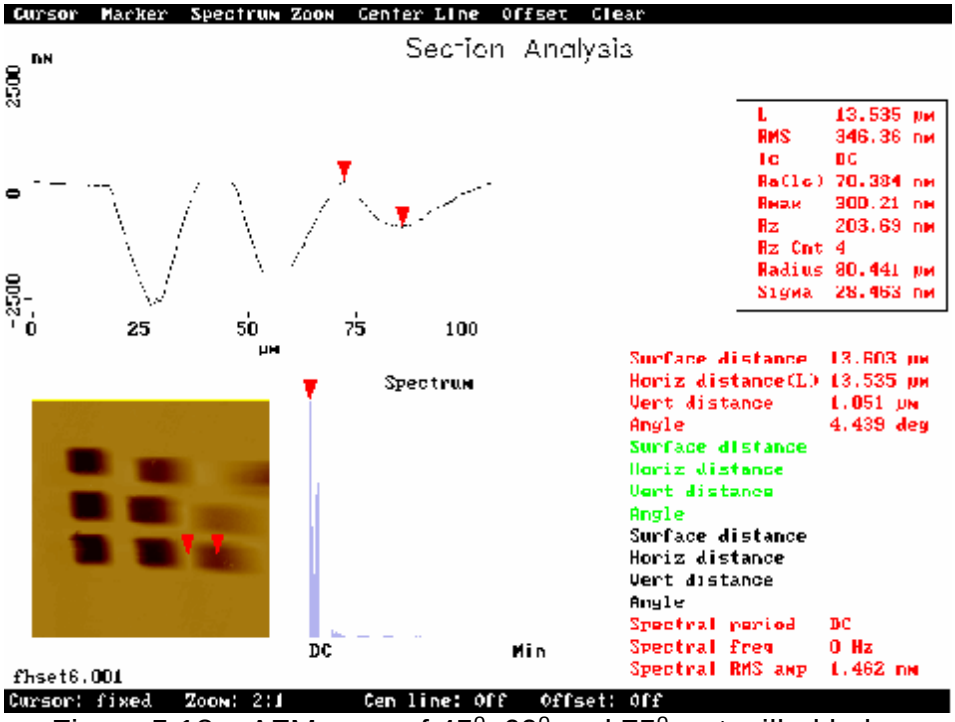

Figure 5.18 – AFM scan of 45°, 60° and 75° wet milled holes

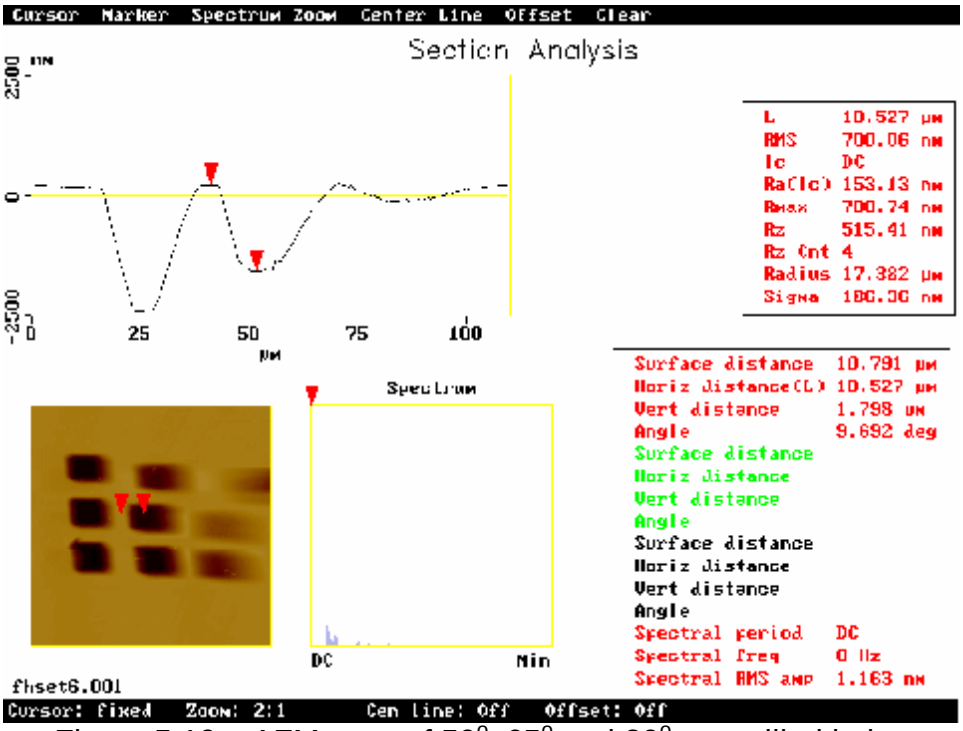

Figure 5.19 – AFM scan of 50°, 65° and 80° wet milled holes

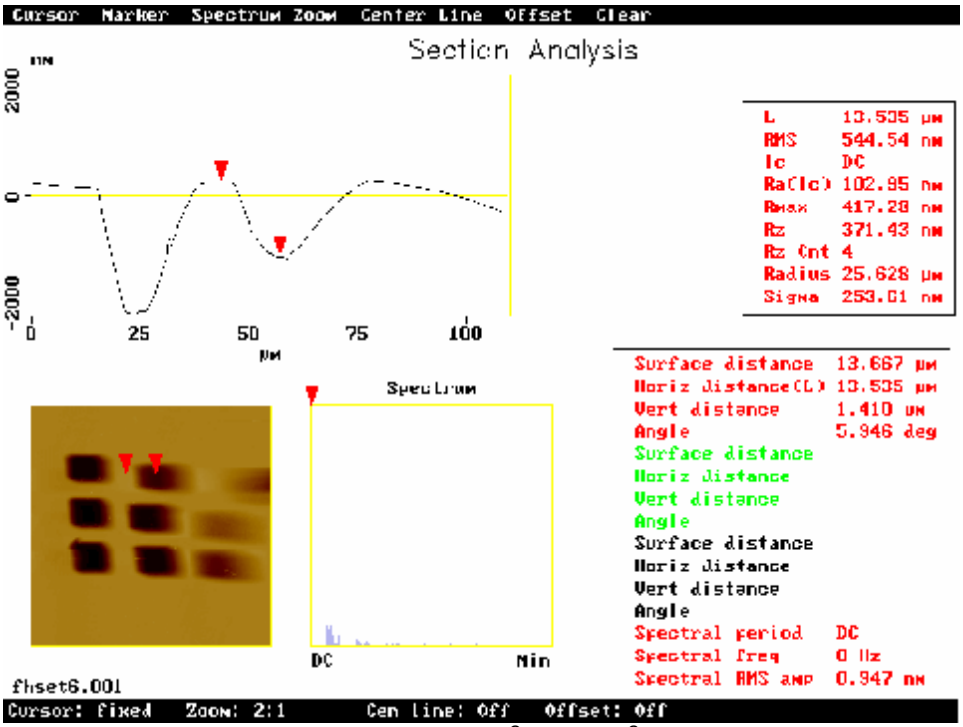

Figure 5.20 – AFM scan of 55° and 70° wet milled holes

The wet hole milled at 85^{o} was not fully scanned because it was so extended that being able to calculate a meaningful hole volume seemed unlikely. The difficulties of milling shapes accurately at 80^{o}+ became apparent at this stage. The need to mill at such high angles during tool production was considered unlikely due to the tripling of the yield for dry milling at 75^{o} (figure 5.21) that had already been calculated by the time the wet holes were being AFM scanned.

The volume of the holes was calculated by measuring the area of the AFM cross section and the surface area of the hole, stretching included. This assumed that the cross section was representative of the hole. This was partially accounted for when placing the profile line across the hole. Several lines were placed across the same hole and when the hole shape was similar for all of them, that shape was taken as being a fair representation of the hole shape. As the process of measuring the cross sectional area was done by hand the estimate of the error on the measurement increased as the milling angle increased. The shape of the holes at low angles was more regular and easier to measure. At higher angles the holes became irregularly shaped and an estimate of area had a greater degree of uncertainty. This is why the error on the wet yield is greater than the dry yield, the shallower more rectangular dry holes being easier to measure. The yields and their errors are shown in figures 5.21 – 5.23 and table 5.1. The yields are given in μm^3/nC and atoms/ion. Both measures are used to describe the mill yield in the literature.

Mill angle (degrees)	Dry yield (μm^3/nC)	+ error (μm^3/nC)	- error (μm^3/nC)	Wet yield (μm^3/nC)	+ error (μm^3/nC)	- error (μm^3/nC)
0	**0.088**	0.007	0.007	**0.222**	0.015	0.005
5	**0.096**	0.007	0.007	**0.255**	0.005	0.005
10	**0.094**	0.007	0.007	**0.246**	0.003	0.005
15	**0.095**	0.001	0.004	**0.199**	0.017	0.019
20	**0.109**	0.004	0.002	**0.230**	0.017	0.017
25	**0.114**	0.004	0.004	**0.245**	0.017	0.018
30	**0.105**	0.004	0.004	**0.239**	0.019	0.017
35	**0.124**	0.006	0.002	**0.256**	0.019	0.019
40	**0.132**	0.004	0.002	**0.280**	0.021	0.021
45	**0.158**	0.009	0.009	**0.282**	0.020	0.020
50	**0.159**	0.008	0.009	**0.329**	0.020	0.020
55	**0.177**	0.009	0.009	**0.354**	0.024	0.006
60	**0.179**	0.009	0.009	**0.389**	0.020	0.020
65	**0.206**	0.010	0.010	**0.334**	0.019	0.020
70	**0.215**	0.009	0.011	**0.412**	0.019	0.009
75	**0.260**	0.012	0.012	**0.447**	0.018	0.018
80	**0.338**	0.015	0.021	**0.308**	0.014	0.014

Table 5.1 – Wet and dry mill yields with error limits

The yield boost from the water is shown in figure 5.23 by the ratio of the yields at that angle. The effectiveness of the water decreases with angle until 80^o where the wet and dry error bars overlap. The yield is at least doubled across the angle range that is most likely to be used. There is also an error of 0.5^o on the tilt angle of the chamber stage for all measurements.

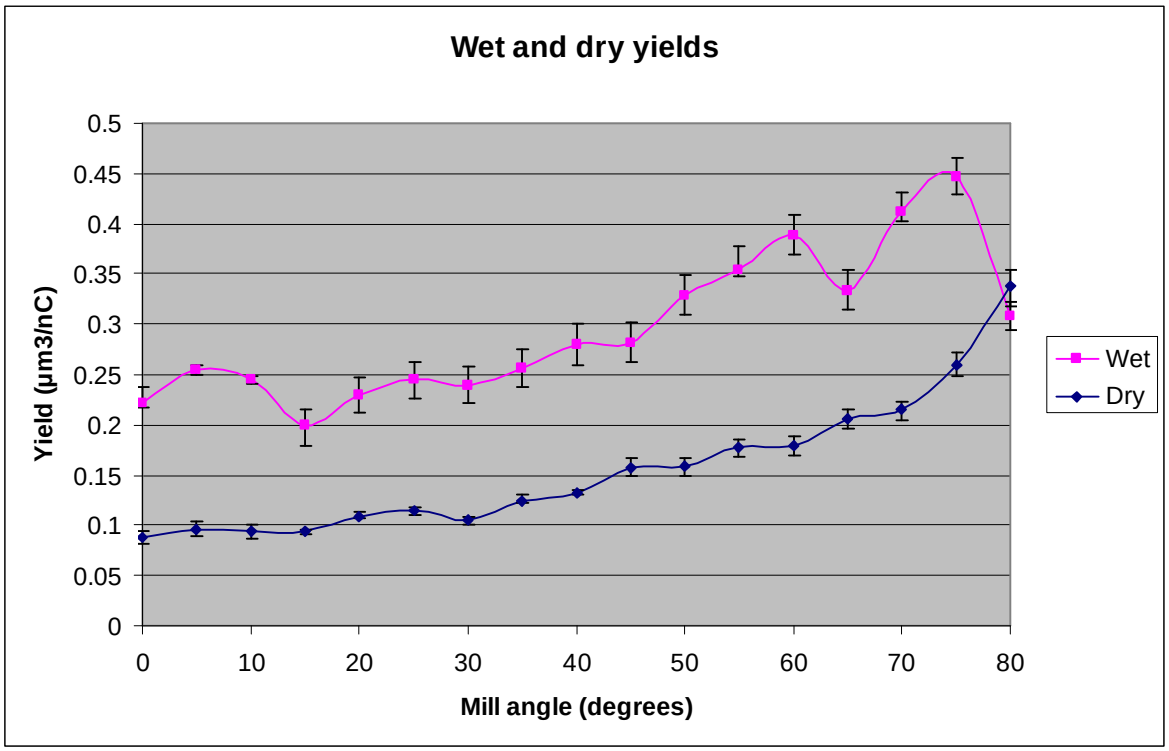

Figure 5.21 – Experimentally derived angle dependent mill yields of SCD (μm^3/nC)

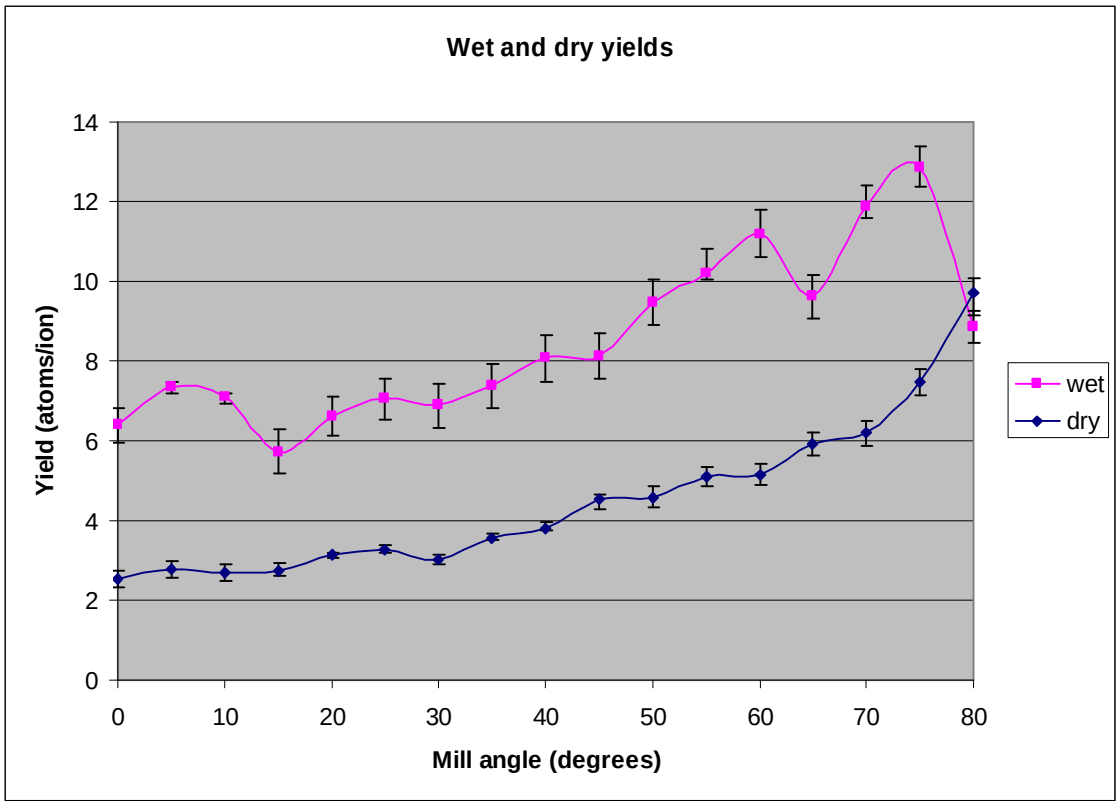

Figure 5.22 – Experimentally derived angle dependent mill yields of SCD (atoms/ion)

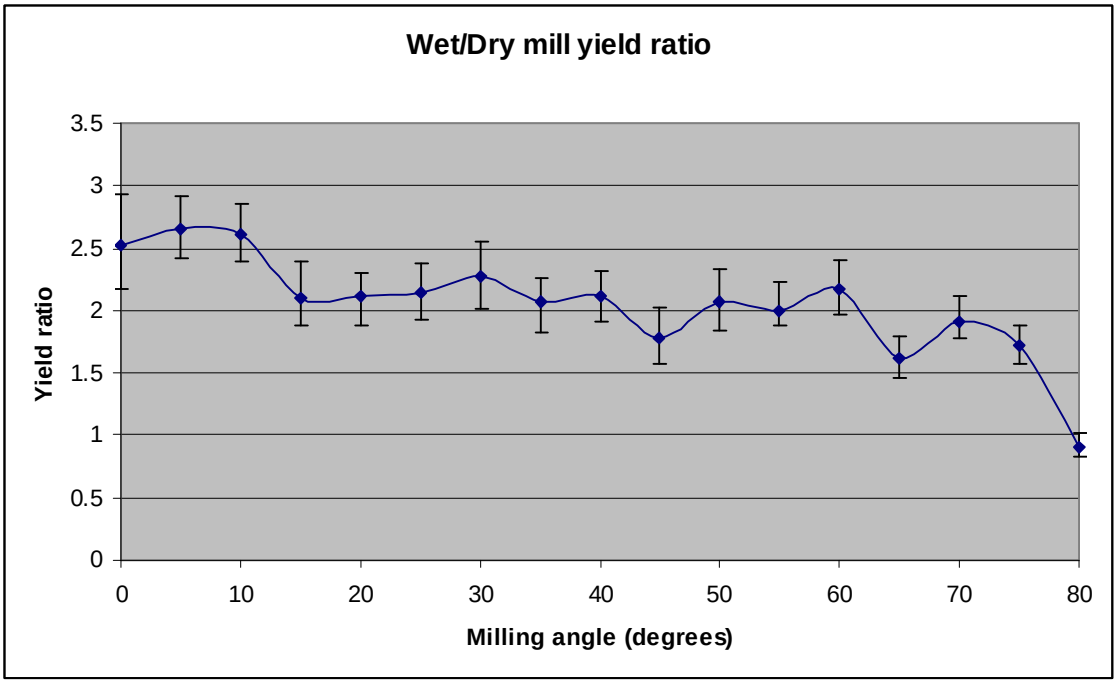

Figure 5.23 – Wet milling / dry milling yield ratio for SCD from 0^{o}-80^{o}

The dry yield at 0^o of 0.09μm^3/nC is the same as that obtained by (Stanishevsky 2001), (Russell 1998) and (Stark 1995). It is higher than the 0.06μm^3/nC achieved by (Taniguchi 1998). Atom/ion yields have been converted to μm^3/nC at 28.8 atom/ion equals 1μm^3/nC. The maximum wet yield of 0.45μm^3/nC compares well with 0.51μm^3/nC in (Russell 1998). It is less than the 0.9μm^3/nC achieved by (Adams 2003) and 1μm^3/nC by (Stark 1995). For comparison (Taniguchi 1998) achieved 0.28μm^3/nC with XeF_2 assisted milling.

The reasons for the wet yields being half that achieved by Adams and Stark could be to do with gas pressure as the dwell times used were short, and the distance between the diamond and the gas tube is 100µm, similar to distances described by Adams. The dry yield is the same as the literature values so the difference has to be related to the water injection and not the ion system in general.
If the FIB 200 has a lower gas pressure than the systems used by Adams and Stark it will provide less conversion of ejected carbon to CO. However, a doubling of the yield is still very useful and although it is possible to adjust the pipe height and the vapour pressure it was decided to stick with a 100% yield improvement.

5.1.5 – Unwanted face angle

At angles around 85^o, because the yield goes to zero, an effect arises that means nominally vertical features in fact have a slope on them. For example, a box milled into a flat surface at normal beam incidence will not have sides that are vertical, in fact the sides will be tilted inwards by ~5^o. This is because, for most of the material that is removed to form the box, the beam incidence angle is zero. However at the edges of the mill pattern, where the walls of the box are formed, the local angle of incidence for the ions is 85^o. The ions are glancing off the walls and delivering zero yield at the wall, this is shown in figure 5.24. The ions that glance off the walls can still cause yield by hitting the box floor.

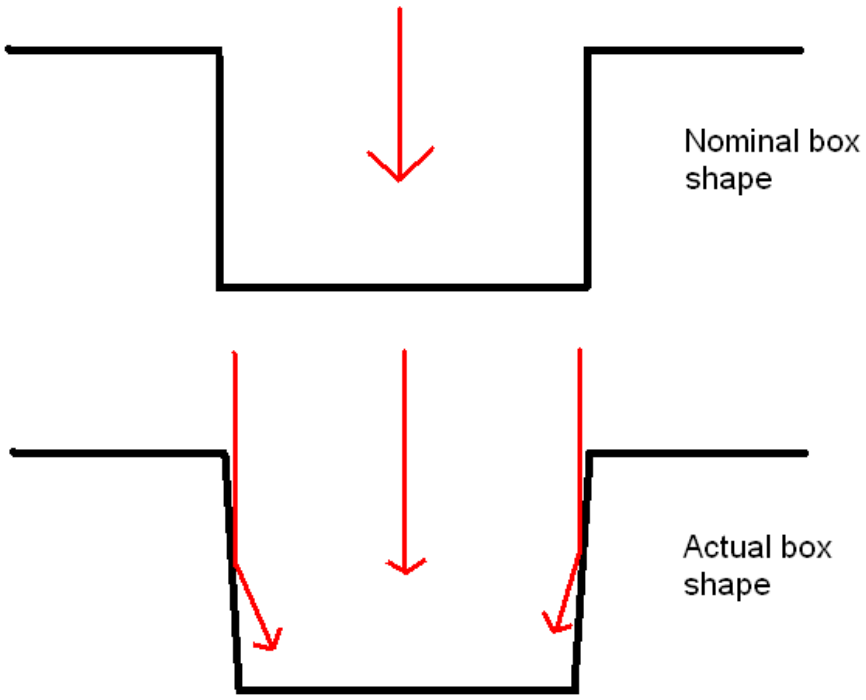

Figure 5.24 – Nominal pattern box shape and the actual milled box shape

Once an initial shallow box has been achieved by the back scattering of atoms, due to ions entering the sample at the normal, the angled wall is formed by a progressive deepening of the following process. Normal ions entering the sample near the shallow, initially vertical, wall scatter atoms in all directions including towards the wall. Those scattered towards the wall eject material and deepen the box. The wall angle created is less than 85^{o}. Incoming ions then strike this angled wall and remove material until the wall angle increases to 85^{o}. At this point the ions bounce off without making the wall steeper. When the wall has reached 85^{o} the ions that strike at the base of the wall will again scatter atoms in all directions, including towards the nominal straight wall. This deepens the box and creates a wall with an angle of less than 85^{o}. This wall is eroded away again, as before, and the process repeats until the ion beam is turned off. As the box deepens, the 5^{o} wall angle is maintained and the base of the wall gets further away from the nominal vertical wall position, see figure 5.25. The blue arrows represent the atoms

scattered by the red gallium ion. I am calling this effect the unwanted face angle (UFA) as there is no definitive term for it in the literature.

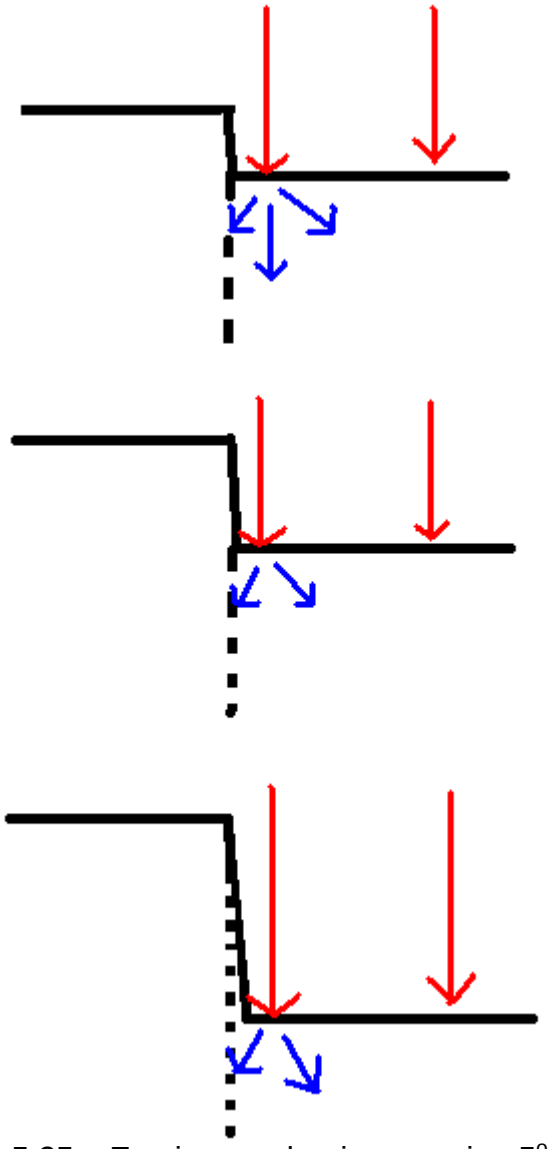

Figure 5.25 – Erosion mechanism causing 5^{o} sloped walls

5.1.6 - Diamond surface morphology

The surfaces of single crystals undergo spontaneous morphology changes when they are FIB machined. This was observed during the yield experiments and was investigated.

Figures 5.26 – 5.29 show the change in surface as the angle of milling is increased. From 0^o to ~40^o the surface is a featureless smooth surface with an unchanged Sa. Above 40^o the surface becomes rippled and stays rippled until the milling angle reaches 70^o at which point the ripples turn into a series of steps. The surface reverts to smooth above 80^o. When the surface is featureless it is of similar smoothness to the original unmilled surface, the Sa of the featureless milled surface is 0.59nm, figure 5.30. The unmilled polished (100) surface was 0.6nm Sa. This is because the top ~50nm of the diamond loses its structure due to the ion bombardment and forms a layer of amorphous carbon (Adams 2006a). The morphology was also imaged when the wet milling was carried out at the above mentioned angles. The ripples and steps still formed but the ripples were less prominent because the amount of redeposited material was lower.

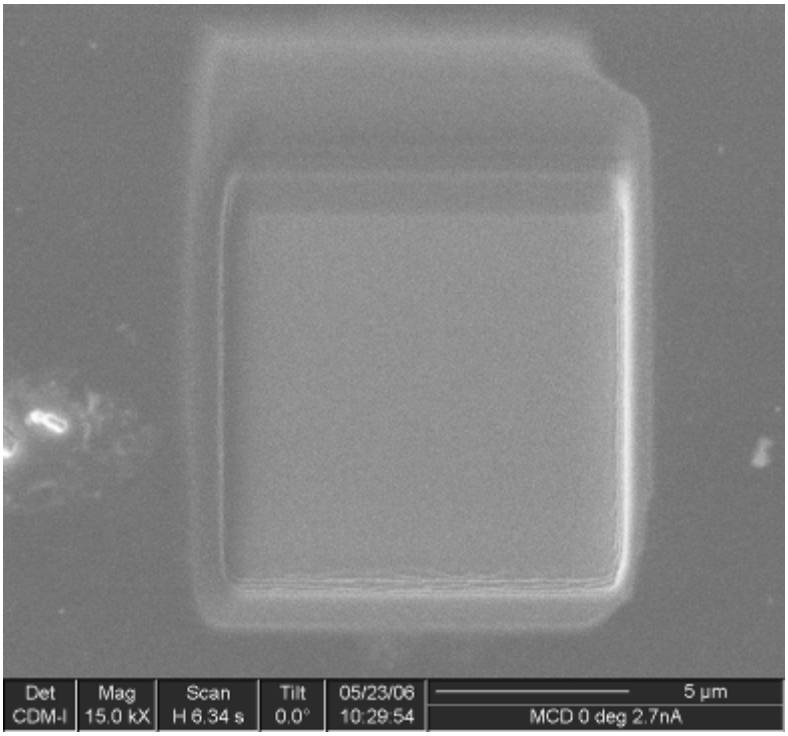

Figure 5.26 – FIB image of smooth surface morphology on SCD for 0^o milling angle. Surface roughness Sa 0.59nm.

The roughness of the ripples milled without water assistance at 45^o was measured by AFM and the Sa was found to be 13.6nm. The terraces formed at 75^o had a Sa

roughness of 7.2nm in the north-south direction and 2.7nm in the west-east direction. The orientation dependent roughness of the terraces will also apply to the ripples, though they were not measured in the west-east direction.

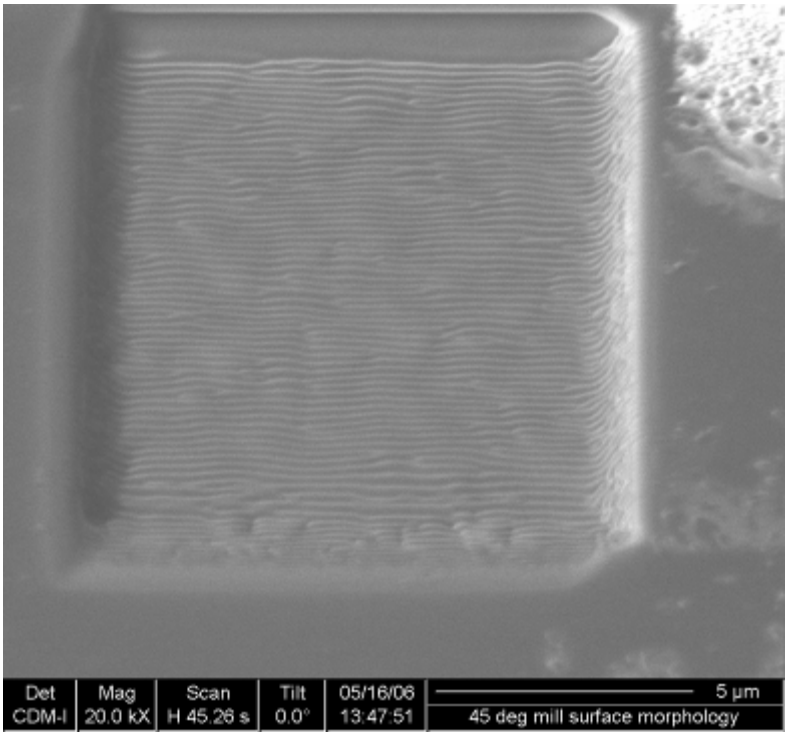

Figure 5.27 – FIB image of rippled surface morphology on SCD for 45^{o} milling angle. Surface roughness Sa 13.6nm north-south.

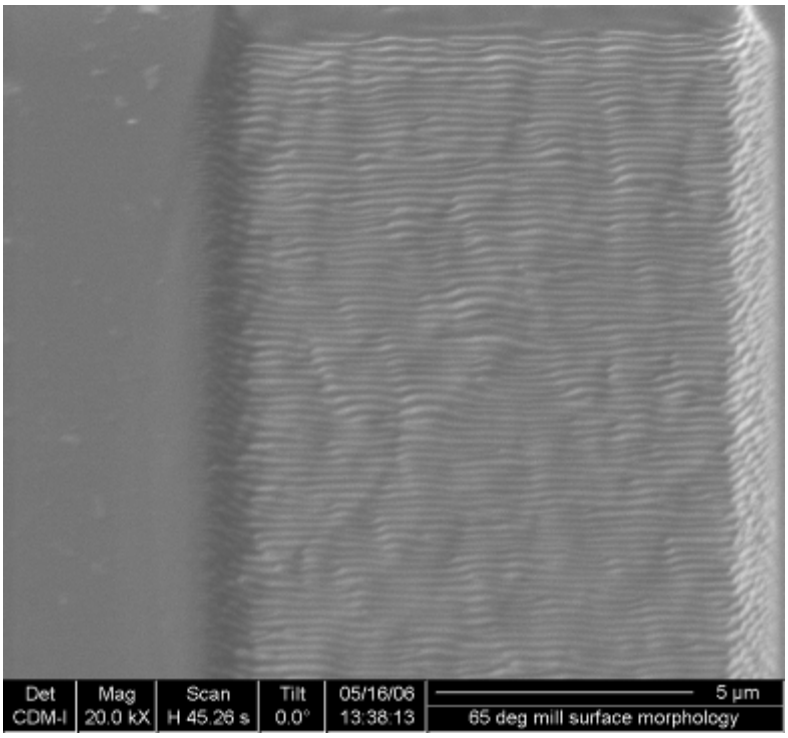

Figure 5.28 - FIB image of rippled surface morphology on SCD for 65^{o} milling angle.

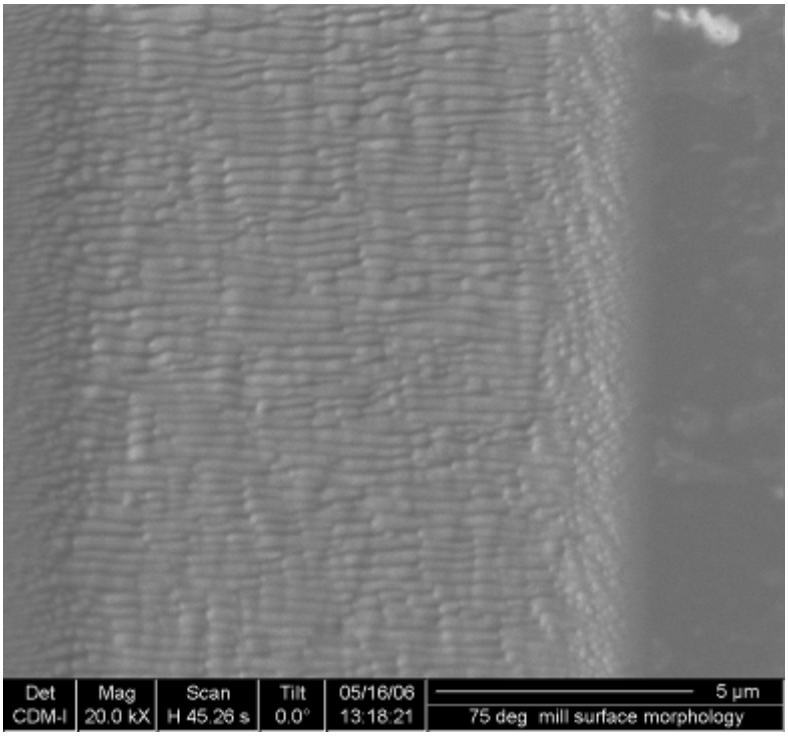

Figure 5.29 - FIB image of stepped surface morphology on SCD for 75^{o} milling angle. Surface roughness Sa 7.2nm north-south and 2.7nm west-east.

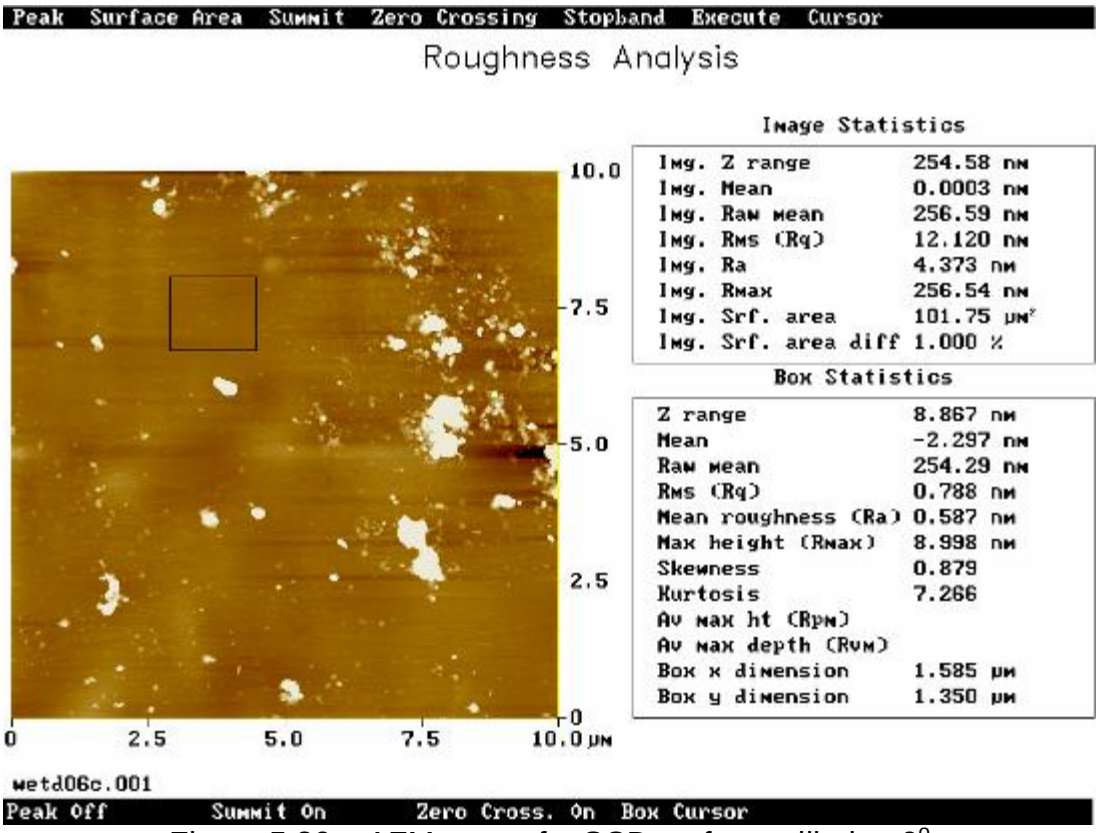

Figure 5.30 – AFM scan of a SCD surface milled at 0^{o}

In the literature, the diamond surface change during milling was discussed by (Datta 2001), (Adams 2003, 2006a) and (Mayer 2005). These suggested various mechanisms which might cause the ripple formation. The layer of featureless carbon at the surface at low mill angles was thought to be caused by ion enhanced diffusion processes. The top layer of the crystal structure was partly broken up by the ion bombardment, and some of the energy of the incoming ions was taken up by the lattice atoms causing them to diffuse.

The ripples were formed by ion scattering and surface transport processes. The ripples grew as a result of subtle dependence of yield on surface curvature. Scratches and contamination on the diamond surface can act as initial features that are amplified by a preferential sputtering action. These are the basis of the periodic structures formed by further amplification. Also, the sputtering of a smooth

surface causes roughening, creating a range of spatial frequencies which are then selectively amplified by more sputtering.

The reason for these features forming above 40^{o} is that below this angle the smoothing processes, mainly enhanced diffusion, outweigh the ripple processes. Around 70^{o} beam angle, terraces form from an initially rippled surface. Because of the high approach angle of the beam initial ripples above a certain height will shadow other parts of the surface. Preferential sputtering occurs causing local planes to form, each at a slightly different height. Surface change also occurs in other materials such as silicon (Xie 2004) (Huang 2005) (Katharria 2007), fused silica (Flamm 2001), tin (Qian 2005) and polycrystalline diamond.

The smoothed and rippled PCD surfaces are obvious in figures 5.31 and 5.32. The PCD in these two images has had its cobalt binder partially leached out, i.e. it is conventional PCD made by compacting diamond grit together. The grain size of the PCD is 5μm.

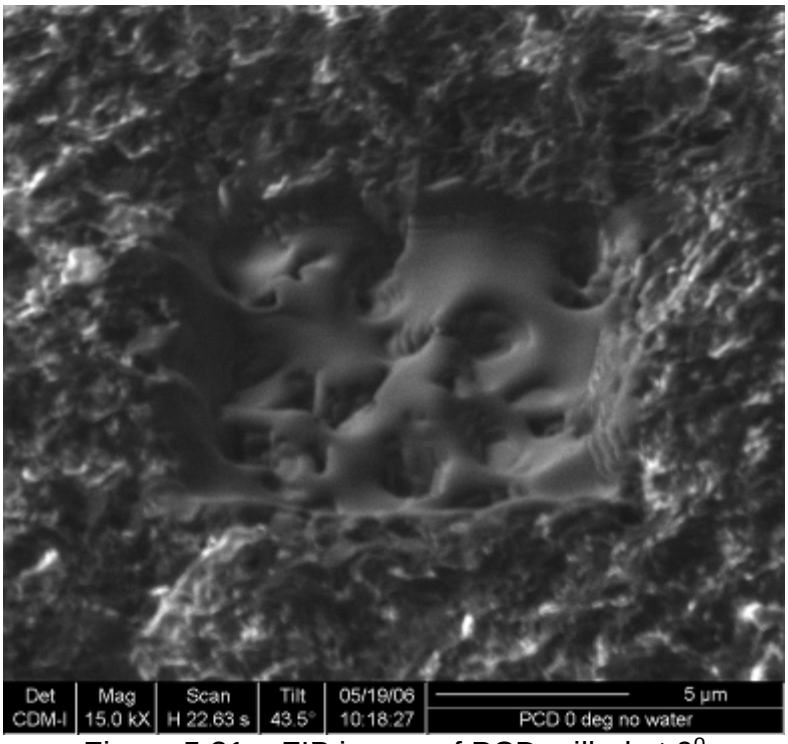

Figure 5.31 – FIB image of PCD milled at 0^{o}

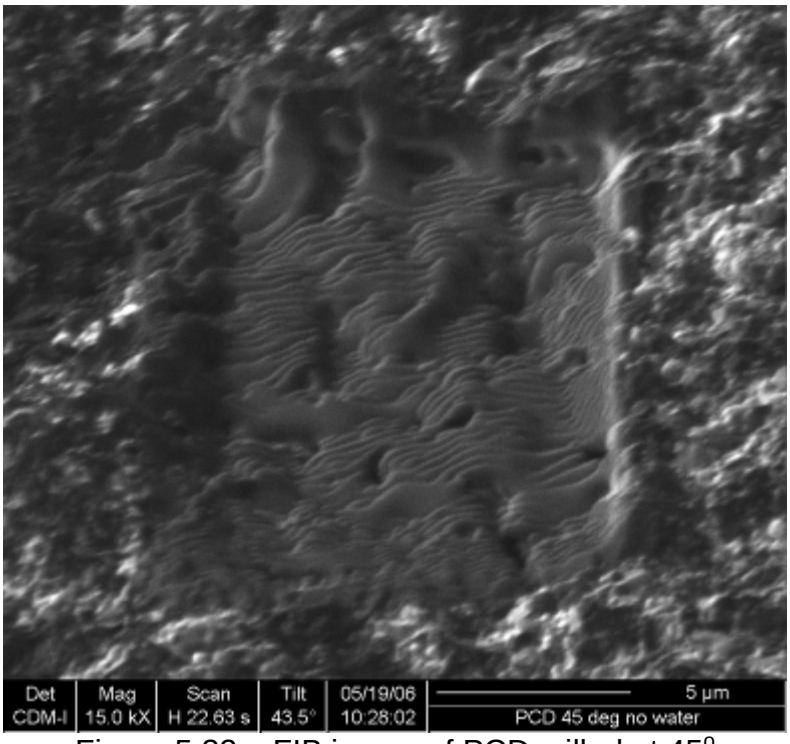

Figure 5.32 – FIB image of PCD milled at 45^{o}

5.1.7 - Ripple spacing

To see if there was any difference between the wet and dry ripples and the two different milling software programmes, the average separation between each line of ripples was measured for SCD squares milled at 45^{o} for 4 beam currents. This was done with and without water assistance using the FEI and Raith software. The Raith software allows you to choose between a continuous meander beam path from top left to bottom right or a series of left to right lines from top to bottom. The FEI uses a meander mill pattern. The theoretical spacing of ripples that would occur if they were caused by overlapping beam spots was calculated, the FEI software has a beam spot overlap factor of 0.2 for diamond.

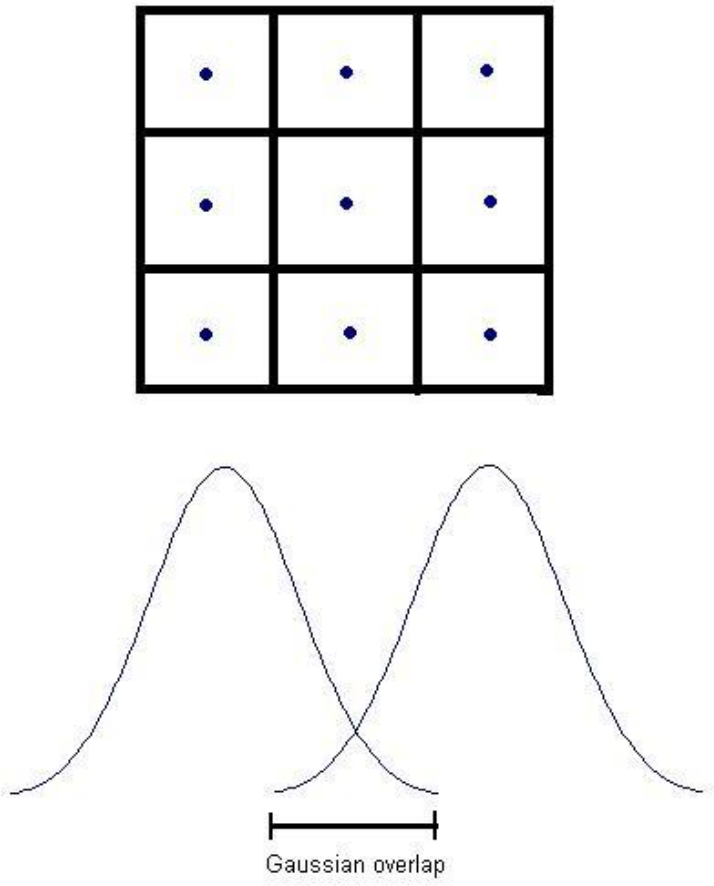

Figure 5.33 – Beam spot overlap into adjacent pixels

The spot overlap of 0.2 refers to the proportion of the beam spot on a given pixel that overlaps with the neighbouring pixels. As described in section 3.1.3, the surface area visible is split into a 4096x4096 square pixel grid. The size of the pixels depends upon the column magnification being used (table 3.2). Figure 5.33 shows a grid of nine pixels with the peak ion density marked as a blue dot. The spot diameter can vary from 8 - 500nm (table 3.1) and the pixel size from 8 – 42nm (table 3.2). The spot size is typically larger than the pixel size, so the spot 'spills over' into its neighbouring pixels. The amount of spill over is the overlap factor. It is possible for the spot to fully overlap all its neighbouring pixels giving a factor of 1 or larger. Assuming the spot is Gaussian is a reasonable approximation when calculating overlap, though the effect of the side tails in the beams actual Holtzmark distribution must also be considered.

The measured ripple spacing for all the different beam modes are all plotted in figure 5.34.

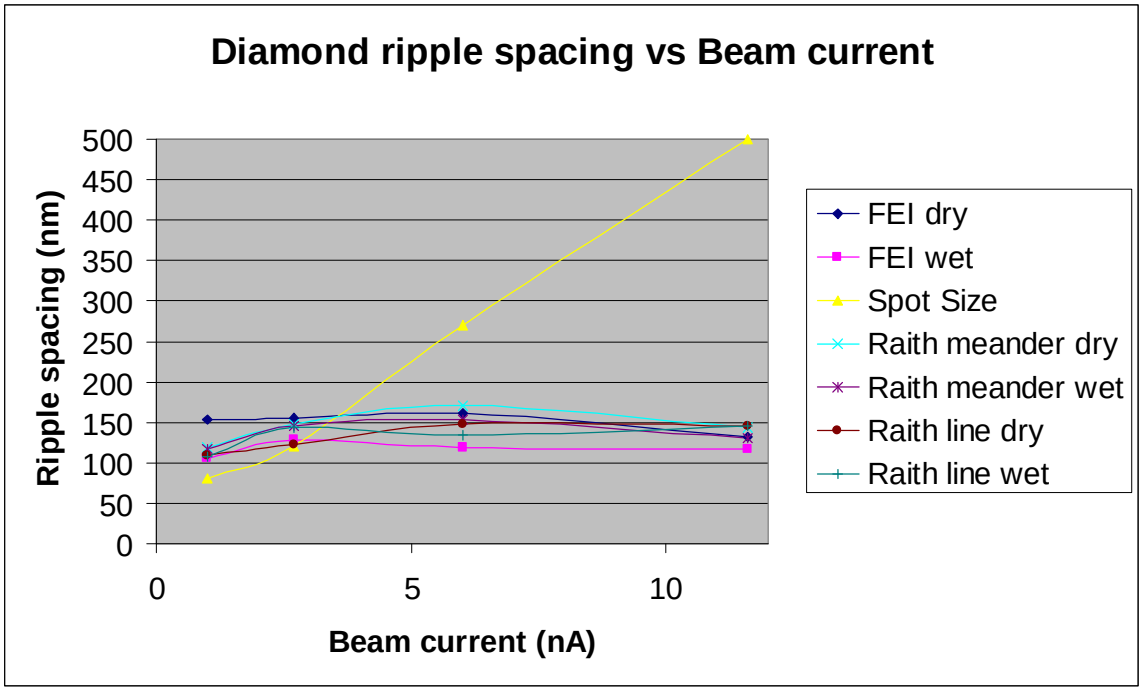

Figure 5.34 - Ripple spacing on SCD for FEI and Raith milling at 45^{o}

The yellow Gaussian spot overlap line shows that the ripple spacing is independent of the spot size.

In the equations of the ripple models there are many parameters, some of which are calculable, e.g. the depth and widths of the ion energy distribution in the material. Values for these were estimated using an ion implantation simulation package TRIM, (SRIM 2008) and a modified version of TRIM called SUSPRE (SUSPRE 2009). They both simulate the path of primary ions and secondary scattered ions in a wide range of materials. The milling parameters of ion energy, ion type, beam angle and target material are selectable. The simulation then gives graphical and numerical outputs of the ion distribution. Both of these programs are based on the Sigmund model (Sigmund 1973) to model the distribution of energy deposited into a sample by the ions. Sigmund's model approximates the spatial distribution of the deposited energy averaged over a large number of ions, each with the same initial trajectory. The sputter yield at the surface is then calculated from the total amount of energy deposited there by every incident ion.

Figure 5.35 shows the primary ion distribution and figures 5.36 – 5.38 the primary and secondary ion distributions for 5000 30keV Ga ions at 0° incidence angle hitting single crystal diamond. These four figures are all from TRIM.

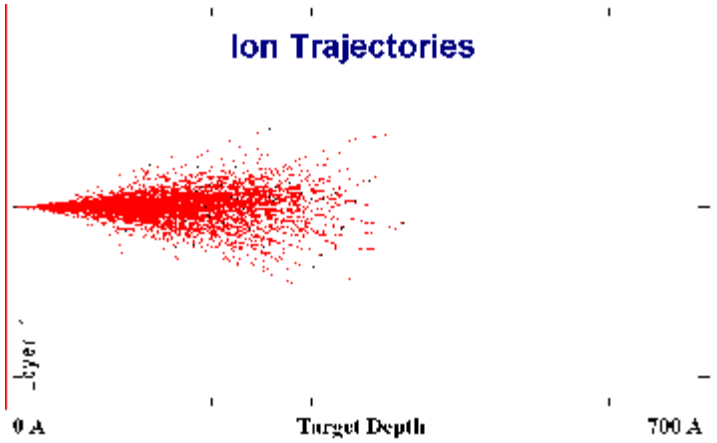

Figure 5.35 – TRIM calculated distribution of 5000 30keV Ga ions in single crystal diamond

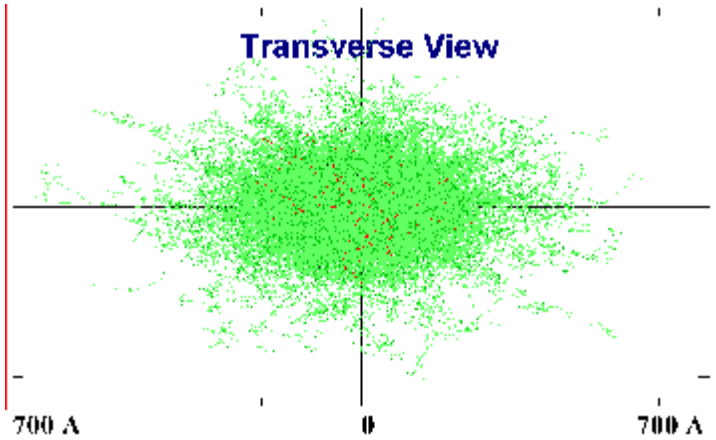

Figure 5.36 - Top view of TRIM calculated distribution of 5000 30keV Ga ions in single crystal diamond and the displaced C atoms

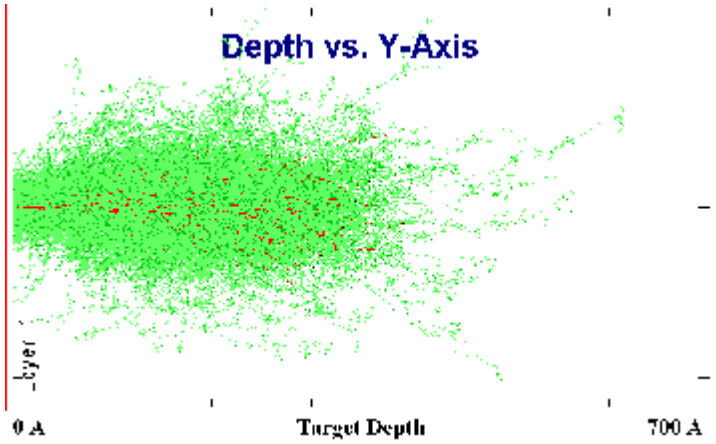

Figure 5.37 – Y-axis profile through TRIM calculated distribution of 5000 30keV Ga ions in single crystal diamond and the displaced C atoms

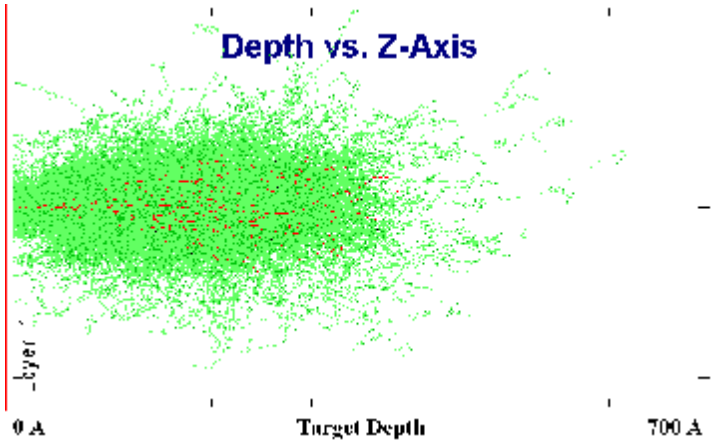

Figure 5.38 - Z-axis profile through TRIM calculated distribution of 5000 30keV Ga ions in single crystal diamond and the displaced C atoms

The same values were also put into SUSPRE. SUSPRE works by a different calculation method and gives a different depth for the disordered region in diamond, 30nm instead of 35nm from TRIM, figure 5.39.

As part of the rotary encoder work described in section 5.2, the ripple behaviour of sapphire was of interest as well.

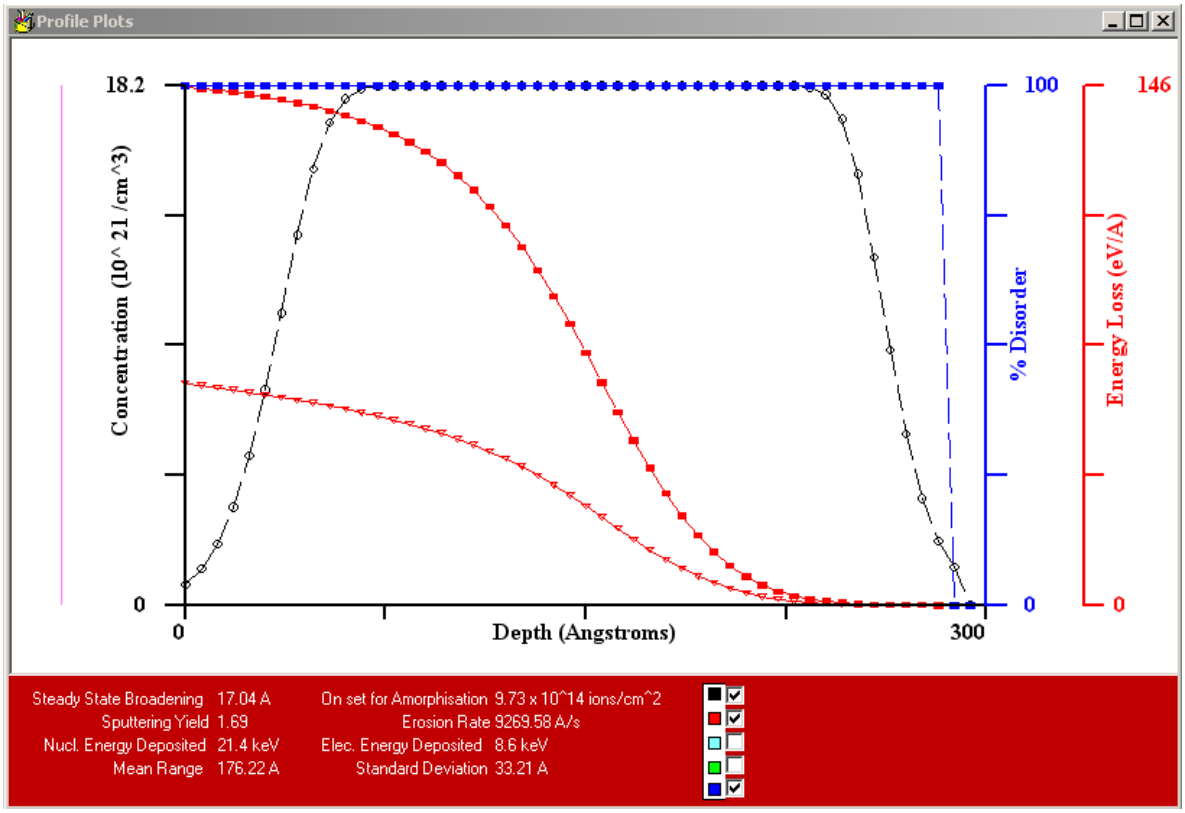

Figure 5.39 – SUSPRE output for 30keV Ga ions impacting into carbon

SUSPRE gives a prediction of the tail off in the concentration of gallium ions, the black line on the plot. The red lines show how the ions lose energy as they penetrate the material. The rectangular symbols are the energy losses due to atomic nuclei and the triangular symbols are the electronic losses. The greater degree of nuclei losses in sapphire, figure 5.40, causes the different tail off in

gallium concentration. In diamond it starts at 23nm, whereas in sapphire it starts at 20nm and has a shallower decrease in concentration gradient.

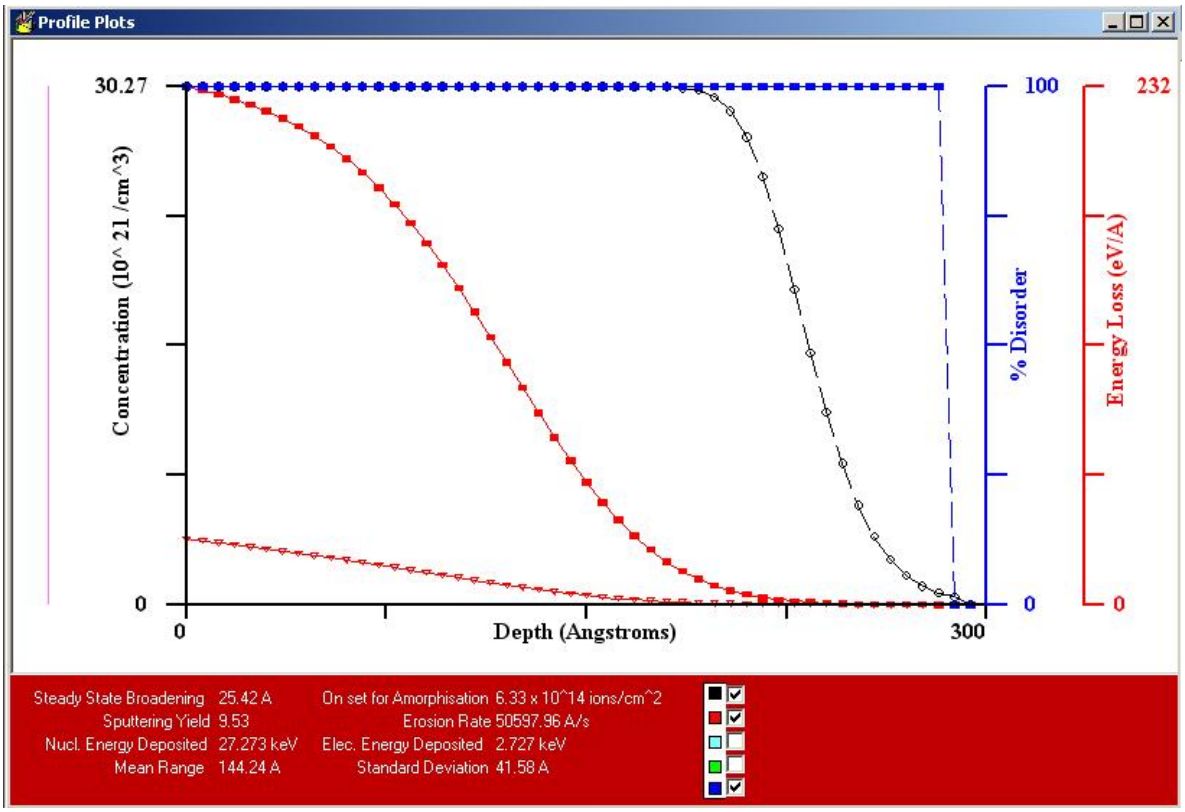

Figure 5.40 - SUSPRE output for 30keV Ga ions impacting into sapphire

After carrying out the TRIM and SUSPRE simulations of diamond and sapphire milled at different angles and beam energies, the output ion distributions and depths where slotted into some of the Bradley-Harper model equations. However these values did not lead to any insights into the differing ripple behaviours. There are too many variables needed, many of which are not in the open literature or which are available for diamond but not for amorphous carbon. The TRIM/SUSPRE outputs are most useful for getting an idea of the depth of the ion damaged region.

Ripples were created on single crystal diamond and sapphire at different beam currents and ion dosages at a constant 45° mill angle. The diamond was milled

with and without water. The ripples were then scanned by AFM and the spacing measured (figures 5.41 – 5.43). The possibility of using the ripples as a naturally forming reflection grating was being considered.

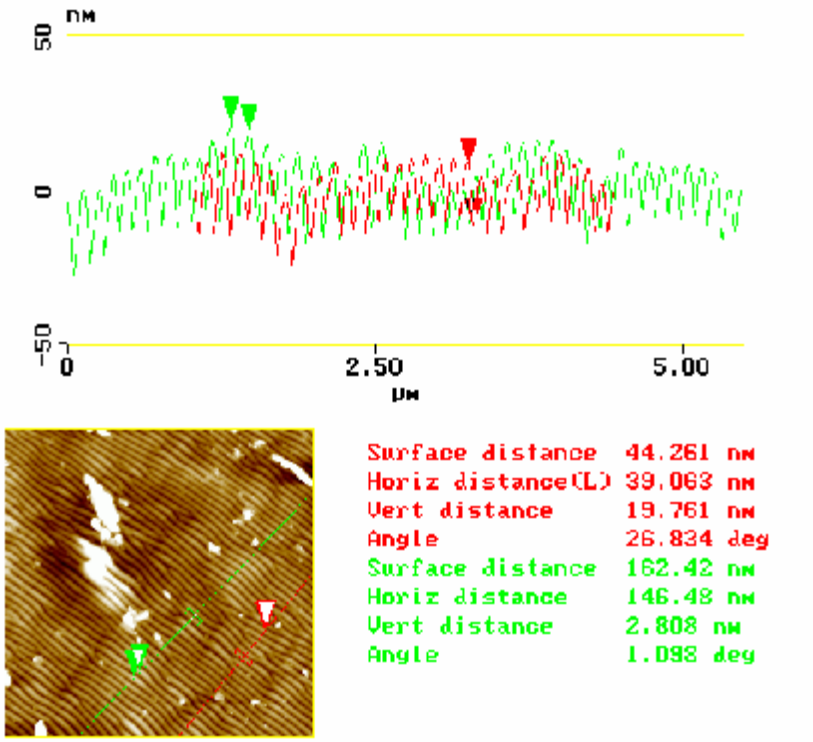

Figure 5.41 - AFM scan of ripples on dry milled SCD

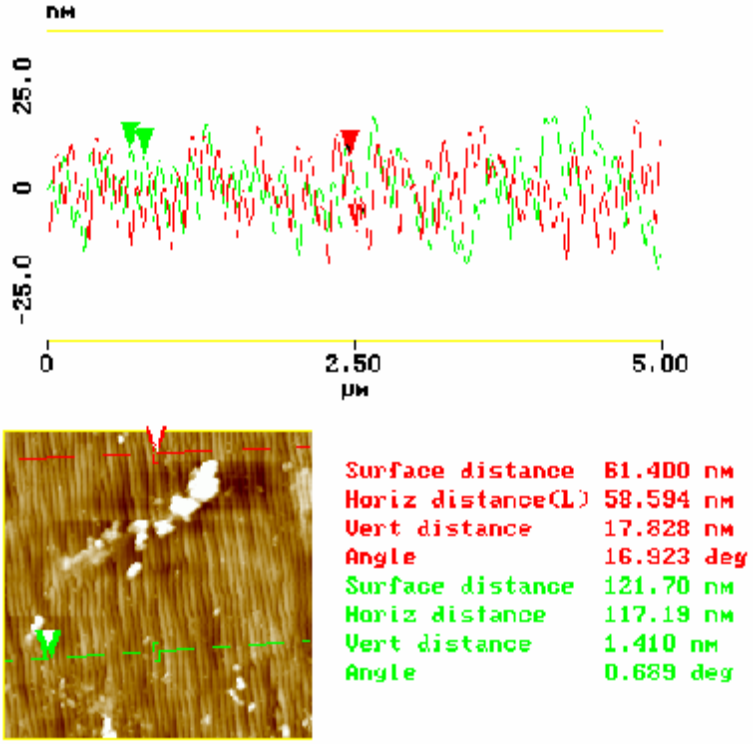

Figure 5.42 - AFM scan of ripples on wet milled SCD

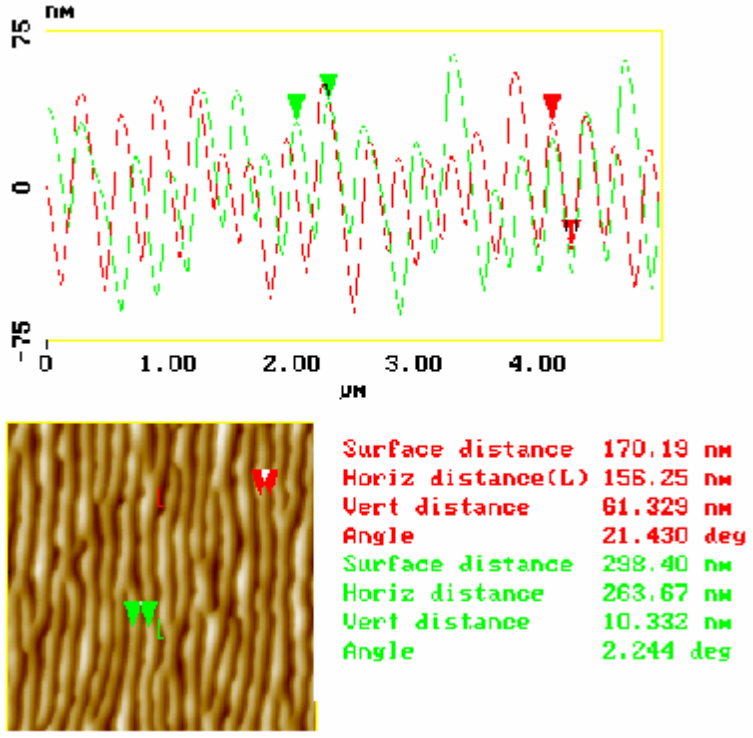

Figure 5.43 - AFM scan of ripples on milled sapphire

The difference in ripple structure between wet and dry milled diamond is very apparent. The dry ripples are regularly spaced with little difference in depth between adjacent ripples. The wet ripples have large variances in spacing and depths across the width of the scan. The regularity of the dry ripples being destroyed by the introduction of an element of randomness due to the slightly differing distribution of water over the surface. There is also the change in surface chemistry which modifies the movement of atoms in the various diffusion processes. The difference between the dry diamond and sapphire ripples is obvious and is due to the different crystal structure and the fact that sapphire is made up of two different atoms which have different collision dynamics figures 5.39, 5.40 and 5.44.

The possible affect of ion damage on the ripples would seem to be very different for the diamond and the sapphire. The maximum amplitude of the ripples on the diamond, measured in figures 5.41 and 5.42, is ~30nm. This is the same as the modelled ion penetration depth from TRIM and SUSPRE. However, the maximum sapphire ripple amplitude in figure 5.43 is ~100nm. The modelled ion depth in sapphire is 30nm, as for diamond. Assuming that the match in depth values for diamond is not just a coincidence, then either the modelling of sapphire has serious flaws or there are surface processes moving material around to create large amplitude ripples. As TRIM and SUSPRE have been in use long enough for large model failures to be noticed and fixed; there must either be different processes at work on diamond and sapphire or they act very differently on the two materials. The different collision dynamics of oxygen and aluminium would help in giving a different outcome for the same surface process.

The chemical make up of the diamond ripples will be a mix of carbon and gallium, with possibly some hydrogen from the water molecules for the wet milled diamond. For sapphire the ripples are a mix of aluminium, oxygen and gallium with the aluminium and gallium forming a GaAl alloy. The proportion of oxygen to

aluminium in the ripples will be less than the original 2:3, as the lighter oxygen atoms are more likely to escape from the surface.

The high variability in the sapphire and wet diamond ripples meant they would be of no use as reflection gratings. The dry diamond ripples were far more uniform but the slight variance in depth and spacing across the 5µm area scanned when scaled up over a much larger area would introduce a surface with too much irregularity.

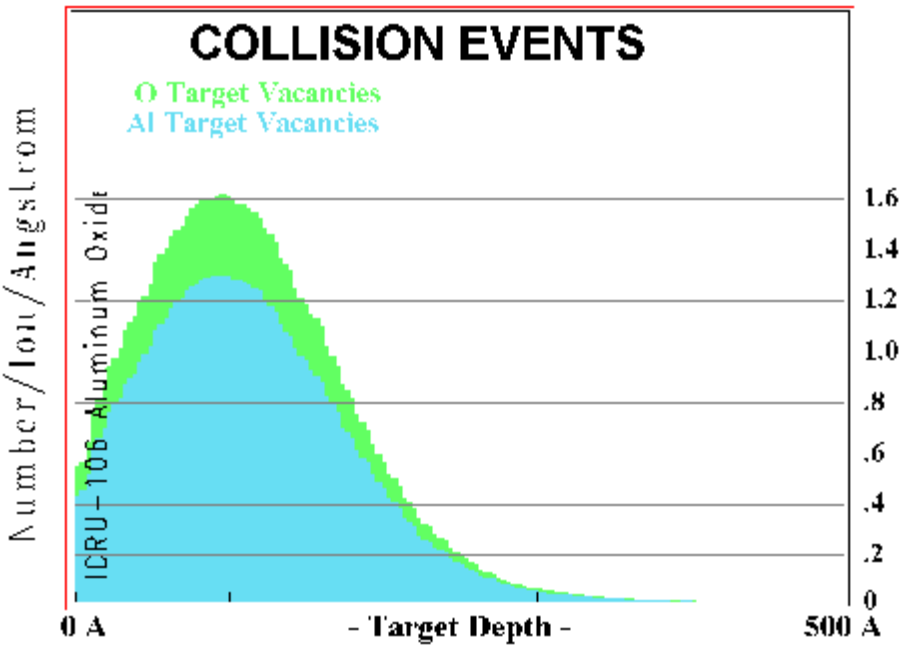

Figure 5.44 - TRIM output of the differing atomic vacancies in sapphire caused by 30keV Ga ion milling at 0°

The work on ripple formation theory and diamond/sapphire ripples was presented at the NanoFIB2007 workshop at Manchester University in June 2007.

This section of work reached something of a natural conclusion in that going any deeper into the ripple mechanisms would have required much more mathematics and is an entire area of study in its own right. Achieving the depth required to get a

proper understanding would not have been a good use of time and would have been a diversion from the main thrust of the project.

5.2 - Sapphire mould for rotary encoder

As part of the work for the 3D-Mintegration rotary encoder demonstrator sapphire (Al_2O_3) was investigated as a possible material for making a mould for producing patterned polymer shafts. The shafts were meant to be part of a rotary encoder, which is an angular position measuring device. The rotational position of a shaft is converted into a digital code giving the shaft location. The readout can be absolute, the markers on the shaft give a unique position or incremental, where the markers give the distance the shaft has rotated since its last position check. The initial plan was to machine patterns directly onto a sapphire shaft similar to the ones used in fluid flow meters. These use sapphire shafts rotating between two sapphire bearings to give a very low friction, hard wearing, rotary unit. The encoder was being developed with aircraft avionics in mind making smaller, preferably cheaper, encoders. The shaft needed to be patterned such that the measuring system could read out a position to 15 bit accuracy.

It was decided to switch to using sapphire as a mould for injection moulding polymer shafts as this would be cheaper. Also the issue of how to rotate the shaft inside the FIB chamber to achieve patterning all the way round was avoided. Sapphire's material properties are conducive to making a mould as it has a melting point of $2313^{o}K$, a hardness of 9 on the mohs scale, is mechanically strong, chemically stable and can be grown to a variety of complex shapes. Also because sapphire has a single crystal structure, it would FIB machine predictably.

Previous FIB work on sapphire by (Steckl 1999) found that the mill yield of sapphire at normal incidence with 30keV Ga ions is $0.1\mu m^3/nC$. (Lee 2006) found that the mill yield increases significantly with the use of XeF_2 in gas enhanced

milling. (Dia 2008) used XeF_2 enhanced milling to produce 2D micro structures. The gas improved the yield by a factor of up to 2.3. There is no XeF_2 gas injection on the Cranfield FIB so the mill yield available was the same as for dry milling of single crystal diamond.

The pattern on the surface of the polymer could be read by either a contact probe or an optical system that picks up reflected light from the shaft, similar to the pits and flats on a CD. An optical system would work by sensing the difference in reflectivity between the pits and smooth areas of the shaft if the difference was high enough. This required a polymer with a reflective post processing finish. Another possible method was to create rippled patterns on the sapphire which would scatter light instead of reflecting it. These can be formed by machining the sapphire at beam angles of 45^o or more. The ripples are formed by similar processes to those that cause diamond ripples (see ripple discussion in section 5.1.6), though the ripples are not as well ordered and uniform, figures 5.45 and 5.46. The initial sapphire work was carried out on a synthetic disc bought from UQG optics, Cambridge.

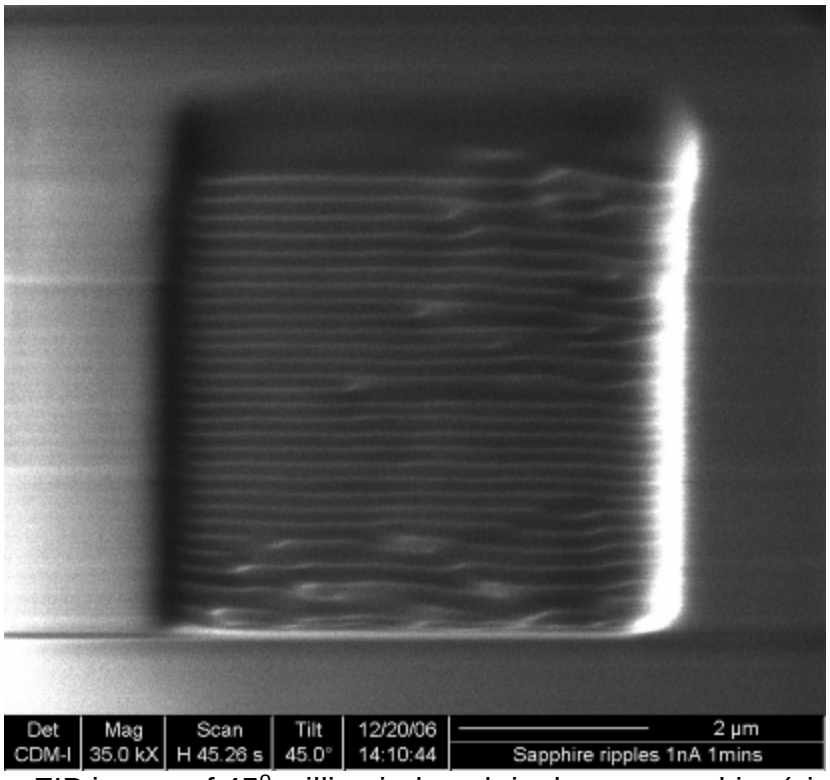

Figure 5.45 – FIB image of 45^{o} milling induced ripples on sapphire (viewed at 45^{o})

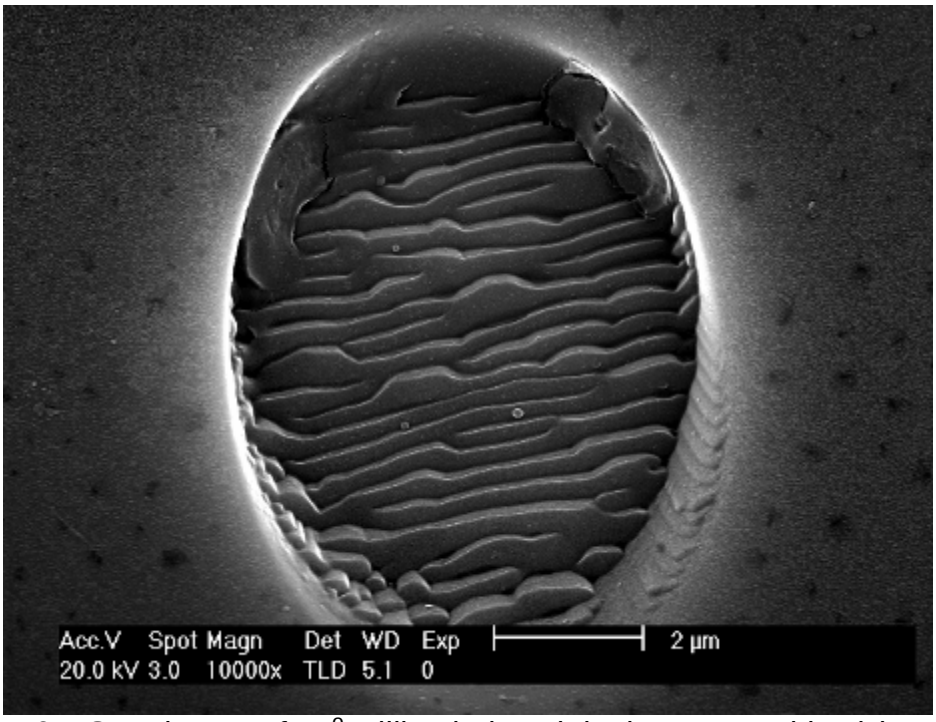

Figure 5.46 – SEM image of 45^{o} milling induced ripples on sapphire (viewed at 0^{o})

5.2.1 – Sapphire milling

The beam drift was found to be a serious problem without the charge neutralizer on. With the neutralizer on the drift was reduced but was still large compared to the size of the holes that needed to be milled. To achieve 15 bits the hole pitch needed to be 1.5µm. To allow for a reasonable gap between holes, the maximum hole size was roughly 600nm. The drift was high compared to the size of the hole, as shown in figure 5.47. The beam movement across the surface is visible as milled out tracks leading to the holes themselves.

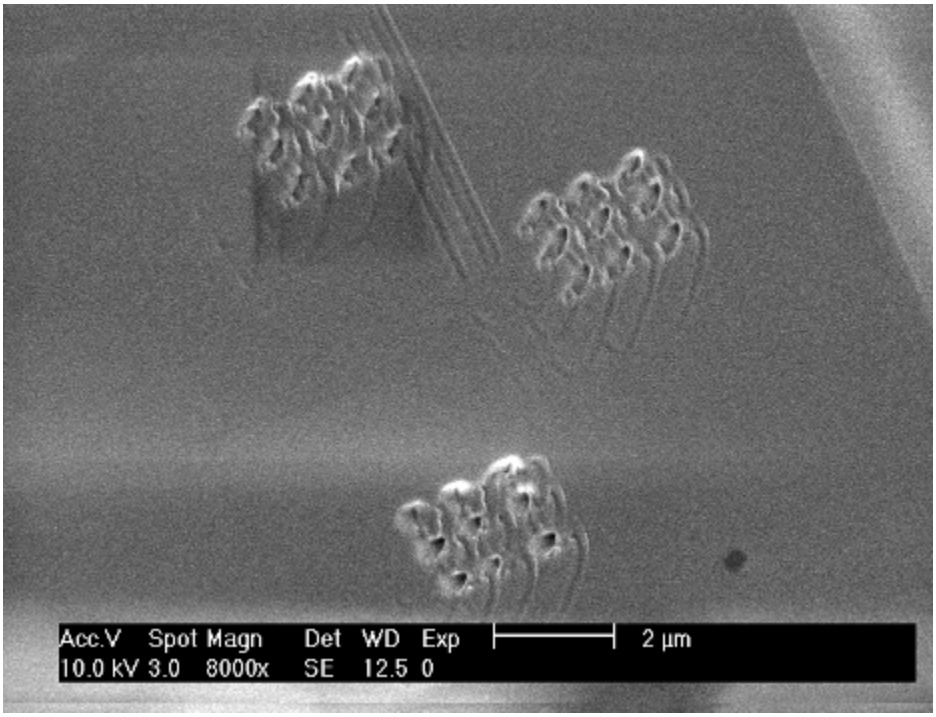

Figure 5.47 – SEM image of beam drift tracks on sapphire

A cure for this problem was found during attempts to image the bottom of the holes milled. This proved impossible with the FIB as images at tens of thousands times magnification were very blurred and the concentration of the beam into such a small area damaged any structures that may have been created. An SEM was used instead as it images at high magnification and won't damage the sample. Because sapphire is insulating it charges up almost instantly in the SEM, requiring it to be coated with ~20nm of conducting metal first. The holes already milled

proved to be misshapen and useless, see figure 5.48. However, when milling further sets of holes the metal coating removes the beam drift giving precise hole locations and shapes. The metal layer was thin enough such that it didn't affect the milling and could be wiped off using alcohol and a cotton bud. Figure 5.49 shows a set of holes of consistent shape and depth with no beam wandering.

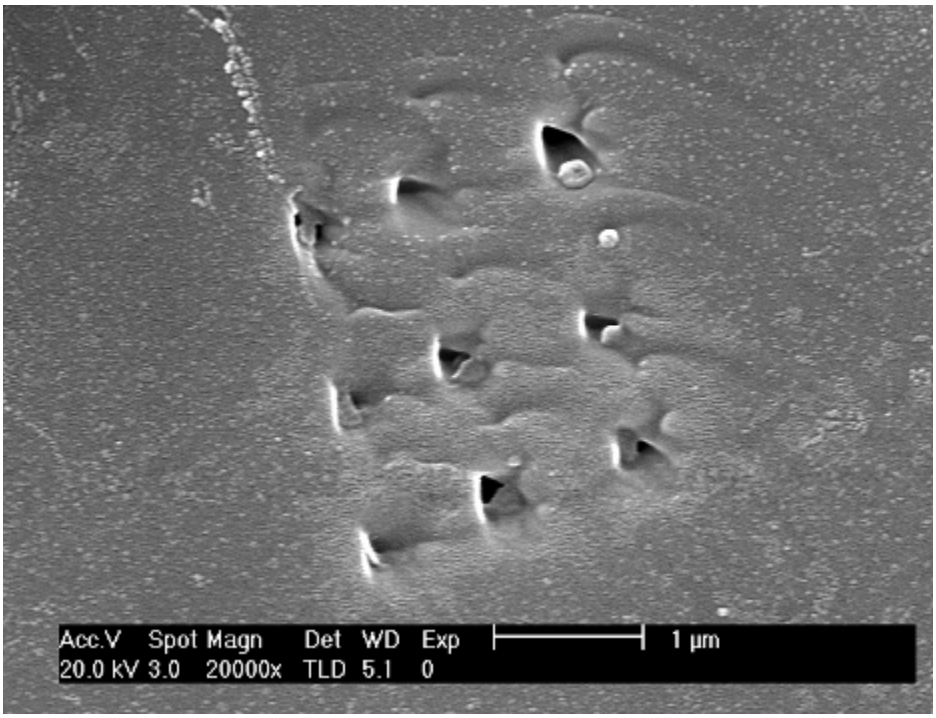

Figure 5.48 - SEM image of the initial set of milled holes in sapphire

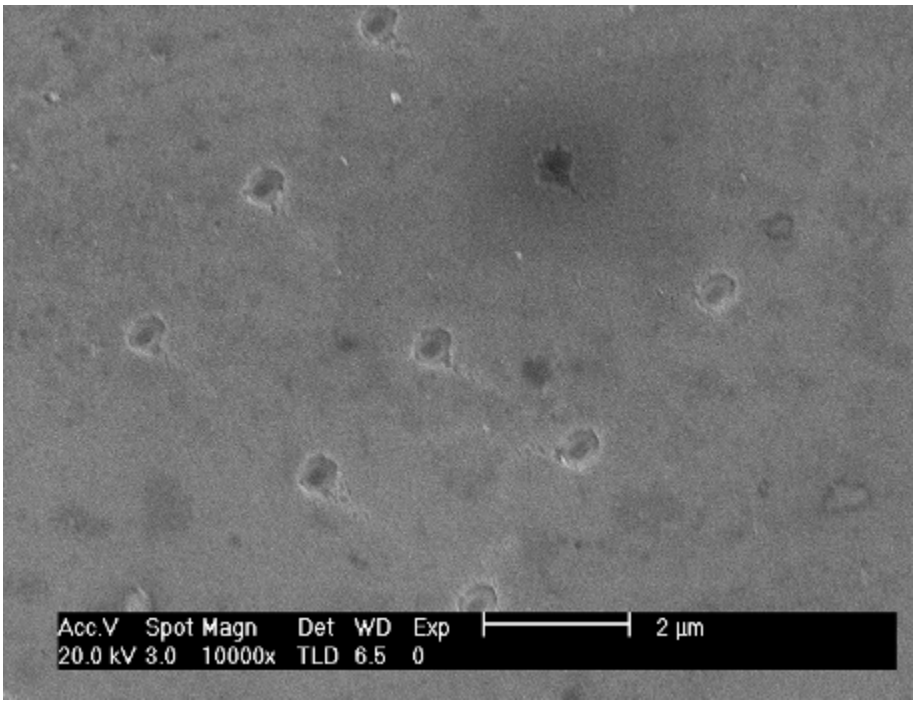

Figure 5.49 – SEM image of milled holes in metal coated sapphire

For holes that have ripples in them for the light scattering detection method, holes were milled at 45^{o} figure 5.50. The ripples are spaced out along the slope into the hole.

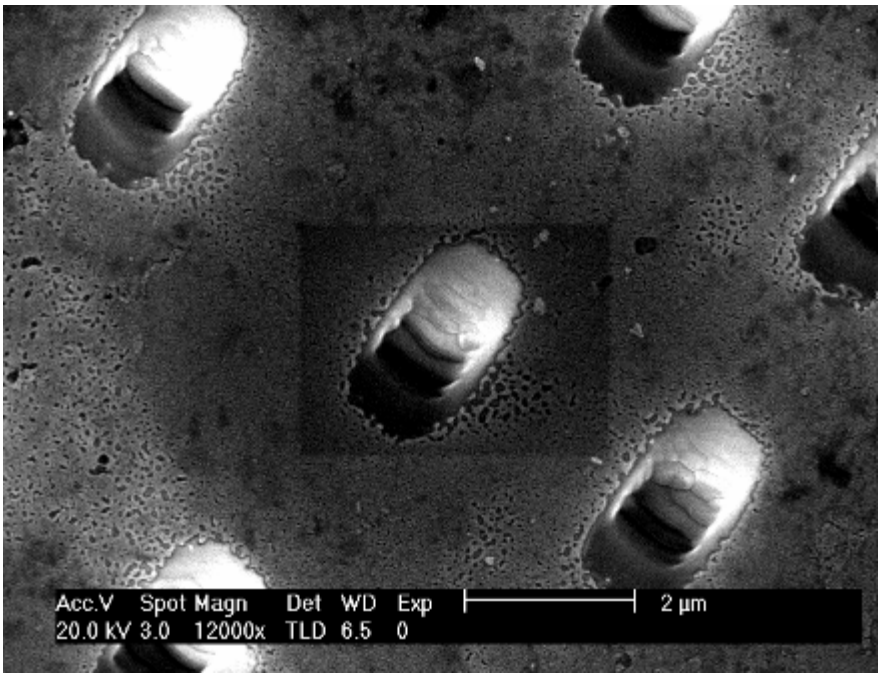

Figure 5.50 - SEM image of rippled holes milled into metal coated sapphire

The Raith FIB pattern design software was used to try out different patterns of holes to see if arrays of holes could be milled accurately. Two different beam currents were used, 11 and 70pA. The larger currents were too imprecise, due to their larger spot sizes, for creating nanometric features, giving vastly oversized, less well defined, shapes compared to the design shape. A matrix design pattern of 200nm sized squares with a pitch of 1.5µm was created and milled at 0^o and 45^o for both currents.

Figures 5.51 and 5.52 show how the 11pA holes were very uniform. These were milled at 2800x magnification. The holes milled were 0.3x0.3µm rounded squares. The lower 1400x magnification milling gave larger, less regular, holes (figures 5.53 and 5.54). The milled circles are 0.9µm in diameter.

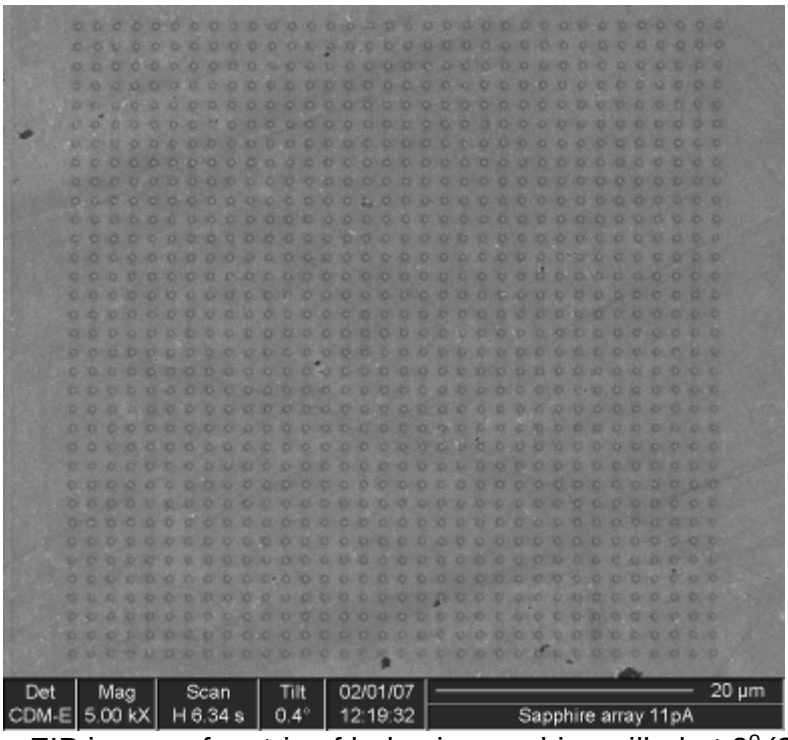

Figure 5.51 – FIB image of matrix of holes in sapphire milled at 0^o (2800x 11pA)

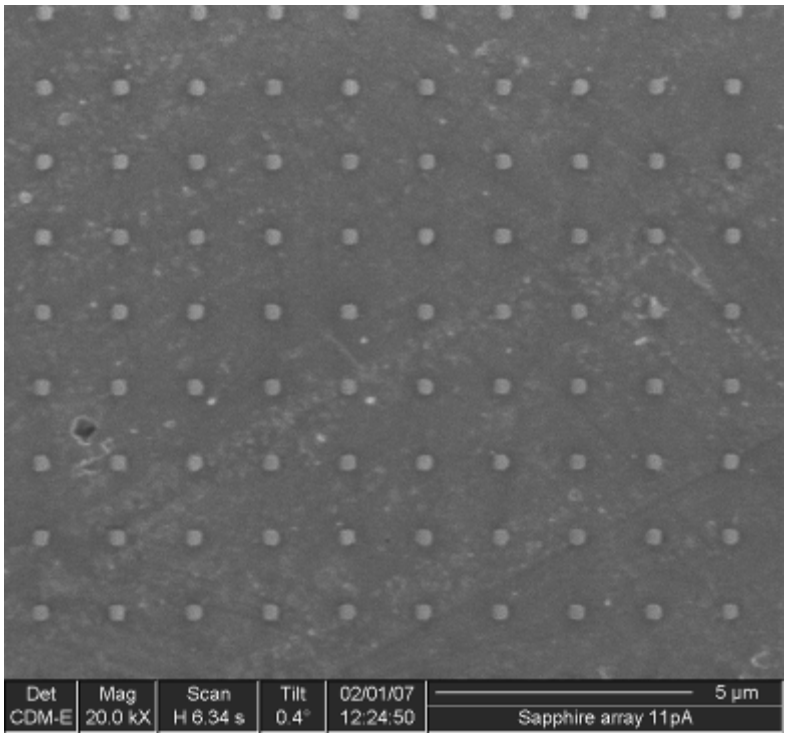

Figure 5.52 – Enlarged view of figure 5.51

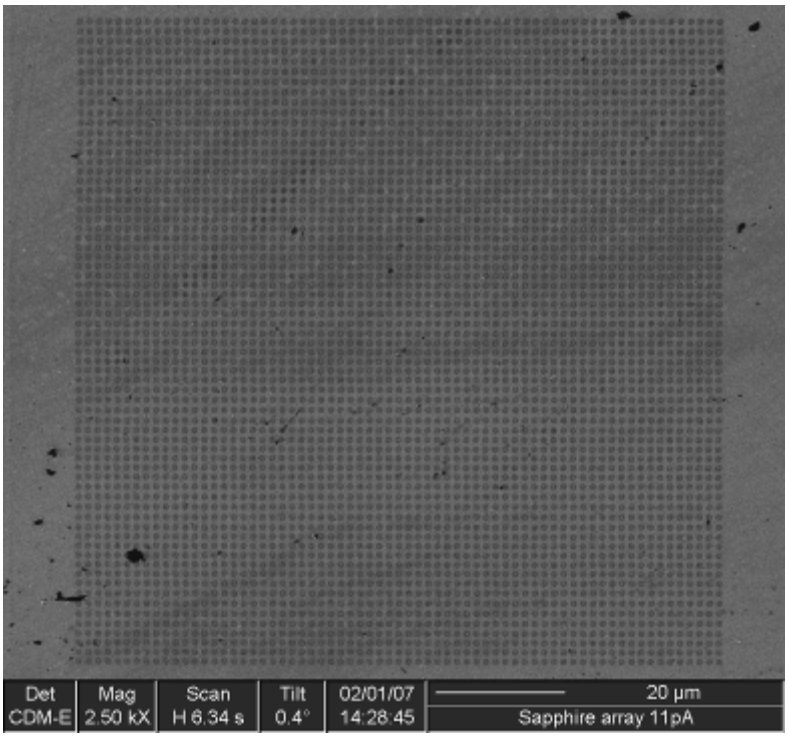

Figure 5.53 - FIB image of matrix of holes in sapphire (1400x 11pA)

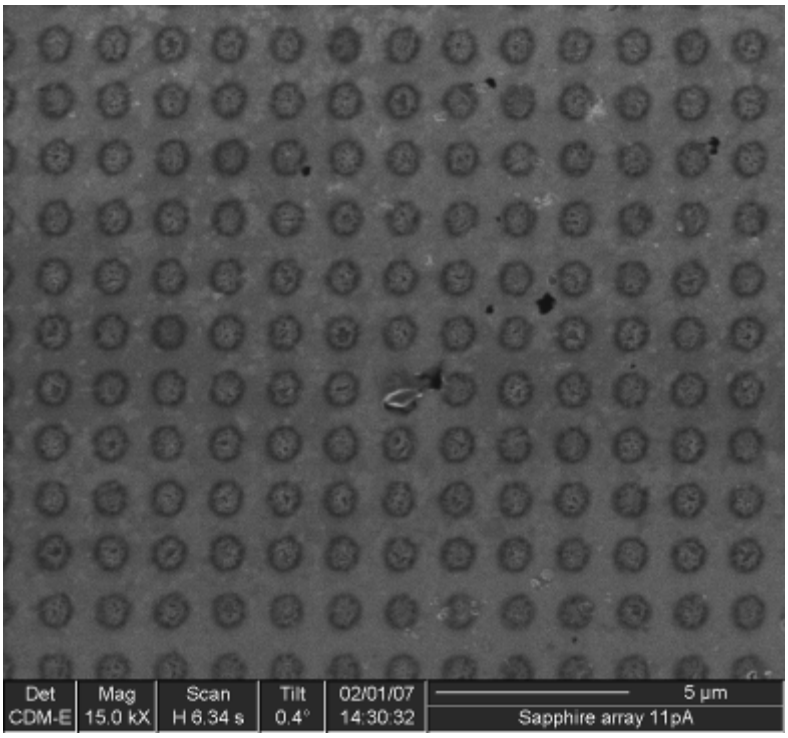

Figure 5.54 - Enlarged view of figure 5.53

Milling at 45^{o} (figures 5.55 and 5.56), gave a y axis extended pattern and slightly extended holes, though the actual length extension of the holes was so small that it was unimportant, 0.3x0.4µm compared to 0.3x0.3µm. The 70pA current gives circles that are 1µm in diameter at 2800x and 1.1µm at 1400x. This means the distance between the hole edges is only about 500nm, too small for comfort given the unknown replication accuracy of the polymer mould. The only settings that gave holes smaller than 500nm were 11pA and 2800x magnification and these settings gave a mill time of 0.5 seconds per hole.

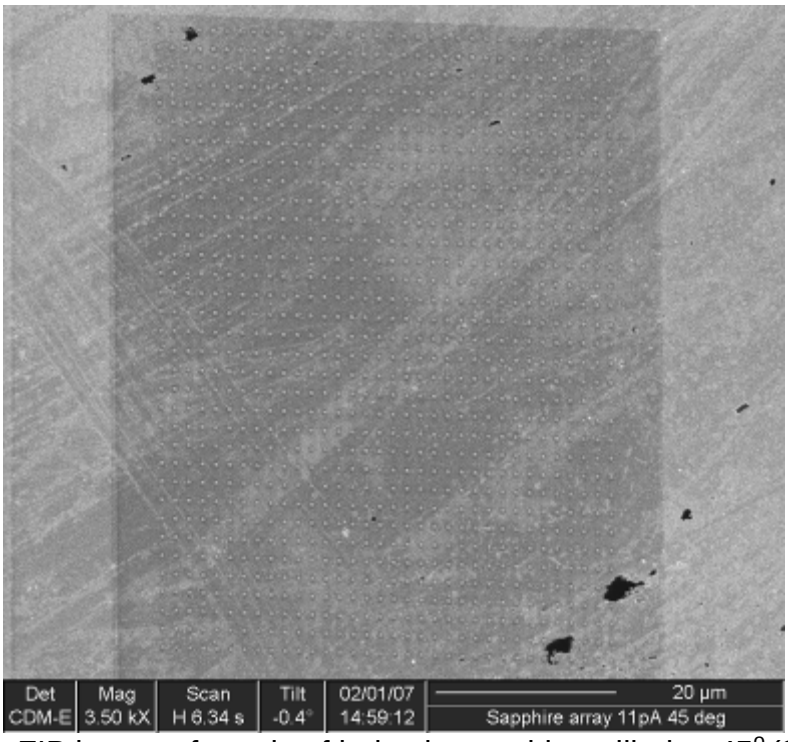

Figure 5.55 - FIB image of matrix of holes in sapphire milled at 45^{o} (2800x 11pA)

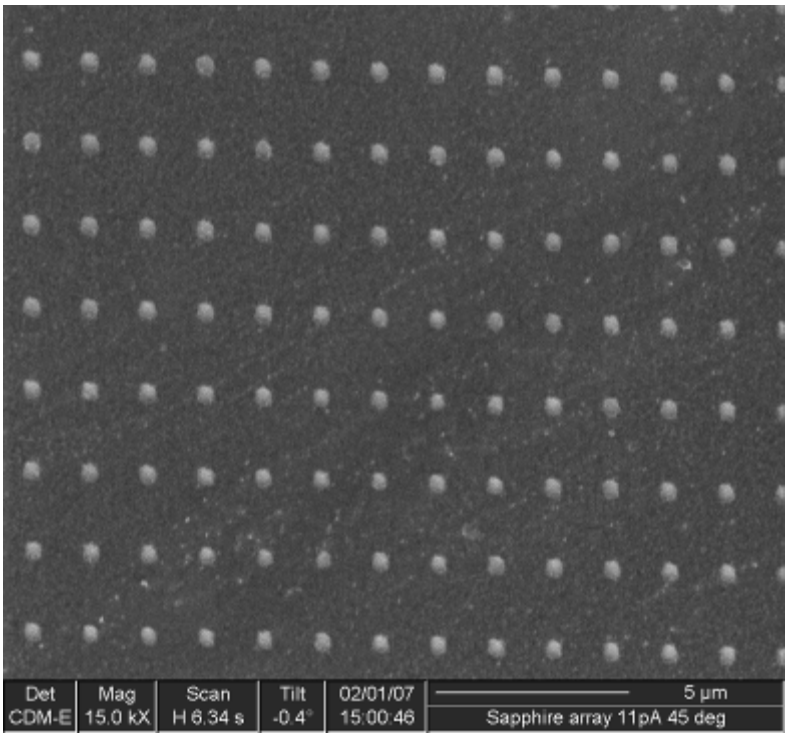

Figure 5.56 - Enlarged view of figure 5.55

5.2.2 – Sapphire gutter (injection mould)

The specifications for the sapphire gutter sections were 15mm in length, 10mm in diameter, and 120^{o} in arc section, figures 4.8 and 5.57. The internal surface of the gutter was polished and the outer surface as grown. The internal surface was polished so that micro features milled into it weren't hidden by the surface roughness.

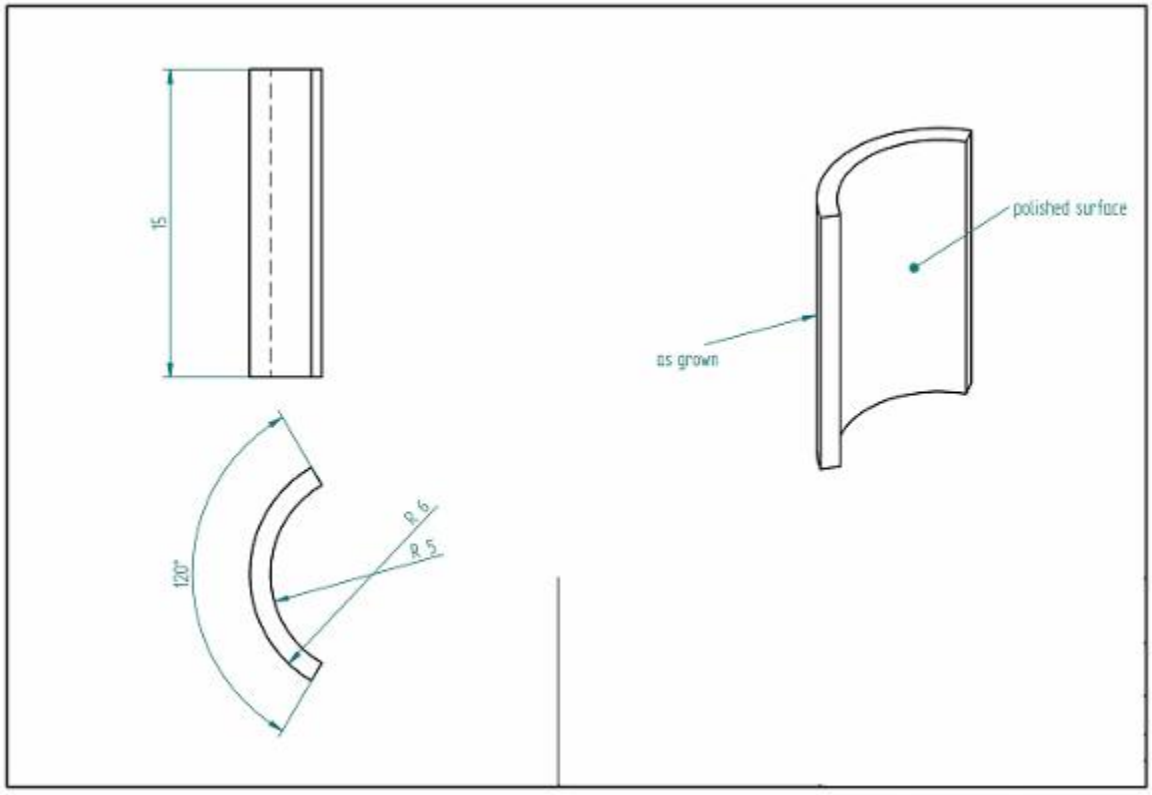

Figure 5.57 – Sapphire gutter specifications

The internal volume of the section was well below the maximum available polymer shot size of the Battenfeld injection moulding machine. The sapphire was ordered from PBTsilicon in Switzerland.

The tilting of the gutter during the patterning process, to keep the milling as close to 0^{o} at all times, required planning. The central 90^{o} arc of the gutter could be milled flat by tilting and rotating the gutter. Using the 60^{o} tilt allowed the whole

prototype gutter to be milled at 0^o. For a 180^o gutter there would be 30^o each side that couldn't be milled flat. Small angle deviations from flat milling should have little effect on the hole dimensions, there being little y direction stretch for 15^o of tilt. For 30^o the stretch would be about 15%. These estimates come from the $1/Cos\theta$ calculation.

To keep the number of times the height of the gutter needed adjusting during the mill to a minimum, the maximum distance up the curve that could be milled without adversely affecting the patterns needed to be found. The Raith software's ability to mill serial patterns, with the stage being moved to a new location for each one, meant that an arc of several degrees could be milled for a given tilt. An arc of 5^o gave a length extension of about 0.5%, 10^o = 1.5%. 5^o sections of the prototype gutter were 0.44mm long. 440µm is equivalent to 293 matrix pitches with nominal 0.2µm square holes and 1.3µm spacing between each hole.

An arc of holes was milled up the curve with the height set for the flat area at the bottom of the curve. The x and y dimensions of the holes were measured (table 5.2). The pitch of the matrix in the y axis was also measured, but this didn't vary over the arc.

Distance from centre (µm)	Angle from centre (deg)	Hole dimension X (nm)	Hole dimension Y (nm)
0	0	350	380
250	2.9	330	370
450	5.2	325	390
550	6.3	335	370
630	7.2	325	370
750	8.6	370	370
850	9.8	370	370

Table 5.2 – Hole dimension variance with angular distance from the centre of the gutter

A possible solution to any increase in hole dimensions with tilt was to decrease the pattern size as milling moved further from the centre. This, however, was not possible since the features being created were already nearly twice the size of the 200nm pattern. The materials resolution limit had been reached, as described in section 3.1.3.

Figures 5.58 – 5.59 show the holes at 0^o, 5^o and 10^o points up the curve. The hole size is visibly the same but the depth of the hole may not be deep enough for sensing purposes. This is due to the loss of focus of the beam spot as the spot size increased with the curve. More holes were milled using one pattern pass and multiple passes to see the effect on depth, figures 5.61 – 5.63.

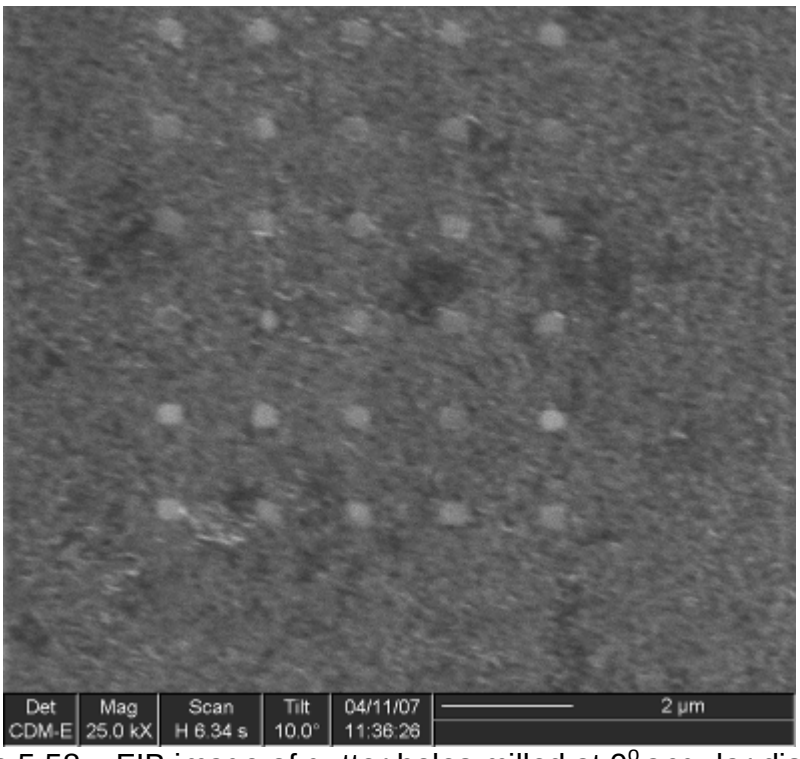

Figure 5.58 – FIB image of gutter holes milled at 0^o angular distance

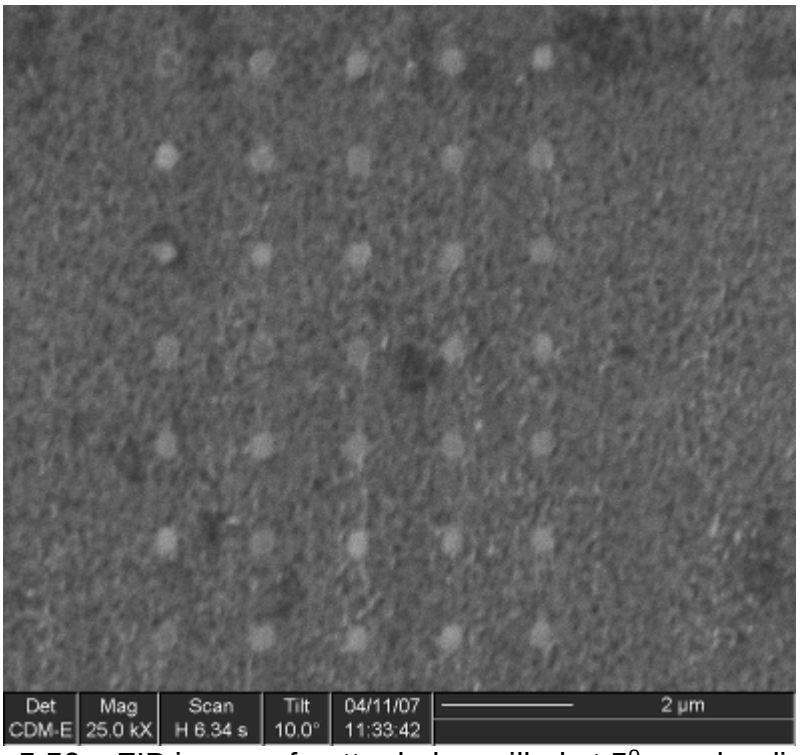

Figure 5.59 – FIB image of gutter holes milled at 5^{o} angular distance

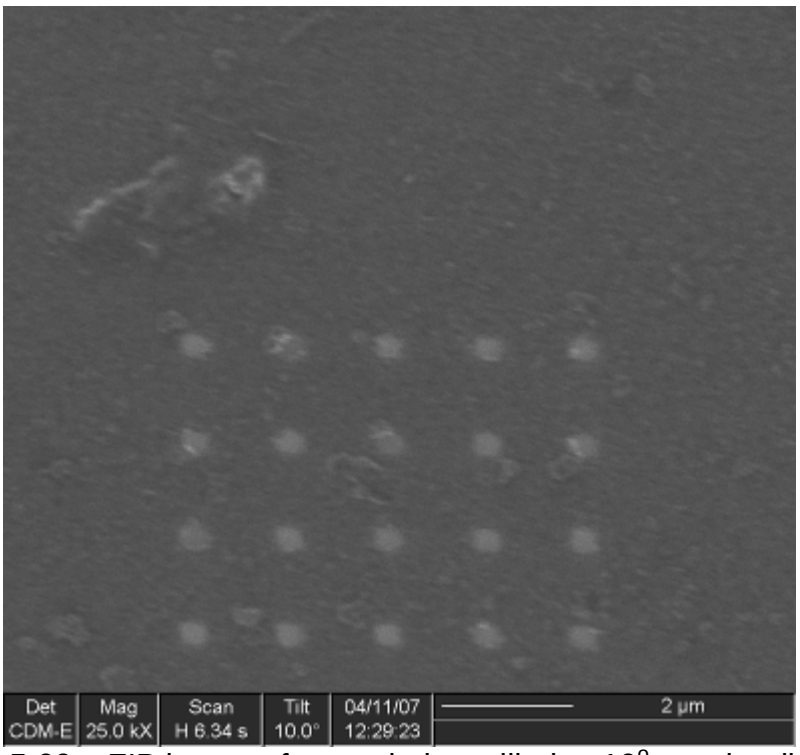

Figure 5.60 – FIB image of gutter holes milled at 10^{o} angular distance

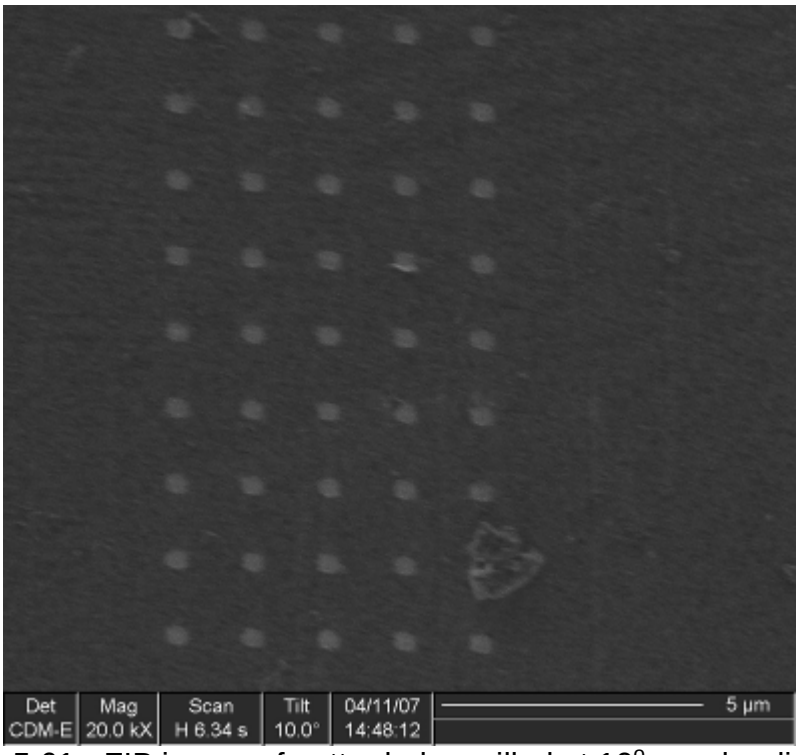

Figure 5.61 - FIB image of gutter holes milled at 10^{o} angular distance (one pattern pass)

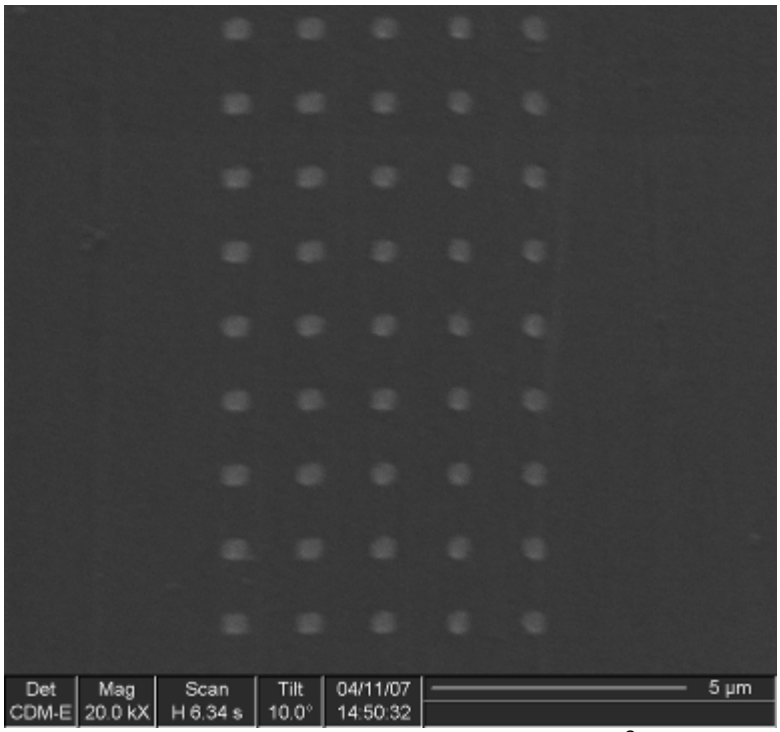

Figure 5.62 - FIB image of gutter holes milled at 10^{o} angular distance (two pattern passes)

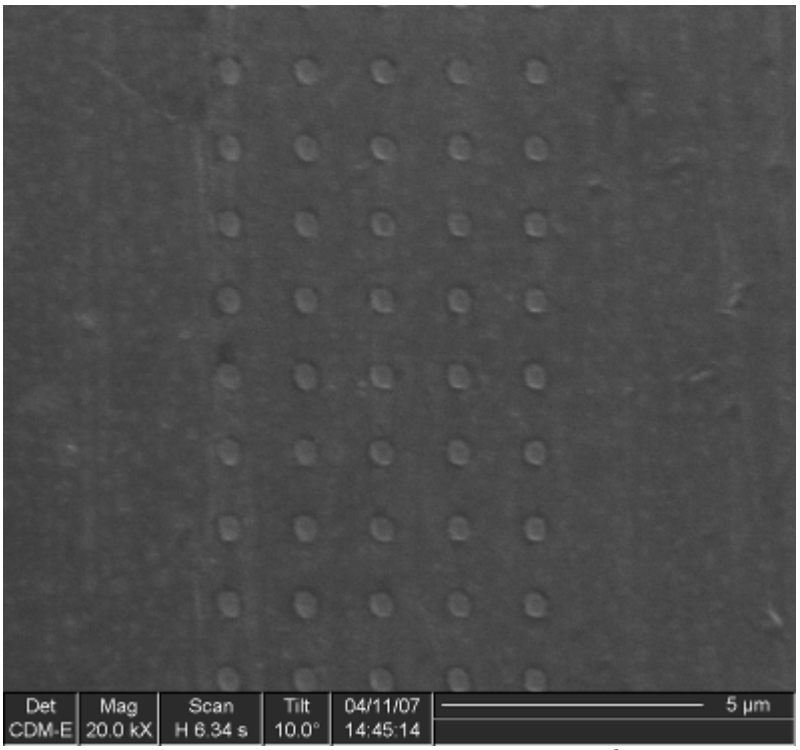

Fig 5.63 - FIB image of gutter holes milled at 10^{o} angular distance (three pattern passes)

The X dimension of the holes in figures 5.61 – 5.63 was 400nm for each set of exposures. The Y dimensions were 340, 370 and 430nm for 1, 2 and 3 exposures respectively.

A series of arrays of 370nm holes were milled down the main axis of a gutter and other arrays were milled up the sides of the curve, perpendicular to the main axis. Also, larger rippled areas and rippled holes like those in figure 5.50 were milled as well. This gutter was to be tested in the Battenfeld injection moulder. These test features were all suitable for incremental type encoders.

About this time the thinking behind the detection system for the encoder changed to an absolute position measurer, not a relative position system. This required non identical patterns to be milled, so binary patterns were milled (figure 5.64) into the test gutter as well. Shortly afterwards the demonstrator was cancelled by the

project managers as it was thought the demonstrator would not produce a workable device by the end of the four year project. The work done by the different project partners on the device had not been managed properly and had diverged in too many directions to be turned into a device given the remaining time. Further work was stopped to concentrate resources onto the other three demonstrators. To ensure that the time and money spent on the Cranfield part of the demonstrator was not wasted, the aim is to replicate some nano/micro features using the Battenfeld injection moulder. Features of this size are possible to replicate (Schift 2000). Extra micro sized features were milled into the test gutter, figure 5.65. This would extend the moulding capabilities and knowledge at Cranfield.

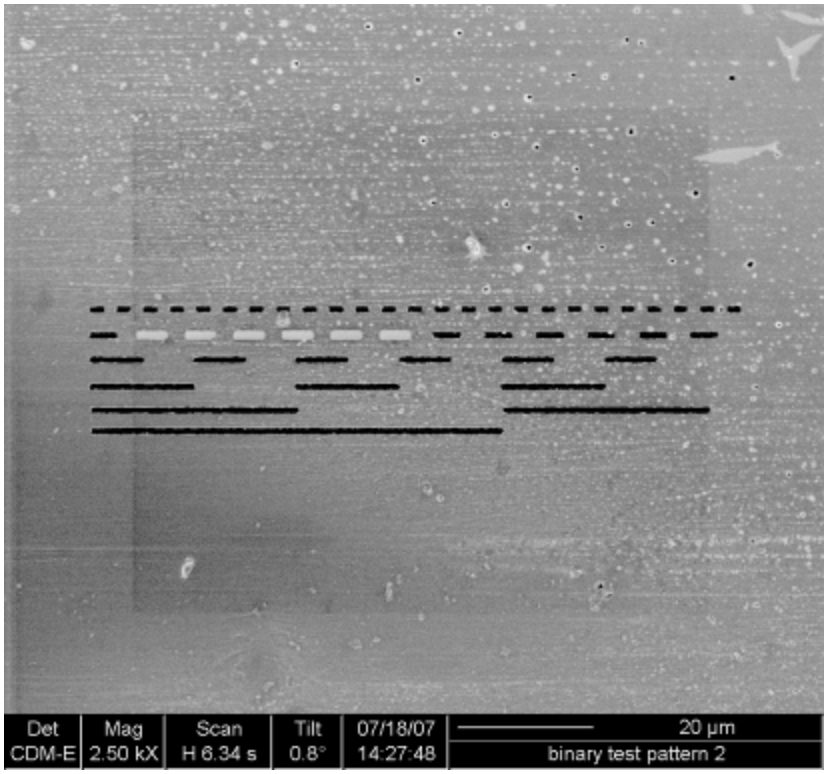

Figure 5.64 - FIB image of binary encoder patterns

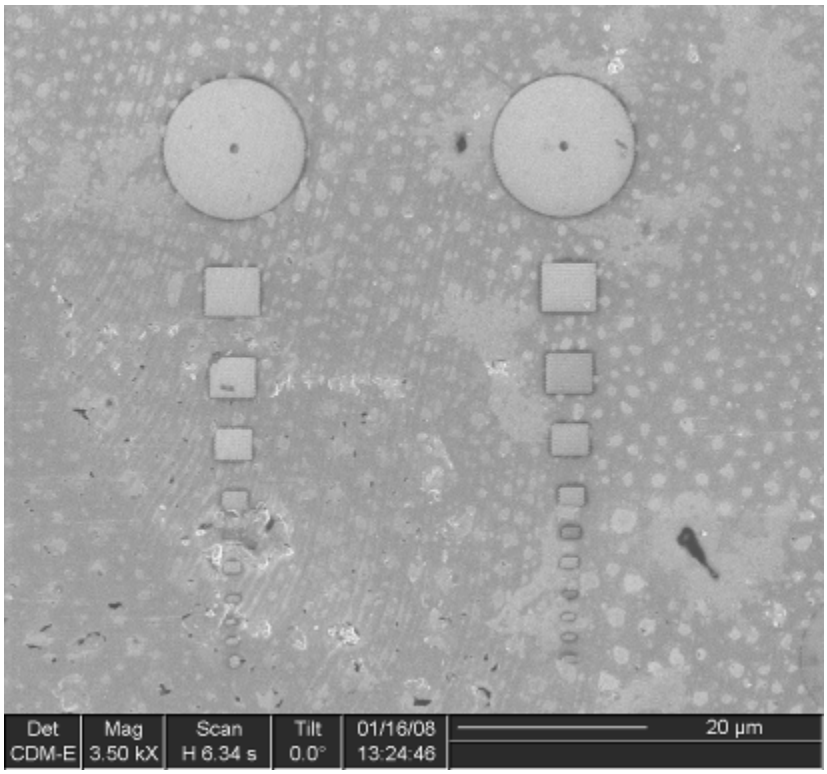

Figure 5.65 – FIB image of sapphire micro patterns

5.3 - FIB produced polycrystalline CVD diamond tooling

5.3.1 - Polycrystalline CVD diamond

After discussions with Mr. Andrew Cox, general manager at Contour Fine Tooling (Contour), it was decided to use polycrystalline chemical vapour deposited (CVD) diamond for the tooling work. This was because Contour had an interest in producing polycrystalline tools where the bulk of the material removal was done with a laser. Using a laser allows the rough shape of the tool to be produced quickly; however it is not capable of giving a sharp edge to the tool. A tool could be produced faster using laser machining than by grinding and at lower cost. The combination of laser and FIB machining was of common interest to Cranfield and Contour. The fine detail capability of the FIB to give good edges meant that the time required for producing a complete tool would decrease. Also of great

importance was the fact that there was no work in the published literature on using FIB to produce tools from polycrystalline diamond, so it would be novel.

CVD polycrystalline diamond maintains the advantages of conventional polycrystalline diamond but doesn't have the disadvantage of including a binder material. The reduction in inhomogeneity makes the diamond less likely to fracture because binder-carbon bonds are weaker than carbon-carbon bonds. The good wear properties of polycrystalline are not reduced by the binder removal (Pierson 1993). From the viewpoint of FIB machining, the more homogenous the material the better, as it will mill more uniformly. Another big advantage of polycrystalline diamond is that, because of the more disordered structure compared to a single crystal, there are more electrons available due to the inter-crystal bonds. This enables the tool to be imaged using the electron detector mode rather than the ion mode in the FIB chamber. The improvement in image quality is very useful for examining the quality of the surfaces post FIB machining. There is little charging up of the surface, meaning the image quality does not degrade with repeated imaging while a tool is being produced. The mill yield of polycrystalline is 25% higher than that of single crystal (Stanishevsky 1999). This is because the grain boundaries act as weak points for the gallium ions to exploit compared to the flat surface of single crystal. The grain boundaries are preferentially milled due to the inter-crystal bonds being weaker than the intra-crystal bonds. There are dangling bonds for the ions to exploit. The grains of the polycrystalline structure are visible on the FIB image of the tool blank tip (figure 5.66) where the gallium ions are channelling down between the grains. The columnar structure of CVD PCD is shown in figures 5.67 and 5.68. These show the increasing width of the grains as they grew away from the substrate upon which the diamond was grown.

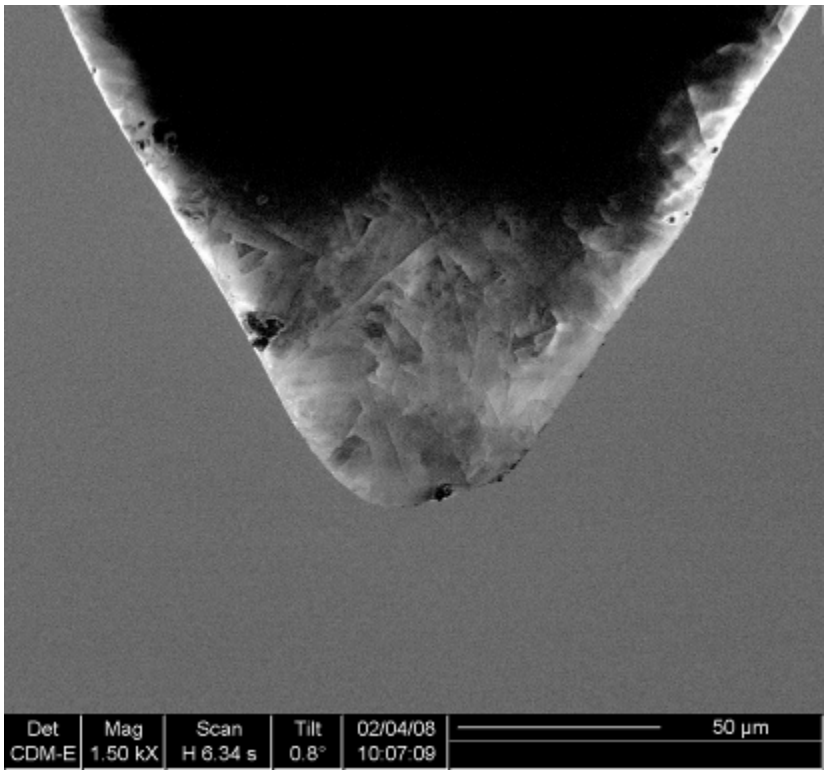

Figure 5.66 – FIB image of the tip of a laser cut CVD blank

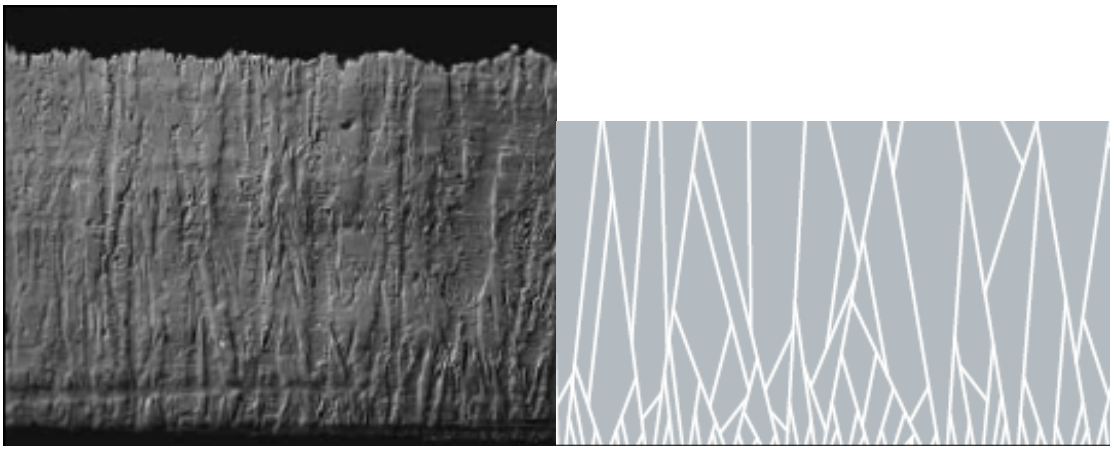

Figure 5.67 – (left) SEM image of CVD PCD cross section
(right) Diagram of the columnar structure of intergrown CVD PCD grains
(after Element 6 PCD)

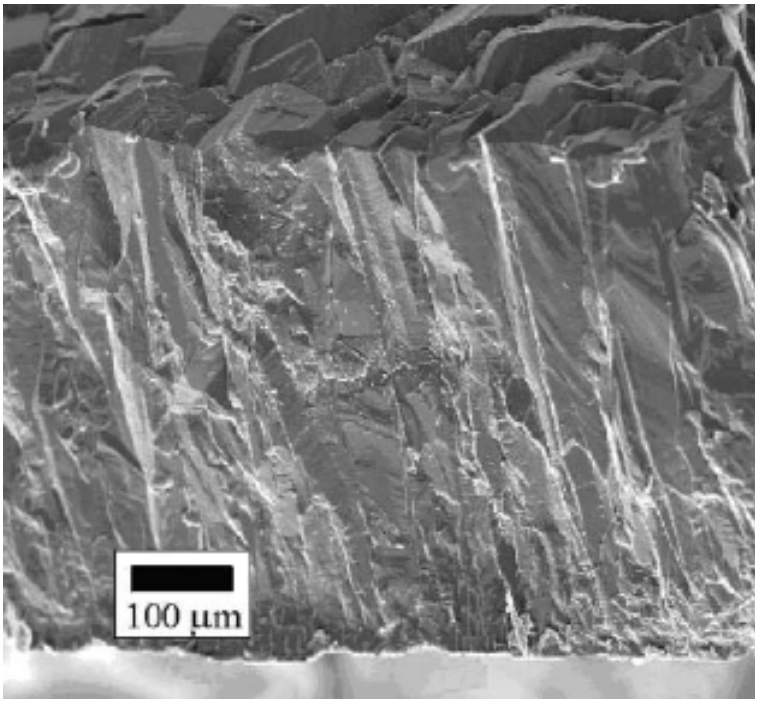

Figure 5.68 – SEM image of CVD PCD cross section showing columnar structure (after Popovich 2005)

5.3.2 – Turning tools

For the first tool it was decided to make a turning tool, as this is a simple tool to manufacture having only one straight cutting edge. The curved front of the tool is milled away to leave a straight edge of the desired length, figures 5.69 and 5.70. The effect of the unwanted face angle (section 5.1.5) is visible in figure 5.70. The front is not flat, the angle of milling being made more visible by the partially removed debris on the front of the tool. The material to the left of the red line would have been removed if the nominal flat surface had been produced. This is a problem when creating tool edges as, if there is no clearance under the edge, the sharp edge will not touch the work piece first when the tool is bought into contact (figure 5.72). Clearance is the air gap between the tool body and the work piece. The body of the tool needs to slope away from the work piece so that there is only one point of contact, the cutting edge at the tool tip. The tool blank, as shown in figure 4.4, has a slope of 12^{o} on its front face. After milling, the slope needs to be maintained right up to the cutting edge.

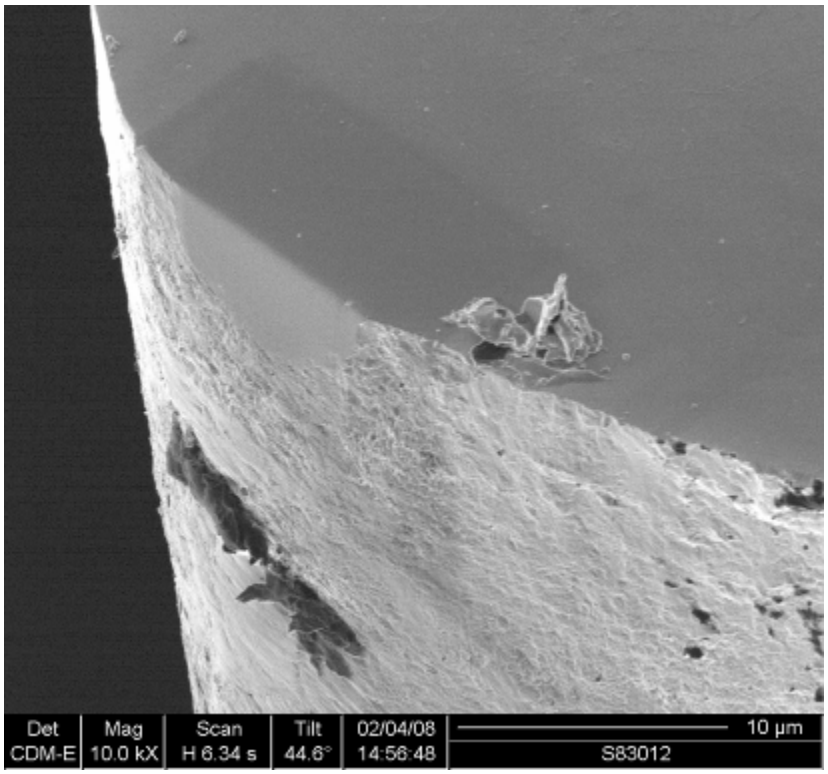

Figure 5.69 - FIB image of a straight tool edge in production

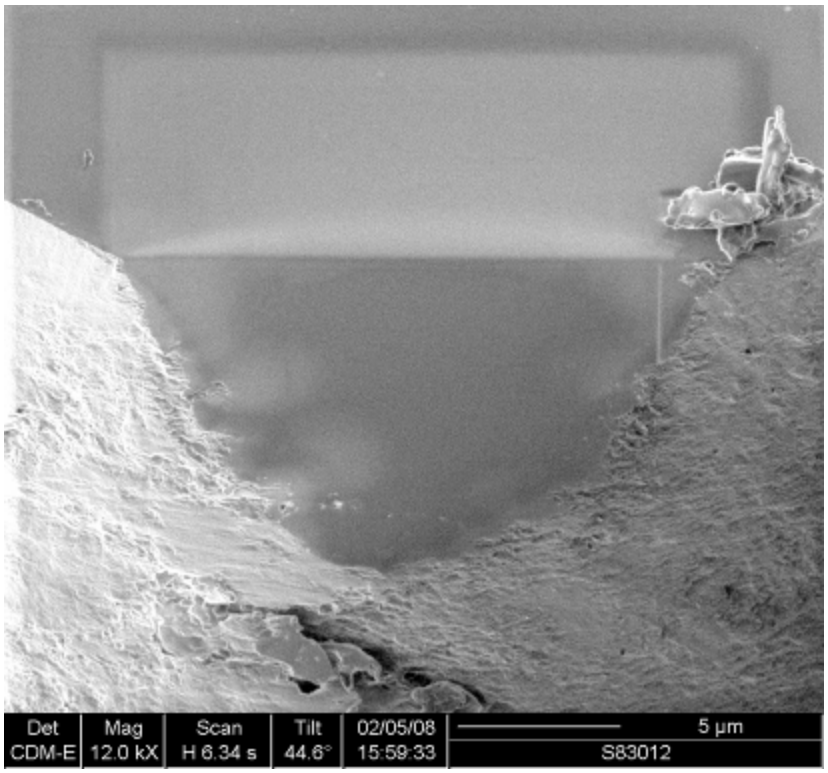

Figure 5.70 - FIB image of the front view of cutting edge in production

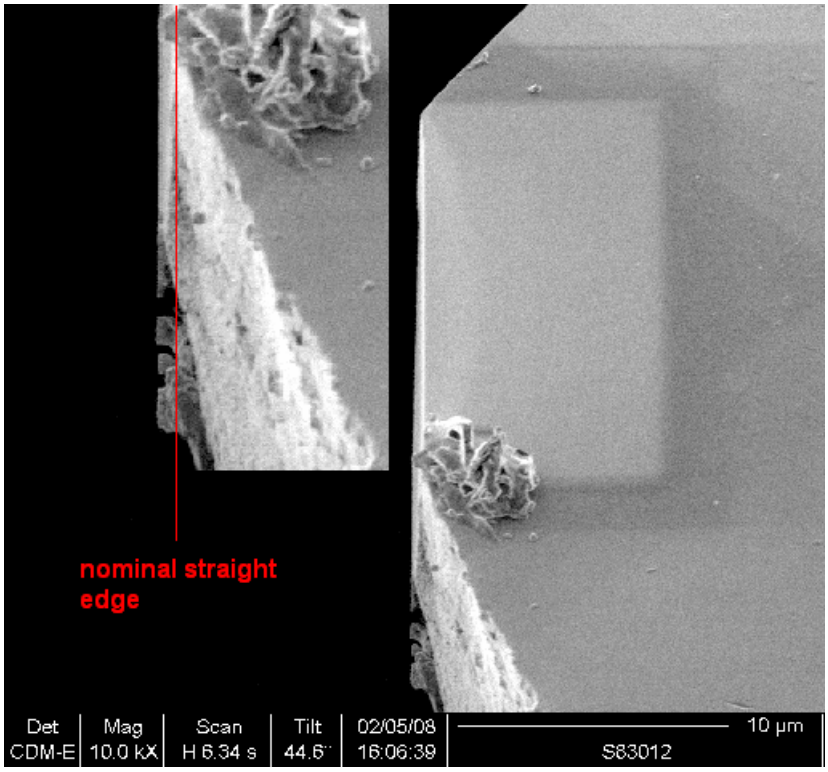

Figure 5.71 - FIB image of the unwanted face angle on tool front

There are two solutions to the problem of not getting clearance on the front face. The first is to produce the edge by milling from the top down, creating a sharp edge but with the unwanted angle on the front face, figure 5.73 (a). The angle is removed by altering the position of the tool in the chamber by placing it in the vertical tool holder. The front face can then be worked on. The sloping material can be removed by milling into the front of the tool until there is clearance on the face, figure 5.73 (b). This requires careful milling when near the cutting edge as achieving clearance means milling to within 1µm of the edge. It is easy to make a mistake when doing this and damage the edge.

The second solution is to mill with the tool mounted upside down in the chamber, figure 5.73 (c). This means that the unwanted face angle leans the same way as the tool face and there is no issue about clearance. This is a faster process than milling away the front of the tool as there is less time spent pumping the chamber

up and down, switching the tool between the vertical and horizontal holders and resetting the eucentric height each time. Thus it is more suitable for the production of large numbers of tools.

However, the first solution was chosen for the tool work as the number of tools being produced was low. Contour Fine Tooling had provided the two mounts matching the kite tool shank we had, meaning the tools were securely held and wouldn't move when tilted in the chamber. An ideal tooling setup is an inverted version of the horizontal tool holder, figures 5.73 (c) and 5.74.

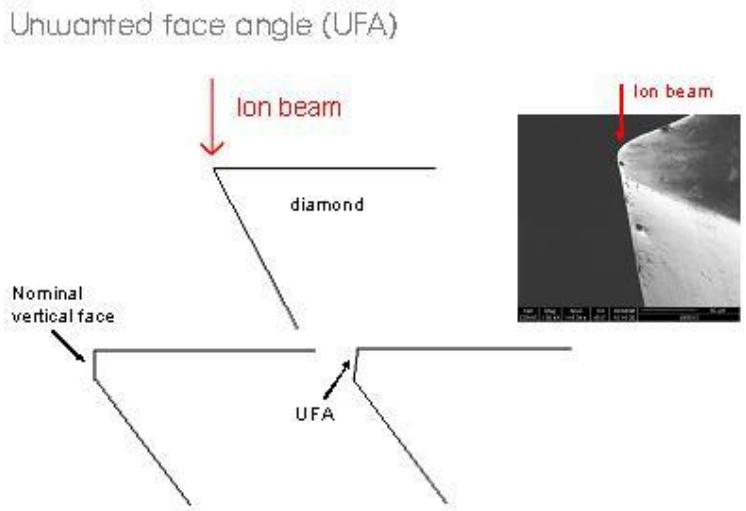

Figure 5.72 – The Unwanted Face Angle (UFA) on tool edges

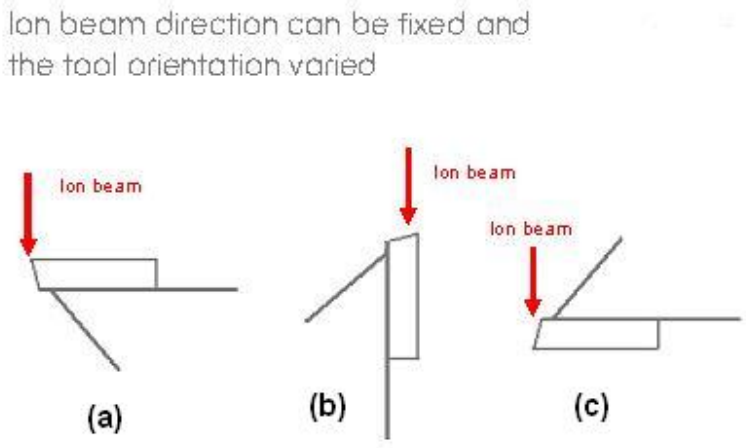

Figure 5.73 - Possible beam approaches to the tool edge

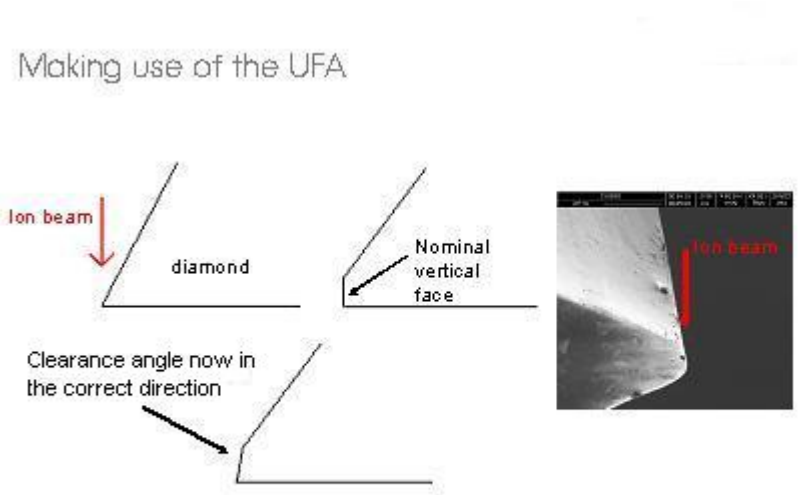

Figure 5.74 – Using the UFA to improve tool edges

The front face of the tool when the edge is complete is as in figure 5.75.

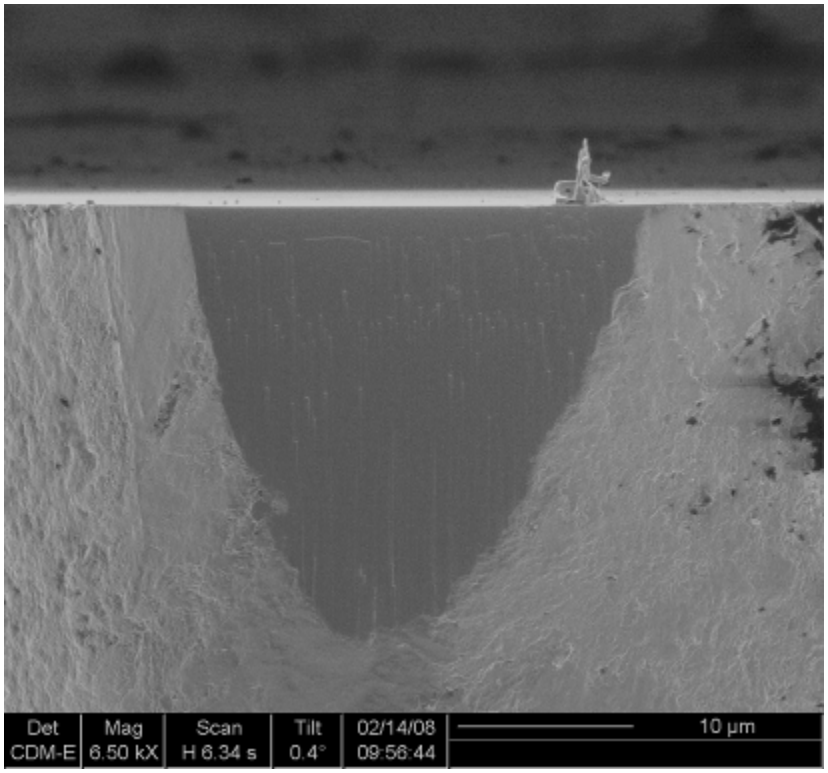

Figure 5.75 - FIB image of the front face of a tool with UFA

The clearance is gained by milling onto the face as in figure 5.76.

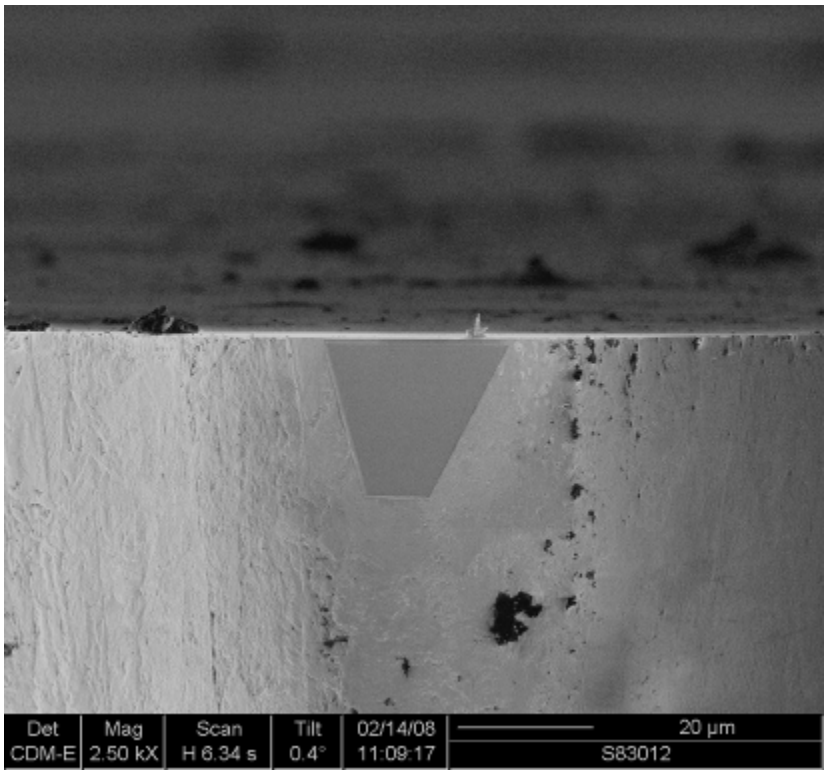

Figure 5.76 - FIB image of the milled back tool front face below the cutting edge

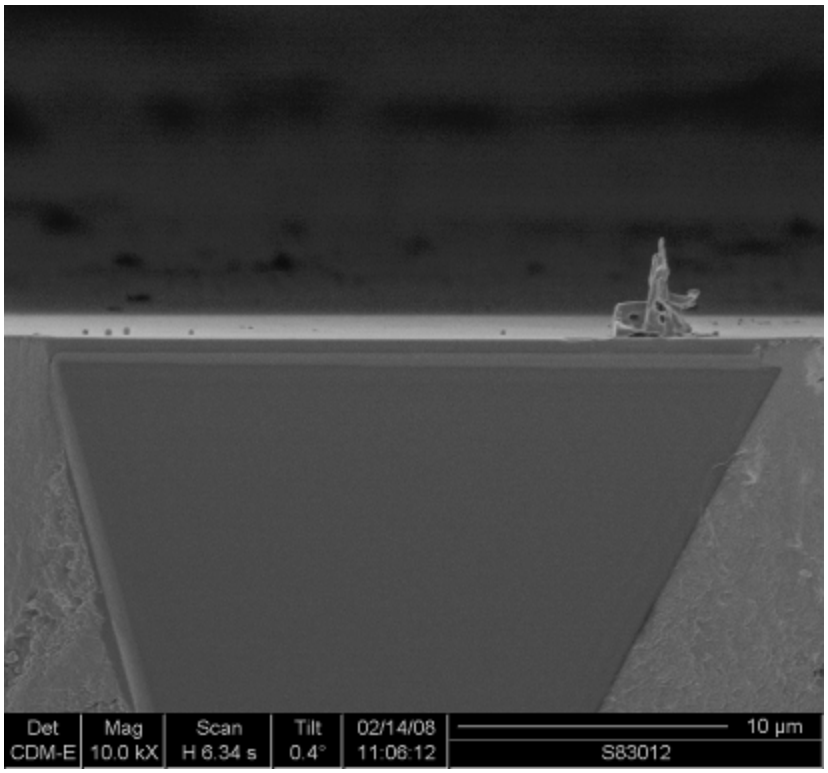

Figure 5.77 – Enlarged view of figure 5.76

The milling is brought up to near the edge figure 5.77, and the face worked back until the protruding parts of diamond visible in figure 5.78 have been removed, figure 5.79.

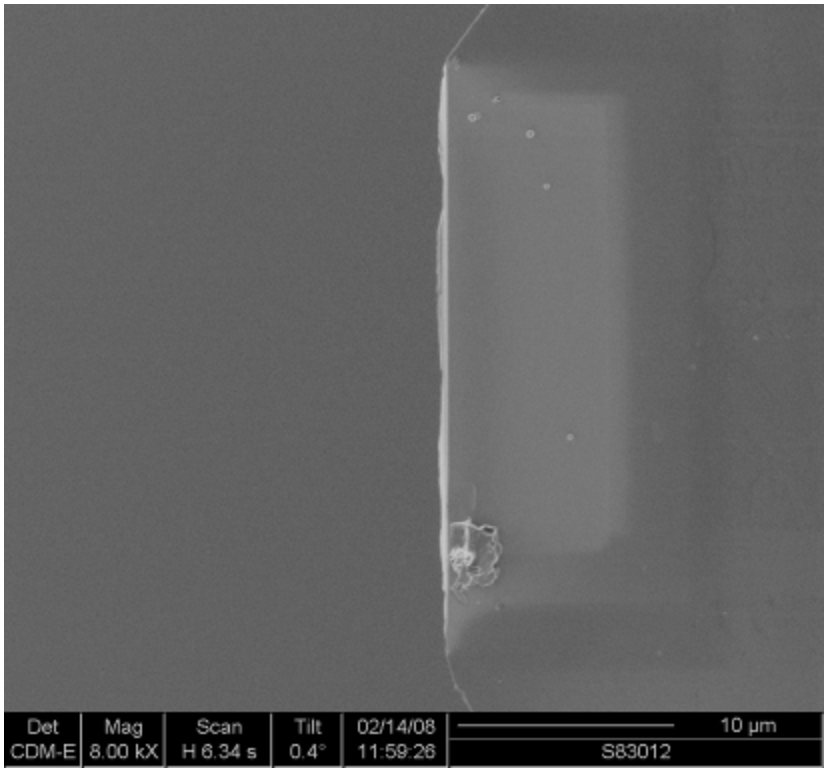

Figure 5.78 - FIB image of the protruding parts of the tool front face

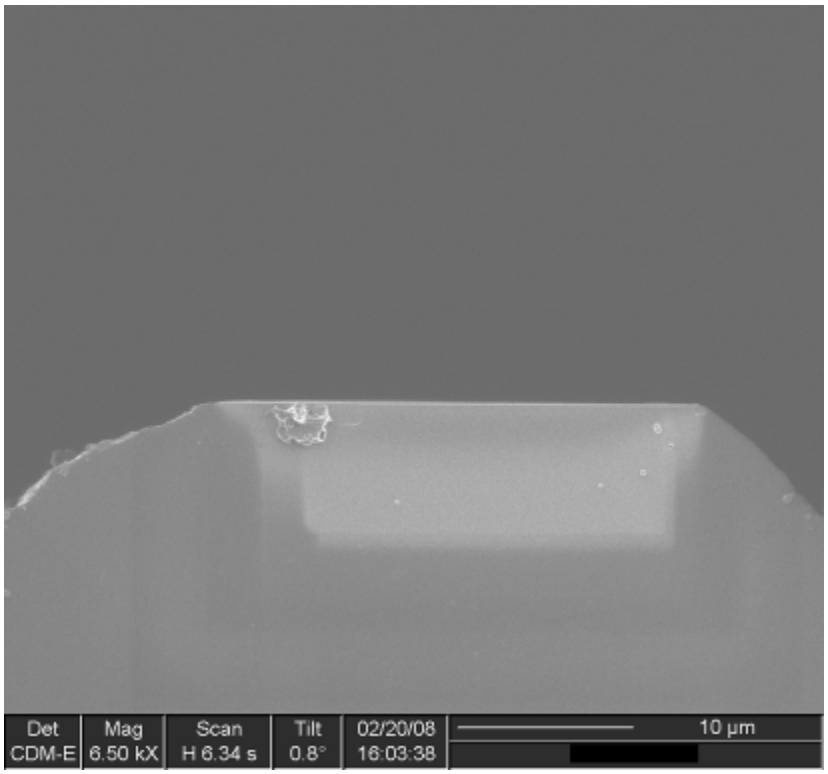

Figure 5.79 - FIB image of the finished tool edge

Two turning tools were produced by the method above with cutting edge lengths of 39µm and 13µm. The tool production steps are summarised in table 5.3.

Step	Process characteristics	Characteristics of the final tool
1	Use a high current (2.7nA - 11.5nA) to remove the tip from a laser machined blank	Cuts tool edge to the desired length
2	Use a low current (0.15nA - 1nA) to smooth the front face and edge	Ensures a clean straight edge
3	Put tool in the vertical position and machine away the UFA – reducing the current as the cutting edge is approached	Gives front face clearance

Table 5.3 – Tool production steps

The two complete tools are shown in figures 5.80 to 5.83. Tool S83011 has an edge of 39µm and S83012 has an edge of 13µm. The tools will be referred to by their numbers from here onwards. The S numbers are the tool identifying code from the tools manufacturer Contour Fine Tooling. S83011 was made first and S83012 was the second tool, incorporating the lessons learned during the first manufacture.

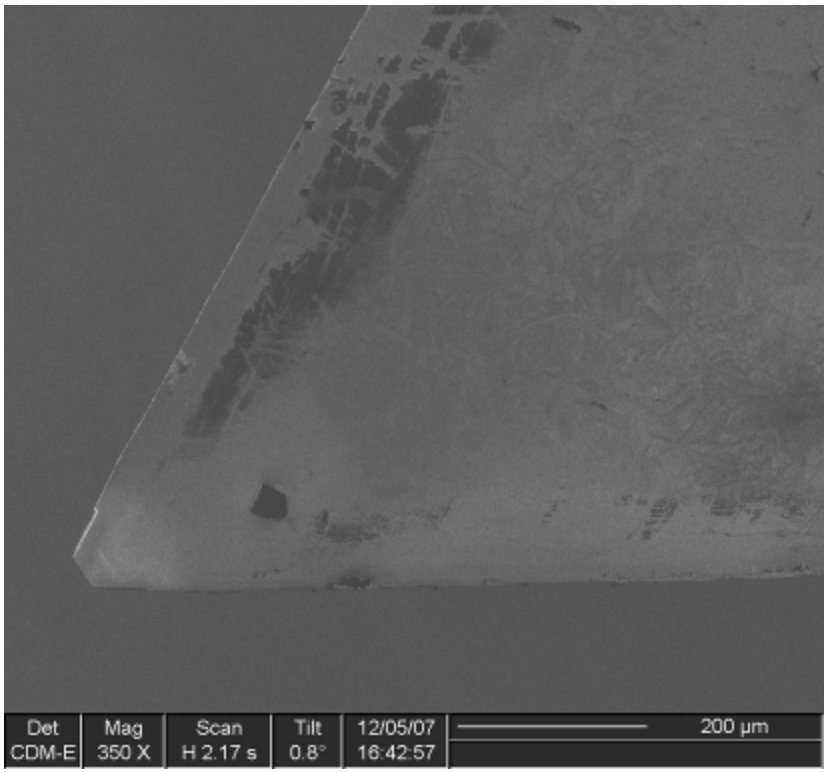

Figure 5.80 - FIB image of S83011 tool tip

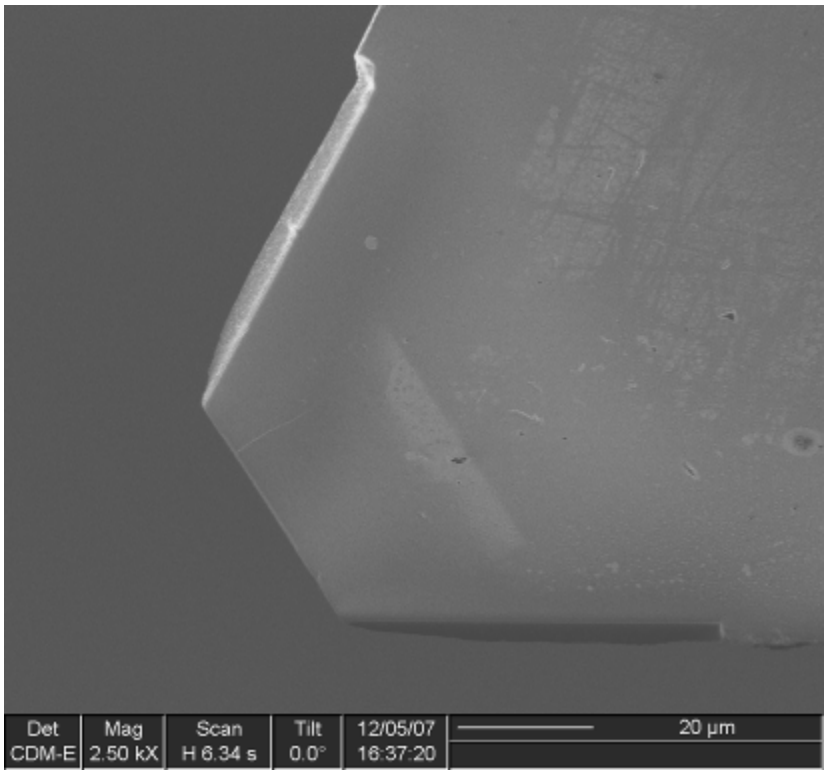

Figure 5.81 - FIB image of S83011 tool edge

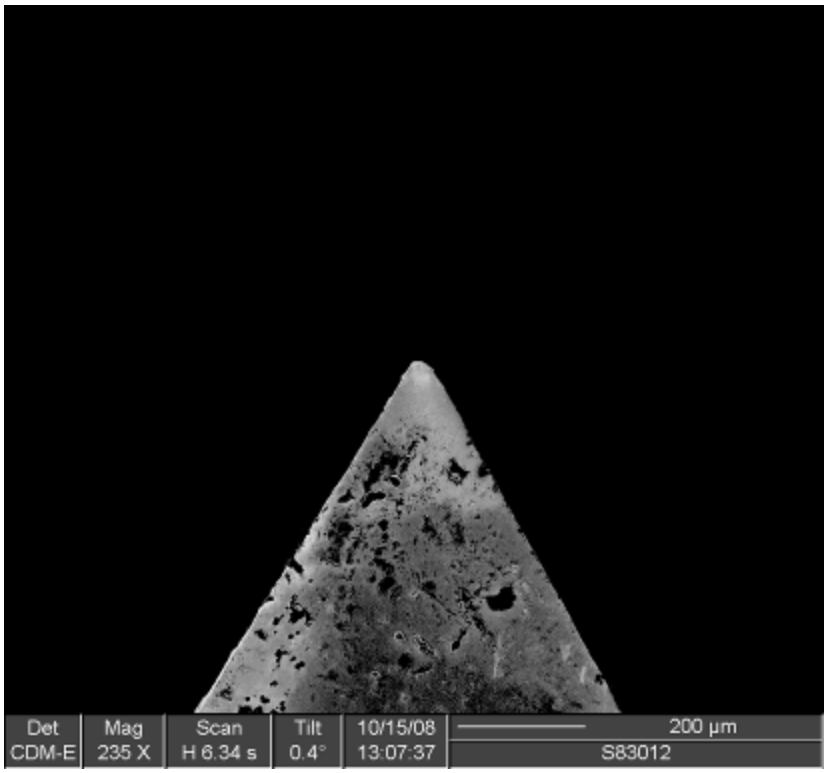

Figure 5.82 - FIB image of S83012 tool tip

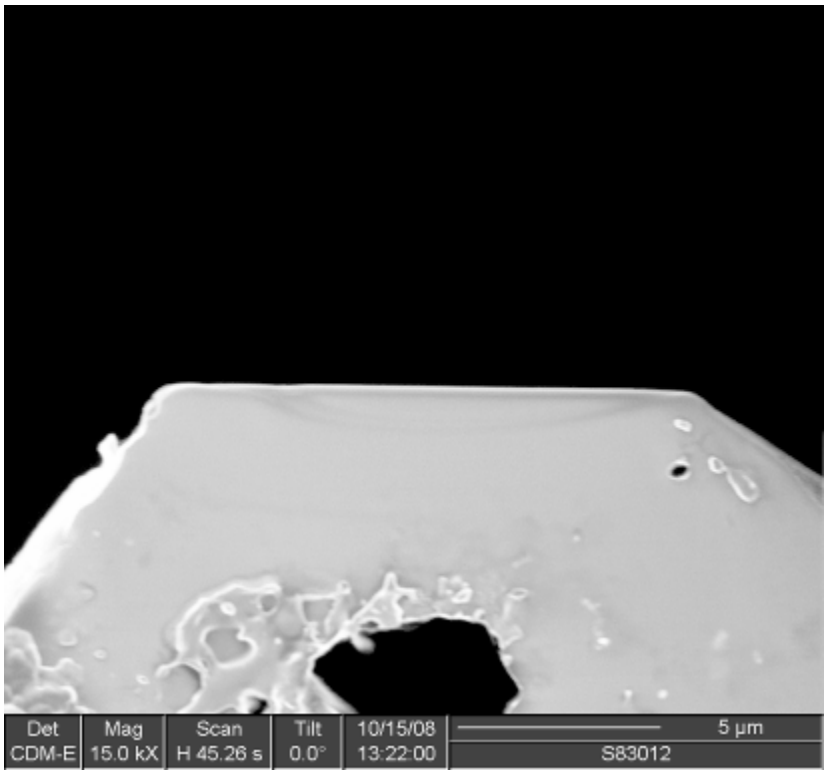

Figure 5.83 - FIB image of S83012 tool edge

5.3.3 – Tool testing: tool S83011

S83011 was used to machine circular trenches 5, 10 and 20µm deep, with three trenches for each depth. The copper work piece was rotated at 1200rpm with a depth of cut of 10nm per revolution. White spirit was sprayed across the work piece and tool tip during milling to remove swarf from the cut zone. The testing is described in greater detail in section 4.5.1. After the machining tool S83011 was examined by SEM. The tool was found to be in good condition (figures 5.84 – 5.86) with no obvious machining damage to the tip.

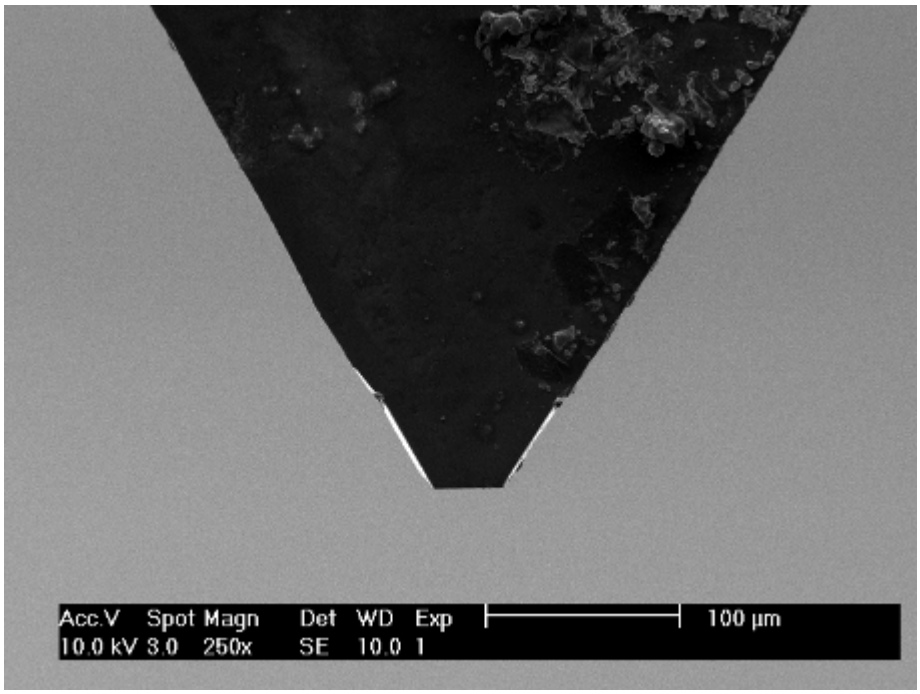

Figure 5.84 - SEM image of S83011 after testing

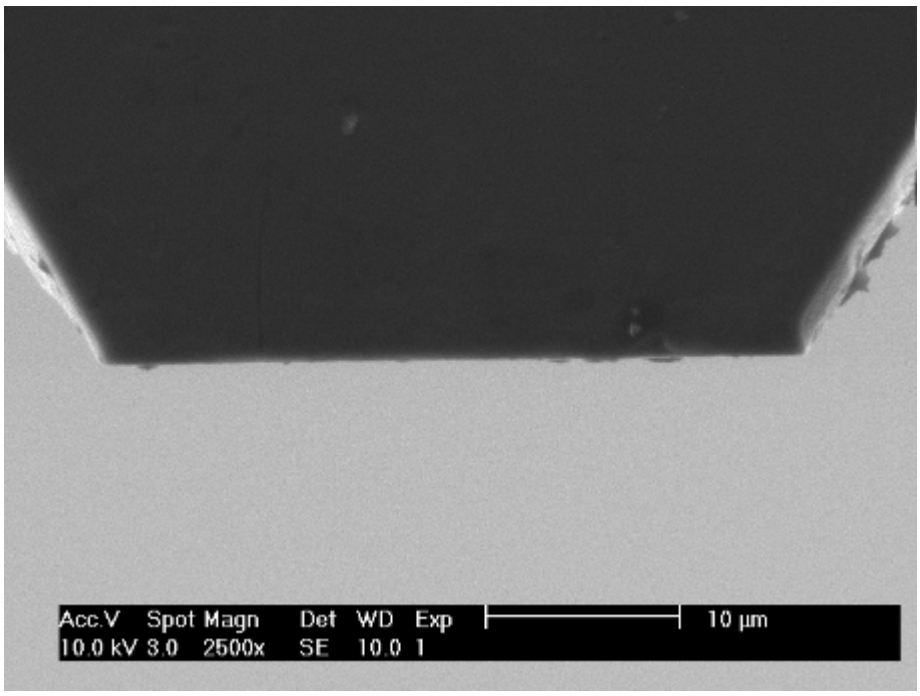

Figure 5.85 - SEM image of S83011 cutting edge after testing

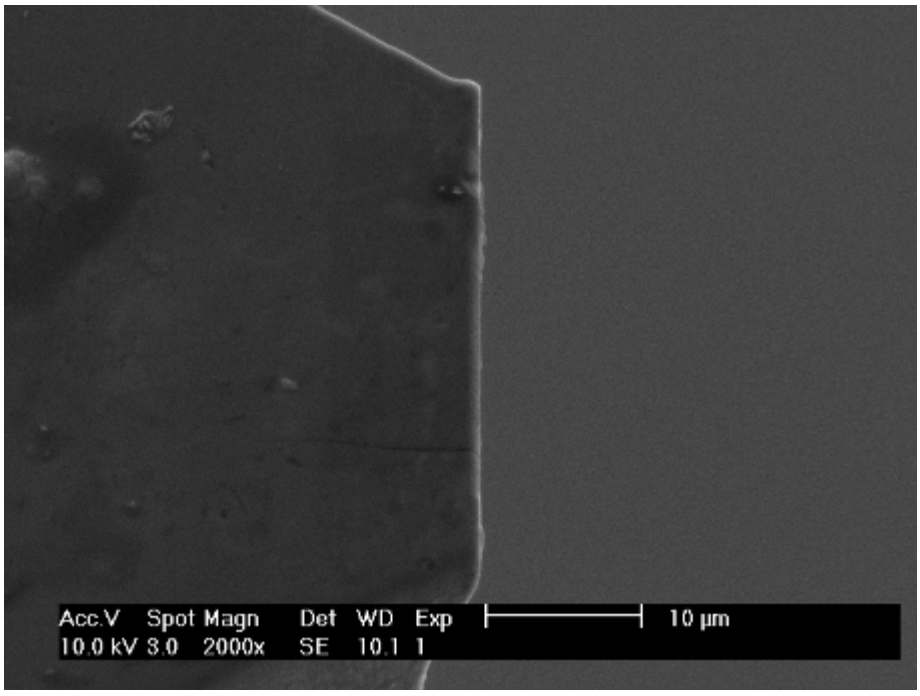

Figure 5.86 – SEM image of S83011 cutting edge before testing

The trench manufactured by the same tool was also imaged by SEM (figures 5.87 – 5.89) which showed a large amount of material on the surface either side of the trench (figure 5.87). This was material that had been pushed aside by the tool as it cut through the copper. The trench walls were angled due to the shape of the tool. Excluding small pieces of swarf and dirt the bottom looked smooth to the limits of SEM's imaging capability apart from a darker area at the foot of the wall (marked with a red arrow) and a faint line near the opposite wall (yellow arrow), figures 5.88 and 5.89.

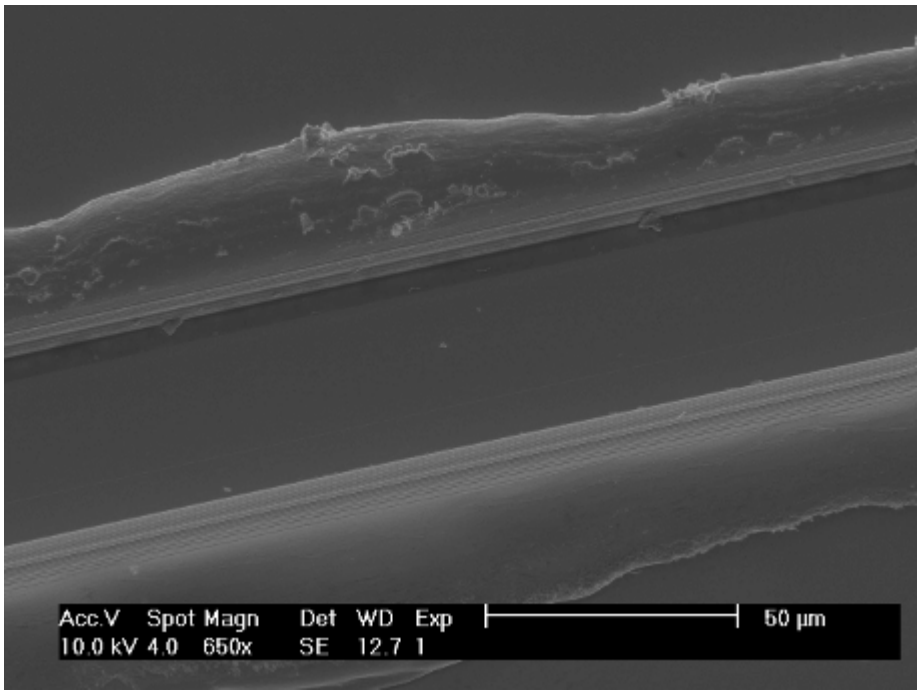

Figure 5.87 - SEM image of 10µm deep trench cut with S83011. Direction of cut left to right.

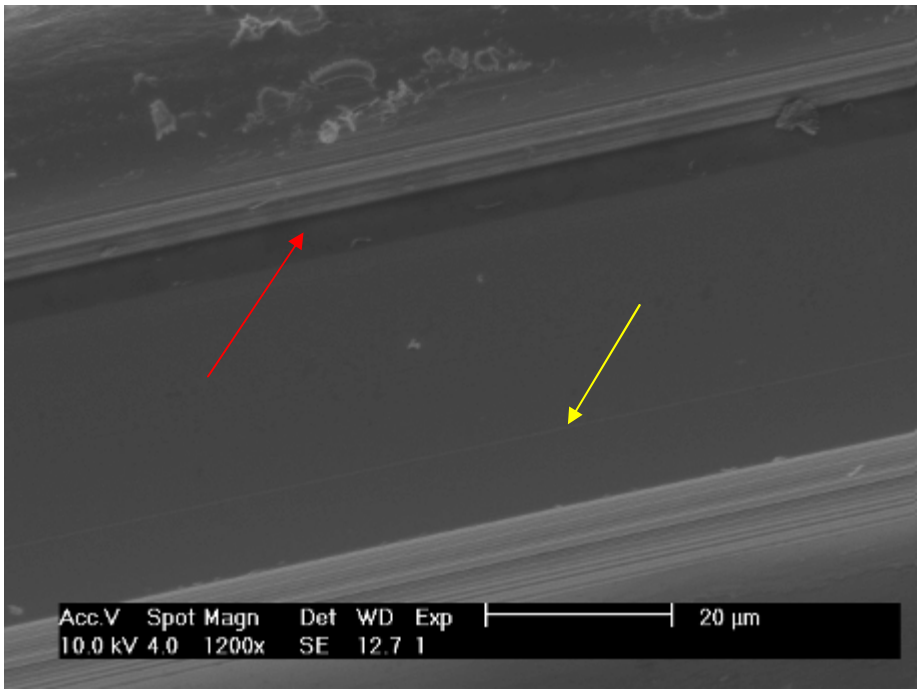

Figure 5.88 – SEM image of floor of 10µm deep trench cut with S83011. Direction of cut left to right.

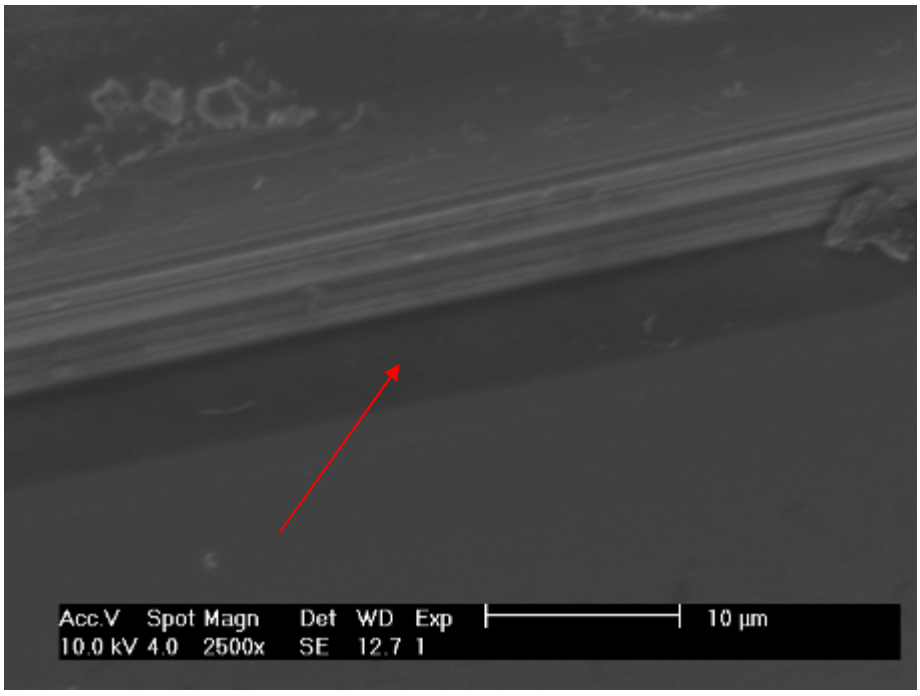

Figure 5.89 – SEM image of enlarged view of floor of 10µm deep trench cut with S83011. Direction of cut left to right.

The trench floors where measured with a Taylor Hobson CCI white light interferometer and with an AFM to obtain roughness values. The Ra value obtained with the interferometer across the width of the trench was 0.5nm. A value this low is normally produced with single crystal tooling and an expert on white light interferometry from the National Physical Laboratory, Prof Richard Leach, who was part of the 3D-Mintegration project, was consulted. He advised not to use the Taylor Hobson data in this instance as the results from white light interferometers are open to interpretation when measuring small scan lengths. Depending on which waviness filters are used and the length of scan (number of data points) it is possible to significantly alter the roughness results. The CCI uses a maximum of a 1024x1024 data point grid when scanning areas larger than 0.5mm square (this area is derived from the x, y resolution of 0.5µm). The trench measured was ~77 data points wide, only 7.5% of the potential data points the roughness calculating algorithm can use. When the number of points is this low the effect of the settings chosen can have a large effect on the final calculated roughness. (Leach 2008) and (Gao 2008) discussed the systemic problems of white light interferometers and

(Gao 2008) recommended caution if sub wavelength (~600nm) features needed to be measured.

The bottom of the 5µm trench was then measured with an AFM to obtain reliable roughness data. The 10µm and 20µm deep trenches could not be measured with the AFM as the Z axis limit on the AFM was 5µm. The 3D view of the trench bottom is shown in figure 5.90 and a 2D profile across the bottom in figure 5.91.

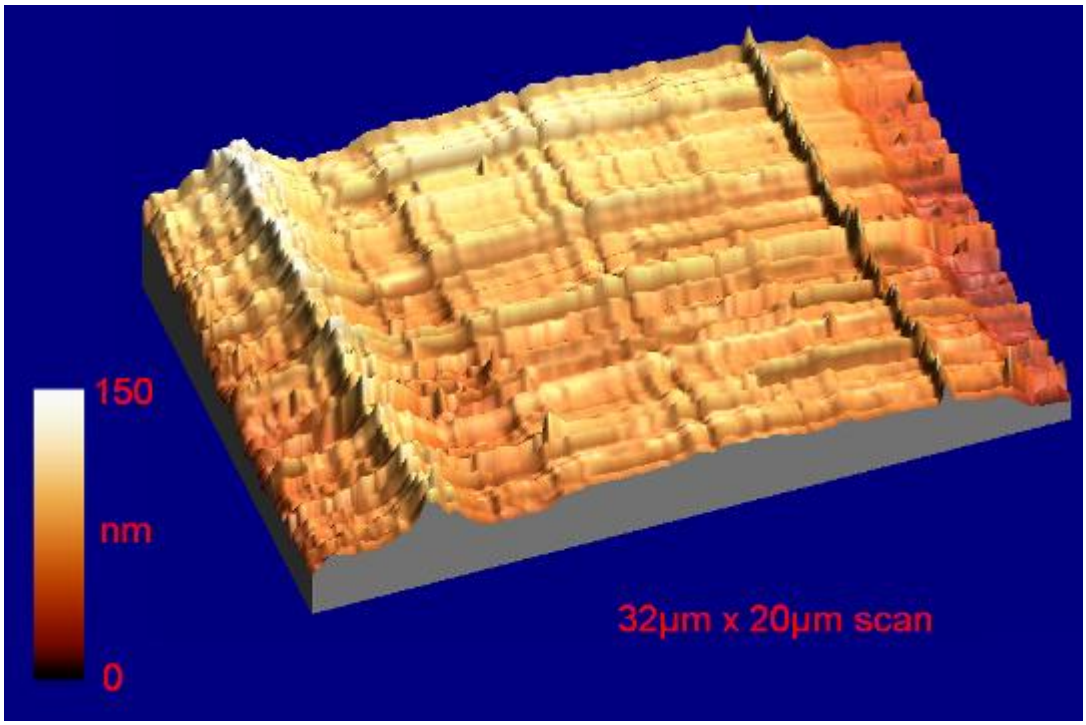

Figure 5.90 – 3D AFM scan of the bottom of a 5µm deep trench cut with S83011. Direction of cut bottom to top.

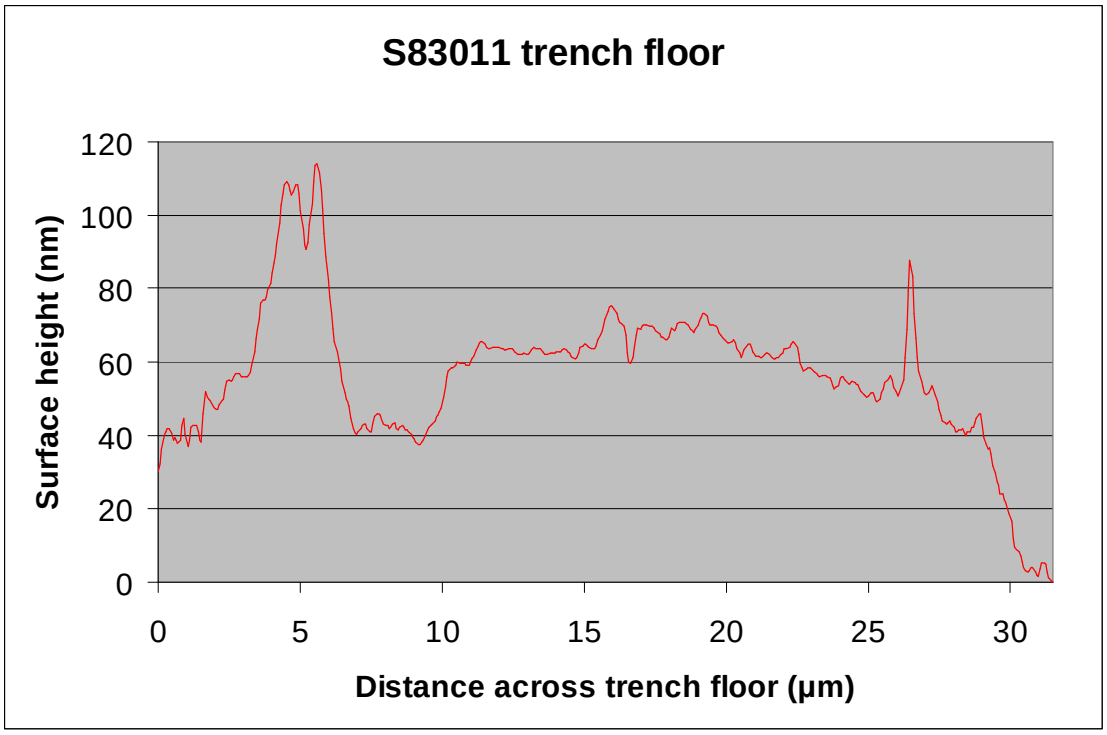

Figure 5.91 – 2D AFM profile across 5µm deep trench cut with S83011

The three obvious features of the bottom, as indicated by the coloured arrows in figure 5.88, are the 70nm high spike on the left of the profile, the 40nm spike on the right and the 40nm deep drop off on the right edge of the scan. The yellow arrow in figure 5.88 points to the 70nm spike and the red arrow to the 40nm drop off. The 40nm spike, being much narrower than the 70nm, is not visible on the SEM images. On the SEM image of the tool edge, figure 5.86, the defects responsible for the two spikes are visible. These are highlighted in figure 5.92 by the blue arrows. The 70nm spike is caused by the small chip and the 40nm spike by where the longer feature meets the tool edge.

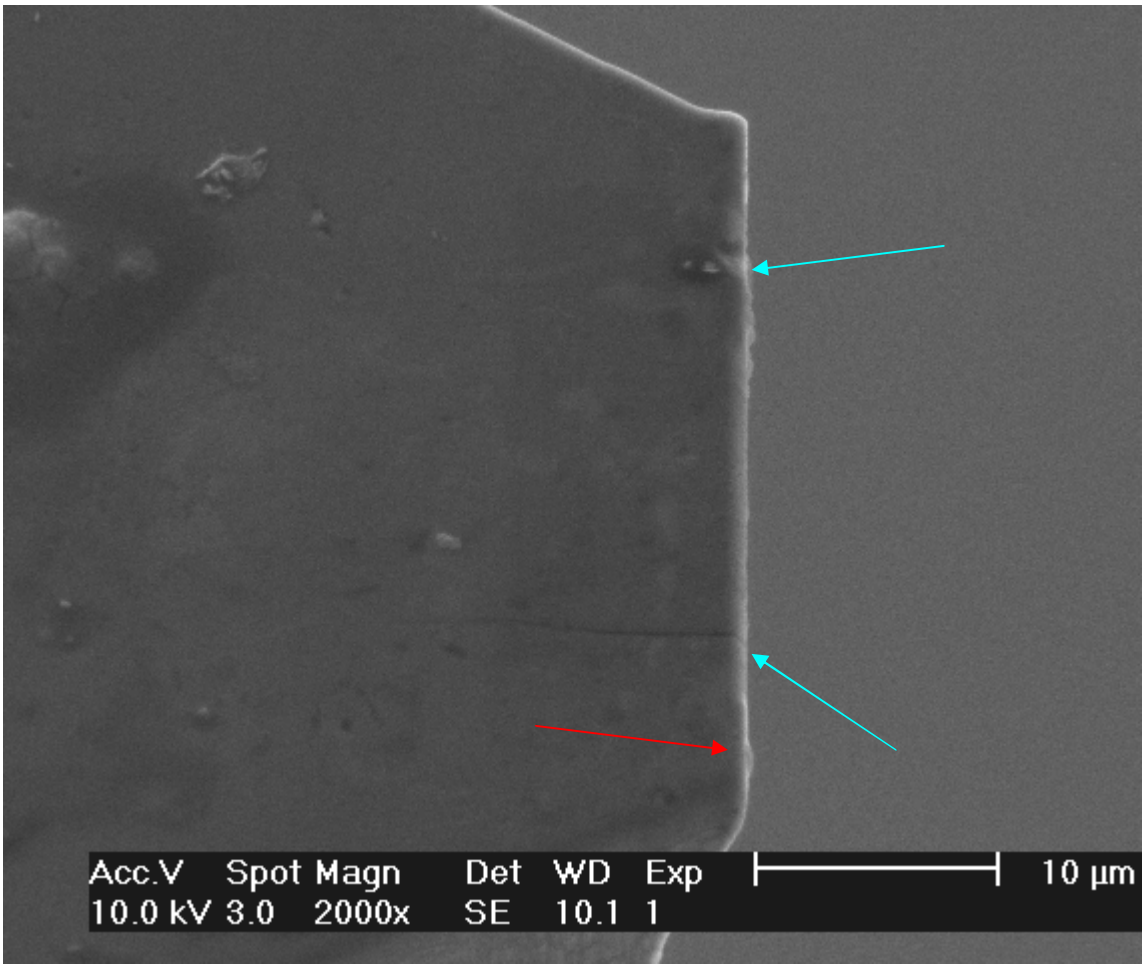

Figure 5.92 – SEM image of S83011 cutting edge defects

The 40nm increase in depth on the right hand side of the scan is due to the tool edge at the bottom (red arrow figure 5.92) being not quite flush with the rest of the edge. There is a slightly protruding section that caused a deeper section of trench to be cut.

The scan along the length of the trench in figure 5.93 shows the effect of the tool chatter. This is the normal variance in nominal depth caused by the tool vibrating as it moves through the work piece. The areal surface roughness of the whole trench floor in figure 5.90 is 37nm Sq as calculated by the AFM software. If the two ridges are ignored and the area between 10 and 25µm on the profile in figure 5.91 is analysed then the Sq is 28nm.

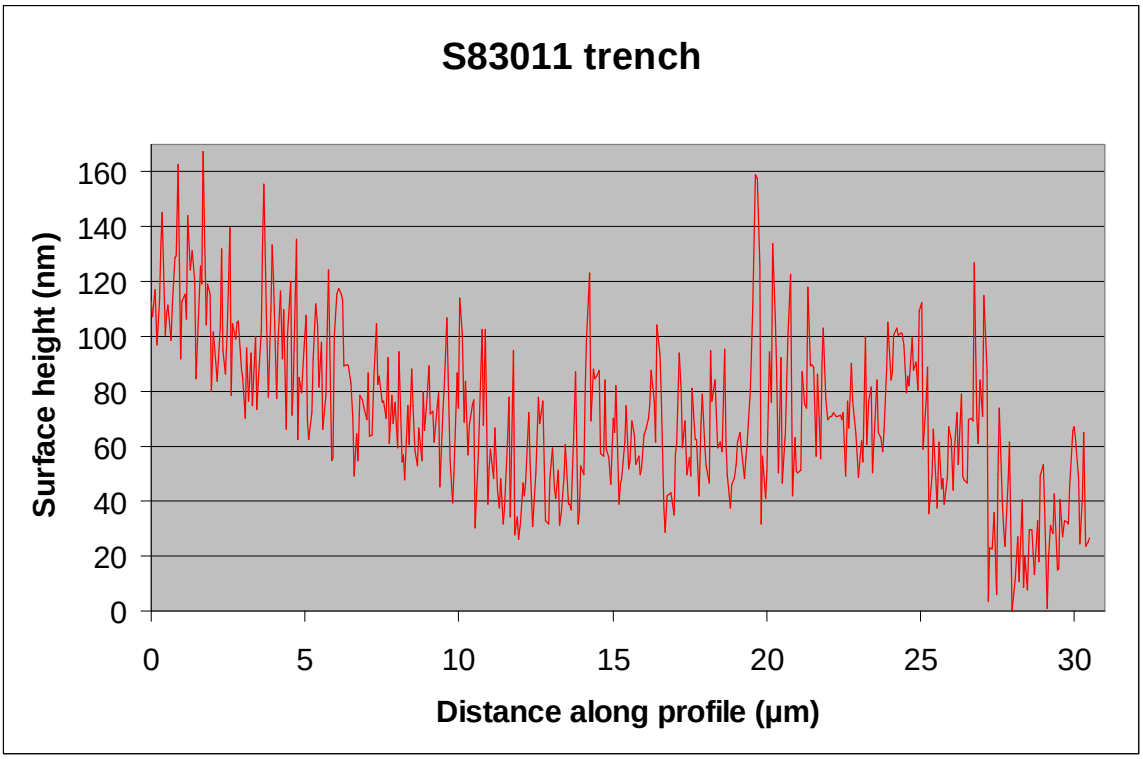

Figure 5.93 – 2D AFM scan along 5µm deep trench

The 5, 10 and 20µm deep trenches were also measured with the Wyko Topo 3D (section 4.2.4). The roughness across and along the trench floor was measured and the Sq, Sa and the P-V obtained. The mean average of the roughnesses for all three depths are shown in table 5.4.

Measurement direction	Sa (nm)	Sq (nm)	P-V (nm)
Across trench	33.4	40.9	153
Along trench	14.2	17.0	68.8

Table 5.4 – Wyko Topo 3D measurement of trenches produced with S83011

The 37nm Sq for the trench floor, measured by the AFM, is comparable to the Sq of 40.9nm from the Wyko Topo. The peak to valley height of 153nm is also comparable to the maximum height of the AFM scan in figure 5.88. The height of the taller ridge in figure 5.90 varies from 100-150nm, the cross sectional profile in

figure 5.89 crosses the ridge below its maximum height. The variance in ridge height is due to the tool chatter.

5.3.4 - Tool testing: tool S83012

The tool, after testing, is shown in figures 5.94 and 5.95. It was found that the edge remained intact following the machining process despite the large amount of copper debris attached to the tool. SEM images of the trenches are shown in figures 5.96 and 5.97. The width of the tool edge is shown in figure 5.97 as a red line on the trench bottom. The trench bottom is very uneven, as shown by the AFM 3D profile in figure 5.98, and the 2D profile in figure 5.99.

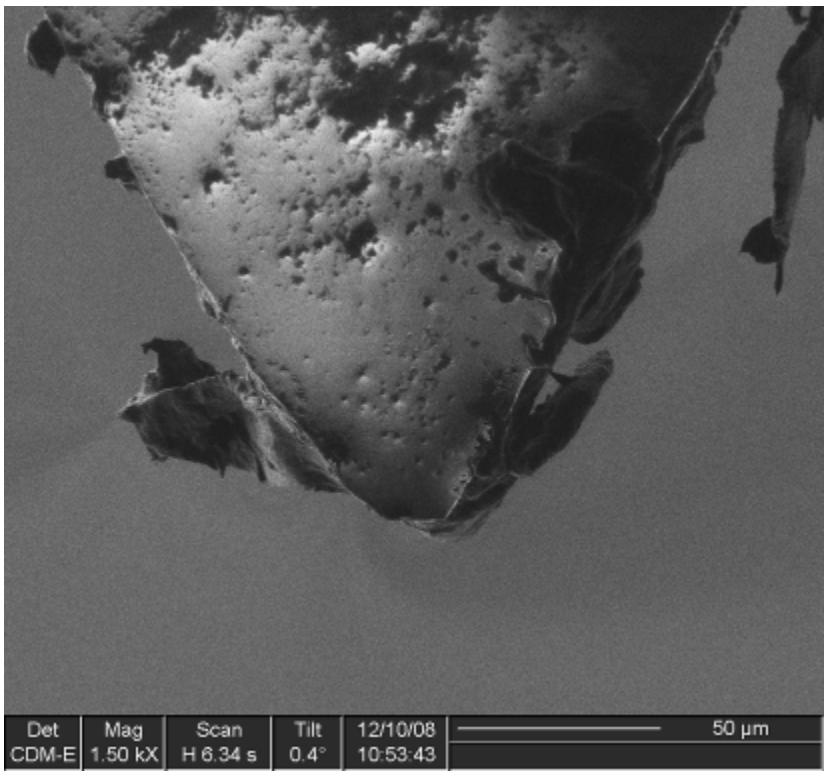

Figure 5.94 – FIB image of tool S83012 after testing

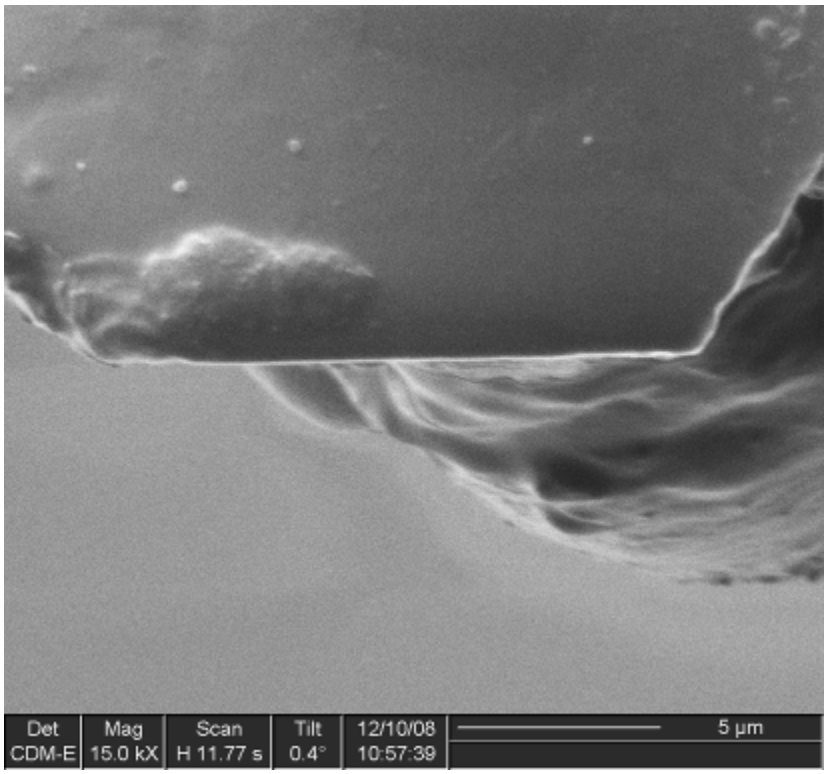

Figure 5.95 - FIB image of S83012 tool edge after testing

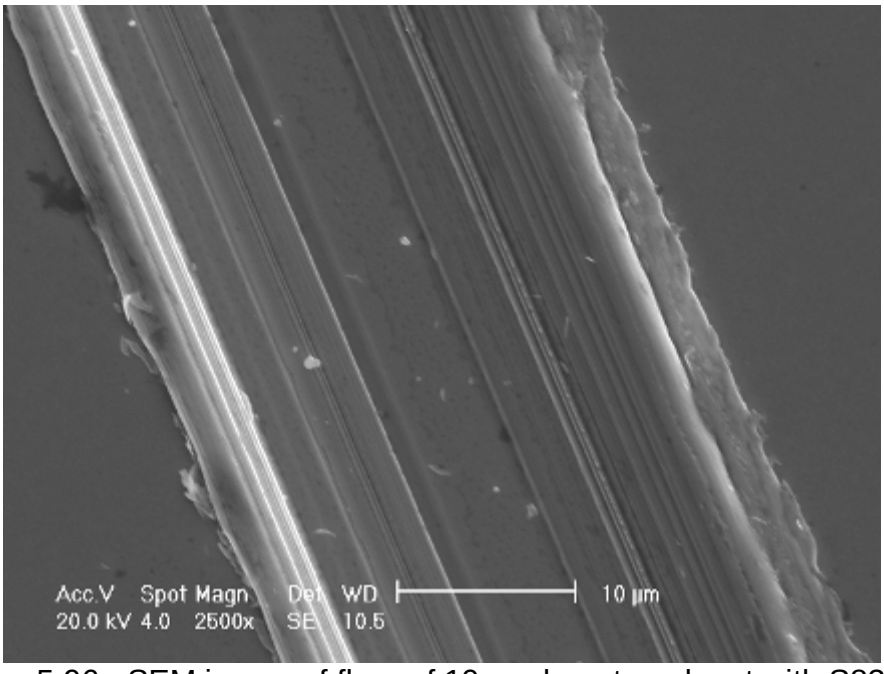

Figure 5.96 - SEM image of floor of 10µm deep trench cut with S83012. Direction of cut top to bottom.

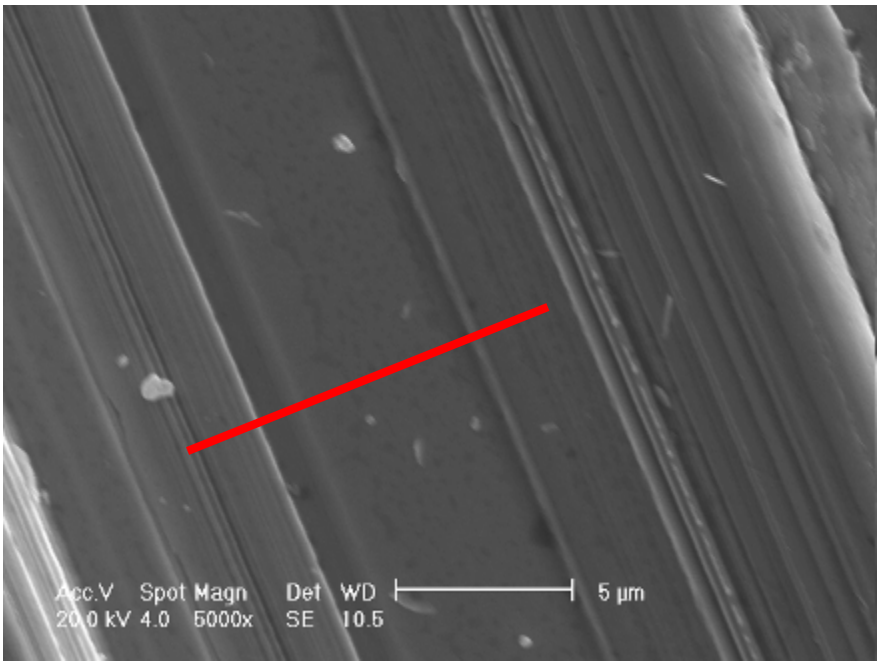

Figure 5.97 - SEM image of enlarged view of trench cut with S83102.
Direction of cut top to bottom

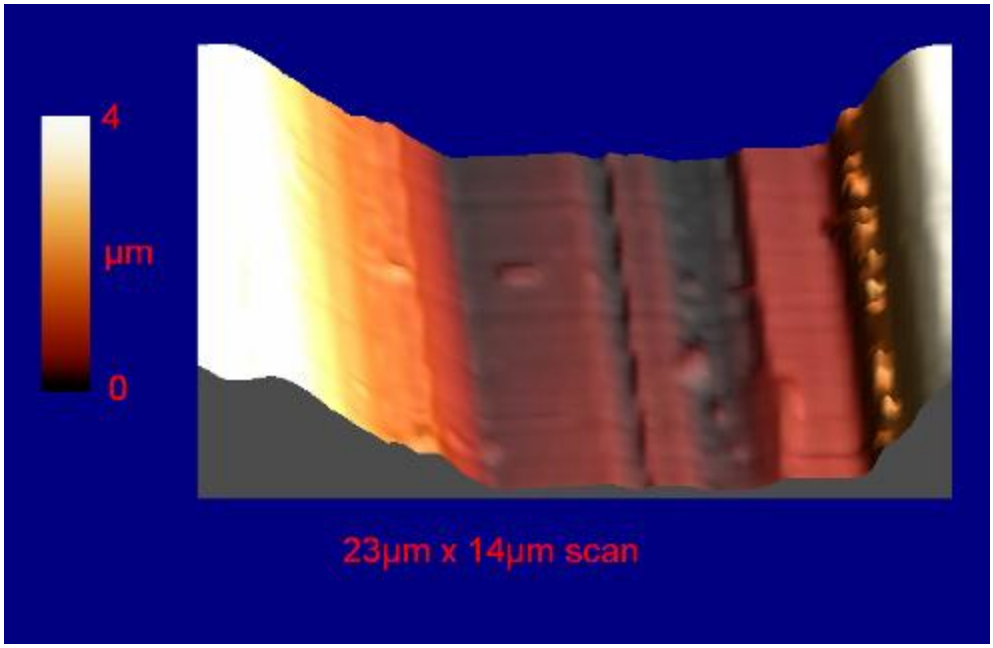

Figure 5.98 - 3D AFM scan of trench cut with S83102.
Direction of cut top to bottom.

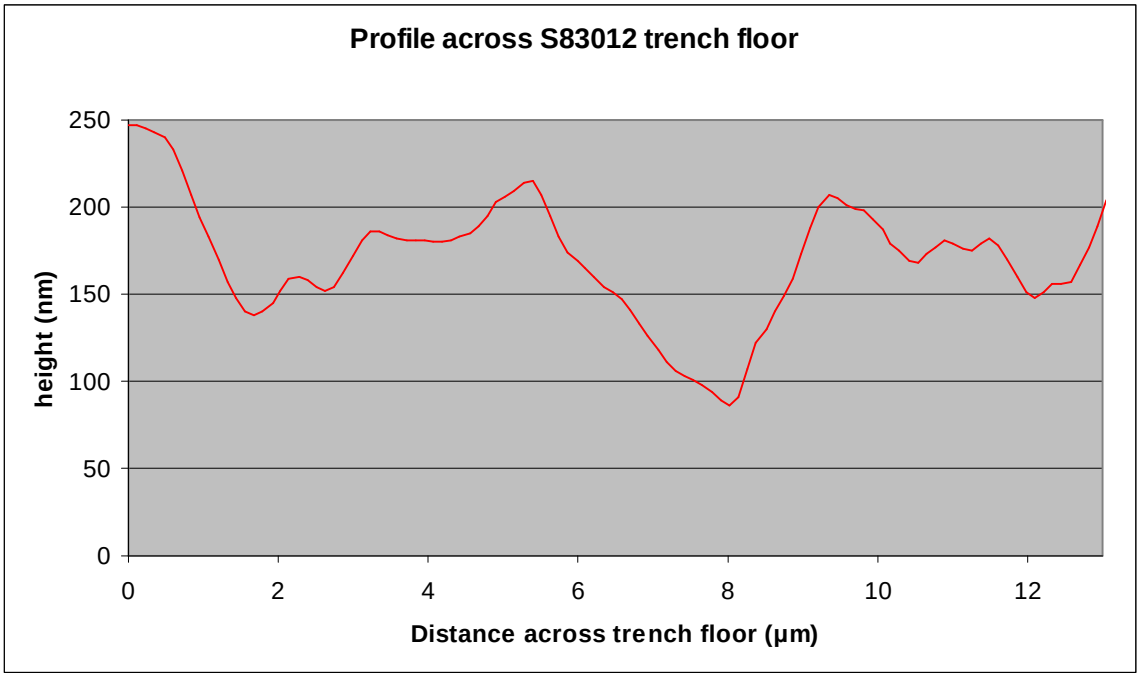

Figure 5.99 – 2D AFM scan of trench cut with S83012

The Sq of the whole floor was 125nm, mainly due to the two gouges running along it. The roughness of the flatter areas to the left and right of the gouges is 36nm Sq. The gouges were probably caused by not getting enough clearance on the tool front face. There was no diamond protruding in front of the tool edge but the clearance angle may not have been large enough to ensure that copper that stuck to the front face during machining would not drag across the surface behind the tool edge. Copper sticking to the face in the last few seconds of machining could cause damage to the trench floor as the deeper of the two gouges is only 100nm deep. A gouge of this depth can be produced in less than 1 second of machining even with the low depth of cut per revolution that was used in these tests.

5.3.5 - Commercial PCD tool test

A commercial PCD tool was tested under the same conditions as the FIB created tools. The tool was a ground, round nose tool with a tip radius of 350µm (figures 5.100 and 5.101).

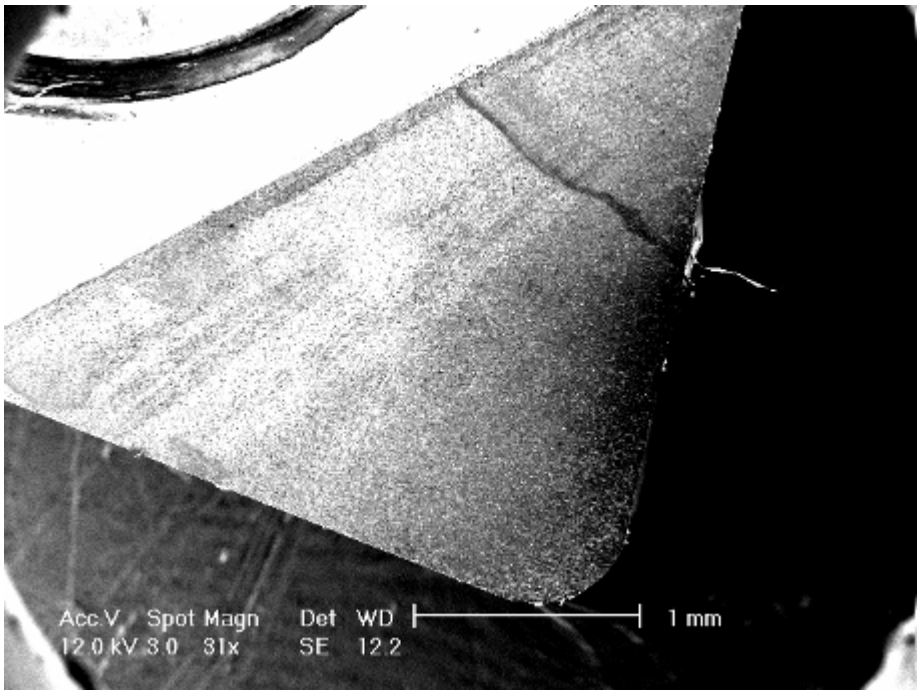

Figure 5.100 – SEM image of commercial PCD tool

The polycrystalline nature of the tool is apparent in figure 5.102 where it is possible to identify the separate grains. This is a typical PCD turning tool although of a much larger radius than tools S83011 and S83012. The large radius of the tool means that the contact area on the work piece is nearly flat and can be measured for roughness using the AFM.

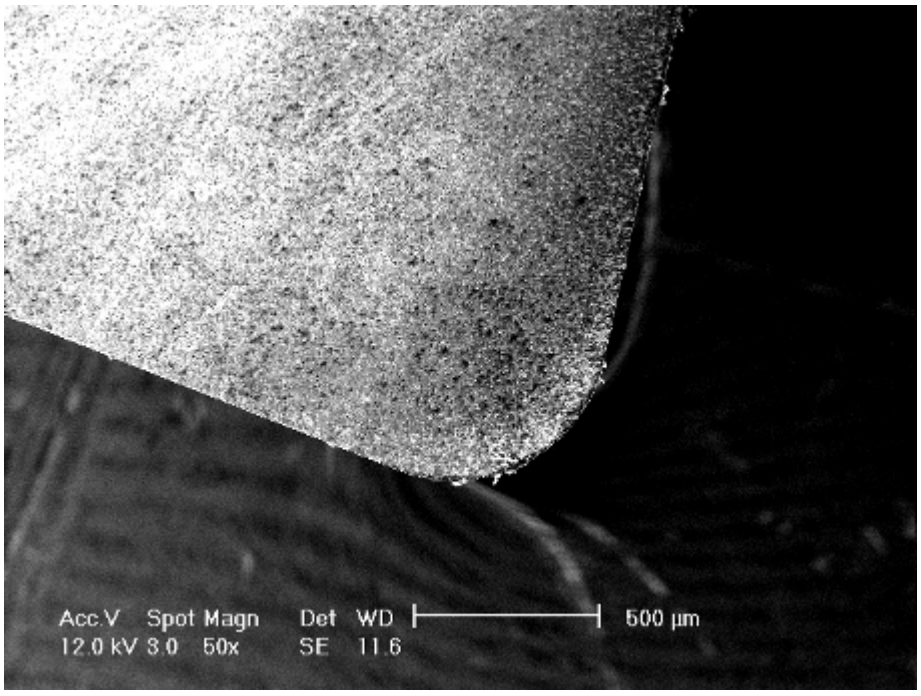

Figure 5.101 – Higher magnification SEM image of commercial PCD tool

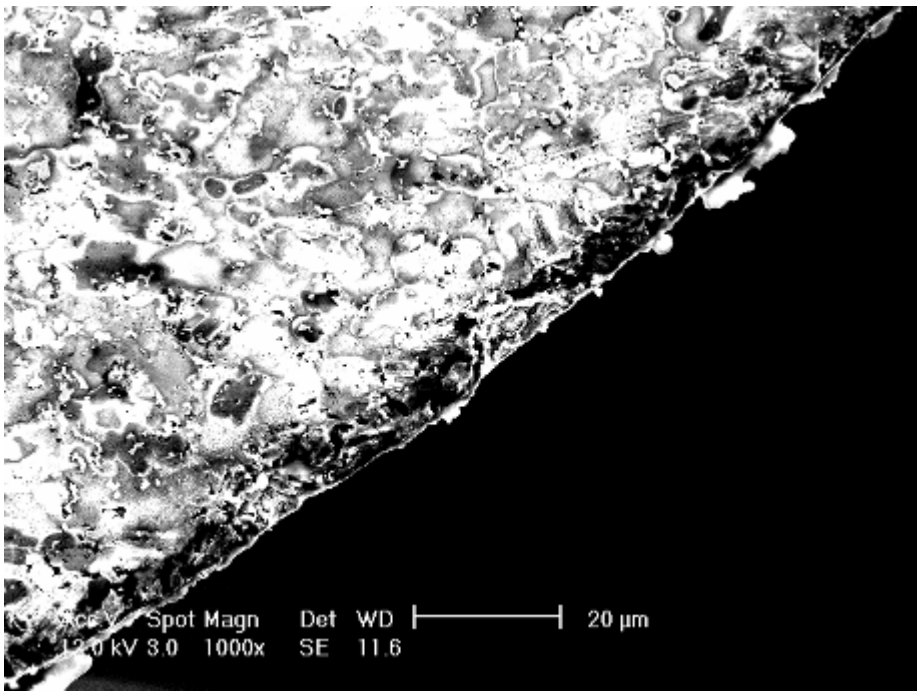

Figure 5.102 – SEM image of commercial PCD tool edge

Trenches were cut in OFHCC using the commercial tool, figure 5.103. The 3D trench profile is shown in figure 5.104. The middle third of the trench (on the long scan axis) is the flattest area as the profile of this area shows in figure 5.105.

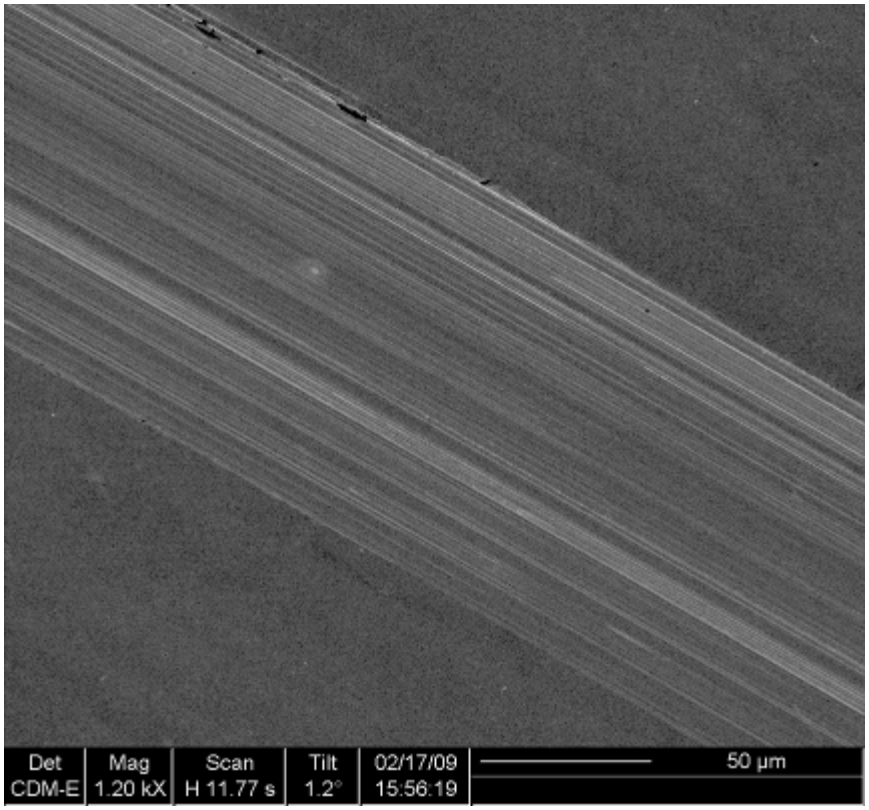

Figure 5.103 – SEM image of trench cut with the commercial PCD tool

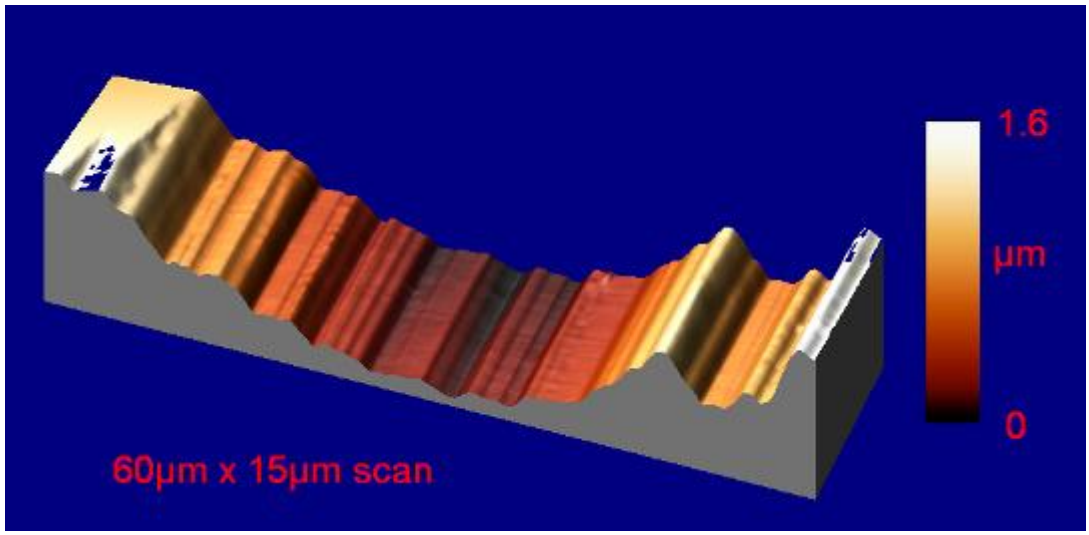

Figure 5.104 – 3D AFM scan of trench cut with commercial PCD tool

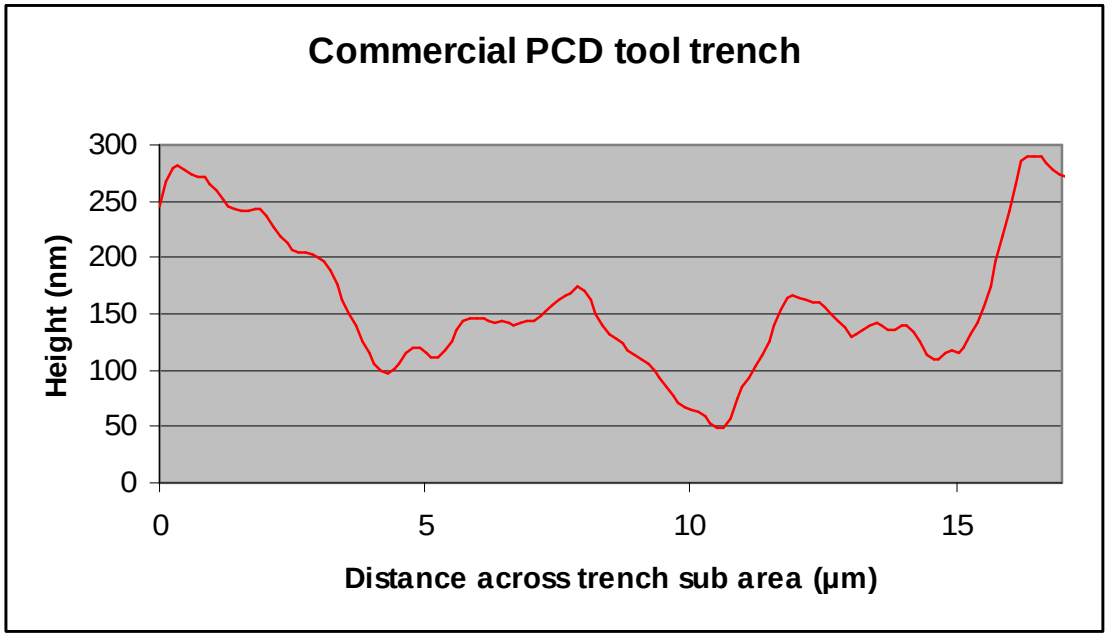

Figure 5.105 - 2D AFM scan of trench cut with the commercial PCD tool

The surface roughness of the trench area in figure 5.105 is 69nm Sq.

5.3.6 – Machined roughnesses and comparisons to the literature

The roughnesses determined with the AFM for the trenches produced with the different tools are summarised in table 5.5.

Tool trench	Sq roughness (nm)
S83011 – whole trench floor	37
S83011 - avoiding ridges	28
S83012 – whole trench floor	125
S83012 – avoiding gouges	36
Commercial – middle third of trench	69

Table 5.5 – AFM measured trench roughnesses

The Sq values of 37nm (AFM) and 41nm (Wyko Topo) for S83011 and 36nm (AFM) for S83012 compare well with the Sq of 69nm for the commercial tool. The improved finish is probably due to the FIB producing an amorphous layer on the

cutting edge which covers the binder free polycrystalline structure. This layer gives a superior edge finish compared to a polycrystalline structure with a binder, which cannot be ground to the same edge finish. As the amorphous edge material is worn away during machining, the polycrystalline CVD structure comes into contact with the work piece. The polycrystalline CVD structure retains its edge better than the polycrystalline binder structure can because of the reduced number of weak points in the structure. These weak points are where chips in the cutting edge are most likely to form.

The roughness of the S83011 trench was lower than figures reported in the literature for other PCD machined surfaces. The roughness results from the literature for PCD machined OFHCC and other metals are discussed below. Metals other than OFHCC are discussed because of the poor availability of information on PCD machining of OFHCC. Single crystal machining roughnesses of OFHCC are also discussed for comparison.

(Morehead 2007) machined a variety of OFHCC that had an ultra fine grain size of 100-200nm with PCD tooling and compared the surface roughness to PCD machined normal OFHCC. The ultra fine grain copper had a Ra of 1.38μm and the normal OFHCC 2.9μm Ra. The roughness values were measured with a white light interferometer. These roughnesses seem to be on the high side, which may be due to the depth of cut per machining pass of 50μm compared to 10nm for the FIB tool tests. (Zhang 1994) achieved a Ra of 6nm on OFHCC with single crystal diamond tooling. (Miyamoto 1990) turned aluminium with ground single crystal tools that had been sharpened by ion beaming. The best surface finish attained was an R_{max} of 30nm. The disparity between the 28nm Sq and 6nm Ra shows there will always be a gap between the best achievable surfaces with the two tool materials. It is a question of whether the extra surface quality of a single crystal tool is actually needed.

The work of (Ding 2008, 2009) is of great interest in relation to the work described in this thesis. Ding has produced single crystal diamond micro tools using FIB and then tested them on multiple metals including OFHCC. The testing was carried using a Moore Nanotech 350 ultra-precision Freeform Generator, a very similar machine to the one used at Cranfield. The diamonds used in their studies of how diamond behaves when FIB machined (Ding 2008) were also bought from Contour Fine Tooling. They are the same as was used for the work described in section 5.1 but cut on the (110) plane not the (100). The Ra surface finish on the machined OFHCC measured with a white light interferometer was 20nm. This is equivalent to ~25nm Rq, only 3nm lower than the best result in table 5.5. This demonstrates that the surface achievable using FIB produced tools is genuinely of good quality and compares favourably with equivalent work in the field. The depth of cut for the OFHCC was 800nm over a length of 1mm with a cutting speed of 1mm per minute. This was 80 times greater than the 10nm per revolution that was used during the Cranfield tool tests. However, the Cranfield cutting speed was 113,000 -173,000 times faster. Ding's cutting forces during machining were measured and, for OFHCC they peaked at 0.04N. The forces did not register during the Cranfield tests, the dynamometer used having a claimed minimum threshold of 0.01N. However, it can measure a maximum force of 500N so it was working at its absolute lower limit of detection during the trials. The other metals machined were Aluminium 6061, RSA095 and nickel phosphorus, the Ra finishes were 28, 58 and 27nm respectively. RSA095 is an aluminium alloy with a maximum grain size of 4μm.

Some results from the literature for other metals machined with PCD are now discussed. (Reis 2005) machined aluminium 6351 at different combinations of feed rates, depth of cuts and cutting speeds. The best surface finish achieved was 0.9μm Ra. (Ezugwua 2007) machined titanium alloy to a finish of 0.5μm Ra. (Luo 2005) used a specially designed PCD tool for burnishing H62 brass and LY12 aluminium alloy. The tool surface had a Ra of 51nm. The best metal surface finish

achieved was 80nm Ra from an initial surface Ra of 0.6µm. This is the closest PCD literature value to the results for S83011 and S83012. However burnishing is a non chipping finishing process compared to the chip producing turning process. The elastic-plastic deformation process is inherently less likely to produce surface damage than a chipping process. (Tso 2002) produced PCD tools by EDM and grinding, the Ra of the tools cutting surface was 270nm for EDM manufacturing and 108nm for grinding. These values are inferior to those obtainable by FIB.

The best Sq value of 28nm achieved during this work can be improved upon. A tool with sufficient clearance, as for S83011, combined with a higher quality edge would give a tool capable of ~20nm Sq. This would be equivalent to a Sa of ~16nm. The edge improvement would come from ensuring that the edge is a continuous straight line without any protrusions or defects. Also, inverting the tool when machining the edge would make the edge sharper. Keeping the cutting edge exactly parallel to the body of the tool and ensuring that the sides leading back from the edge are symmetrical would also help. S83012 had its edge slightly off parallel by ~1^{o} and had non symmetrical sides which are obvious in figure 5.96.

The ability to produce a surface finish of this level could remove the need for using single crystal tools for making surfaces that do not need to be extremely high quality. The ability to machine metal to a finish of less than 30nm Sq with a cheaper, harder wearing, tool is desirable for reducing the cost of machining.

5.4 - Sinusoidal tools

The Precision Engineering group at Cranfield was asked by the target fabrication group at the Rutherford Appleton Laboratory to produce some sinusoidal shaped grooves in OFHCC. The grooves were to have an RMS roughness of 25nm. These were to be used as a mandrel for reproducing the grooves by coating the mandrel with gold or plastic to produce a thin sinusoidal laser target (Spindloe 2008). The grooves were produced using a single crystal diamond tool with no nominal radius,

i.e. a sharp point. The maximum tool tip radius for the grooves had been calculated as 228nm, hence using a tool as sharp as was possible to make (Durazo 2008). A side on view of the desired profile is shown in figure 5.106.

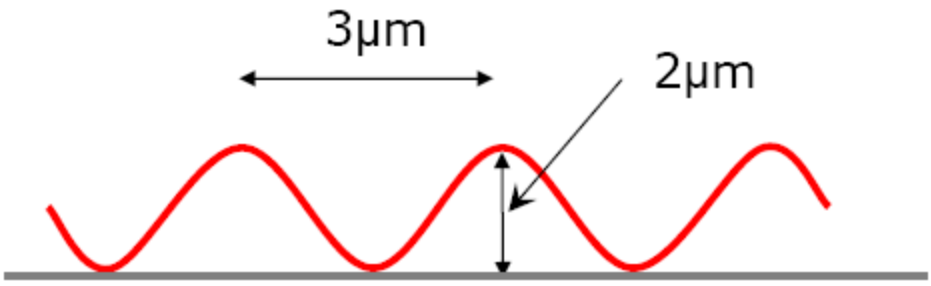

Figure 5.106 – Desired sinusoidal profile (after Durazo 2008)

An AFM scan of the machined grooves is shown in figure 5.107.

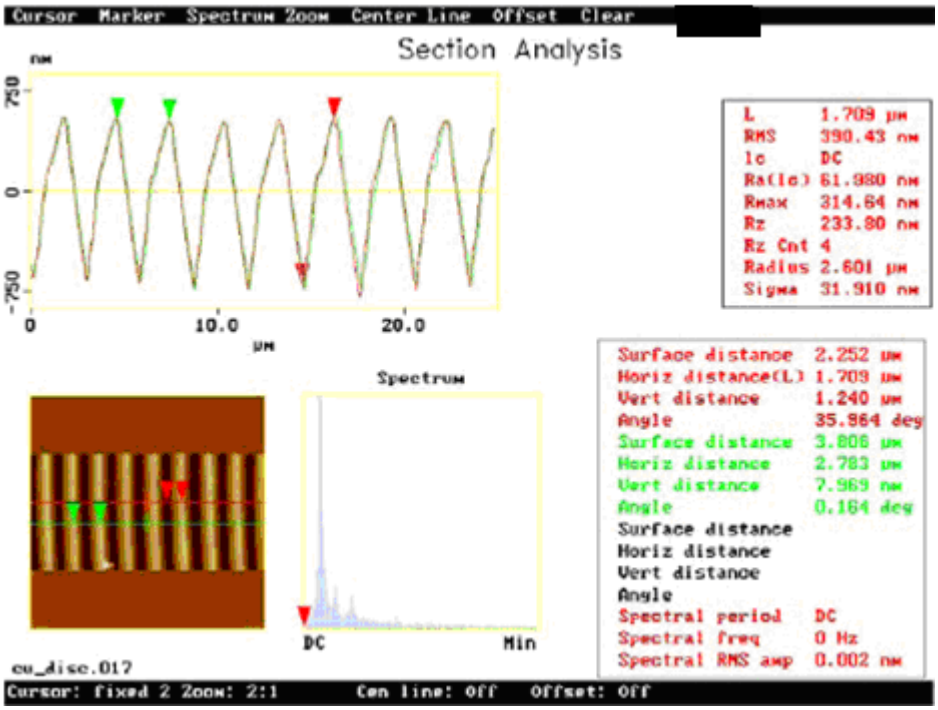

Figure 5.107 – AFM scan of conventional tool machined grooves (after Durazo, 2008)

When the grooves were replicated, the plastic and gold target profiles where not sinusoidal, figures 5.108 and 5.109.

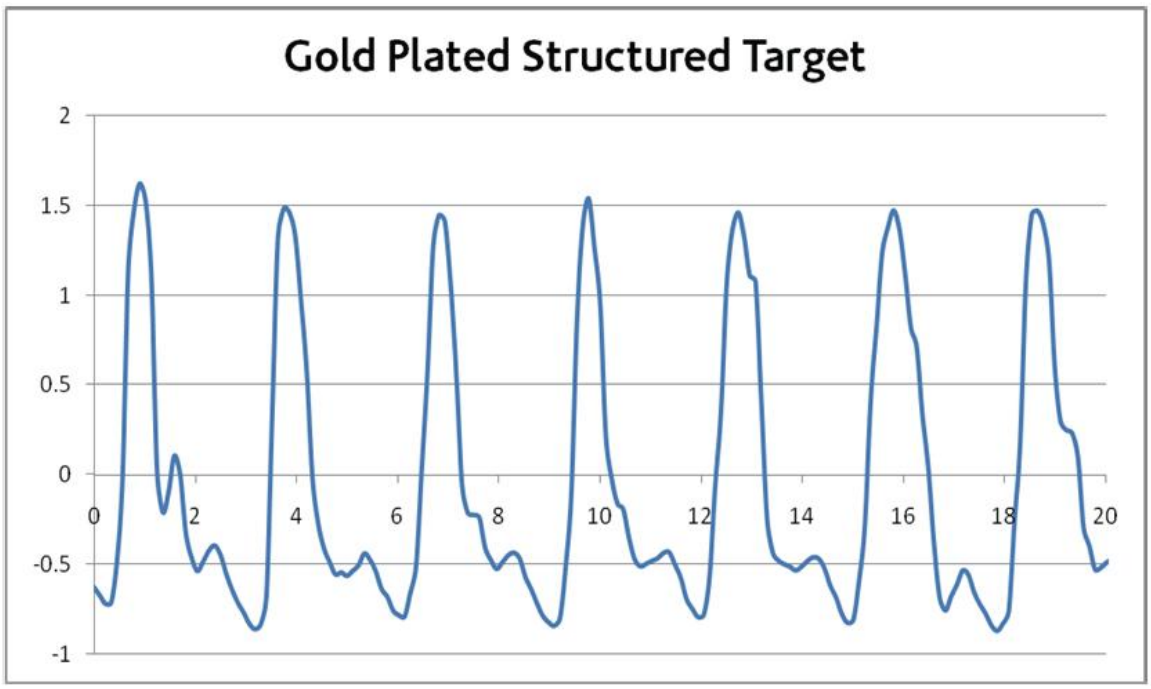

Figure 5.108 – Gold replicated target profile (after Durazo, 2008)

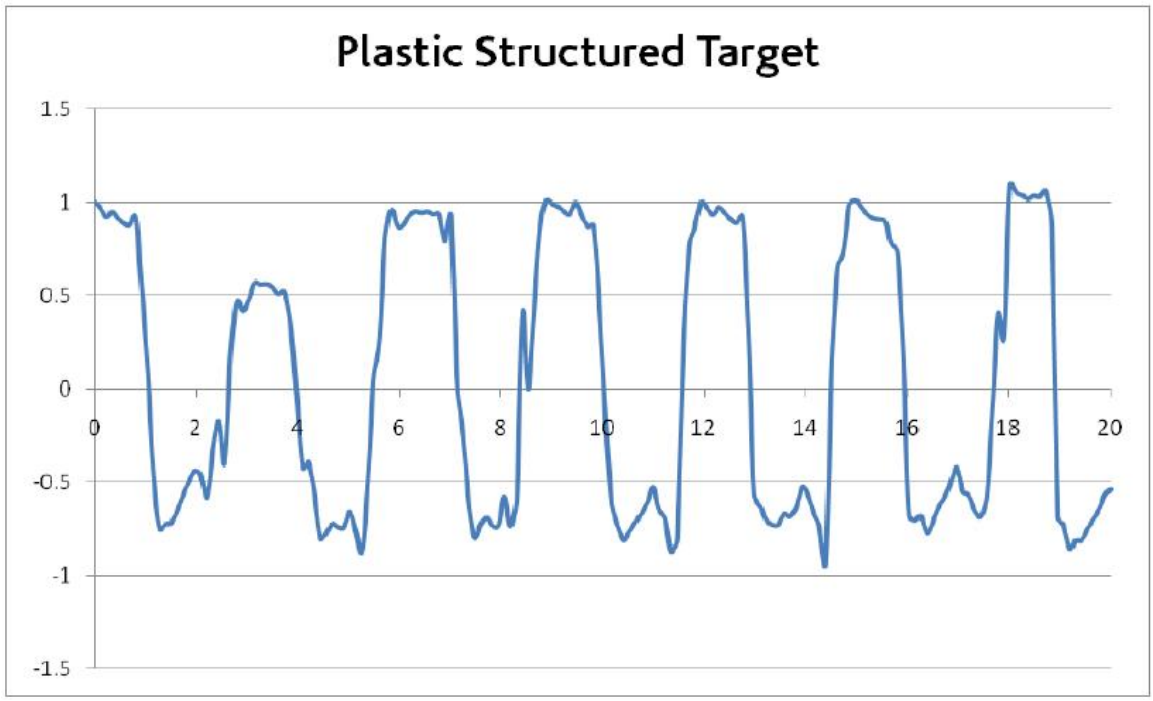

Figure 5.109 – Plastic replicated target profile (after Durazo, 2008)

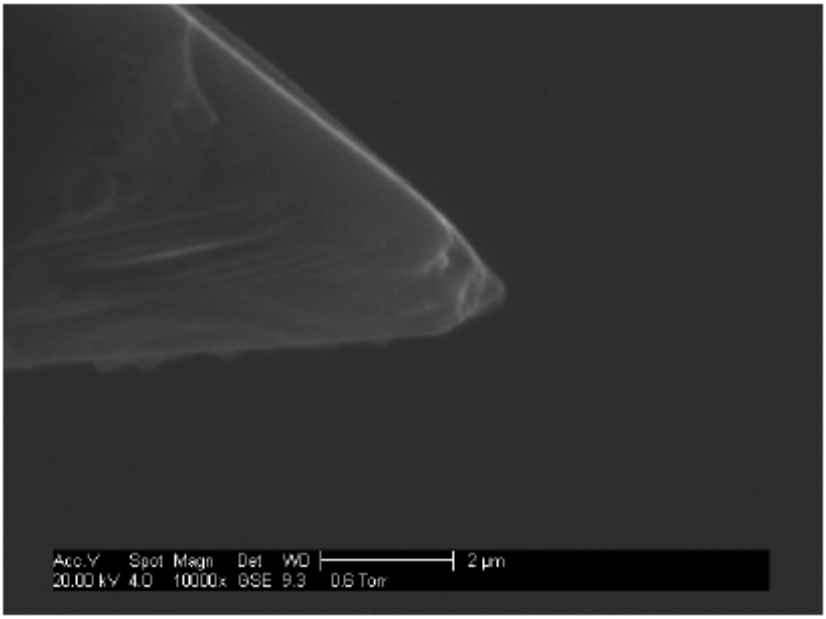

Figure 5.110 – Sharp tool after machining (after Durazo, 2008)

The tool, after machining the grooves, is shown in figure 5.110, it had been badly chipped and worn leading to a poor surface finish on the OFHCC. The sharpness of the tool makes it more likely to chip as the cutting forces are concentrated through the small volume at the tip. It was decided to try FIB machining a diamond tool with a sinusoidal profile as the cutting tip.

5.4.1 – Sinusoidal pattern

A sinusoidal pattern was generated using the Raith software on the FIB. The software has a curve generating function allowing a sine wave of the required dimensions to be incorporated into a milling pattern. Due to a software problem however the pattern would not mill completely, instead producing a series of rectangles. The components that the software breaks the pattern into were not all being milled. Enquiries to Raith's technical help failed to fix the problem so a CAD model of a sine wave was produced and this was imported into the software and modified to give the milling shape in figure 5.111. The test patterns were milled into a flat piece of single crystal diamond.

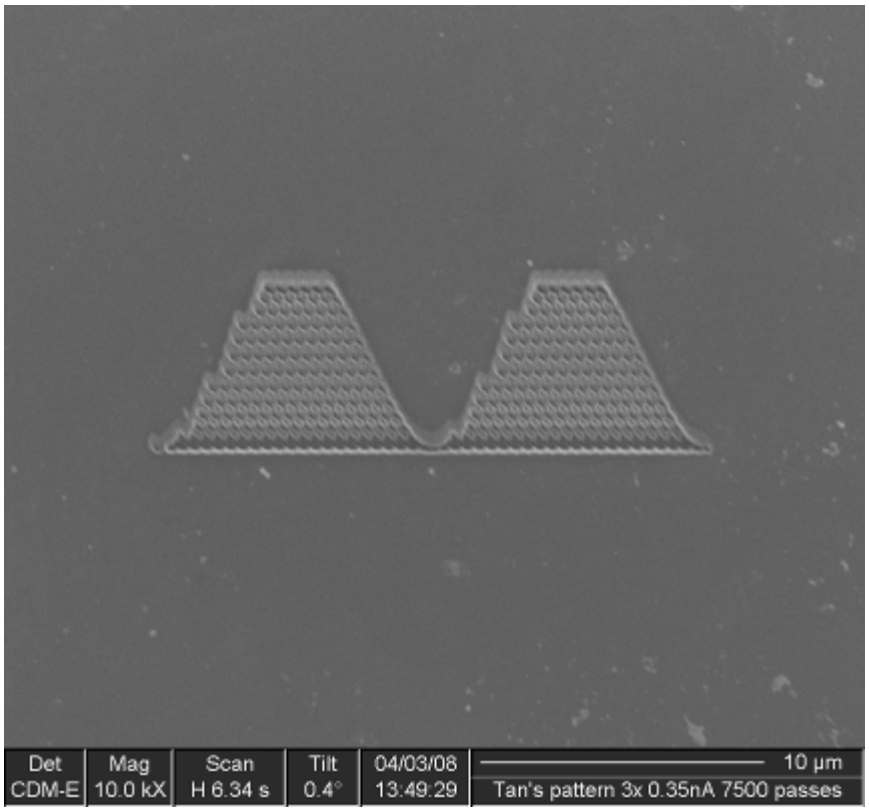

Figure 5.111 – FIB image of CAD sinusoid model, 350nm step size

The rough nature of the curved lines in figure 5.111, and the pitted appearance of the inside of the pattern, was due to the large step size parameter that the software had applied automatically. Having discrete beam positioning steps of 350nm leads to the milling of pits instead of a smooth uniformly milled area. 350nm is larger than the beam spot size for all but the largest beam current on the FEI 200. The effect of reducing the step size to 200nm and then 100nm is shown in figures 5.112 and 5.113. The smooth sine curve was achieved and the inside of the pattern was free of pits and lines. The pattern mill quality improved as the step size was decreased further, down to the minimum step size of 10nm. This step size was used for the actual tool creation pattern shown in figure 5.114. The two diamond prongs starting to appear in figure 5.114 have clean smooth edges. The small step size and a spot size of ~100nm gave an even milling coverage of the surface.

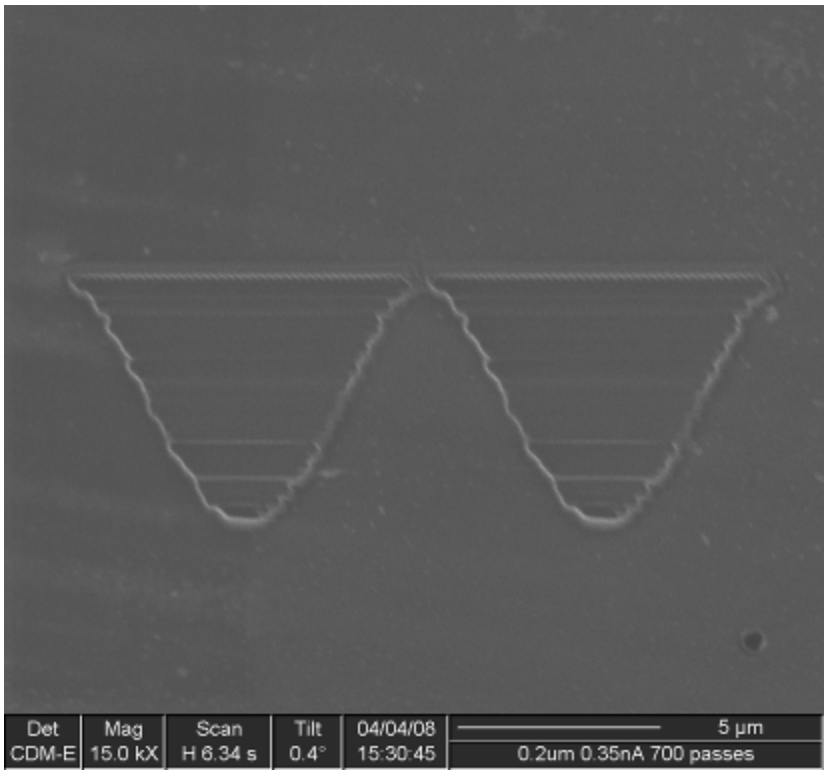

Figure 5.112 – FIB image of CAD sinusoid model, 200nm step size

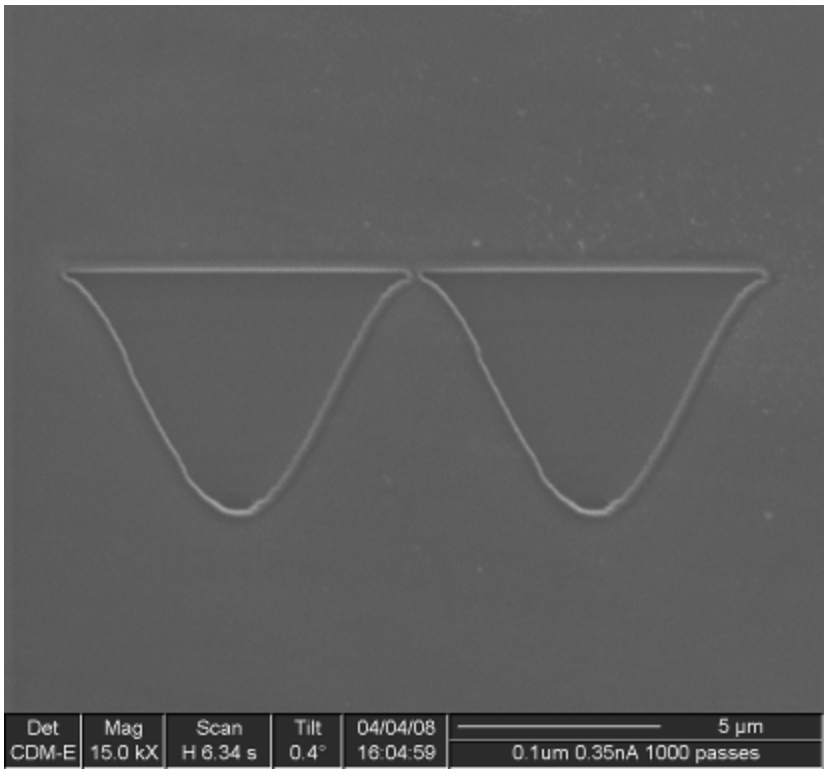

Figure 5.113 – FIB image of CAD sinusoid model, 100nm step size

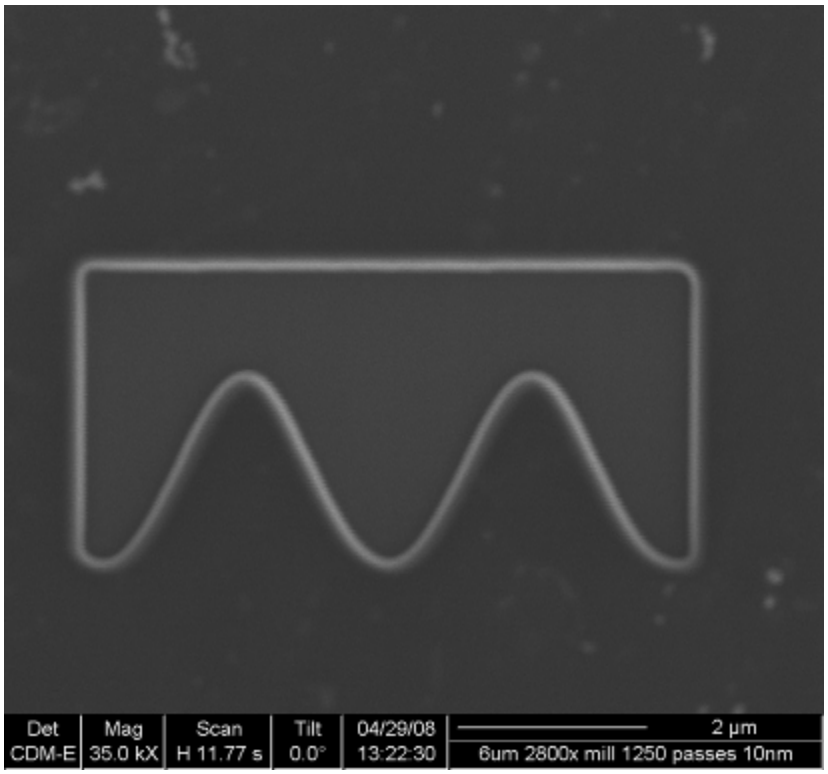

Figure 5.114 - FIB image of CAD sinusoid model, 10nm step size

5.4.2 – First Sinusoidal tool: S87355

Tool blank number S87355 was used for the first sinusoidal tool, this is a round nosed laser cut CVD PCD as used for the turning tools. The pattern in figure 5.114 was scaled up by a factor of three and positioned over the tip. The pattern was scaled up from the requested sine groove size for the first tool to give a greater margin of error when machining. A small error of less than a micron in size is less damaging to the overall tool shape for a larger tool pattern. Repeated milling produced figures 5.115 and 5.116. Chopping back of the sides gave figure 5.117.

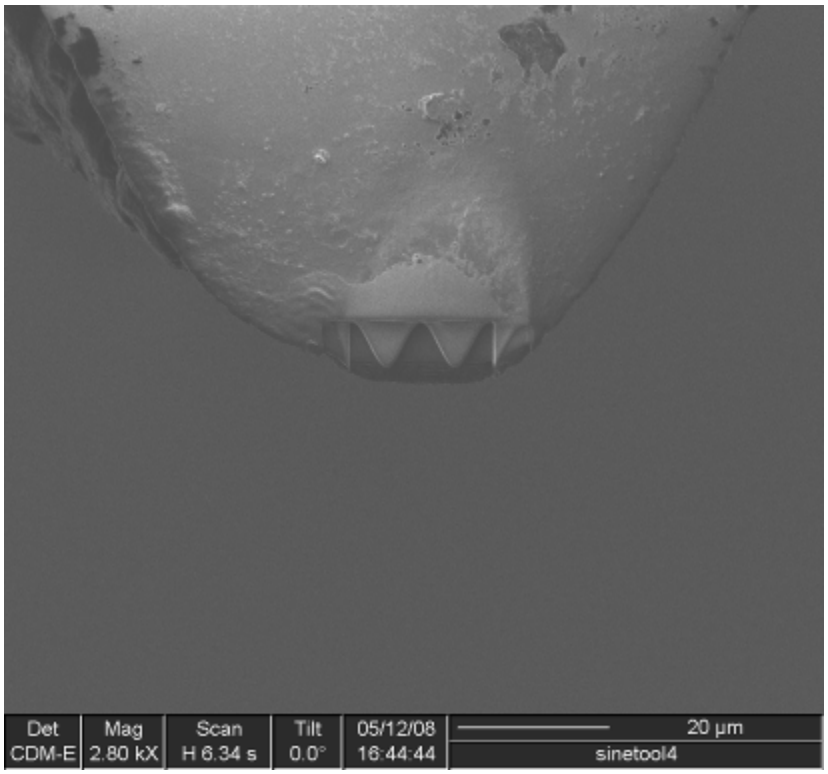

Figure 5.115 – FIB image of the beginning of tool S87355

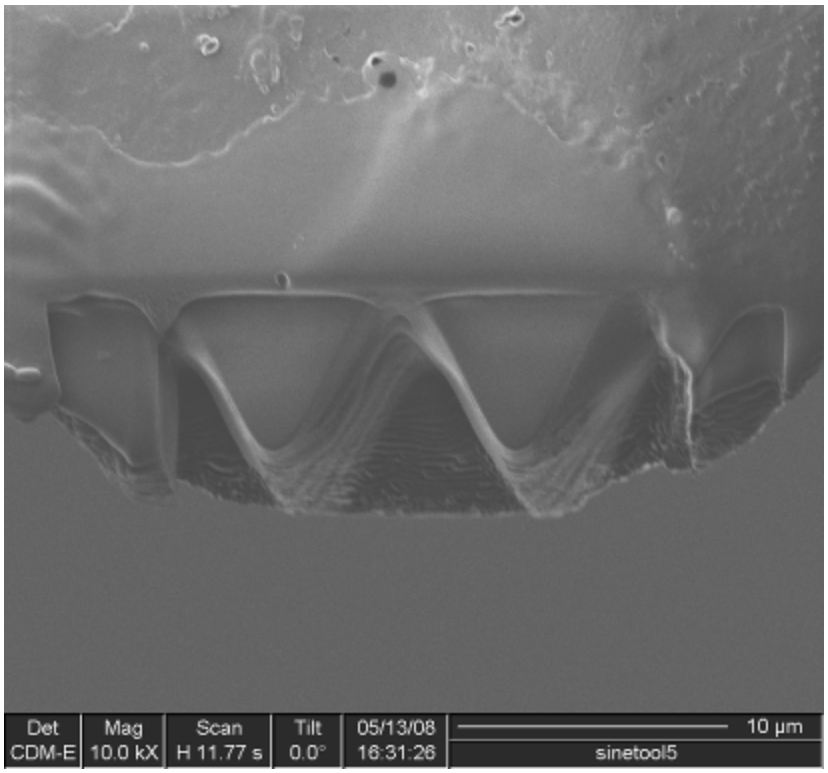

Figure 5.116 – FIB image of S87355 in progress

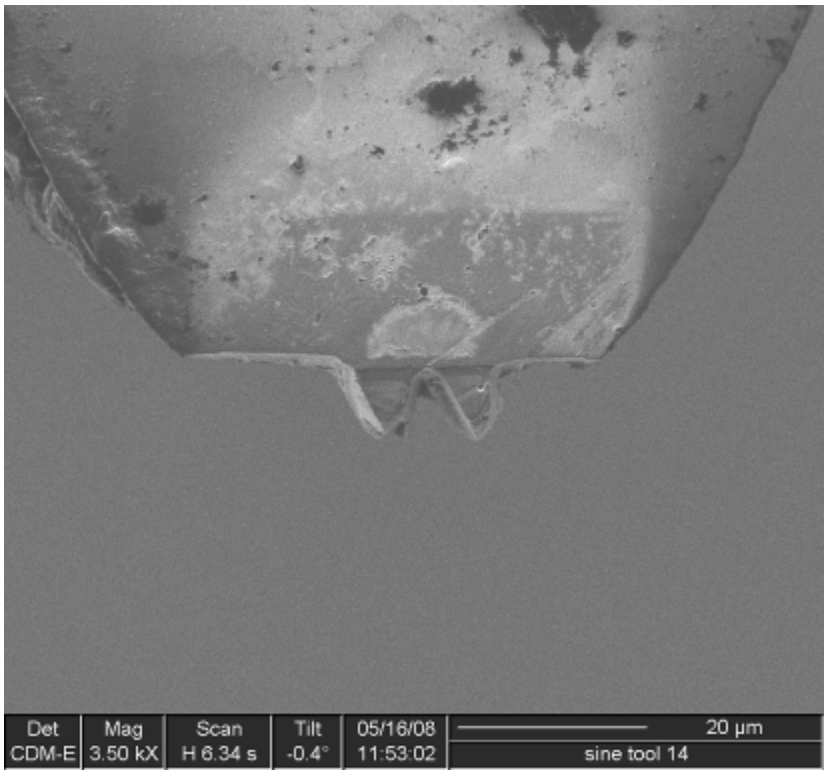

Figure 5.117 – FIB image of tool S87355 progressed further

Several problems arose after prolonged milling: the need to repeatedly place the pattern accurately and the effect of the unwanted face angle.

The Raith software works by breaking the pattern into a number of elements, the larger the pattern the more elements. The number of times the pattern is to be repeated is then selected, 'the loop count'. This decides the depth to be milled. This is instead of selecting the depth to be milled and an appropriate material file as for the FEI software. The number of elements that can be stored in the programme cache is limited to 100,000. This limits the number of loops that can be milled in each run. After each run the tool tip is reimaged via the Raith software and the image of the tool tip can appear in a slightly different place due to charging up. The drift of the image is less than a micron but when producing tools with dimensions of only a few microns this is important. The pattern then needs to be repositioned by changing the coordinates of the pattern centre. This can be done to

a resolution of 10nm and is generally an error free process but errors were made during the production of both sine tools. The second problem of the unwanted face angle is shown well by figure 5.118.

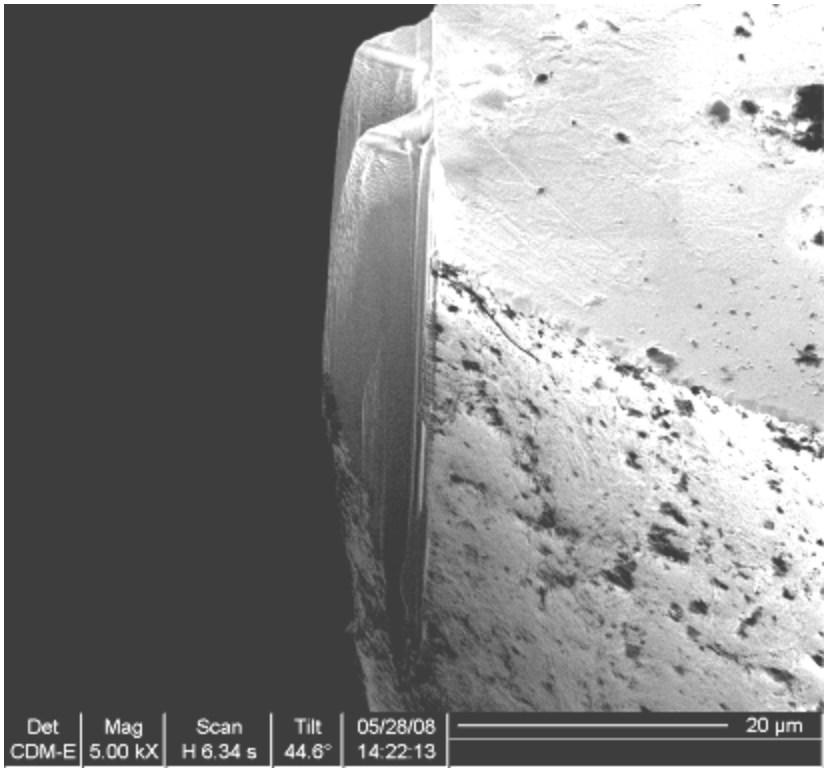

Figure 5.118 – FIB image of side view of angled diamond prongs on S87355

The size of the diamond prong increases the further down the tool face it goes until it meets the curvature of the tool front face and then curves back in again. Unless removed, the parts of the prong bodies extending beyond the top of the prong will contact the work piece during milling. The front of the prongs is angled out by ~ 5^{o} and, due to the depth of the prong, the prong body extends out by 2.8µm. The extended prong parts are also partially caused by mistakes in pattern placement where the pattern is placed further back towards the main tool body than it should be. This causes the top of each prong to be out of line with the rest of the prong.

The prong bodies were reduced in size by milling on to the front of the tool to slim them down and to clear out the channel between the two prongs. The reduced prongs are shown in figures 5.119 and 5.120. The top view of the tool in figure 5.121 is the state of the tool when it was decided to stop working on it. There were multiple problems with it, the major faults being the lack of smoothness in the sine curve and the roughness of the sides of the prongs. However, making further changes to the tool was starting to produce other problems, so as a first effort the tool was left as it was.

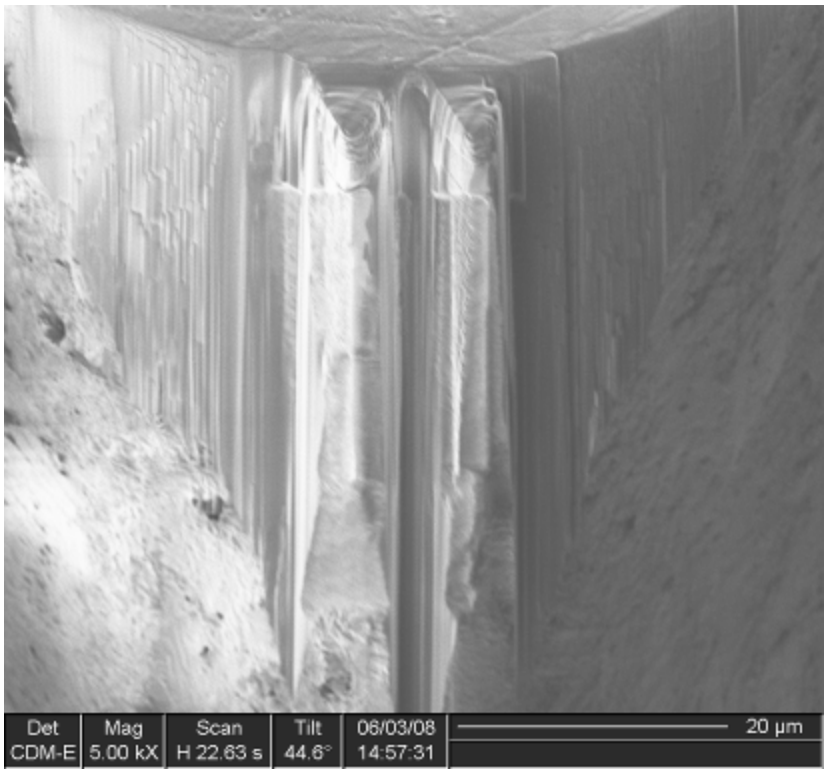

Figure 5.119 – FIB image of front view of milled back prong bodies on S87355

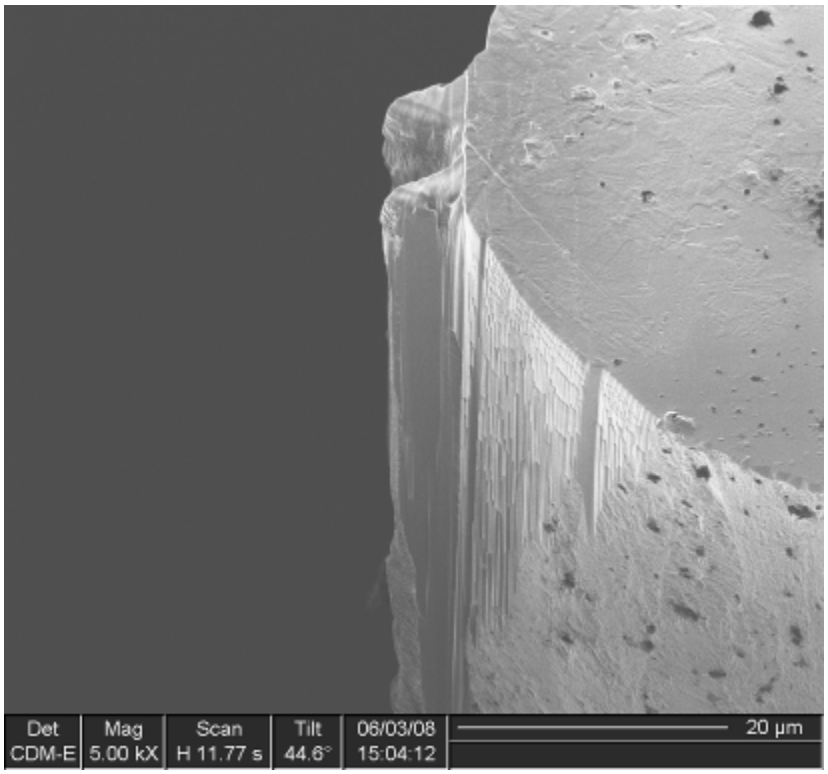

Figure 5.120 – FIB image of side view of milled back prong bodies on S87355

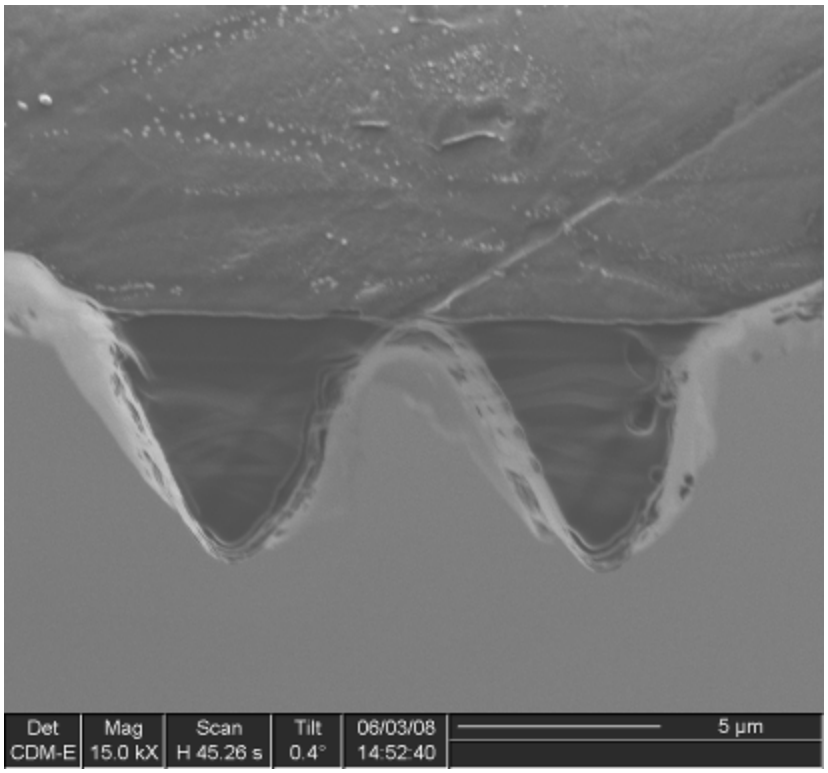

Figure 5.121 – FIB image of the finished S87355 tool

5.4.3 – Tool testing: tool S87355

The tool was tested using the same machining conditions as for the turning tools, table 4.1. A problem faced during the sinusoidal test, that didn't occur for the turning tools, was knowing when the tool had been bought into contact with the work piece. The tool was bought close to the surface of the work piece and then moved closer in small steps of a few microns at a time. A thin piece of metal foil 20μm thick was moved between the tool and the copper after each step until the foil no longer fitted between the two. The tool was then moved in steps of 100nm and the work piece rotated to see if there was a faint machining mark left on the copper signifying that the tool tip has made contact. Once a mark was visible the z axis coordinate was saved as the zero reference point for the depth of cut for the tests. This was no problem for the turning tools as they had a flat nose. However, the small size of the diamond prongs on the sinusoidal tool meant that when these were in contact, and the copper was rotated, the machining mark was very small. This was difficult to spot by eye and once a definite machining mark appears it was likely to mean that the main body of the tool had made contact.

This was discovered after the first test of S87355 carried out at the same time as the initial test of S83011. When the 5, 10 and 20μm deep trenches were cut the machining mark was made by the main tool body. The Talysurf contact probe measurement of the 10μm trench revealed a trench that was ~16μm deep, figure 5.122. The exact depth was not certain because the probe ball is 2μm in diameter and cannot measure the bottom of the trench properly. However 10μm depth of cut plus 6μm of diamond prong gives this depth. The white light interferometer is of no use in this situation as there are no flat surfaces to get a refection off.

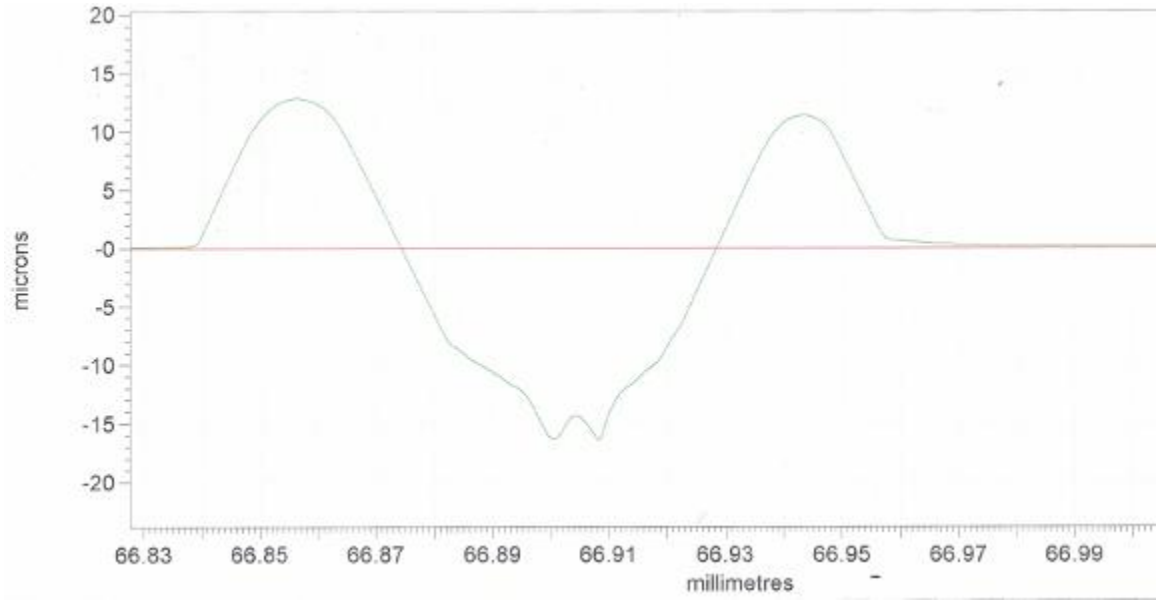

Figure 5.122 – Talysurf measurement of 10µm deep trench cut with S87355

When S87355 was retested the tool approach to the copper was carried out as before. However, when the machining mark became visible the tool was retracted by 3µm. This ensured that when a 2µm deep cut was done the resulting trench would be no more than 5µm deep and measurable by AFM.

The positive outcome of the initial test was that the tool survived intact as it had been feared that the prongs would be damaged or destroyed by machining.

S87355, after the initial test, is shown in figures 5.123 and 5.124. Apart from some machining debris stuck between the prongs and some other pieces of copper on the tool front the tool is undamaged. The trench milled on the initial test is shown in figure 5.125.

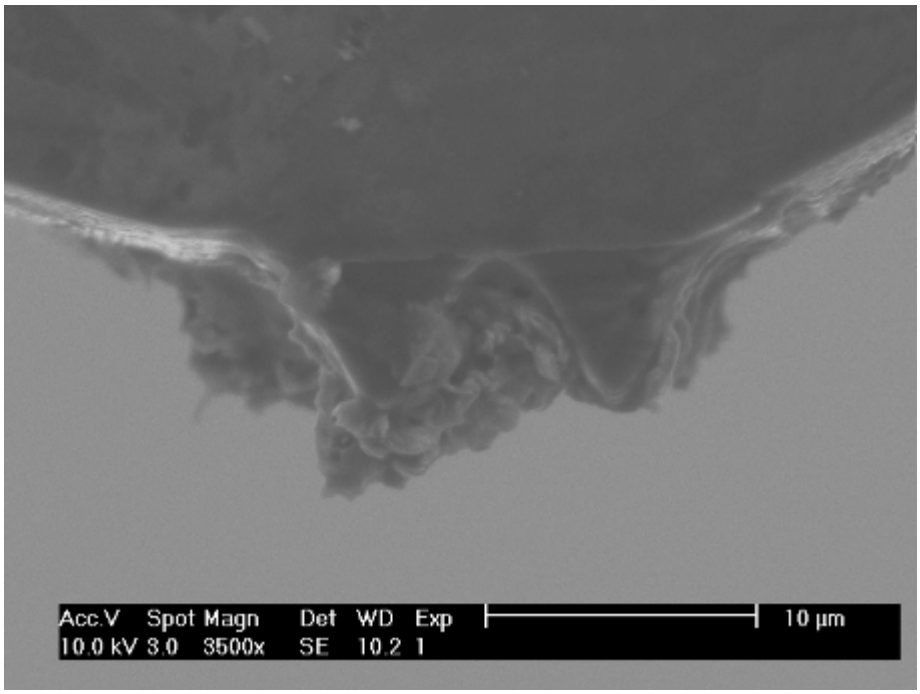

Figure 5.123 – SEM image of S87355 after the initial test (top view)

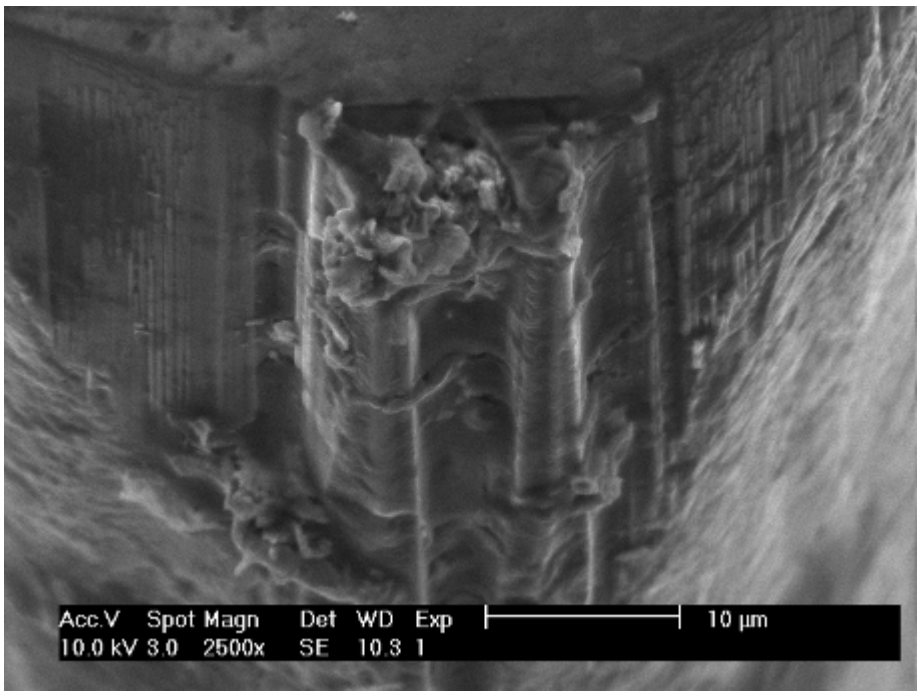

Figure 5.124 – SEM image of S87355 after the initial test (front view)

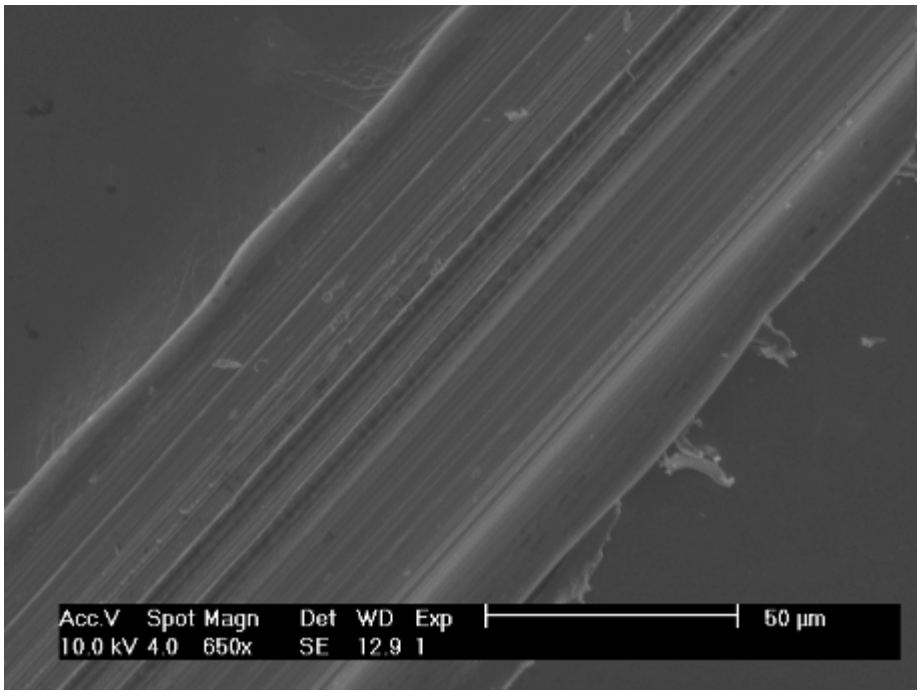

Figure 5.125 – SEM image of initial test trench cut with S87355

The lack of depth perception with SEM makes analysis of the trench difficult. There are features at the bottom but what they were was not clear. One of the 2µm deep trenches cut in the retest is shown in figure 5.126.

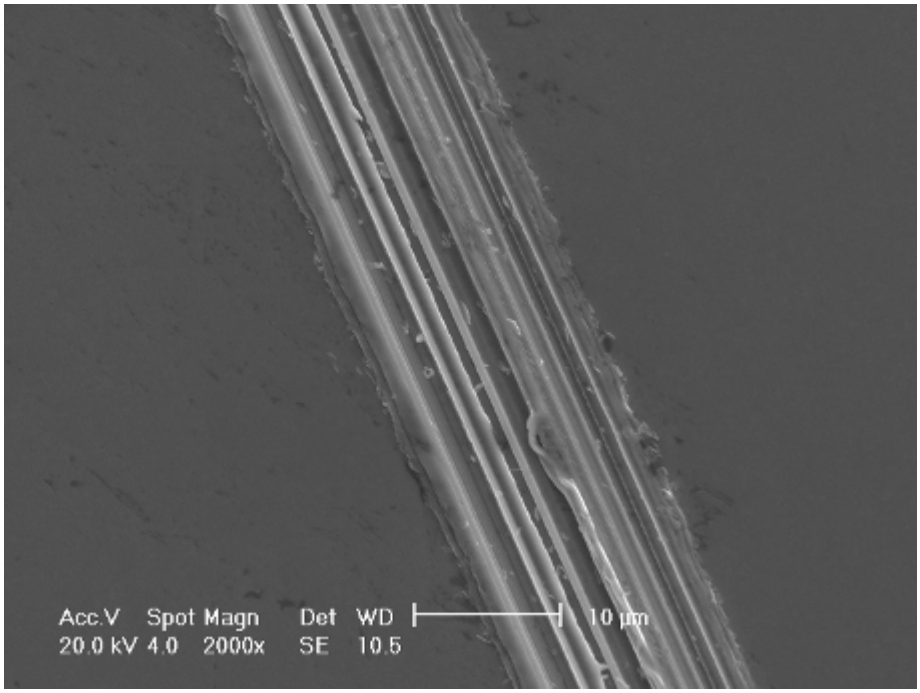

Figure 5.126 – SEM image of retest trench cut with S87355

The trench is messier than for the deeper test. The extra swarf may be due to the diamond prongs not being as good at sweeping the trench clean compared to the sweeping action of the bulk of the tool as in the previous trench.

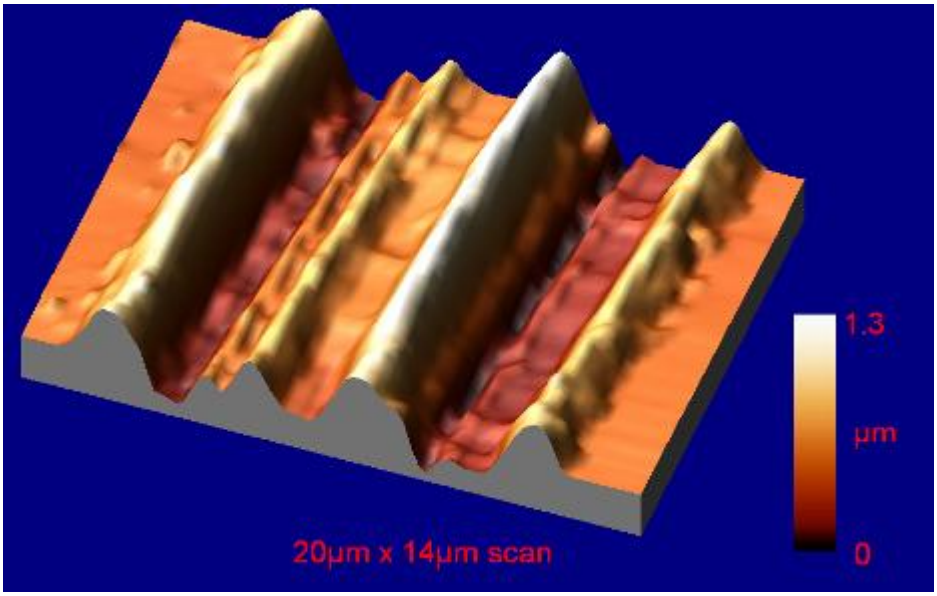

Figure 5.127 – 3D AFM scan of retest trench cut with S87355

The 3D AFM scan of a section of trench is shown in figure 5.127 and a profile across the trench in figure 5.128. The black arrows in 5.128 point to where the front of the prongs of the tool passed relative to the trench walls.

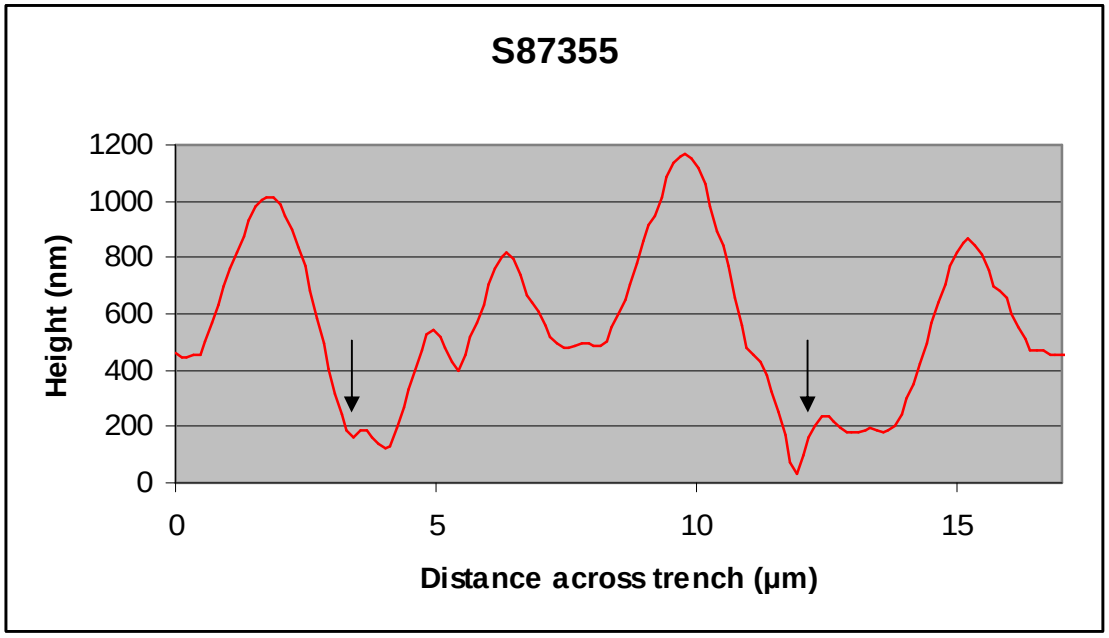

Figure 5.128 – 2D AFM scan of retest trench cut with S87355

The prongs failed to replicate properly and the tool face between the prongs was not smooth enough. The gouges, in what should be the rounded centre of the profile, demonstrate that there were protruding pieces of diamond between the prongs. The maximum height of the profile centre is greater than the machining debris piled up on the edges of the trench. The copper is being squeezed between the prongs instead of all being removed by the pushing action of the rotating work piece as for the turning tools. The volume of material moved by the prongs below the 450nm point in figure 5.128 is less than the volume of material above 450nm. As this isn't possible, given that some copper has been removed from the work piece entirely during machining, it must be due to the flattening of the scan area by the AFM software. This removes tilt from the scan but can alter some of the depths measured while still maintaining the overall profile shape.

5.4.4 – Second sinusoidal tool: S87356

A second sinusoidal tool S87356 was produced to see if a more accurate pattern replication was possible. It was made to the RAL specifications. S87356 was a blank identical to the other three but this one had been chipped at the tip due to

poor handling. The chipped area is partly visible in figure 5.129. The sine prongs have split levels due to the problem with repeat pattern placement mentioned in section 5.4.2. However the lower part of the prongs retained its sine shape so production was continued and clearance achieved on the face below the prongs. The higher part of the prong contacts the copper first and clears out most of the material with the lower part finishing the cut. The tool was tested under the same conditions as S87355, with the tool bought into contact then pulled back and a 2.5µm deep cut machined.

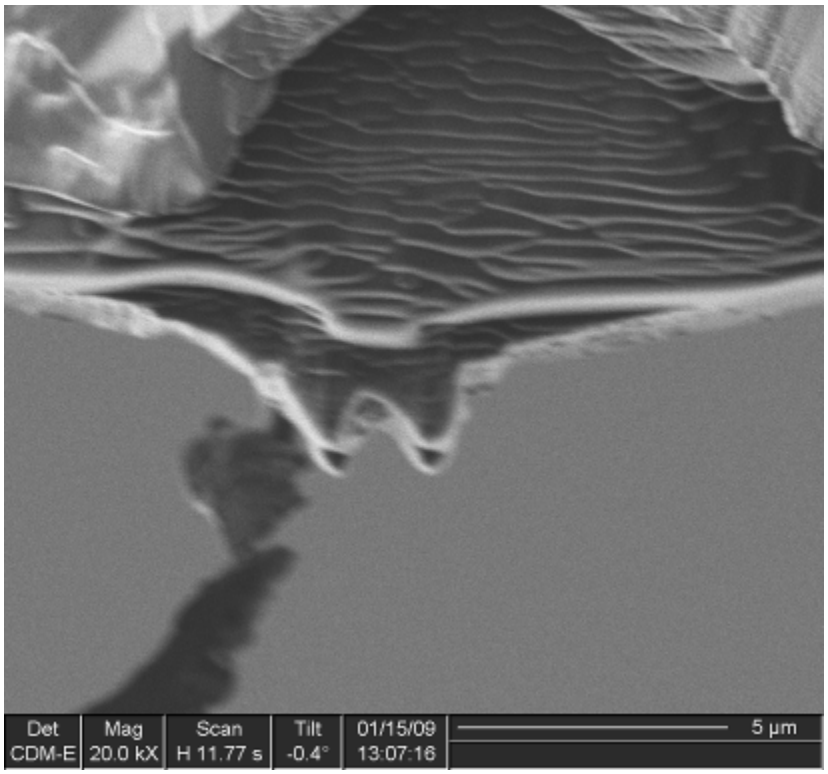

Figure 5.129 – FIB image of S87356 before testing

The tool again survived the machining process with machining debris stuck between the prongs, figure 5.130. The resulting trench is shown in 3D and cross section profile in figures 5.131 and 5.132. The trench has no evidence at all of the prongs which, with the prongs being fully intact, implies a failure in the machining conditions.

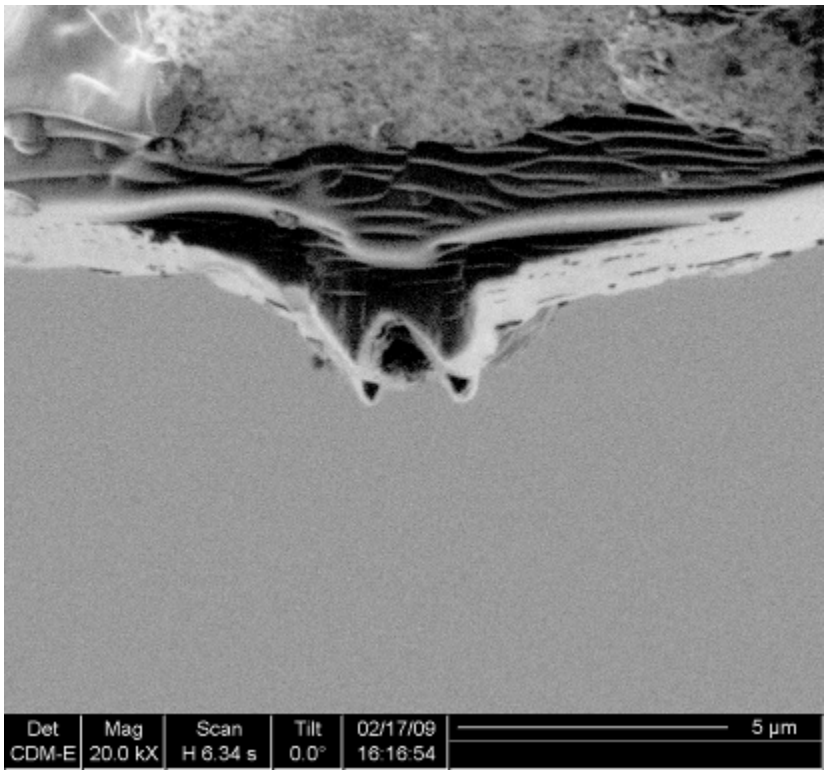

Figure 5.130 – FIB image of S87356 after testing

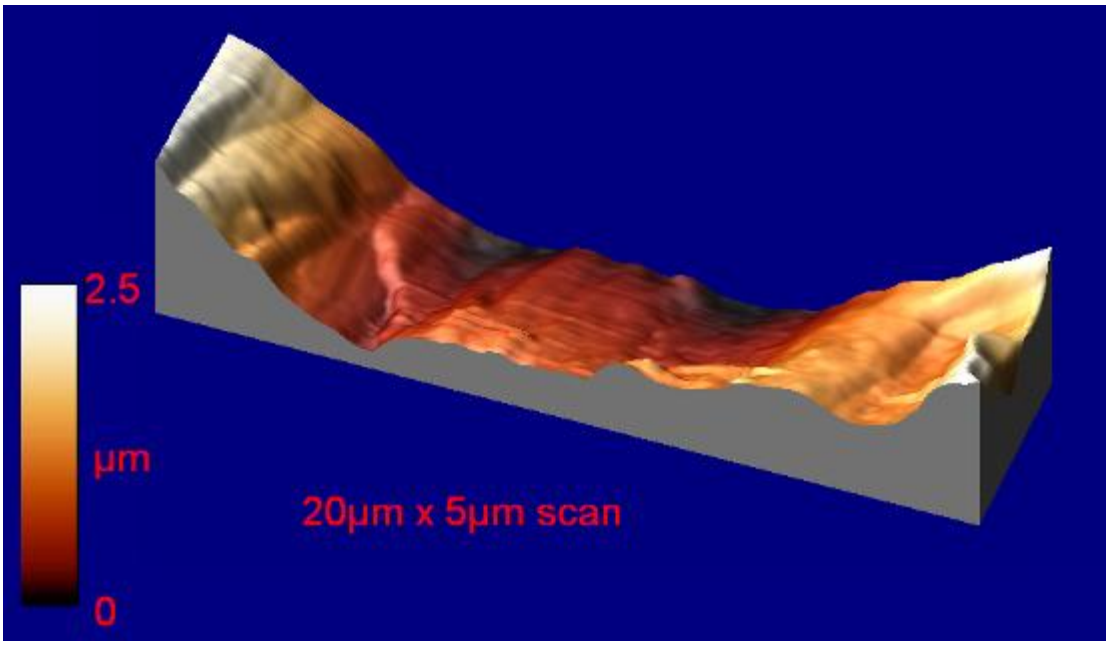

Figure 5.131 – 3D AFM scan of trench cut with S87356

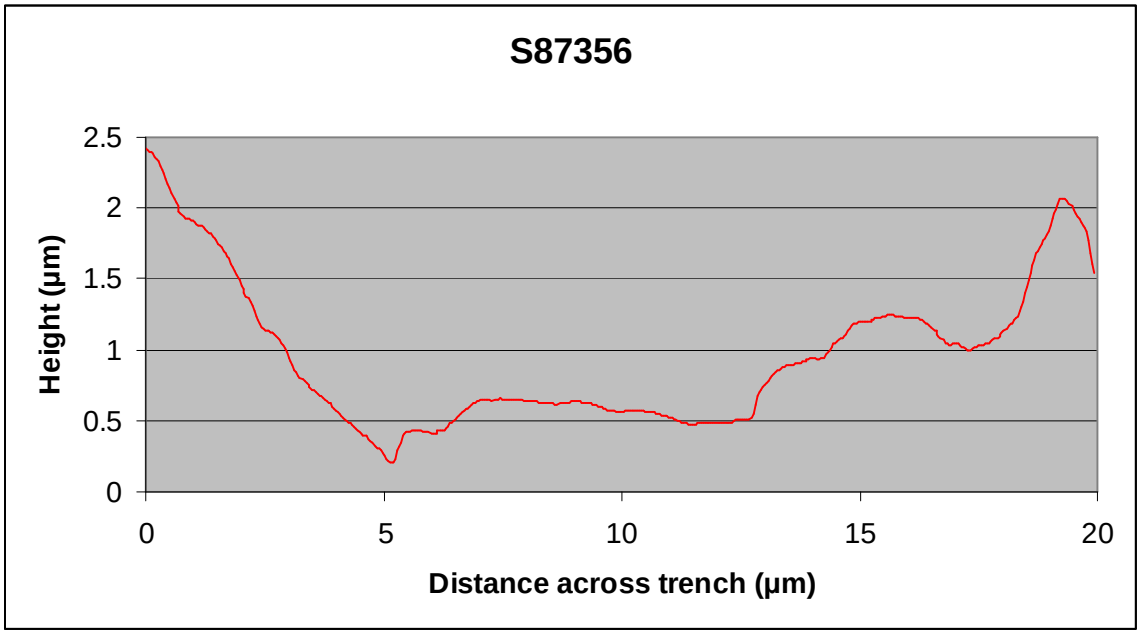

Fig 5.132 – 2D AFM scan of trench cut with S87356

The failure to replicate the sine shapes for both tools could be due to a too small total depth of cut. If not all of the sine prong is in the metal then the diamond area pushing on the metal may not be enough to ensure that the resulting profile is sinusoidal. The cutting force associated with these machining trials was very low and not measurable. This low force was not a problem for the turning tools because their larger, simpler, edge could still push the copper out of the way. The smaller, more complex, sinusoidal tools may need more force to achieve the desired shape. A higher cutting speed and/or a greater depth of cut per revolution might improve shape replication.

5.4.5 - Costs of FIB produced tooling

An important question is how much it costs to produce tools by FIB. For a bespoke tool, when there is no other way of creating it, industry may be prepared to spend thousands of pounds. This sort of work has previously been outsourced by tooling companies to universities (Cox). For companies wanting tools that are more orthodox, but still outside of what diamond tooling companies normally supply, the

FIB process has to provide an economical tool. Single crystal diamond tools cost anything from £70 to ~ £350 depending on the size, shape and complexity.
The cost of operating a FIB is high, due to the large initial amount of capital needed for purchasing a FIB system. A new dual beam system (combined FIB and SEM) will cost £600,000+, depending on what extra equipment is specified e.g. gas injection systems, stage size etc. Second hand single column FIBs built in the late 1990s sell for around $250,000. The servicing costs and consumables have to be included as well, for example new Ga sources are ~£5000 each.

The hourly cost of FIB usage at Cranfield for external users is £70 for the machine and £50 if the work is being done by the Cranfield technician. The rates for internal users are £30 for the machine and £25 for the technician's time. The internal user machine cost is a realistic measure of how much it costs to run the machine in terms of consumables, sources, detectors, gas injection units etc. This doesn't include the purchase cost of the machine.

The length of time needed for making S83011 was seven days (~45 hours machining), due to the number of errors made, meaning the front had to be chopped back repeatedly. The time for S83012 was less, due to the cutting edge being 1/3 the length of S83011 and there being almost no errors, taking 5.5 hours. However, as it turns out, the tool needed more clearance machined onto the front face so another 1-1.5 hours of machining would have ideally been done.

I estimate that having the tool mounted upside down could cut the machining time to around one hour for a turning tool made from a pre laser machined blank. There would no need to work on the tool in the vertical position, which is a major source of machine time. Once the learning curve has been overcome and a procedure has been set up for producing turning tools in the inverted position, the FIB machining could be done for ~£55, ~1 hour per tool as long as the tool cutting edge is no more than ~20µm long. Wider tools will take longer and the time will not scale in a

linear way due to the increasing amount of material that needs removing the further back from the rounded tip you machine.

The cost of the machine has to be factored in on top of the £55. This cost is spread over every tool made using the machine, given that the machine has a lifetime of over ten years and still has a reasonable resale value at that point. The purchase cost of the FIB can be significantly reduced by buying a second hand FIB as mentioned above. Nearly all new FIB's are dual beam and this is not actually necessary for tool production, an older single beam with a water injection unit meets the requirements for producing tools.

Given the uncertainty over applying the cost of a FIB to a tool I cannot estimate the final cost of the tool. Also Contour Tooling will not supply the price information about the laser processed tool blanks as it is commercially sensitive. The details of the laser processing and the associated costs is again commercially sensitive.

Chapter six

6.0 - Conclusions, main contributions to knowledge and further work

6.1 – Conclusions

Focused ion beaming is a powerful technique for micro and nano machining which has become increasingly common since the 1990's. It is capable of machining hard materials like diamond and sapphire to a high degree of detail and accuracy, with resolutions of tens of nanometres. However, there some aspects of its behaviour that need to be remembered when milling.

At high incidence angles it is important to compensate for the extension in the y axis to maintain the shape of the pattern. FIB is poor at milling high aspect structures where the ejected material has difficulty escaping. This leads to redeposition and final feature shapes different from the design pattern.

The natural occurrence of walls with a slope of 5^{o} instead of vertical walls must be allowed for when vertical edges are desired. If the surface makeup is of great importance for a sample then the disorder created in the top few tens of nm of crystal structure has to be considered.

The surface area milled may not match the pattern entered due to the effects of beam drift caused by positive charge build up. Also the milling by the exponential tails of the beam spot, non circular astigmatic beam spots and charge asymmetries caused by metal objects in the sample chamber can affect the milled pattern.

From a FIB machining viewpoint, single crystal diamond is far from ideal to work with. Its tendency to charge up during milling, requiring the use of the ion imaging mode, makes fine feature imaging difficult at times. Normally the charge neutraliser can counteract this, however problems remain at the highest beam currents. The movement of the beam during milling can be a serious problem at higher currents if the neutraliser settings are incorrect.

The injection of water onto the sample surface during gas assisted milling is useful in doubling the low mill yield compared to normal dry milling.

The spontaneous rippled surface morphology is not a problem as it can be removed by briefly milling at a low angle after the feature has been created. The ripple formation process is still not fully understood in spite of several models of the surface processes being created. The models suggest several possible surface mechanisms but the low ion fluxes used in the existing models predict behaviour that is not observed in normal FIB processing. The ripple formation is not repeatable enough to be useful as a method of forming optical gratings.

The production of micro tools from polycrystalline CVD diamond is easier due to the electrical conducting properties of CVD compared to single crystal diamond. The superior wear and fracture toughness of CVD over single crystal is desirable when machined surfaces do not need to be of ultra high quality.

Turning tools have been produced capable of machining OFHCC to a finish of 28nm Sq. This can be improved to ~20nm Sq with improved FIB technique and an altered tool position during tool production. 28nm Sq is comparable to similar work carried out on single crystal diamond. It is also better than other figures in the literature for OFHCC machined by PCD tooling made by grinding or EDM.

There are no reports of the combination of laser and FIB machining used to create tooling in the literature. The literature only contains reports of single crystal tooling created from ground blanks by FIB processing. The production time for CVD turning tools is estimated to be ~1 hour with an optimised process, when starting from a laser machined tool blank.

Sinusoidal CVD tools have been produced by FIB and these have survived metal cutting tests in OFHCC, however the machining conditions need improving to achieve better shape replication. The small tips of the tool complicate the process of achieving measurable surface cuts due to the difficulty of knowing when the tool is contact with the work piece.

FIB processing of sapphire encounters the same problems of low yield and pattern drift due to charging up as single crystal diamond. However it is still possible to machine large numbers of nano sized features into it with a high degree of accuracy when a thin conducting coating is applied. These features were produced on flat and curved surfaces.

6.2 - Main contributions to knowledge

I consider that the main contributions of this thesis to the existing body of knowledge to be:

- The extension of focused ion beam machining to polycrystalline diamond building on the previous work on single crystal.
- The combining of laser machining with FIB for the creation of micro tooling which does not appear in the literature previously.
- The creation of tools capable of giving a surface roughness of 28nm Sq on OFHCC, matching similar work using single crystal diamond. This is superior to the finish given by conventional PCD tooling.
- Showing that complex diamond micro features on tools can survive the metal machining process.

6.3 - Further work

My suggestions for continuing the work described in this thesis are as follows.

- Production of PCD tools mounted upside down in the chamber. These should have a sharper edge than the tools made so far. They will also have a much shorter fabrication time.
- Micro channel cutting with the new tools.
- Longer test runs of S83011 to get an idea of how quickly the tool wears and the effect on surface quality. Also long runs of the other tools.
- Repeating the sinusoidal tool tests with a greater depth of cut per revolution to increase the machining forces. A higher spindle speed may also help achieve superior shape replication.

- Integration of the patterned sapphire gutter into a micro injection mould and testing of the feature replication in polymer.

List of references

(3D-Mintegration) www.3d-mintegration.com (last accessed 13/3/09).

(Adams 2000) Microgrooving and microthreading tools for fabricating curvilinear features. Adams.D.P, Vasile.M.J and Krishnan.A.S.M. Precision engineering 24 pp347-356 (2000).

(Adams 2001) Micromilling of metal alloys with focused ion beam-fabricated tools. Adams.D.P, Vasile.M.J, Benavides.G and Campbell.A.N. Precision engineering 25 pp107-113 (2001).

(Adams 2003) Focused ion beam milling of diamond: effects of H_20 on yield, surface morphology, and microstructure. Adams.D.P, Vasile.M.J, Mayer.T.M and Hodges.V.C. J. Vac .Sci. Technol. B 21(6) pp2334-2343 (2003).

(Adams 2006a) Focused ion beam sculpting curved shape cavities in crystalline and amorphous targets. Adams.D.P, Vasile.M.J and Mayer.T.M. J. Vac. Sci. Technol. B 24(4) pp1766-1775 (2006).

(Adams 2006b) Effects of evolving surface morphology on yield during focused ion beam milling of carbon. Adams.D.P, Mayer.T.M, Vasile.M.J and Archuleta.K. Applied Surface science 252 pp2432-2344 (2006).

(Allen 2009) Ion Beam, Focused Ion Beam, and Plasma Discharge Machining Allen.D.M, Shore.P, Evans.R.W, Fanara.C, O'Brien.W, Marson.S and O'Neill.W. Keynote paper for 59th CIRP General Assembly, Boston, 23rd-29th August 2009.

(Belmonte 2003) Wear resistant CVD diamond tools for turning of sintered hard metals. Belmonte.M, Ferro.B, Fernandes.A.J.S, Costa.F.M, Sacramento.J and Silva.R.F. Diamond and related materials 12 pp738-743 (2003).

(Benade 2007) Rheology of blood through micro constrictions, Benade.M.
MSc thesis, Cranfield University (2007).

(Bradley 1988) Theory of ripple topography induced by ion bombardment. Bradley.R.M and Harper.J.M.E. J. Vac .Sci. Technol. A 6(4) pp2390-2395 (1988).

(Brunetto 2005) Amorphization of diamond by ion irradiation: a Raman study.
Brunetto.R, Baratta.G.A and Strazzulla.G. Journal of physics: Conference Series 6 pp120-125 (2005).

(Carson 2004) An investigation into potential processing routes for the large scale manufacture of a microfluidic device. Carson.D and Lloyd.J. MSc group project report, Cranfield University (2004).

(Carter 2001) The physics and applications of ion beam erosion. Carter.G.
J. Phys. D: Appl. Phys. 34 R1–R22 (2001).

(Chan 2007) Making waves: kinetic processes controlling surface evolution during low energy ion sputtering. Chan.W.L and Chason.E. J.Appl.Phys. 101, 121301-1 – 121301-46 (2007).

(Chason 2006) Kinetic mechanisms in ion induced ripple formation on Cu(001) surfaces. Chason.E and Chan.W.L. Nucl. Instr. And Meth. In Phys. Res. B 42 pp232-236 (2006).

(Collins 1998) Station 16.3: a high resolution single crystal diffraction facility at the SRS, Daresbury. Collins.S.P, Cernik.R.J, Fell.B, Tang.C.C, Harris.N.W, Miller.M.C and Oszlanyi.G. J. Synchrotron Rad. 5 pp1263-1269 (1998).

(Collins 1999) SRS station 16.3: description and utilization of a high-resolution diffraction facility. Collins.S.P, Murphy.B.M, Tang.C.C, Miller.M.C and Oszlanyi.G. J. Phys. D: Appl. Phys. 32 A81-A83 (1999).

(Contour) Contour Fine Tooling, Stevenage, UK. www.contour-diamonds.com (last accessed 21/02/09).

(Cox) Personal communication with Andrew Cox, Managing Director of Contour Fine Tooling Ltd.

(Dai 2008) Study and formation of 2D microstructures of sapphire by focused ion beam milling. Dai.T, Kang.X, Zhang.B, Xu.J, Bao.K, Xiong.C and Gan.Z. Microelectronic Engineering 85 pp640–645 (2008).

(Datta 1999) Gas assisted focused ion beam lithography of a diamond (100) surface. Datta.A, Wu.Y and Wang.Y.L. Applied Physics Letters vol 75(17) pp2677-2679 (1999).

(Datta 2001) Real time observation of ripple structure formation on a diamond surface under focused ion beam bombardment. Datta.A, Wu.Y and Wang.Y.L. Physical review B vol 63 pp1254071-1254076 (2001).

(Ding 2008) Fabrication of a micro-size diamond tool using a focused ion beam. Ding.X**,** Lim.G.C, Cheng.C.K, Butler.D.L, Shaw.K.C, Liu.K and Fong.W.S. J. Micromech. Microeng. 18 075017(10pp) (2008).

(Ding 2009) Machining with micro-size single crystalline diamond tools fabricated by a focused ion beam. Ding.X**,** Butler.D.L, Lim.G.C, Cheng.C.K, Shaw.K.C, Liu.K, Fong.W.S and Zheng.H.Y. J. Micromech. Microeng. 19 025005 (11pp) (2009).

(Dresselhaus 1992) Ion implantation in diamond, graphite and related materials. Dresselhaus.M.S and Kalish.R. Springer-Verlag (1992) ISBN 3540549560.

(Durazo 2008) Fabrication of micro structured surfaces for diagnosing the proton source by single point diamond turning. Durazo.I.S, Shore.P and Morantz.P. 2nd European Target Fabrication Workshop 27-28th October 2008. www.laserlab-europe.net/imperia/md/content/laserlab_europe/tf_15._fabrication_of_micro-structured_surfaces_for_diagnosing_.pdf (last accessed 18/3/09).

(Edinger 2001) Modelling of focused ion beam induced chemistry and comparison with experimental data. Edinger.K and Kraus.T. Microelectronic Engineering 57-58 pp263-268 (2001).

(Element 6 Monodite) http://www.e6.com/en/businessareas/e6advancedmaterials/products/title,329,en.html (last accessed 12/12/09)

(Element 6 PCD) http://www.e6.com/en/businessareas/e6advancedmaterials/literature/cvddiamond/#d.en.1237 (last accessed 12/12/09)

(Ezugwua 2007) Surface integrity of finished turned Ti–6Al–4V alloy with PCD tools using conventional and high pressure coolant supplies. Ezugwua.E.O, Bonneya.J, Da Silva.R.B and Cakir.O. International Journal of Machine Tools & Manufacture 47 pp884–891 (2007).

(FEI manual 2000) FEI FIB 200 reference guide (2000).

(Flamm 2001) Evolution of surface topography of fused silica by ion beam sputtering. Flamm.D, Frost.F and Hirsch.D. Applied Surface Science 179 pp95-101 (2001).

(Frey 2003) Nanoscale effects in focused ion beam processing. Frey.L, Lehrer.C and Ryssel.H. Appl. Phys. A 76 pp1017-1023 (2003).

(Friedrich 1996) Development of the micromilling process for high aspect ratio microstructures. Friedrich.C.R and Vasile.M.J. J. Microelectromechanical systems 5 pp33-38 (1996).

(Friedrich 1997) Micromilling development and applications for microfabrication. Friedrich.C.R, Coane.P.J and Vasile.M.J. Microelectronic Engineering 35 pp367-72 (1997).

(Gao 2008) Surface measurement errors using commercial scanning white light interferometers. Gao.F, Leach.R.K, Petzing.J and Coupland.J.M. Meas. Sci. Technol. 19 015303 (13pp) (2008).

(Gerlach 2001) Focused ion beam methods of nanofabrication: Room at the bottom. Gerlach.R. Proc SPIE Vol 4510 pp96-106 (2001).

(Giannuzzi 2005) Introduction to focused ion beams. Giannuzzi.L.A and Stevie.F.A. Springer (2005) ISBN 0387231161.

(Gierak 2006) Exploration of the ultimate patterning potential of focused ion beams. Gierak.J, Bourhus.E, Madouri.A, Strasser.M, Sagnes.I, Bouchoule.S, Merat Combes.M.N, Mailly.D, Hawkes.P, Jede.R, Bardotti.L, Prevel.B, Hannour.L, Melinon.P, Perez.A, Ferre.J, Jamet.J.-P, Mougin.A, Chappert.C and Mathet.V. J. Microlith. Microfab. Microsyst. 5(1) pp1–11 (2006).

(Horcas 2007) WSXM: A software for scanning probe microscopy and a tool for nanotechnology. Horcas.I, Fernandez.R, Gomez-Rodriguez.J.M, Colchero.J, Gomez-Herrero.J and Baro.A.M. Rev. Sci. Instrum. 78, 013705 (2007).

(Huang 2005) Self-organized amorphous material in silicon (001) by focused ion beam (FIB) system. Huang.Y, Cockayne.D.J.H, Marsh.C, Titchmarsh.J.M and Petford-Long.A.K. Applied Surface Science 252 pp1954-1958 (2005).

(Kalish 1993) Ion beam modification of diamond. Kalish.R. Diamond and related materials 2 pp621-633 (1993).

(Katharria 2007) Nano and micro scale patterning of Si(100) under keV ion irradiation. Katharria.Y.S, Kumar.S, Sharma.A.T and Kanjilal.D. Applied Surface Science 253 pp6824-6828 (2007).

(Kawabata 2004) XPS studies on damage evaluation of single crystal diamond chips processed with ion beam etching and reactive ion beam assisted chemical etching. Kawabata.Y, Taniguchi.J and Miyamoto.I. Diamond and related materials 13 pp93-98 (2004).

(Kersaudy-Kerhoas 2007) Design, Manufacturing and Test of Disposable Microfluidic System for Blood-Plasma Separation. Kersaudy-Kerhoas.M, Amalou.F, Kavanagh.D, Marson.S, Attia.U.M, Summersgill.P, Ryan.T and Desmulliez.M.P.Y. Lab-on-a-chip World Congress, Edinburgh, May 2007. accessed at http://www.eposters.net/index.aspx?ID=1046 (29/03/09), ref number: EP10396.

(Kersaudy-Kerhoas 2008) Blood flow separation in microfluidic channels. Kersaudy-Kerhoas.M, Resham Dhariwal and Desmulliez.M.P.Y. MicroFLU08, December 2008, Bologna, Italy.

(Kim 2007a) Simulation of ion beam induced micro/nano fabrication. Kim.H, Hobler.G, Lugstein.A and Bertagnolli.E. J. Micromech. Microeng. 17 pp1178–1183 (2007).

(Kim 2007b) Full three dimensional simulation of focused ion beam micro/nanofabrication. Kim.H, Hobler.G, Steiger.A, Lugstein.A and Bertagnolli.E. Nanotechnology 18 245303 (2007).

(Koponen 1997) Simulations of ripple formation on ion bombarded solid surfaces. Koponen.I, Hautala.M and Sievanen.O.P. Physical review letters vol 78 (13) pp2612-2615 (1997).

(Langford 2002a) Application of a focused ion beam system to micro and nanoengineering. Langford.R.M, Petford-Long.A.K, Rommeswinkle.M and Egelkamp.S. Materials Science and Technology 18 pp743-748 (2002).

(Langford 2002b) Focused ion beam micromachining of three dimensional structures and three dimensional reconstruction to assess their shape. Langford.R.M, Dale.G, Hopkins.P.J, Ewen.P.J.S and Petford-Long.A.M. J. Micromech. Microeng. 12 pp111-114 (2002).

(Langford 2007) Focused Ion Beam micro and nanoengineering. Langford.R.M, Nellen.P.M, Gierak.J and Fu.Y. Materials Research Bulletin Vol 32 pp417-423 (2007).

(Leach 2008) Guide to the Measurement of Smooth Surface Topography using Coherence Scanning Interferometry : NPL Measurement Good Practice Guide No. 108. Leach.R, Brown.L, Jiang.X, Blunt.R, Conroy.M and Mauger.D. Downloadable from www.publications.npl.co.uk/npl_web/search.htm.

(Lee 2006) Gas assisted etching of sapphire using focused ion beam. Lee.M and Kuo.K. Japanese Journal of Applied Physics Vol 45, pp2447-2450 (2006).

(Li 2007) A study of fused silica micro/nano patterning by focused-ion-beam. Li.W, Lalev.G, Dimov.S, Zhao.H and Pham.D.T. Applied Surface Science 253 pp3608-3614 (2007).

(Lowe 2007) White light interferometric profilometry of surface structured glass for high power laser microtargets. Lowe.H.F and Spindoe.C. Central Laser facility annual report 2006/2007 pp249-252. www.clf.rl.ac.uk/reports/2006-2007/pdfs/ar06-07_s7tf_whitelightsurfacestructuredglass.pdf.

Luo (2005) Investigation of the burnishing process with PCD tool on non-ferrous metals. Luo.H, Liu.J, Wang.L and Zhong.Q. Int J Adv Manuf Technol 25 pp454–459 (2005).

(Makeev 1997) Ion induced effective surface diffusion in ion sputtering. Makeev.M.A and Barabasi.A. Appl. Phys. Lett 71 (19) pp2800-2802 (1997).

(Marson 2007) Replication of polymer microcomponents: the economics of hot embossing versus injection moulding. S.Marson, R.Evans and D.M.Allen. Proceedings of the 20th International Conference on Computer-Aided Production. Engineering (CAPE 2007), Glasgow, 6th-8th June 2007.

(Marson 2008) Study of blood flow behaviour in microchannels. Marson.S, Benade.M, Attia.U.M, Allen.D.M, Kersaudy-Kerhoas.M, Hedge.J, Morgan.S, Larcombe.L and Alcock.J.R. euspen 10th anniversary International Conference, Zurich, 18th-22nd May 2008. Proceedings Vol 2 pp620-623.

(Marson 2009a) Reconfigurable micro mould for the manufacture of truly 3D polymer microlfuidic devices. Marson.S, Attia.U, Allen.D.M, Tipler.P, Jin.T, Hedge.J and Alcock.J.R. 19th CIRP Design Conference, Cranfield, 30th-31st March 2009.

(Marson 2009b) 3D polymer microfluidic device for blood/plasma separation. Marson.S, Attia.U.M, Xue.X and Allen.D.M. In press.

(Mayer 2005) Morphology evolution on diamond surfaces during ion sputtering. Mayer.T.M, Adams.D.P, Vasile.M.J and Archuleta.K.M. J. Vac. Sci. Technol. A 23(6) pp1579-1587 (2005).

(MeIngailis 1987) Focused ion beam technology and applications. MeIngailis.J. J. Vac. Sci. Technol. B 5(2) pp469-495 (1987).

(Miyamoto 1982) Polishing and sharpening of diamond point tools by ion sputter-machining. Miyamoto.I and Taniguchi.N. Precision Engineering 4 pp191-194 (1982).

(Miyamoto 1983) Profile forming of a sub-micron radius circular cone-shaped diamond tool tip by ion sputter-machining. Miyamoto.I and Taniguchi.N. Precision Engineering 5 pp62-64 (1983).

(Miyamoto 1987) Ultra fine finishing of diamond tools by ion beams. Miyamoto.I. Precision Engineering 9 pp72-78 (1987).

(Miyamoto 1989) Crystallinity and strength of diamond bombarded with low energy ion beams. Miyamoto.I, Nishimu.K, Kawata.K, Kawarada.H and Shimada.S. Nuclear Instruments and Methods in Physics Research B39 pp689-691 (1989).

(Miyamoto 1990) Ion beam machining of single point diamond tools for nano-precision turning. Miyamoto.I, Ezawat.T and Nishimura.K. Nanotechnology 1 pp44-49 (1990).

(Moberlychan 2007) Fundamentals of Focused Ion Beam nanostructural processing: below, at, and below the surface. Moberlychan.W.J, Adams.D.P, Aziz.M.J, Hobler.G and Schenkel.T. Materials Research Bulletin Vol 32 pp424-432 (2007).

(Moore 1988) X-ray studies of the growth of natural diamond. Moore.M. Industrial Diamond Review 48 pp59-64 (1988).

(Moore 1995) Synchrotron x-ray topography. Moore.M. Radiat. Phys. Chem. Vol 45 pp427-444 (1995).

(Moore 2001) ‘Diamond: Natural’ Encyclopedia of Materials: Science and Technology, Elsevier Science, pp2133-2143 (2001) ISBN 0080431526.

(Moore 2002) Diamonds – Much more than a girls best friend. Moore.M.
Inaugural Professorial lecture booklet, Royal Holloway, University of London (2002).

(Morehead 2007) Machinability of ultrafine-grained copper using tungsten carbide and polycrystalline diamond tools. Morehead.M, Huanga.Y and Hartwig.K.T.
International Journal of Machine Tools & Manufacture 47 pp286–293 (2007).

(Murakawa 2004) Fabrication of 3D shaped micro body structures of diamond by use of focused ion beam. Murakawa.M, Hayashi.M and Noguchi.H.
New diamond and frontier carbon technology 14(3) pp173-179 (2004).

(Olsen 2004a) Machining of electrically conductive CVD diamond tool blanks using EDM. Olsen.R.H, Dewes.R.C and Aspinwall.D.K. Journal of Materials Processing Technology 149 pp627–632 (2004).

(Olsen 2004b) Electrical discharge machining of conductive CVD diamond tool blanks Olsen.R.H, Aspinwall.D.K, and Dewes.R.C. Journal of Materials Processing Technology 155–156 pp1227–1234 (2004).

(O'Neill 2009) Personal communication with Dr Bill O'Neill, University of Cambridge.

(Picard 2003) Focused ion beam shaped microtools for ultraprecision machining of cylindrical components. Picard.Y.N, Adams.D.P, Vasile.M.J and Ritchey.M.B.
Precision engineering 27 pp59-69 (2003).

(Pierson 1993) Handbook of carbon, graphite, diamond and fullerenes.
Noyes publications (1993) ISBN 0815513399.

(Popovich 2005) Thermal conductivity of poly and nanocrystalline diamond films grown in microwave plasma. Popovich.A, Ralchenko.V, Konov.V, Saveliev.A, Khomich.A and Zharikov.E. France-Russia Seminar New achievements in materials science IV.13 (2005).

(Prawer 1995) Ion implantation of diamond and diamond films. Prawer.S. Diamond and related materials 4 pp862-872 (1995).

(Prentner 2009) Effects of channel surface finish on blood flow in microfluidic devices. Prentner.S, Allen.D.M, Larcombe.L, Marson.S, Jenkins.K and Saumer.M. DTIP of MEMS and MOEMS, Rome, 1st-3rd April 2009.

(Qian 2005) Crystallographically dependent ripple formation on Sn surface irradiated with focused ion beam. Qian.H.X, Zhou.W, Fu.Y.Q, Ngoi.B.K.A and Lim,G.C. Applied Surface Science 240 pp140-145 (2005).

(Raith 2009) ELPHY Quantum software www.raith.com/index.php?xml=solutions|SEM+%26+FIB+lithography+kits|ELPHY+Quantum&page=1

(Reis 2005) The machining of aluminium alloy 6351. Reis.D.D and Abrao.A.M. Proc. IMechE Vol. 219 Part B: J. Engineering Manufacture pp27-33 (2005).

(Reyntjens 2001) A review of focused ion beam applications in microsystem technology. Reyntjens.S and Puers.R. J. Micromech. Microeng. 11 pp287-300 (2001).

(Russell 1998) Chemically and geometrically enhanced focused ion beam machining. Russell.P.E, Stark.T.J, Griffis.D.P, Phillips.J.R and Jarausch.K.F. J. Vac. Sci. Technol. B 16(4) pp2494-2498 (1998).

(Schift 2000) Nanoreplication in polymers using hot embossing and injection molding. Schift.H, David.C, Gabrielt.M, Gobrecht.J, Heyderman.L.J, Kaiser.W, Koppel.S and Scandella.L. Microelectronic Engineering vol 53 pp171-174 (2000).

(Shabalin 1992) Current density distribution at the periphery of submicron probes. Shabalin.A.L. Journal of Applied Mechanics and Technical Physics vol 33 pp769-775 (1992).

(Sigmund 1973) A mechanism of surface micro-roughening by ion bombardment. Sigmund.P. Journal of Materials Science 8 pp1545-1553 (1973).

(Spencer 1972) Ion machining of diamond. Spencer.E.G and Schmidt.P.H. Journal of applied physics 43(7) pp2956-2958 (1972).

(Spindloe 2008) STFC High power laser micro-target fabrication. Spindloe.C, Lowe.H and Tolley.M. 2nd European Target Fabrication Workshop 27-28th October 2008.
www.laserlab-europe.net/imperia/md/content/laserlab_europe/tf_3._an_overview_of_the_target_fabrication_activities_at_the_.pdf (last accessed 18/3/09).

(SRIM 2008) www.srim.org (last accessed 5/11/08).

(Stanishevsky 1999) Focused ion beam patterning of diamond like carbon films. Stanishevsky.A. Diamond and Related Materials 8 pp1246-1250 (1999).

(Stanishevsky 2001) Patterning of diamond and amorphous carbon films using focused ion beams. Stanishevsky.A. Thin solid films 398-9 pp560-565 (2001).

(Stark 1995) Enhanced focused ion beam micromachining. Stark.T.J, Shedd.G.M, Vitarelli.J, Griffis.D.P and Russell.P.E. J. Vac. Sci. Technol. B 13(6) pp2565-2569 (1995).

(Steckl 1999) Focused ion beam micromilling of GaN and related substrate materials (sapphire, SiC, and Si). Steckl.A.J and Chyr.I. J. Vac .Sci. Technol. B 17(2) pp362-365 (1999).

(Stoyanov 2009) Modelling and Process Capability Analysis of Focussed Ion Beam. Stoyanov.S, Tang.Y.K, Bailey.C, Evans.R, Marson.S and Allen.D.M. 32nd International Spring Seminar on Electronics Technology, Brno, 13th-17th May 2009.

(SUSPRE) Downloaded from www.ee.surrey.ac.uk/IBC/index.php?target=6:35 (last accessed 13/03/09).

(Tang 2009) Modelling of focused ion beam. Tang.Y.K, Bailey.C and Stoyanov.S. Internal 3D-Mintegration report, March 2009.

(Taniguchi 1989) Energy beam processing of materials: Advanced manufacturing using various energy sources, chapters 1 and 4. Taniguchi.N, Ikeda.M, Miyamoto.I and Miyazaki.T. Oxford University press (1989) ISBN 0198590059.

(Taniguchi 1998) Focused ion beam assisted etching of diamond in XeF_2. Taniguchi.J, Ohno.N, TaKeda.S, Miyamoto.I and Komuro.M. J. Vac. Sci. Technol. B 16(4) pp2506-2510 (1998).

(Taniguchi 2000) Beam-assisted-etching technique for fabrication of single crystal diamond field emitter tip. Taniguchi.J, Yokoyama.J, Komuro.M, Hiroshima.H and Miyamoto.I. Microelectronic Engineering 53 pp415-418 (2000).

(Thoe 1996) Polycrystalline diamond edge quality and surface integrity following electrical discharge grinding. Thoe.T.B, Aspinwall.D.K, Wise.M.L.H and Oxley.I.A. Journal of Materials Processing Technology 56 pp773-785 (1996).

(Tseng 2004) Recent developments in micromilling using focused ion beam technology. Tseng.A. J. Micromech. Microeng. 14 R15-R34 (2004).

(Tseng 2005) Recent developments in nanofabrication using focused ion beams. Tseng.A. small, no 10 pp924-939 (2005).

(Tso 2002) Study on PCD machining. Tso.P and Liu.Y. International Journal of Machine Tools & Manufacture 42 pp331–334 (2002).

(Vasile 1996) Micrometer scale machining: tool fabrication and initial results. Vasile.M.J, Freidrich.C.R, Kikkeri.B and McElhannon.R. Precision engineering 19 pp180-186 (1996).

(Vasile 1998) Focused ion beam technology applied to microstructure fabrication. Vasile.M, Nassar.R and Xie.J. J. Vac. Sci. Technol. B 16(4) pp2499-2505 (1998).

(Vasile 1999) Microfabrication techniques using focused ion beams and emergent applications. Vasile.M.J, Nassar.R, Xie.J and Guo.H. Micron 30 pp235-244 (1999).

(Volkert 2007) Focused Ion Beam microscopy and micromachining. Volkert.C.A and Minor.A.M. Materials Research Bulletin Vol 32 pp389-395 (2007).

(West 1982) Copper and its alloys. West.E.G. Ellis Horwood Ltd (1982) ISBN 0853125058.

(West 1979) The selection and use of copper rich alloys, Engineering Design Guides no 35. West.E.G. Oxford University Press (1979) ISBN 019859173X.

(Winter 2007) Redeposition characteristics of focused ion beam milling for nanofabrication. Winter.D.A.M and Mulders.J.J.L. J. Vac. Sci. Technol. B 25(6) pp2215-2218 (2007).

(WSxM user manual) Downloaded from www.nanotec.es/products/wsxm/index.php (last accessed 13/3/09).

(Xie 2004) Fabrication and thermal annealing behavior of nanoscale ripple fabricated by focused ion beam. Xie.D.Z, Ngoi.B.K.A, Zhou.W and Fu.Y.Q. Applied Surface Science 227 pp250-254 (2004).

(Yang 2006) A microfluidic device for continuous real time blood plasma separation. Yang.S, Undar.A and Zahn.F.D. Lab Chip 6 pp871-880 (2006).

(Yongqi 2000) Experimental study of 3D microfabrication by focused ion beam technology. Yongqi.F, Bryan.N.K.A, Hung.N.P, and Shing.O.N. Review of scientific instruments Vol 71(2) pp1006-1008 (2000).

(Zdebski 2008) An initial study on the diamond planning process to produce microgrooves for a microfluidic device. Zdebski.D, Hedge.J, Jin.T, Marson.S, Shore.P, Stephenson.D.J and Allen.D.M. CIRP International conference on high performance cutting and micromachining, Dublin 12th-13th June 2008.

(Zhang 1994) Factors affecting surface quality in diamond turning of oxygen-free high-conductance copper. Zhang.H and Zhang.X. Applied Optics Vol. 33, No.10 pp2039-2042 (1994).

(Zhou 2007) Wavelength tunability of ion bombardment induced ripples on sapphire. Zhou.H, Wang.Y, Zhou.L, Headrick.R.L, Sozcan.A, Wang.Y, Ozaydin.G, Ludwig.K.F, Siddons.D.P. Physical Review B 75, 155416 (2007).

Conference papers

A review of focused ion beam technology for the fabrication of ultra precision diamond cutting tools. R.W.Evans, S.Marson and D.M.Allen. 6th International Conference on Materials for Microelectronics & Nanoengineering (MFMN 2006), Cranfield, 29th-31st October 2006.

Replication of polymer microcomponents: the economics of hot embossing versus injection moulding. S.Marson, R.Evans and D.M.Allen. Proceedings of the 20th International Conference on Computer-Aided Production Engineering (CAPE 2007), Glasgow, 6th-8th June 2007. (Keynote paper)

Fabricating diamond microtools with focused ion beam machining. R.W.Evans and D.M.Allen. euspen 10th anniversary International Conference, Zurich, 18th-22nd May 2008.

Modelling and Process Capability Analysis of Focussed Ion Beam. Stoyanov.S, Tang.Y.K, Bailey.C, Evans.R, Marson.S and Allen.D.M.
32nd International Spring Seminar on Electronics Technology, Brno, 13th-17th May 2009.

Ion Beam, Focused Ion Beam, and Plasma Discharge Machining. Allen.D.M, Shore.P, Evans.R.W, Fanara.C, O'Brien.W, Marson.S and O'Neill.W. Keynote paper for 59th CIRP General Assembly, Boston, 23rd-29th August 2009.

Conference poster

PCD tooling made by combined laser beam machining and focused ion beam machining. Evans.R.W, Durazo-Cardenas.I.S and Allen.D.M. euspen 9th International Conference, San Sebastian , 2nd-5th June 2009.

Workshop abstract/presentation

Analysis of ripple formation on diamond and sapphire during FIB machining. R.W.Evans, S.Marson and D.M.Allen. NanoFib2007 workshop at Manchester University, 29th June 2007.

Internal conference posters

Focused ion beam machining of diamond. 1st annual 3D-Mintegration conference, September 2006.

Focused ion beam machining of diamond and sapphire. Cranfield mid stage PhD poster conference, June 2007.

Focused ion beam surface patterning. 2nd annual 3D-Mintegration conference, October 2007.

Formal presentations

Focused ion beam machining of diamond. 1st annual 3D-Mintegration conference, September 2006.

A review of focused ion beam technology for the fabrication of ultra precision diamond cutting tools. R.W.Evans, S.Marson and D.M.Allen.
6th International Conference on Materials for Microelectronics & Nanoengineering (MFMN 2006), Cranfield, 29th-31st October 2006.

Analysis of ripple formation on diamond and sapphire during FIB machining. R.W.Evans, S.Marson and D.M.Allen. NanoFib2007 workshop at Manchester University, 29th June 2007.

Focused ion beam machining of diamond. 2nd annual 3D-Mintegration conference, October 2007.

Fabricating diamond microtools with focused ion beam machining. Cranfield multi strand conference, April 2008.

Fabricating diamond microtools with focused ion beam machining. R.W.Evans and D.M.Allen. euspen 10th anniversary International Conference, Zurich, 18th-22nd May 2008.

Appendix

7 - X-ray synchrotron study of FIB machined single crystal diamond

The effect of implanted gallium on the single crystal diamond structure is a potential problem for FIB produced tools. Even though the ion machining software models predict that the deepest the gallium will reach into the crystal is less than 100nm, experimental evidence of this is lacking. The amorphous layer of carbon on cross sectioned diamond tools has been measured (Adams 2003) and was found to be ~35nm in depth. As to whether there is any gallium implanted further down is not clear. There is also the chance that penetrating ions may create clusters of graphite inside the crystal (Dresselhaus 1992), (Kalish 1993), (Prawer 1995) (Brunetto 2005). These clusters can then act as weak points in the structure. In an effort to measure the amount of gallium and its distribution in milled diamond, synthetic single crystal diamond was investigated at the now closed X-ray synchrotron at Daresbury. The work was done at station 16.3, which was designed for single crystal diffraction studies, (Collins 1998) and (Collins 1999).

Pieces of SCD cut along the (100) plane sourced from element six were milled with 50μm squares at normal beam incidence and at 45^{o}. X-ray topographs were taken of the diamonds to see if there was any evidence of gallium implantation. X-ray topography is a method of viewing a slice of the inside of a sample. The resulting diffraction pattern gives an image for each crystal plane (Moore 1988, 1995, 2002).

Diamond has a highly symmetrical structure which means that there are few reflections when diamond is analysed by x-ray diffraction. The crystal planes that can be seen with x-ray synchrotron radiation are 111, 220, 311, 400 and 331 (Moore 2001).

The diamonds were orientated to the (400) plane and a white light x-ray beam was used. The station had a six circles diffractometer giving the very high degree of

adjustability needed for setting the crystal to the desired plane orientation. Using a spread of wavelengths, and allowing the crystal to self select the dominant diffractions, causes the (400) plane to be one of the strongest reflections as long as the crystal tilts and rotations required have been calculated properly. The alternative of using a monochromated beam, which gives images that are easier to interpret due to the smaller number of image spots, wasn't used because the positioning of the crystal has to be extremely precise and requires a lot of images to be taken before getting the alignment right. The (400) plane was chosen as this preferentially scatters radiation of ~0.1nm, this being a good wavelength for diamond studies.

Reflection and transmission imaging were both used, figures 7.1 and 7.2; the resulting slice through the diamond being imaged onto the imaging medium.

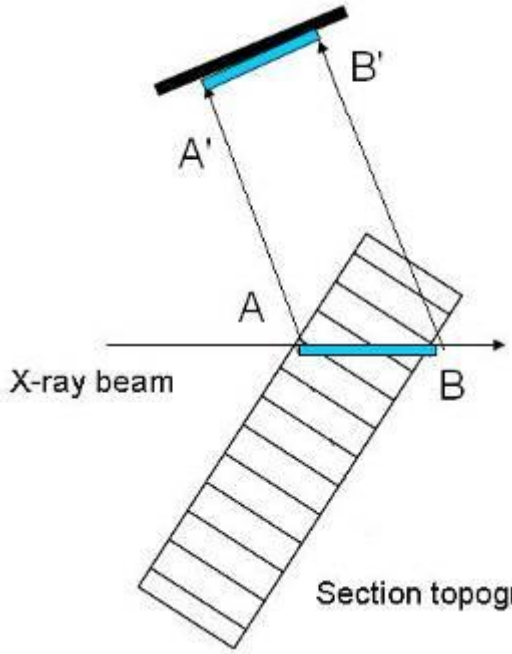

Figure 7.1 - Reflection imaging of diamond (image plate not to scale)

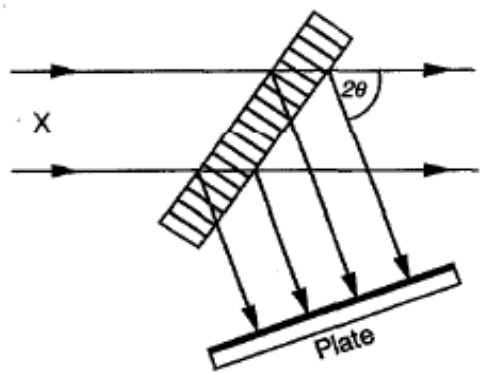

Symmetrical Laue geometry

Condition for X-ray diffraction

nλ = 2dsinΘ (Bragg's law)

n = integer
λ = x-ray wavelength
d = planes spacing
Θ = diffraction angle

Figure 7.2 - Transmission imaging of diamond (image plate not to scale)

The images were recorded on Polaroid film when aligning the crystal and then on x-ray film when adjusting the exposure time. Final images were recorded on nuclear plates, a 50μm thick x-ray sensitive emulsion spread on glass plates. The diffractometer and the beam delivery equipment are shown in figure 7.3, and the diamond in position in front of the beam exit point in figure 7.4.

Figure 7.3 - X-ray station 16.3

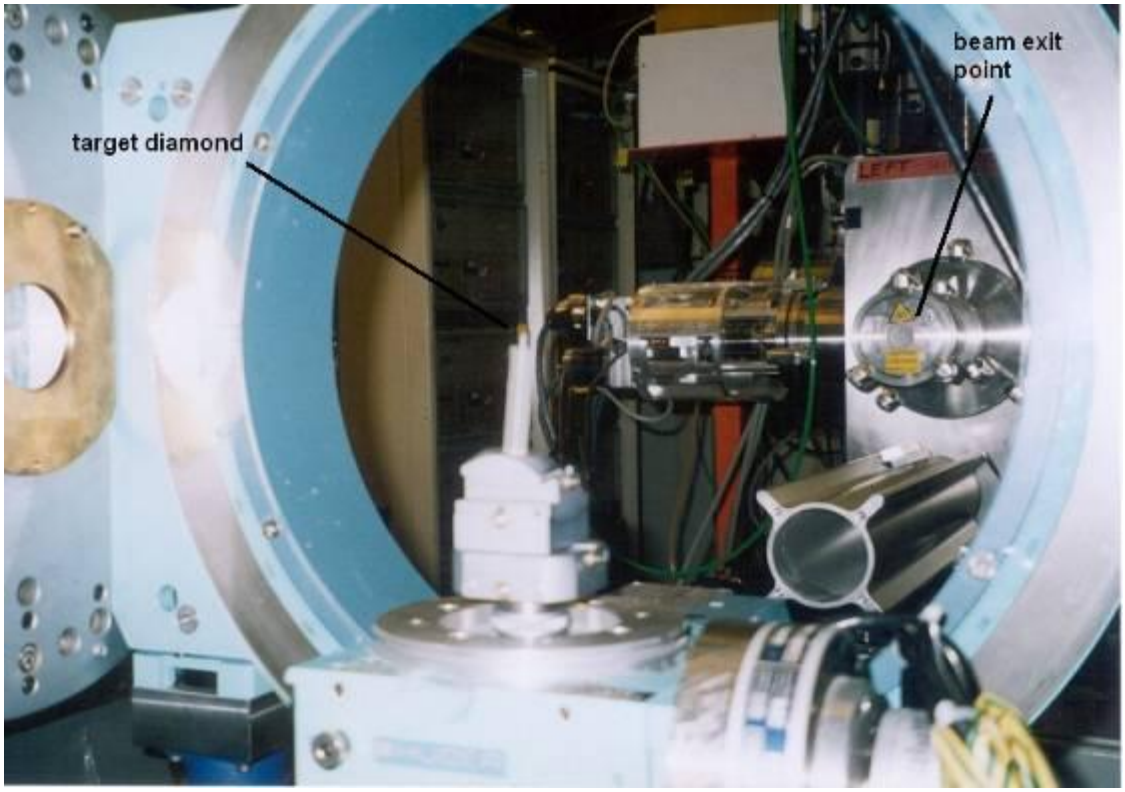

Figure 7.4 - Diamond in place in front of the beam exit point

The x-ray synchrotron studies of the diamond proved to be problematic. The exposure times required for the films and plates needed to obtain an image, but avoiding catastrophic over exposure, turned out to be less than a second. This was far less than had been predicted. With the short required exposure time the images recorded on film were as in figure 7.5.

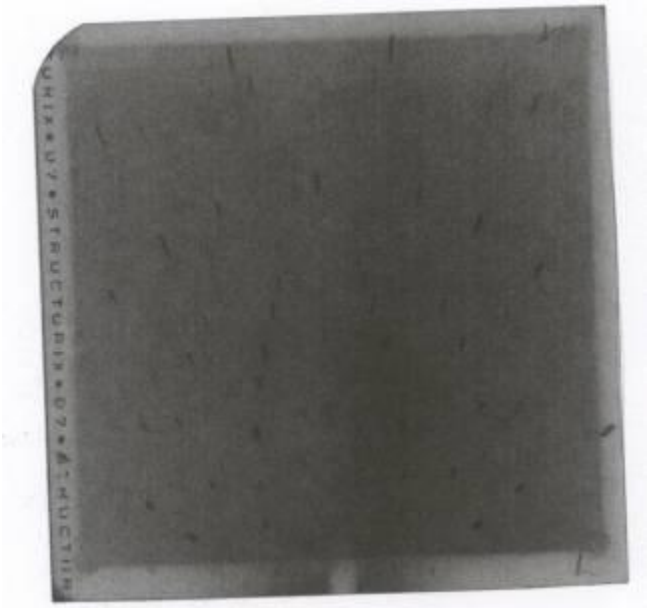

Figure 7.5 – X-ray film transmission image of diamond

Each black area on the film corresponds to a crystal plane in the diamond. The images for analysis of the internal structure were recorded on x-ray plates which have a higher resolution than films. Figures 7.6 and 7.7 are two sets of plates showing the reflected planes of the crystal. The information about the crystal structure is within each image of the diamond recorded on the plate. Enlarged images of some of the sub images are shown in figure 7.8.

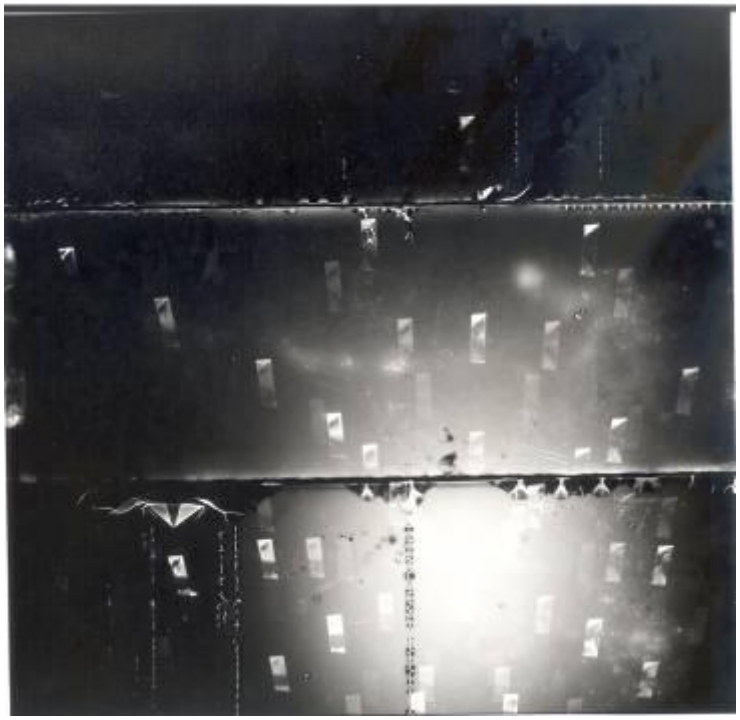

Figure 7.6 – Nuclear plate reflection image, 0.1x1.7mm beam through smaller side face of the diamond

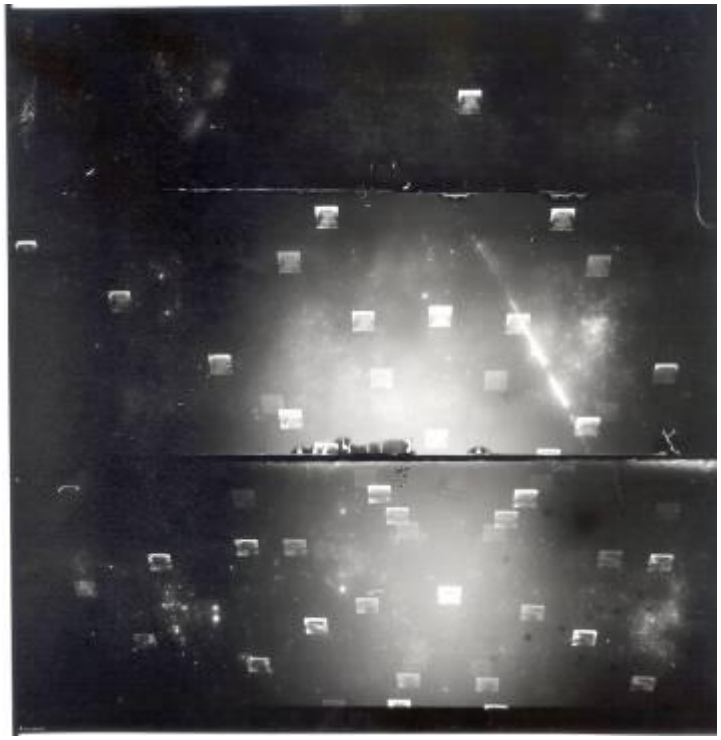

Figure 7.7 – Nuclear plate reflection image 0.1x4.4mm beam through large front face of the diamond

Figure 7.8 - Enlargement of detail from figure 7.7

The interpretation of these images requires experience and help was sought from Prof Moreton Moore at Royal Holloway University, he being an expert in this field who had helped us before we went to Daresbury. He concluded that useful information about crystal structure could not be gathered from the plates as the images were not of the highest quality due to our inexperience of working with x-rays. He also thought that, even if the plate images had been of better quality, the features of interest would have been too close to the resolution of the plate emulsion to be certain of exactly what had been recorded.

The failure of the x-ray work to provide answers to the questions about internal weaknesses generated by FIB machining means that the answers must be

provided by use of the tools generated. Unexpected or unusual failure modes of the tools will have to be examined if they occur.